NANYANG TECHNOLOGICAL UNIVERSITY
SINGAPORE

SMART WINDOW FOR TUNING TRANSPARENCY AND NOISE ABSORPTION

MILAN SHRESTHA

SCHOOL OF MECHANICAL AND AEROSPACE ENGINEERING

2019

SMART WINDOW FOR TUNING TRANSPARENCY AND NOISE ABSORPTION

MILAN SHRESTHA

School of Mechanical and Aerospace Engineering

A thesis submitted to Nanyang Technological University
in partial fulfillment of the requirement for the degree of
Doctor of Philosophy

2019

Statement of Originality

I hereby certify that the work embodied in this thesis is the result of original research, is free of plagiarised materials, and has not been submitted for a higher degree to any other University or Institution.

22/04/2019 Milan Shrestha

. . . .

Date Shrestha Milan

Supervisor Declaration Statement

I have reviewed the content and presentation style of this thesis and declare it is free of plagiarism and of sufficient grammatical clarity to be examined. To the best of my knowledge, the research and writing are those of the candidate except as acknowledged in the Author Attribution Statement. I confirm that the investigations were conducted in accord with the ethics policies and integrity standards of Nanyang Technological University and that the research data are presented honestly and without prejudice.

22/04/2019

. . . . . .

Date

. . . . . .

Associate Professor Liu Erjia

Authorship Attribution Statement

This thesis contains material from four paper(s) published in the following peer-reviewed journal(s) where I was the first and/or corresponding author.

Chapter 4 is published as M. Shrestha and G.-K. Lau, "Tunable window device based on micro-wrinkling of nanometric zinc-oxide thin film on elastomer," Optics Letters, vol. 41, p. 4433, 2016.

The contributions of the co-authors are as follows:

- A/Prof Lau Gih Keong provided the initial project direction and edited the manuscript drafts.

Chapter 5 is published as M. Shrestha, A. Asundi, and G.-K. Lau, "Smart window based on electric unfolding of microwrinkled TiO2 nanometric films," ACS Photonics, vol. 5, pp. 3255-3262, 2018.

The contributions of the co-authors are as follows:

- I wrote the drafts of the manuscript. The manuscript was revised together with A/Prof Lau Gih Keong and Prof A. Asundi.

Chapter 8 is published as Z. Lu, M. Shrestha, and G.-K. Lau, "Electrically tunable and broader-band sound absorption by using micro-perforated dielectric elastomer actuator," Applied Physics Letters, vol. 110, p. 182901, 2017.

The contributions of the co-authors are as follows:

- I assisted in idea formulation and fabricated all the test samples. I designed all other experimental setup and conducted all experiments. I derived the Mechanics formulation.
- Dr. Z. Lu provided the initial project direction. He also assisted in obtaining the theoretical and experimental data for acoustic absorption curves.

- A/Prof Lau Gih Keong edited the manuscript drafts and aided in the idea formulation.

Chapter 9 is published as M. Shrestha, Z. Lu, and G.-K. Lau, "Transparent Tunable Acoustic Absorber Membrane Using Inkjet-Printed PEDOT: PSS Thin-Film Compliant Electrodes," ACS applied materials & interfaces, vol. 10, pp. 39942-39951, 2018.

The contributions of the co-authors are as follows:

- I devised and fabricated the test samples and fabrication procedure. I conducted all the experiments and I prepared the manuscript draft.
- A/Prof Lau Gih Keong edited and revised the manuscript drafts and added valuable insights.
- Dr. Z. Lu assisted in obtaining the experimental data for acoustic absorption curves.

22/04/2019 Milan Shrestha

. . . .

Date Shrestha Milan

Acknowledgment

I would like to heartily express my gratitude to the following people who have helped me in my research work. First, I express my sincere gratitude to my supervisor Asst. Prof Lau Gih Keong for his patient guidance, continuous support, and encouragement throughout the course of the research. Regular meetings and discussions with him have been a great motivating factor to carry on with my work. I am equally thankful to Prof Anand Krishna Asundi for his valuable suggestions and continuous guidance during my research work. In addition, I really appreciate the technical assistance and guidance from Dr. Lu Zhenbo, Dr. Mohan Rosmin Elsa, Dr. Anansa Sasha Shakil Ahmed, Mr. Pek Soo Siong, Mr. Cheo Hock Leong and all technical staff from different labs at Nanyang Technological University (NTU) who helped me with their knowledge, skill and warm-hearted gesture. I also extend my gratitude to my friends and lab-mates Mr. Chin Yao Wei, Mr. Tan Wei Yee, and all friends in Mechanics of Microsystem lab and Materials Lab 1 for their assistance. In addition, I would also like to acknowledge Singapore Centre for 3D Printing (SC3DP), NTU and Singapore Millennium Foundation (SMF) for supporting my Ph.D. projects. Finally, I express my heartfelt thanks to my father Mr. Krishna Kaji Shrestha, my mother Mrs. Radha Shrestha, my brothers Mr. Hari Babu Shrestha, Mr. Badri Babu Shrestha, my sister Mrs. Mamata Shrestha, friends Mr. Niroj Maharjan, Miss. Shilpa Manandhar, Mr. Dipu Manandhar, Mr. Ujjal Manandhar, Mr. Pradeep Shakya, Mr. Rakesh Katuwal and all other family and friends for their continuous blessing, love, and support.

Table of Contents

List of Figures

List of Tables

Abstract

Sound and light are everywhere in a city. The unwanted noise of traffic and direct or reflected glares of the sun are annoyances to urban residents which adversely affects the urban livability. As parts of the high-rise-building facades, smart windows could mitigate the sound-and-light pollutions by replacing the conventional glass glazing and curtains.

Existing solutions of smart windows are imperfect and costly for simultaneous control of light transmission and sound absorption. For example, an optical smart window based on polymer dispersed liquid crystals (PDLC) ages when exposed to UV for years; an electrochromic window is pricey and prone to leakage; micro-perforated glass absorbers are only effective to absorb mid-frequency sound over a moderate bandwidth. Their absorption spectrum is fixed and was not tunable to target spectrum variation of noise. Alternative technology of smart window is in need of tunable acoustic and optical properties.

This work presented novel smart windows capable of regulating the light transmission and the sound absorption. Being useful for daylighting and privacy, the smart optical window can switch between transparent and opaque. In addition, they can be equipped with a transparent micro-perforated dielectric elastomer actuator (DEA) for tunable and broader sound absorption. These smart windows can be used to make green smart building and could potentially enhance the urban livability.

While glass is the choice of material for making a window panel, the rigidity of glass prohibits its electro-mechanical activation to tune its optical and acoustic properties. Instead, soft dielectric elastomers are preferable as electroactive materials. Recently, dielectric elastomer actuators (DEA) with metallic or graphene electrodes were used to make tunable window devices. Their surface roughness is variable by means of surface microwrinkling or unfolding through dielectric elastomer actuation. As a tunable optical surface scatter, it turns transparent with a smooth surface like a flat glass; but it turns ‘opaque’ (translucent) with the micro-rough surface. However, nanometric metallic thin films are not clear enough while few-layer graphene electrodes cannot be frosted enough

to switch between clear and translucent. In addition, they needed a large area strain to unfold the microwrinkles, covering only a small fraction of the window. These issues motivate the present development of tunable optical films based on microwrinkling of TiO2 and poly (3, 4-ethylene dioxythiophene)-poly styrene sulfonate (PEDOT-PSS) thin films on a dielectric elastomer. While using a low-strain induced microwrinkling and unfolding, these optical tunable devices exceed the performance of a PDLC based smart window device.

Recently, a tunable acoustic membrane absorber has been developed based on a membrane DEA. Its resonant frequency is tunable by controlling membrane tension through voltage activation. While the peak absorption is high, the absorption bandwidth for this absorber is very narrow. To solve this problem, this work developed a micro-perforated dielectric elastomer actuator (MPDEA) absorber with tunable acoustic absorption spectrum. The elastomer membrane's tension and holes diameter are changed using voltage activation; this, in turn, tunes its acoustic resonant frequency. In addition, PEDOT:PSS thin film electrodes were ink-jet printed on the elastomer substrate to make transparent MPDEA absorber, which promises to make large-area tunable absorber for windows.

Chapter 1 Introduction

1.1 Background

Glass panels are widely used as transparent facades to buildings. They are optically transparent to allow daylighting while being acoustic barriers to isolate the outdoor noise. However, these transparent glasses cannot be tuned to provide privacy in the buildings. In addition, the glass panels reverberate sound in a large indoor space [1]. This indoor echo reduces the speech intelligibility, for example in a crowded restaurant [2-4].

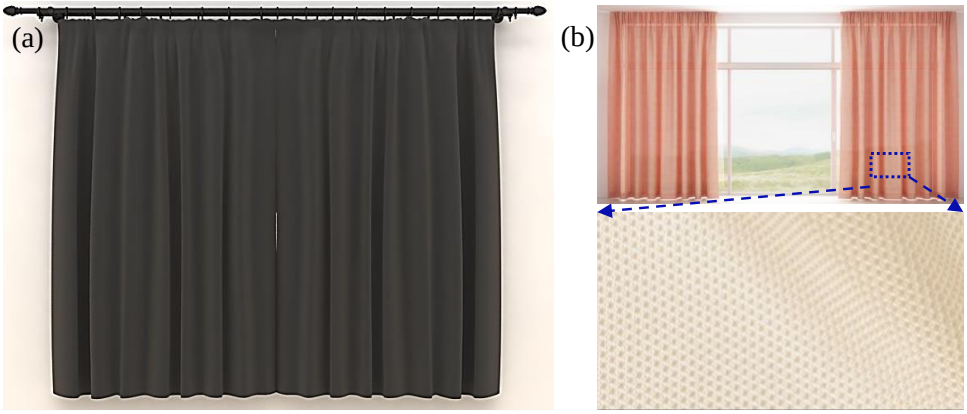

Figure 1-1. Curtains for blocking visibility and absorbing sound: (a) Opaque and porous absorber type curtain; (b) Translucent perforated curtain (Absorber Light, Gerriets GmbH (adapted from [5]).

There are needs for window solutions to regulate optical visibility and absorb sound. Curtains are the simplest solution but require manual handling. Opaque textile curtains can provide privacy by blocking light (see Figure 1-1(a)); being porous acoustic absorbers, curtains can also attenuate the indoor noise [6]. Yet, curtains cannot allow light transmission while absorbing sound. A translucent sound-absorbing curtain provides a solution to this need. For example, Absorber Light curtains developed by Gerriets GmbH can absorb sound while allowing diffuse lighting (see Figure 1-1(b)) [5]. But, it is a hassle to manually open and close large curtains to regulate visibility.

Glasses can be manufactured for a specific optical or acoustic property. For example, frosted glasses can diffuse light; tinted glasses can absorb light; perforated glasses can absorb sound [7-9]. However, the optical or acoustic properties of these glasses are fixed. The frosted glass cannot turn to be clear once manufactured. Likewise, the resonant frequency and the absorption spectrum of micro-perforated glasses are fixed once manufactured. A novel smart window can actively tune the acoustic absorption spectrum and optical transmittance to regulate the indoor ambiance. This regulation ensures a comfortable indoor ambiance.

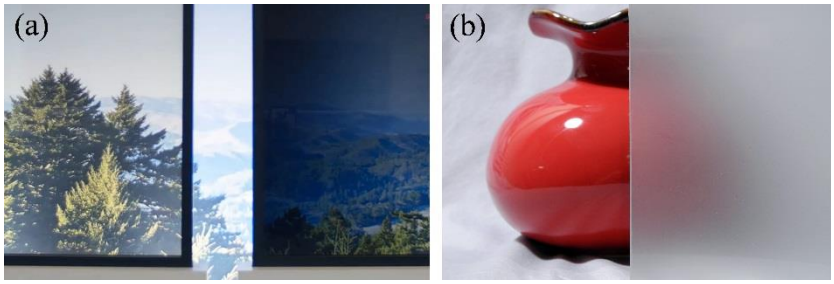

Figure 1-2. Transparency tuning by commercial smart windows based on: (a) Electrochromic devices; (b) Polymer dispersed liquid crystal devices.

Existing smart windows can switch between transparent and opaque or translucent by changing their optical properties. They are used to regulate the indoor daylighting while providing privacy as an indoor partition. Current technologies of commercial smart windows are based on (1) electrochromic glasses [10, 11], (2) polymer-dispersed liquid crystal (PDLC) devices [12, 13] and (3) suspended particle devices (SPD) [14]. Electrochromic devices having a battery construction can change color and thus absorb light upon charging or discharging of the electrochromic layer (see Figure 1-2(a)). PDLC devices is a polymer matrix that is impregnated with the liquid crystal droplets. The PDLC device appears milky due to refractive index inhomogeneity of the randomly oriented birefringent liquid crystal droplets. AC Activation turns the PDLC to appear clear by aligning the orientation of liquid crystals such that its refractive index is directionally matched with the solid polymer matrix (see Figure 1-2(b)). Similarly, SPD

can operate like a blind or light shutter by electrical re-orientation of the light absorbing nanorods which was initially randomly oriented.

Common existing technologies of smart windows are costly for adoption. For example, a PDLC costs $200 per square foot [10]. In addition, the complex construction of electrochromic devices leads to high manufacturing cost and worsen the durability. Speed can be an issue for electrochromic windows which takes 5 minutes to switch (a $0.01m^2$ panel) [15]. The transparency tuning range of PDLC and SPD are limited. Their clear state is not so transparent and ranges between 50% to 80% transmittance [14]. Moreover, their power consumption is high over a large area. Furthermore, aging can decolorize an electrochromic window or deteriorate the birefringent liquid crystals in PDLC. This will fail the tunability of the optical transmittance. (refer to Table 1-1 for a detailed comparison).

Table 1-1. Performance comparison of existing transparency tuning smart windows.

Smart window [Ref]	Substrate	Transmittance change@550nm	Response time	Power	Sale price (brand) as in 2016
Electrochromic [11, 14]	Glass	5%-65%	300sec (5x20 cm2)	0.1-0.5 Whr/sq.m	$1000/sq.m (View glass)
Polymer dispersed liquid crystal [14]	Polymer composite	6%-62%	500 ms	5-20 W/sq.m	$396/sq.m (sonte) $100-300 (Alibaba)
Suspended Particle Device [14]	Glass	2.4%- 59%	100-200 ms	1.9-16 W/sq.m	-

The transparent sound absorber is recently proposed to be installed next to window glazing for dampening the indoor noise (echo) [7-9] (see Figure 1-3). The existing solutions are micro-perforated glasses and porous translucent curtains [6, 16]. The porous translucent curtains can absorb broadband sound from low-frequency to mid-high frequency. These curtains which are made of weaves of transparent fabrics, however, are optically diffusive (refer to Figure 1-1). In comparison, micro-perforated glass is good at

absorbing the mid-frequency sound over a moderate bandwidth due to the nature of acoustic resonance (see Figure 1-4(c)). They are proposed to be integrated into the modern architecture which makes use of structural glass panel (see Figure 1-3). So far, the absorption spectrum of these transparent or translucent absorbers is fixed and thus cannot be adjusted to match the varying indoor noise spectrum.

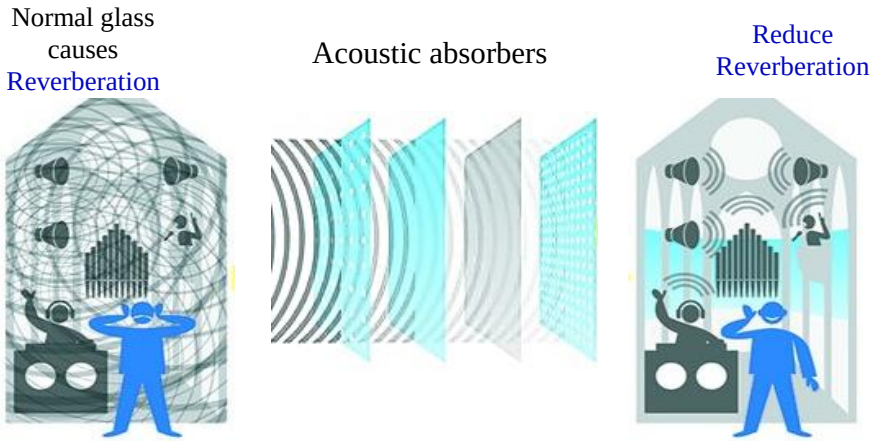

Figure 1-3.Effect of sound absorbing glasses in dampening reverberation in a room (adapted from [17]).

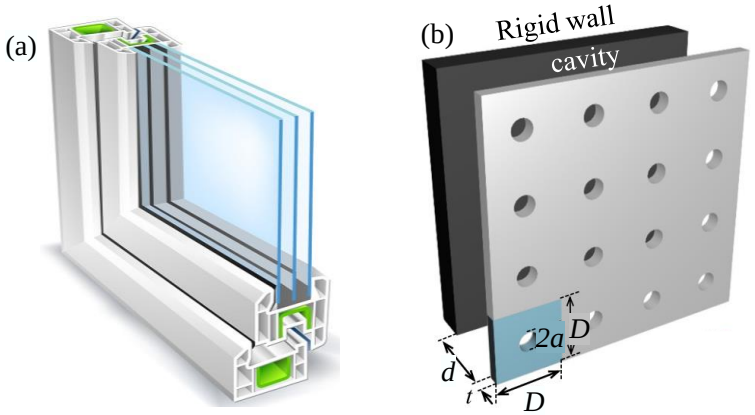

Multiple window glazing Micro-perforated panel absorber

Figure 1-4. (a) Transparent triple glazing windows for soundproofing house (adapted from [18]); (b) micro-perforated panel absorber for windows (adapted from [19]).

1.2 Motivation and Objectives

While glass is the choice of material for making a window panel, the rigidity of glass disables its electro-mechanical activation for variable optical and acoustic properties. Instead, soft dielectric elastomers are the choice of electroactive materials to make a capacitive actuator for tunable optics and acoustics. A soft capacitive actuator or dielectric elastomer actuator (DEA) in short can undergo a large deformation under Maxwell stress upon high-voltage activation. With active strain and stress comparable to natural muscles, DEAs were initially used to drive bioinspired robots, such as human-like robotic arms and robotic fingers. Their maximum active stress is less than 1MPa because soft dielectric elastomer shows limited strength, mechanical and electrical.

Recently, dielectric elastomer actuators found new applications in tunable optics and acoustics as the silent distributed actuators. In the application to tunable optics, DEA drives either a deformable lens for variable focal length or tune the optical transmittance (light diffusion) of a smart window. In the application of the tunable acoustics, a DEA can be used as a loudspeaker or an acoustic membrane absorber. These DEA tunable devices can potentially realize a smart window capable of optical and acoustic tuning. However, the performance of the reported transparency tunable windows are merely average as compared to the commercial PDLC or electrochromic devices [20-24]. For example, the DEA-based window devices using crumpled graphene cannot switch to be fully frosted for concealing images [22]. In addition, large area strain (>50%) is required to switch to a frosted state, making it impractical to be a window device. Further, the previous prototype of DEA based tunable acoustic membrane absorbers are not transparent and their acoustic absorption bandwidth is narrow.

This project is thus motivated to develop a novel window device for tunable optical transmittance and acoustic absorption. For a window device of variable optical transmittance, additional challenges of device design lie with the need for microwrinkle-formation at a low area strain (possibly less than 5%). To this end, we first use a nanometric optical coating of high-refractive-index oxides to form microwrinkles on a soft dielectric elastomer substrate. For a transparent acoustic absorber, the challenges lie

with the need for transparent compliant electrodes and the achievement of tunable broadband absorption. To this end, we first use PEDOT:PSS as a transparent compliant electrode and first realized a tunable micro-perforated membrane absorber with voltage-variable hole size. Finally, we shall integrate these DEA-based devices for tunable optics and tunable acoustic into a module of the multifunctional smart window (see Figure 1-5).

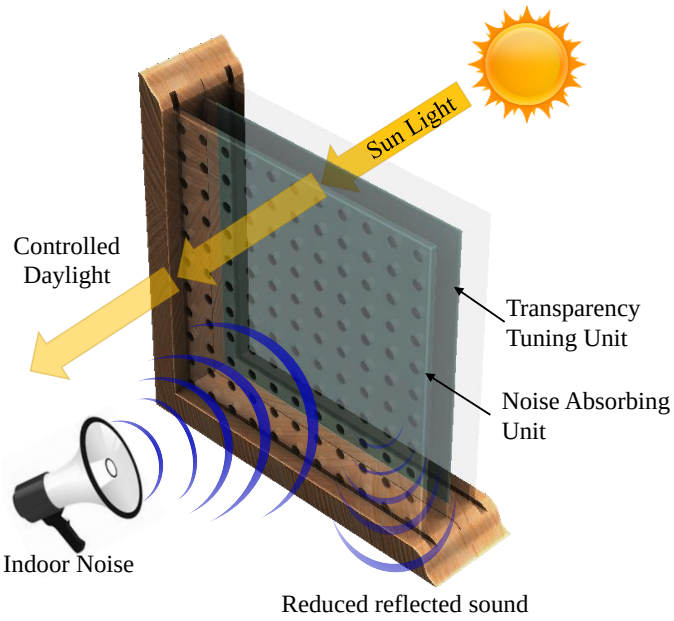

Figure 1-5. Schematic of the smart window made of two components, the first component can tune its transparency and second can absorb broader band noise while adapting to the varying noise frequency.

1.3 Novelty of the study

The novel contributions of this research work are: 1) material selection, design, and analysis of multilayer microwrinkled compliant electrodes for optical diffusers, and 2) design and development of transparent microperforated membrane absorber with tunable resonant frequency using voltage controllable hole-size in the microperforated dielectric elastomer actuators.

The existing smart windows based on microwrinkling is limited by their need of high area-strain (>50%) for transparency tuning. For the first time, this work showed microwrinkling of nanometric films of optical oxides such as ZnO and TiO_2 of high refractive index being effective to diffuse light down to 1-2% inline transmittance (very frosted) upon less than 5% axial compressive strain. Moreover, bulk ZnO and TiO_2 are hard and brittle. There was no previous work showing thin film of these materials can make a crack-free microwrinkled compliant electrode. Through theoretical analysis, we have shown that upon wrinkling even hard coating of TiO_2 can obtain compliance comparable to an elastomer substrate. In addition, we show crack-free reversible wrinkling and unfolding of a brittle coating like TiO_2 is possible provided the bending strain of the wrinkled thin film is lower than its fracture tensile strain. In addition, a conductive overcoat on the oxide film made of conductive polymer or metal provides electrical conductivity. Such multilayer thin film can make microwrinkled compliant electrode suitable for activating DEA and thus enables voltage induced unfolding of the microwrinkles to tune the transparency.

Moreover, existing tunable microperforated panel (MPP) absorber use impractical noisy stepping motors and moving parts. Here, we show the first proof of concept on DEA-based tunable MPP absorbers which can provide quiet actuation. We first devised a mechanism of tuning hole-diameter by activation of an MPDEA. Also, we developed an elastic model to predict the voltage-induced hole-diameter change. These MPDEA can shrink hole size by applying Maxwell stress that reduces the membrane's tension. This helps electrically tuning the resonant frequency of the DEA-based acoustic membrane. Consequently, the DEA-based absorber's peak-frequency can adapt to a varying broadband noise in real-time. This quiet and distributed actuation of DEA is suitable for large-area windows.

1.4 Organization of Thesis

This report presented two parts of the DEA-based smart window devices. In Part 1 Chapter 2-5 and presents the work on transparency tuning. In Part 2 Chapter 6-8 presents the work on tunable acoustic absorbers. The chapters are organized as follows:

Chapter 1 introduces the background and the motivation of this research.

In Part I, Chapter 2 reviews the literature on existing technologies of smart windows and some low-cost alternative for transparency tuning. The pros and cons of these devices will be discussed and compared. Chapter 3 presents the mechanics to make compliant electrode out of microwrinkled thin films. We shall review the material selection and fabrication technique to make conductive thin films. Chapter 4 presents the preliminary results of transparency tuning by mechanically microwrinkling of ZnO thin film on elastomer substrate. Chapter 5 presents electrically tunable optical diffuser as a smart window using hybrid multilayer of PEDOT:PSS/TiO_2 as the microwrinkled electrodes.

In Part II, Chapter 6 reviews the literature of acoustic absorbers and discusses the feasibility of using them for window appliance has been discussed. Chapter 7 presents the various DEA design and mathematical models suitable for tunable acoustic devices. Chapter 8 presents the novel tunable acoustic absorber based on micro-perforated dielectric elastomer actuators (MPDEA). Chapter 9 presents the inkjet-printing of PEDOT:PSS electrodes suitable for making DEA and tunable acoustic absorbers.

Finally, Chapter 10 concludes the thesis with a possible outlook for the future directions for this research.

Part I Transparency Tuning

Chapter 2 Review of Smart Optical Windows

This chapter reviews various technologies for active smart windows. Smart window glass or glazing can switch between transparent and translucent or opaque. Their optical transmittance is responsive to one of the following external stimuli; electric field, heat or light. Conventional commercial smart window technologies include: (1) electrochromic glasses, (2) polymer dispersed liquid crystal devices (PDLC) and (3) suspended particle devices (SPD). There are also new technologies recently developed and reported for active smart windows.

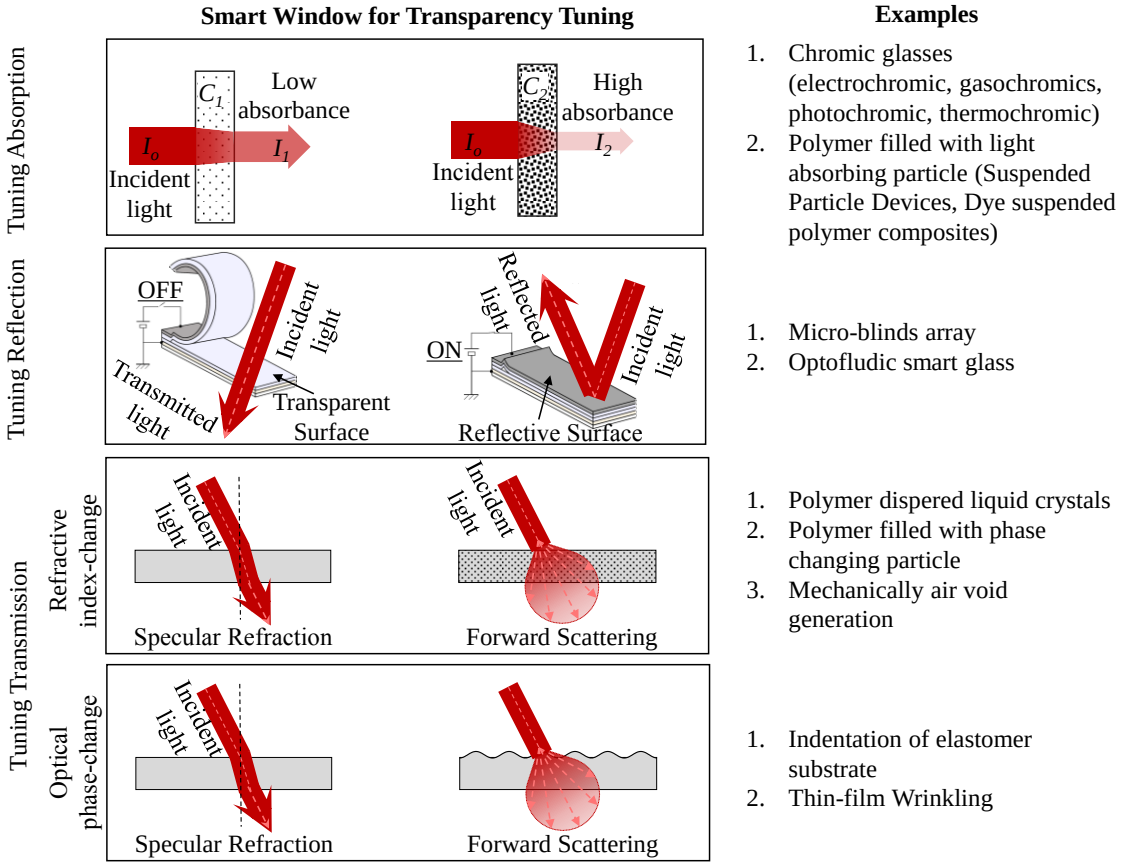

Figure 2-1. Classification of the smart window devices for transparency tuning according to optics principle.

Smart windows work on various optical principles, namely: (a) by tuning light absorption, (b) by tuning light reflection and (c) by tuning diffuse transmission [25].

Figure 2-1 classifies various smart window technologies according to the three optical principles. For example, electrochromic glass or SPD shows tunable optical absorbance and thus can alter the optical transmittance [26]. Meanwhile, optofluidic glasses and micro-blinds tune the reflection and thus alters the transmittance. Diffuse transmission or scattering can also reduce the optical clarity (visibility). It can be obtained firstly by tuning the refractive index of the blended particles and secondly by the optical phase difference. For example, PDLC appears hazy by light scattering across the interfaces between liquid crystal droplets with random anisotropic refractive index and the polymer matrix (i.e. material phase difference). It switches to be clear when the liquid crystal droplets are realigned to have the normal refractive index matched with the polymer matrix's refractive index. On the contrary, rough surfaces of the transparent optical medium can scatter light by means of random optical path difference (i.e. optical phase). For example, while a flat glass is clear; a ground glass appears hazy. Hence, tunable surface roughness provides a means for tunable optical diffusion and thus change the specular optical transmittance.

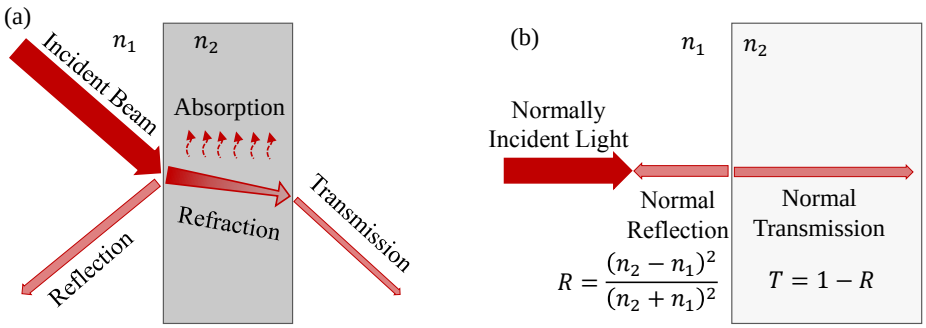

Figure 2-2. Schematic showing: (a) light reflection, absorption, and transmission; (b) same for normal incidence.

When a light beam interacts an optical medium, it is partially transmitted, reflected, and absorbed (see Figure 2-2(a)) [27-29]. The ratio of the transmitted, reflected, and absorbed light intensity to incident intensity is called transmittance (*T*), reflectance (*R*) and absorbance (*A*) respectively. For example, clear glasses usually have fixed transmittance of 90-92%, reflectance of 6-8% and the absorbance of 2-4%. Based on energy conservation, the transmittance, reflectance, and absorbance follow the relationship:

$$R + A + T = 1 \quad \textbf{(2.1)}$$

This relationship suggests optical transmittance can change in response to the change of absorbance and reflectance.

Due to the ease of measurement, the performance of smart window devices is usually measured in terms of inline or specular optical transmittance. Inline or specular transmittance is defined as $T_{spec} = I_{spec}/I_o$, i.e. the ratio of the specular transmitted light intensity I_{spec} to the incident light intensity I_o. A specular transmittance of $T_{spec} = 1$ suggests perfect optical clarity; whereas $T_{spec} = 0$ suggests complete translucence or opacity. These smart window technologies are further discussed and compared in subsequent sections.

2.1 Conventional Smart Windows

Smart windows have been around for decades. They have been used in airplanes like Boeing 787 Dreamliner, in cars like Mercedes-Benz SLK and in corporate buildings. These commercial smart windows are based on one of the following technologies: (1) electrochromic glasses, (2) polymer dispersed liquid crystal devices (PDLC) and (3) suspended particle devices (SPD).

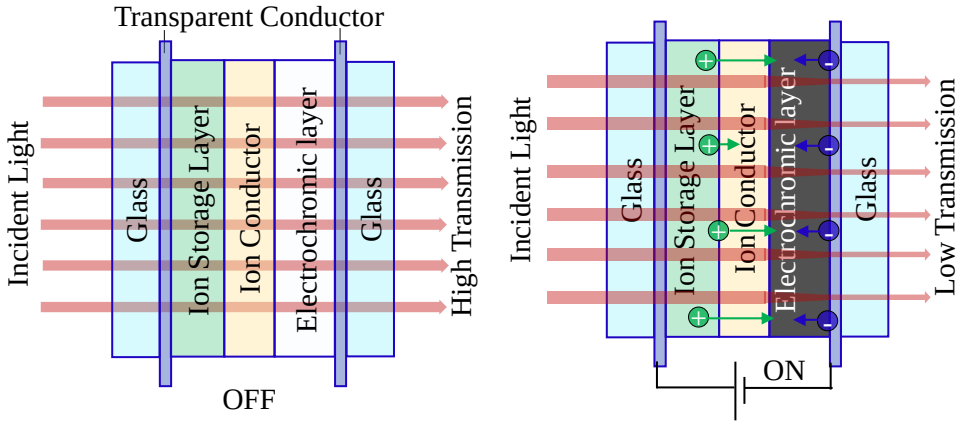

Figure 2-3. Schematic diagram of an electrochromic glass at: (left) Off state; (right) On state.

Electrochromic glasses can change color thus tunes the amount of light absorption. They consist of an electrochromic, electrolyte and ion storage layer sandwiched between two transparent conductive layers. The electrochromic materials are mostly based on inorganic materials like oxides of tungsten and nickel [25, 26]. Some organic compounds based on viologens, anthraquinones, diphthalocyanines, and tetrathiafulvalenes can also make an electrochromic layer [30]. The inorganic electrochromic layer changes color as ions like H^+ and Li^+ are inserted or extracted from them by applying an electric field. Organic electrochromics achieve coloration by oxidation-reduction reaction.

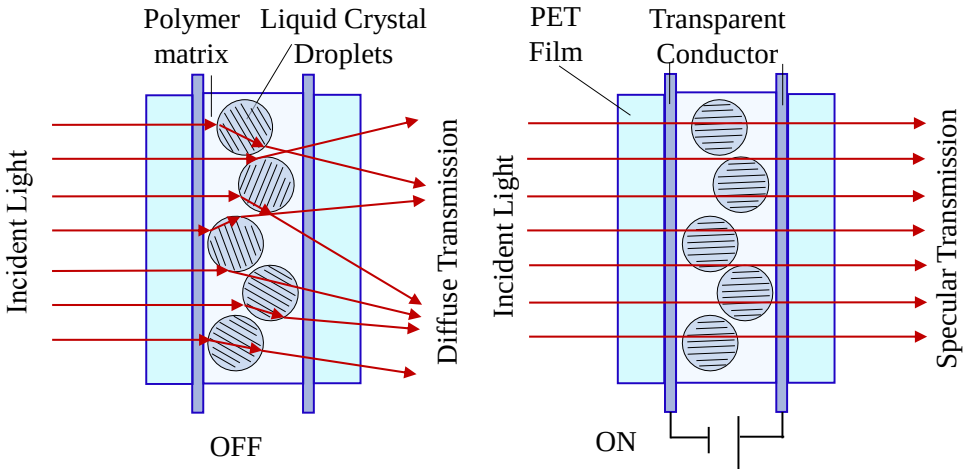

Figure 2-4. Schematic diagram of a smart window based on polymer dispersed liquid crystals at: (left) Off state; (right) On state.

PDLC can tune light scattering to switch between hazy and clear. It consists of micrometer-sized liquid crystals droplets dispersed in a polymer matrix. This matrix is sandwiched between two transparent conductive films like ITO. The liquid crystals are birefringent materials with different refractive index along different orientations. For example, MLC-9200-100 is a commercial liquid crystal with an orientation dependent refractive index of n_e=1.61 (along extraordinary orientation) and n_o=1.49 (along ordinary orientation) for the light of 550nm [31]. The polymer matrix is chosen such that its refractive index matches the liquid crystal's ordinary index. At the off state, the liquid crystals of anisotropic refractive index are randomly orientated and thus they scatter incident light to appear hazy and milky [12, 30, 32]. They behave like optical shutters;

They become clear upon applying AC electric field, which normally reorients the liquid crystals such that their refractive index is matched with the polymer matrix's. This maximizes the specular transmission through the composite.

SPD can electrically tune the amount of light absorption. It consists of needle-shaped dipole particles suspended in organic liquid or gel matrix. The particles are made of ~1μm long polyiodides or paraphathite [30]. The matrix is sandwiched between two transparent conductive films. At off state, particles are randomly oriented to absorb light and appear opaque. Upon application of an electric field, the particles align to transmit more light and appear transparent (see Figure 2-5) [14, 30].

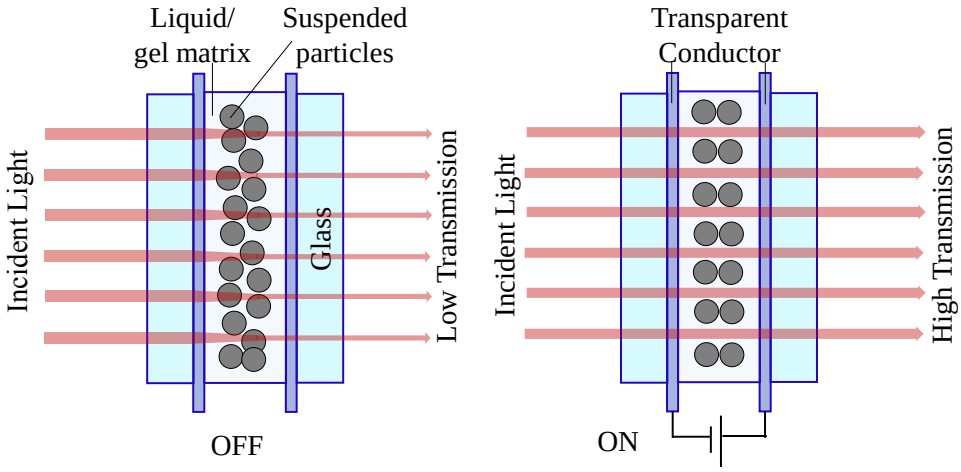

Figure 2-5. Schematic diagram of a suspended particle device at: (left) Off state; (right) On state.

Existing technologies of smart windows are costly for adoption. For example, a PDLC costs $200 per square foot [10]. In addition, the complex construction of electrochromic devices leads to high manufacturing cost and worsen the durability. In addition, activation of electrochromic windows is slow, e.g. a 0.01m^2 panel takes 5 minutes to switch [15]. The transparency tuning range of PDLC and SPD are limited. Their clear state is not so transparent and ranges between 50% to 80% transmittance [14]. Moreover, their power consumption is high over a large area. Furthermore, aging can decolorize an electrochromic window or deteriorate the birefringent liquid crystals in PDLC. This will

fail the tunability of the optical transmittance. (refer to Table 1-1 for a detailed comparison). There are a few new technologies which can replace the conventional smart windows. They are discussed in subsequent sections.

2.2 Tunable Light Absorption

This type of active smart window shows tunable optical absorbance. For example, electrochromic glasses tunes absorbance by using electrochemical reaction of the chromic layer (e.g. WO_3(transparent) + x(H^+ or Li^+ or Na^+) + xe^- ↔ (H^+ or Li^+ or Na^+)$_x WO_3$ (Blue)), which changes its color from light to dark [26]. According to Beer-Lambert law, the transmitted light (I) across an optical absorbent medium follows

$$I = I_o e^{-\mu h}, \tag{2.2}$$

where I_o is the incident intensity, h is the optical depth of the material and μ is the linear attenuation coefficient. The attenuation coefficient changes with the color change in the electrochromic glass. On the other hand, a suspension with light absorbing dyes can show variable light absorbance by changing the concentration of the dyes (see Figure 2-6 (a) and (b)). Linear attenuation coefficient of such dye-filled suspensions follows the relationship $\mu = \sigma C$, where C is dye concentration and σ is dye's cross-section area.

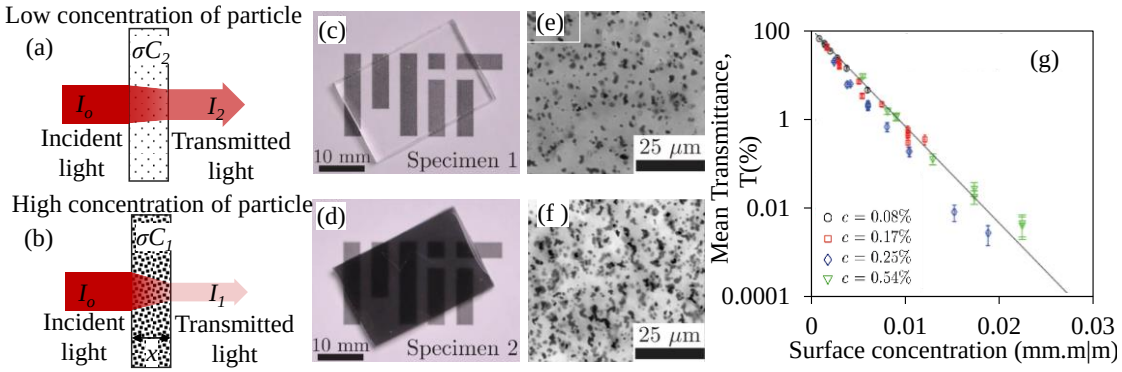

Figure 2-6. Schematic of the Beer-Lambert law of light absorption: (a) lower concentration of particles; (b) higher particle concentration; (c) and (d) visibility through polymer with low and high dye concentration; (e) and (f) the optical micrograph of the same polymers; (g) transparency changes with surface concentration of the dye. (adapted from[33])

Similarly, the dye-filled transparent polymer can absorb light. Its light absorption increases with increasing the dye concentration. Given a constant volume concentration, the surface concentration decreases by thinning of the dye-filled polymer. This provides a means of mechanical tuning of optical absorbance and eventually optical transmittance tuning of the dye-filled transparent polymer (see Figure 2-6(g)). Based on this principle, dye-suspended polymer composites shows tunable light absorption [33].

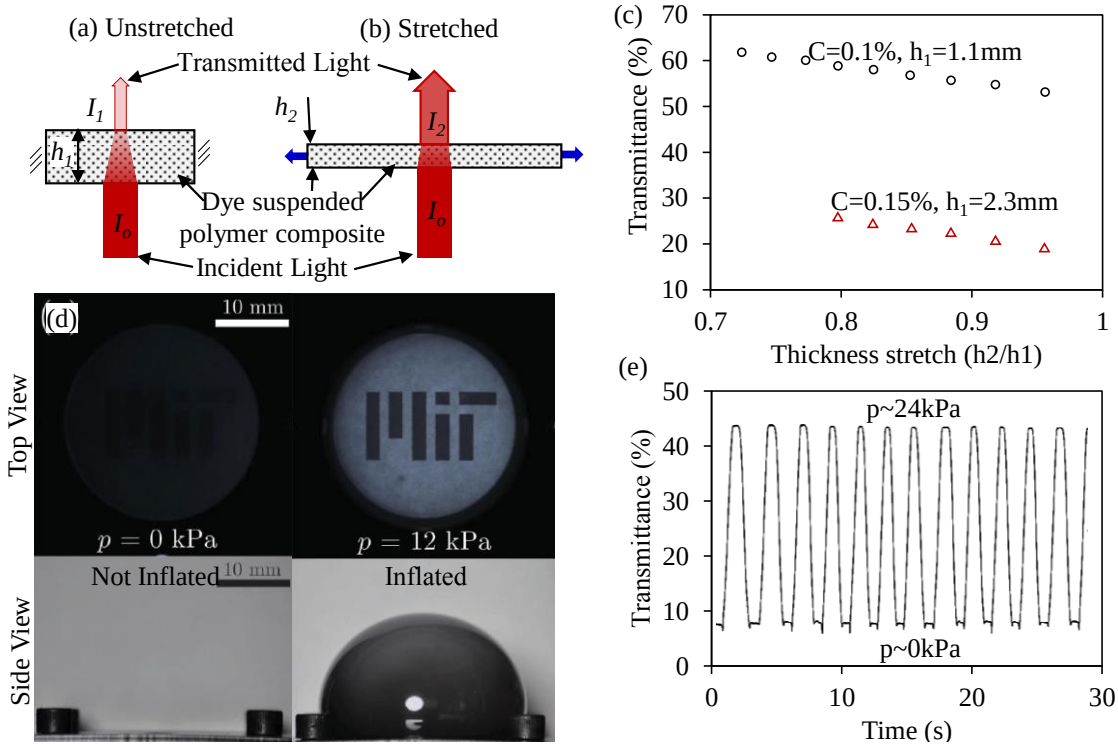

Figure 2-7. Tuning transparency by a stretch-induced reduction in surface concentration. Schematic showing change in the amount of light absorbed by mechanically thinning the dye suspended polymer: (a) unstretched state; (b) stretched to thin down; (c) Transmittance change of the same composite polymer with thickness stretch; (d) change in visibility obtained by inflating the balloon of the polymer composite with *C*=0.5% and h_o=1.8mm ; (e) plot of the corresponding transmittance change upon cyclic loading and unloading (adapted from [33]).

Dye-Suspended Polymer Composite. Dye-suspended polymer composites consist of micron-sized light absorbing dye particles dispersed in a transparent PDMS matrix. Their

light absorbance is related to the spatial density of the dye particles following the experimental correlation: $A = \log(e^{\mu h})$, where A is the light absorbance, μ is the linear attenuation coefficient and h is the polymer thickness. Tuning of the light absorbance is achieved by stretch-induced thinning of the polymer composite (see Figure 2-7) [33]. The composite polymeric membrane can be stretched by inflation and bulging like blowing a balloon (see Figure 2-7). This method of actuation demonstrates a transmittance change from 5% at 0kPa and 45% at 24kPa. The transmittance change is repeatable under cycles of inflation and deflation (see Figure 2-7(e)) [33]. Yet, the area strain required for this transmittance change is more than 100%.

2.3 Tunable Light Reflection

A smart window can also tune visibility by switching between a reflective and a transmissive surface. A typical mirror consists of a glass and a permanent reflective coating of silver. On the contrary, a switchable mirror can switch between a reflective metallic state and a transparent state with the formation of metal hydride. A microblind is developed to tune light reflectance by opening and closing bendable micro-mirror strips [34]. Meanwhile, optofluidic glasses change from the light transmitting state to total internal reflecting state upon filling its prism-shaped compartments with fluids [35].

Micro-blinds. Devices based on micro-blinds can switch between transparent to reflective by opening or closing their micro-apertures using reflective metal coated strips. As an ideal mirror, these strips can specularly reflect an incident light ray at an angle of the same magnitude as the incident angle with respect to the normal of the mirror surface. Reflection of the glass/metal interface follows Fresnel equations. For a light traveling from a medium of refractive index (n_1) at normal incidence to another medium of refractive index (n_2), the normal reflectance is given by Fresnel equation following (see Figure 2-2(b)) [36]:

$$R = \frac{(n_2 - n_1)^2}{(n_2 + n_1)^2} \quad \textbf{(2.3)}$$

When light is incident at an angle, it is partially transmitted along the angle of refraction and partially reflected following Fresnel equations. For example, at the interface between air and silvered mirror the reflection coefficient is as much as 80-90% at 550nm wavelength where n_1=1 for air and n_2=0.05 for silver.

The micro-blinds-based devices consist of an array of electrostatically reconfigurable roll-up micro-shutters. Each micro-shutter is made of microcantilever of laminated metal-SiO_2 and rolled up using the mechanical unimorph effect. At the inactive state, the laminates are rolled up to produce a micro-aperture of glass. These micro-apertures allow light to transmit and the device appears transparent. Voltage activation generates an electrostatic force to unroll the cantilever to reduce the micro-aperture. It covers the aperture by the reflective flat metalized cantilever and switches the device from its transparent state to a reflective view concealing state. These micro-blinds require 55V to tune mechanical aperture between 0% to 55% which consequently tunes optical transmittance from 36% to 53% respectively [34].

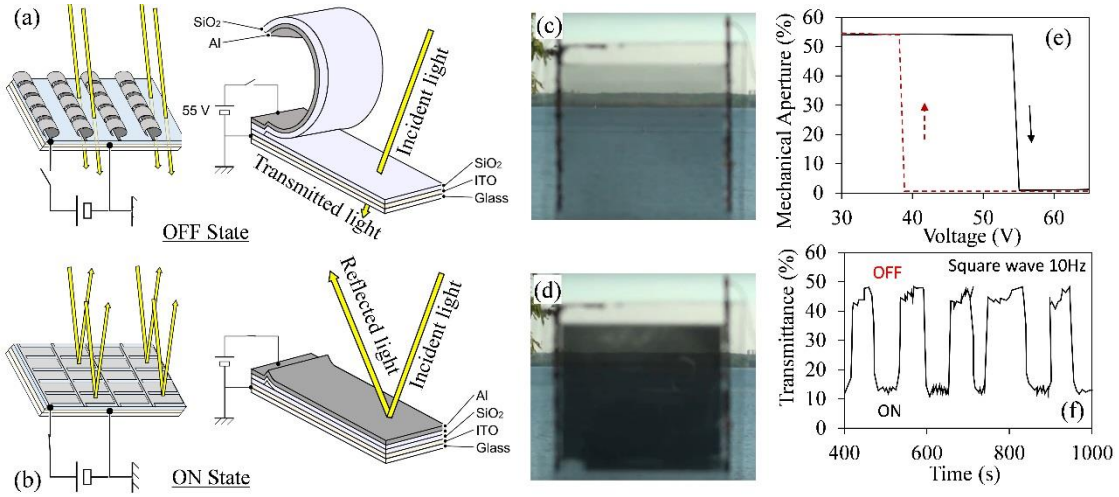

Figure 2-8. Schematic of an electrostatically reconfigurable roll-up micro-shutter array: micro-shutters arrays at; (a) inactive rolled-up state; (b) active unrolled state; Visibility at: (c) off state; (d) on state; (e) change in the aperture size with voltage activation; (f) change in transmittance with activation. (adapted from [34])

Optofluidic Smart Glass. Optofluidic glass uses total internal reflection to switch from transparent to opaque. Total reflection happens when the incident angle is greater or equal to the critical angle (θ_c) as derived from the Snell's law:

$$\theta_c = arcsin\left(\frac{n_1}{n_2}\right). \quad \textbf{(2.4)}$$

All the incident light is reflected by total internal reflection (see Figure 2-10(f)). For total internal reflection to occur the light must travel from a medium of higher refractive index (n_2) to the lower index medium (n_1). For example, a diver can observe the reflection of a fish due to total internal reflection (see Figure 2-9). Optofluidic smart glass utilizes this phenomenon which involves light transmission (refraction) across two optically transparent dielectric mediums of which one is replacable [35].

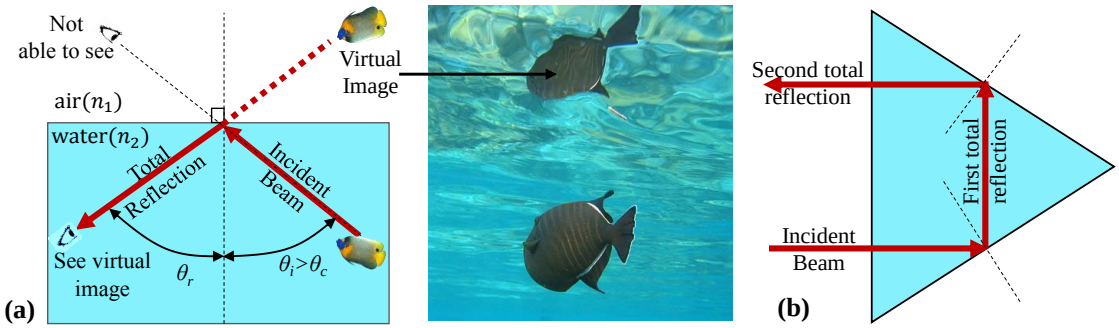

Figure 2-9. (a)(Left) Schematic of the total internal reflection; (Right) Real example of total internal reflection under water; (b) Total internal reflection in a prism.

Optofluidic smart glasses consist of a compartment with an array of prism-like corner cube reflectors (see Figure 2-9(b) and Figure 2-10(e and f)), made of transparent material (Vero Clear by Stratasys with a refractive index of 1.52 at 589nm) [35]. The corner cubes are designed such that the cube faces are angled more than $\theta_c = 41.14^o$ with respect to device normal. Hence, light traveling normal to the device is subjected to multiple total internal reflections between the material-air interface (retroreflective). This makes the device opaque. When the compartments are filled with refractive index matching fluid (methyl salicylate whose refractive index is close to Vero Clear), light simply refracts though it. Inline transmittance modulation from 85% to 8% has been demonstrated using

this method. Their optical transmittance varies with the viewing angle, for example, the transmittance increased to 63% when the air-filled device was tilted by 55°. Moreover, they need a fluidic pump for operation and involvement of liquid makes sealing and safety an issue.

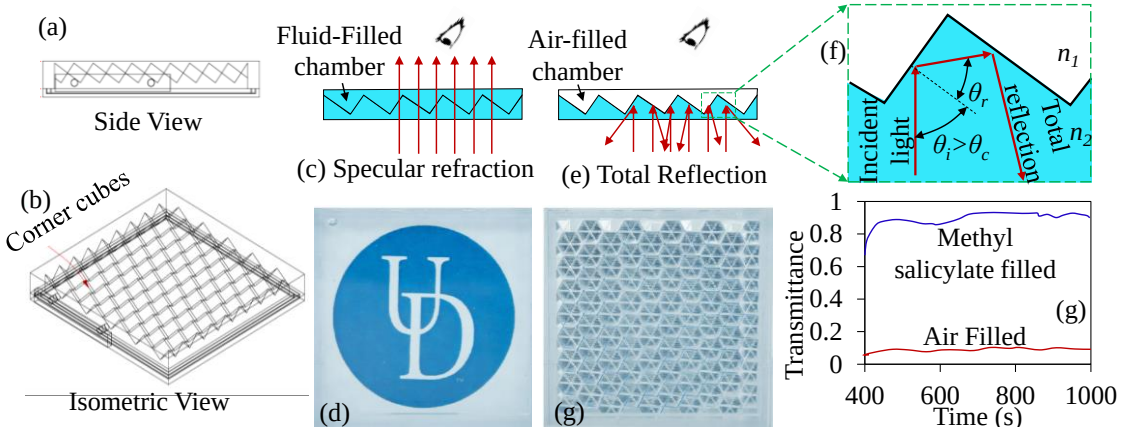

Figure 2-10. Schematic of an optofluidic smart glass: (a) side view; (b) Isometric view; (c) specular transmission through the chamber filled with refractive index matching fluids; (d) visibility through the same device; (e) total reflection when the chambers are empty; (f) magnified view illustration total internal reflection; (g) Transmittance of the device when empty and filled with methyl salicylate. (adapted from [35])

2.4 Tunable Optical Diffuser

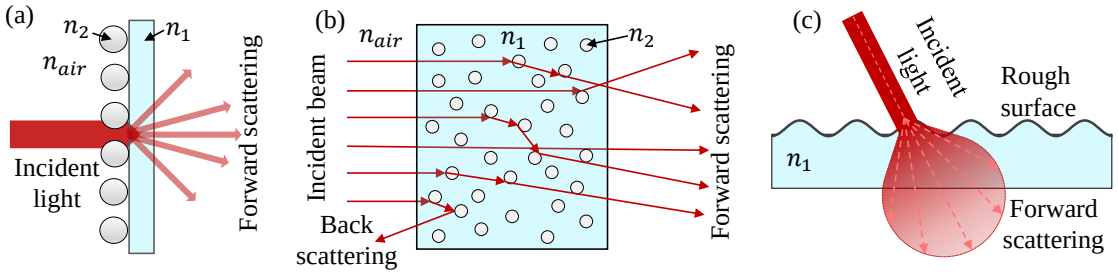

Figure 2-11. Various method of forward scattering of light. (a) by surface scatterer; (b) by bulk scatterer; (c) by a microrough surface.

An optical clear matrix or substrate can turn hazy or translucent in the presence of optical scatterer or diffusive materials. There are three types of scatterers, namely 1) surface

scatterer, 2) bulk scatterer, and 3) microrough surface. To tune the optical diffusion, active smart window device can vary micro-geometry of these inherently transparent light scatterers. First, surface scatterers are transparent particles or micro-defects on a transparent polymeric substrate. Second, bulk scatterer is transparent particles, micro-defect, or micro-droplet (of distinct refractive index) embedded in a transparent polymer matrix. Both bulk and surface scatterer consists of particles whose refractive index is mismatched form the substrate material to scatter light. Third, the micro-rough surface of a transparent media causes the random spatial distribution of optical phase and thus diffuses light.

2.4.1 Variable Scattering by Surface and Bulk scatterers

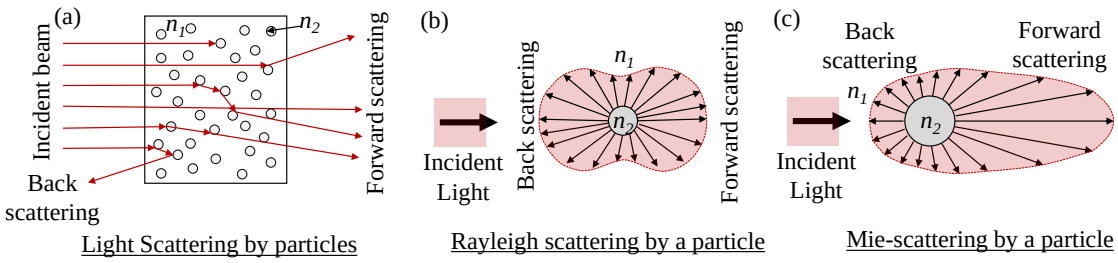

Figure 2-12. (a) Scattering of light by particles; (b) Rayleigh scattering and (c) Mie scattering of light by a particle.

Recently, tunable light scattering was demonstrated using variations in surface and bulk scatterers. A tunable diffraction grating was demonstrated by varying the spacing of the surface scatterer particles. Also, other work demonstrated haze tunability by changing the phase of the blended particles to tune its refractive index to match the polymer matrix's index. It was obtained firstly by the inclusion of air bubbles or voids in the polymer matrix. Secondly, the haze was tuned by melting bulk or dispersed paraffin in a polymer matrix.

In principle, both surface scatterer and bulk scatterer involves particle based light scattering to appear hazy. The principle of light scattering varies with scatterer size. Rayleigh scattering is the elastic scatter of light that happens to homogenous particles of a diameter smaller than the wavelength of incident light (see Figure 2-12(b)). Rayleigh scattering power is inversely proportional to the fourth power of wavelength. For

example, the presence of blue sky happens because air molecules scatter blue and violet light more strongly than they do to the yellow or red light of longer wavelength [29]. Mie scattering is the elastic scattering of light caused by particles of diameter similar to or larger than the wavelength of incident light (see Figure 2-12(c)) [37]. Mie scattering power is inversely proportional to the square of wavelength. Mie scattering power is stronger than Rayleigh scattering. Whitish appearance of fog and cloud is a result of Mie scattering by microscopic water droplets, dust, pollen and smoke in the fog or clouds.

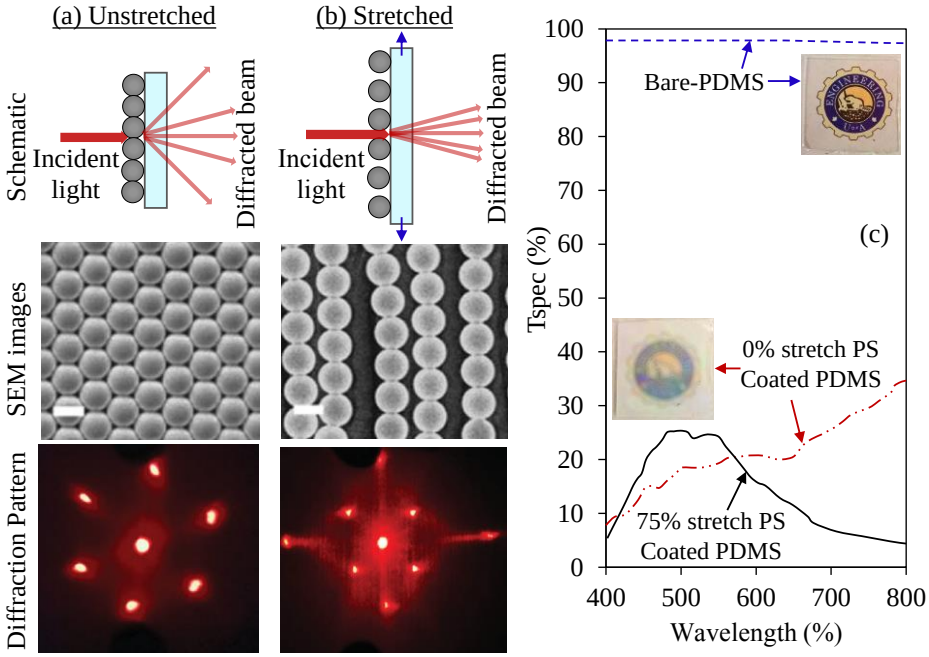

Figure 2-13. Mechanically stretching a PDMS substrate with PS microspheres assembled on its surface to make a tunable optical diffuser. Schematic diagram, SEM image, and corresponding diffraction pattern by the device: (a) at unstretched state, (b) when uniaxially stretched by 75%i to increase the particle distribution period; (c) corresponding change in the inline transmittance through the devices. (adapted from [38])

Tunable Diffraction Grating with Variable Spacing of Surface Scatterer. A tunable hexagonal diffraction grating was obtained by applying polystyrene (PS) nanosphere of 1μm diameter (and 1.58 refractive index at 550nm wavelength [39]) on the surface of0 a plasma-treated PDMS substrate [38]. This tunable hexagonal diffraction grating can blur out an image logo placed behind it but not completely conceal it. The PS nanospheres

were closely packed to form a hexagonal ball-grid array on the elastomeric substrate (see Figure 2-13). This hexagonal array of PS nanosphere can diffract a collimated laser beam into a hexagonal diffraction pattern, which consists of six minor bright spots at the vertices of hexagon and a major center spot. Stretch of the elastomer substrate can increase the distance between PS nanospheres. While its total transmittance is always high and independent of the stretch, the specular transmittance varies slightly with the stretch. For example, a 75% uniaxial stretch can increase the specular transmittance from 19% to 26%.

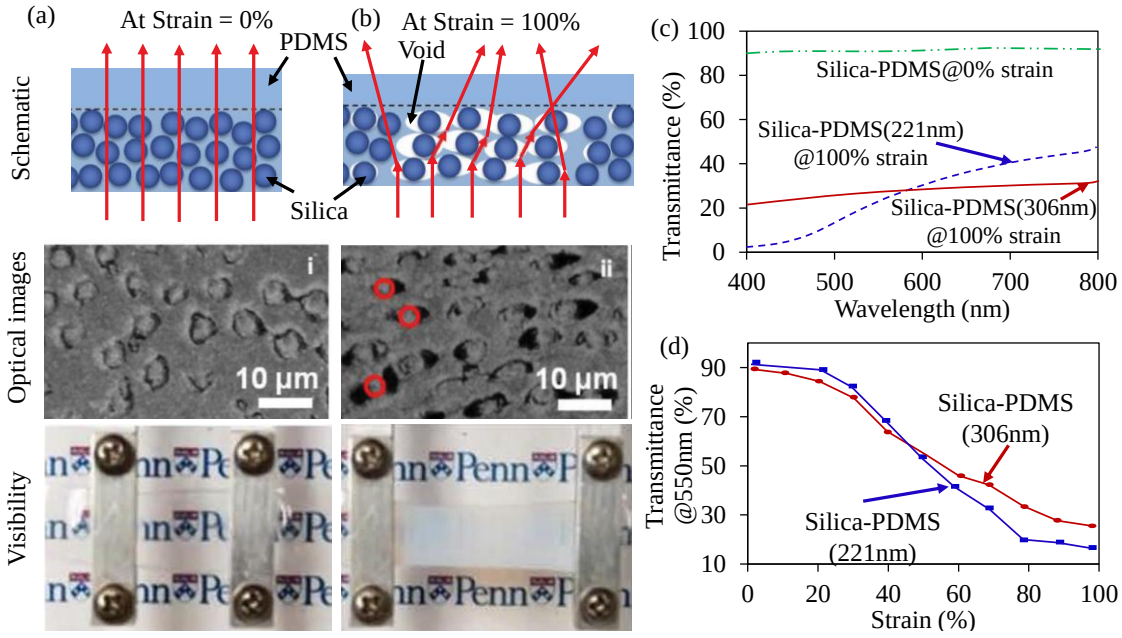

Figure 2-14. Formation of voids in a silica nanoparticle-PDMS composite upon mechanical strain: (a) Schematic illustration of unstretched composite (first row); optical image of the same (second row); corresponding visibility through the films (third row); (b) same composites when subjected to 100% strain; (c) compassion of the transmittance of the stretched composite with different nanoparticle size; (d) plot of change in transmittance upon straining the composite film. (adapted from [40])

Variable Void Formation. A blend of silica nanoparticles (of 1.457 refractive index at 632.8nm wavelength) in a silicone rubber matrix (of 1.423 refractive index at 632.8nm wavelength) makes a transparent elastomeric composite of nearly uniform distribution

of refractive index. The transmittance of the non-stretched nano-silica-elastomeric composite is as high as 90%. When this elastomer composite is subjected to a large mechanical stretch, air voids are formed around the silica nanoparticles due to the delamination of the elastomeric matrix. A stretch of 100% strain can introduce enough air voids to reduce the transmittance down to 20%. The air void volume V_{void} is estimated to be linearly proportional to the applied strain ε, following the relationship $V_{void} = \varepsilon V_{silica}$, where V_{silica} is the loading volume of silica nanoparticles [40]. Figure 2-14(c) shows the normal transmittance reducing with increasing the applied strain. It is noted that the strain-induced transmittance reduction of the 306nm-diameter silica-filled PDMS is gradual than of 221nm-diameter silica-filled PDMS. But, the reduced transmittance by the 306nm-diameter silica-filled PDMS is relatively less dependent on the wavelength of light. This suggests the scattering by the air void of 306nm-diameter silica-filled PDMS is mostly due to Mie scattering effect. Meanwhile, Rayleigh scattering is dominant for air voids of 221nm-diameter silica-filled PDMS.

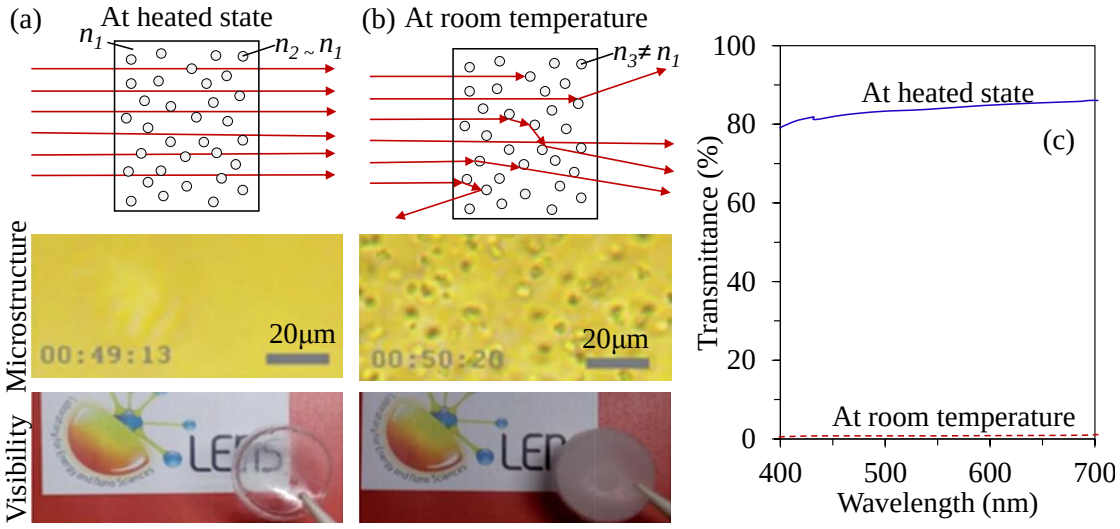

Figure 2-15. Paraffin-PDMS composite film which is transparent when heated and opaque at room temperature (a) Schematic of the light transmission through the heated composite (top row); corresponding microstructure (mid row) and the corresponding visibility through the films (bottom row); (b) Same for the composite at room temperature, Paraffine crystals are visible in the microstructure; (c) plot of the transmittance of the heated and cooled composite of 1.3mm thickness. (adapted from [41])

Melting Wax. Melting of Solid paraffin wax can change it from optically diffusive to a transparent state. Solid paraffin appears hazy or opaque due to the presence of crystallites of long alkyl chains that scatter light. Upon melting, the liquid paraffin becomes optically clear because the crystallites melt into an amorphous liquid [41, 42]. An elastomeric composite with homogenous microstructure can be obtained by dispersing and loading 10 weight % of paraffin crystals of 5μm diameter into a silicone elastomer pre-polymer matrix at room temperature (see Figure 2-15) [41]. Refractive index of the paraffin crystals is 7% higher than that of PDMS matrix at room temperature; this leads to the hazy appearance of the paraffin-crystal-elastomeric composite at room temperature. When being heated above 46°C, this paraffin-loaded elastomeric composite turns to be clear.

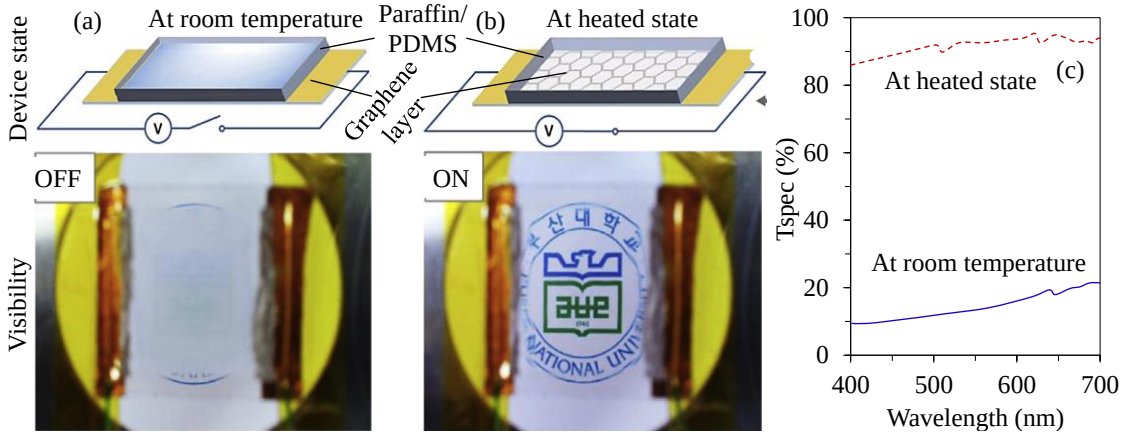

Figure 2-16. Paraffin-PDMS organogel layer with graphene film as a resistive heating element. Schematic of the device at (a) room temperature/ off state; (b) heated/on state; (c) specular transmittance of the device at heated and cooled states. (adapted from [43])

Another configuration of the device is based on a laminate of paraffin-PDMS organogel composite film sandwiched between a polyethylene terephthalate (PET) substrate and PDMS overcoat. It appears hazy (0.5% transmittance haze) below the 56-58°C melting point of paraffin. Electro-thermal activation of an integrated heater (graphene film on the PET substrate) at 18V and 0.33W/cm^2 can melt the paraffin and increase the transmittance to 85% [43].

2.4.2 Variable Surface Roughness

Another type of active smart window is based on a tunable optical diffuser with variable rough surfaces. This is motivated by the fact that a flat glass with smooth surfaces is optically clear while a ground glass with a rough surface is hazy or translucent. A flat glass allows specular transmission of light, which is refracted twice, first while entering through the air/glass interface and second while exiting the glass/air interface (see Figure 2-17(a)). Upon incidence on a rough surface, the light is scattered into different directions, deviated from the specular direction (see Figure 2-17(b)). Though the total transmittance across a perfect transparent material with diffusive surface remains constant, the specular transmittance becomes lesser to only a fraction of the total transmittance.

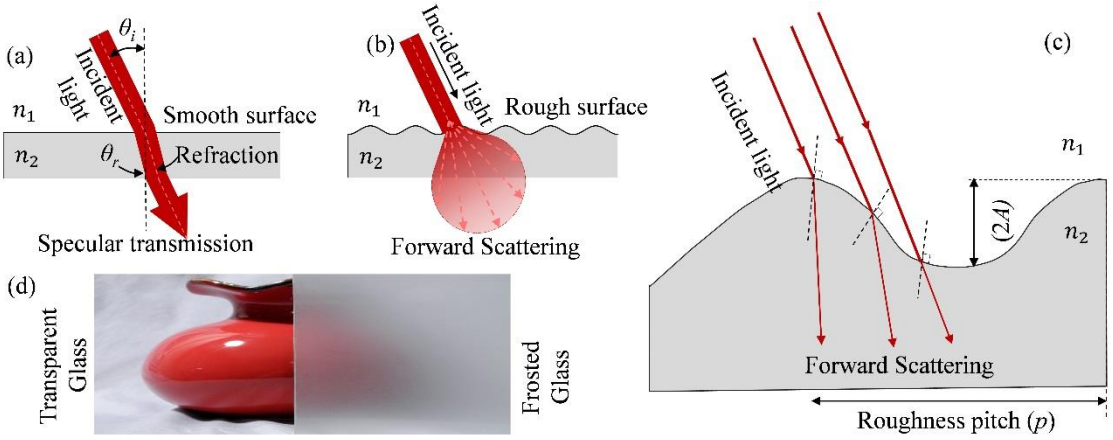

Figure 2-17. Schematic of light transmission through: (a) smooth surface; (b) rough surface and (c) magnified view of a roughened surface showing the forward scattering of an incident beam; (d) visibility through a smooth and roughened glass.

A glass has a fixed surface roughness once it is manufactured. However, a soft optical media shows the potential of surface roughness changing in response to various physical stimuli. Three methods of electrically roughening a surface have been reported in the literature. First, the simplest method to vary the surface roughness is by inducing microwrinkles through mechanical compression of a hard-coated elastomer membrane. Unfolding of this buckled surface or microwrinkles can be done by mechanical stretching

or voltage-induced area expansion in a configuration of dielectric elastomer actuator. Second method to vary the surface roughness is by nanowire indentation of a dielectric elastomer membrane, whose surface was initially flat and smooth. Third method uses voltage induced surface instability of the soft DE membrane which can also be accompanied by nanowire indentation of the elastomer. The first method works only with a free membrane substrate and operates like folding a curtain and it is less practical for a smart window of fixed size. The second and the third methods, however, can also work on a membrane bonded to a rigid glass. Details of their working principles and performance are described in the following subsections.

What is an optically smooth surface? A surface is considered smooth if the rms surface roughness σ is a small fraction of the wavelength of light λ, fulfilling the Rayleigh criteria $\sigma \ll \lambda/(8\cos\theta_i)$, where θ_i is the incident angle on the surface [44]. A Rayleigh smooth surface does not scatter much light and the total integrated scattering (*TIS*) across it is given by $TIS \cong \left(\frac{4\pi\sigma\cos\theta_i}{\lambda}\right)^2$.

A rough surface can be a better optical scatterer. Height variation of the rough surface between two optical media of distinct refractive index can induce phase difference (due to optical path difference) to scatter light rays. Consider two parallel rays incident at the rough surface at an incident angle θ_i. If the surface of variable height induces a phase difference greater than $\pi/2$ to the scattered light, it is considered rough according to Rayleigh criteria [45, 46].

According to Beckman and Spizzichino,[47, 48] the specular transmittance T_{spec} across a Gaussian surface is only a fraction of the total transmittance *T*. The fraction is an exponentially decaying function with an index of wavelength normalized by surface roughness and refractive index mismatch. The specular transmittance across two identical Gaussian surfaces becomes [47, 49, 50]:

$$T_{spec} = T.exp\left\{-\left[\frac{2\pi\sigma}{\lambda}cos\ \theta_i\,(n_1 - n_2)\right]^2\right\} \qquad \textbf{(2.5)}$$

where $T = 1 - R = \frac{4n_1 n_2}{(n_2+n_1)^2}$ is the total transmittance of the medium given by Fresnel equation [36], n_1 and n_2 are the refractive indices of two optical media which defines the interface. For example, for air/glass interface, the air refractive index is $n_1 = 1$ while the glass refractive index $n_2 = 1.4$. The formula is valid to rms roughness which is smaller than the correlation length (i.e. a spatial pitch between adjacent peaks or adjacent valleys). This suggested that increased surface roughness relative to the wavelength can reduce the specular transmission. This provides a means for making a tunable optical diffuser by varying the surface microroughness of a transparent media.

Microwrinkling on Free Elastomeric Membrane. Tunable microwrinkles on an elastomeric membrane can make smart windows (tunable diffuser). Such smart windows can be made of diverse materials. The material for the soft substrate includes silicone rubber (polydimethylsiloxane, PDMS), acrylate dielectric elastomer and so on [24, 51, 52]. The hard-coating materials include a polyimide film, graphene oxide thin film, silicate film, metal films and so on. To enable electromechanical activation, the transparent coating needs to be conductive as well. The transparent conductive materials suitable for this application include few-layer graphene, metallic nanometric film, indium tin oxides, and other transparent conductive oxides or polymers. Table 2-1 compares some of these smart window devices based on microwrinkling reported in the literature.

Table 2-1. Comparison of the smart windows using microwrinkling of a free elastomer.

S. N	Coating Film (Thickness)	Substrate material	Strain state (%)	Wrinkle Amplitude & (Pitch)	T_{spec} change @ 550nm	Ref.
1.	Silicate (UVO & silane treated)	PDMS (Nano-pillars)	0%-30% (uniaxial mechanical stretch)	4.4 μm (31μm)	40%-90%	[51]
2.	Polyimide film (12.5μm)	PDMS	5% (uniaxial compression)	~88 μm *(680μm)*	-	[53]
3.	Graphene Oxide (20nm)	Silicon Rubber	100% -300% (areal mechanical stretch)	4-5 μm (1-2 μm)	10%-90%	[24]

4.	Gold (13nm)	3M VHB 4910	0%-70% (Biaxial mechanical stretch)	2-4μm (8μm)	0%-55%	[54]
5.	Graphene (3-10 layer)	Silicon Rubber	0%-100% (DEA areal expansion)	N/A (0.2-2μm)	40%-60%	[22]
6.	Indium Tin Oxide (ITO) (50nm)	3M VHB 4910	0%-37% (DEA areal expansion)	N/A (2-3μm)	39.14%-52.08%	[23]

Mechanical compression of hard-coated elastomer membrane can induce microwrinkles on its surface. It can also be induced by releasing the pre-stretch in the coated-elastomer substrate [23, 55-58]. The surface roughness σ is related to the sinusoidally wrinkled surface's amplitude (A) by $\sigma = A/\sqrt{2}$. This surface buckling or wrinkling can thus optically diffuse the light transmitting through it.

The amplitude of the surface wrinkles needs to be large relative to the wavelength to cause effective optical diffusion. With an increase in the compressive strain, the wrinkle amplitude increases to form even rougher surface. The amplitude of the post-buckled wrinkles is given by [57],

$$A = 2\pi t_f \sqrt[3]{\left(\frac{E_f}{3E_s}\right)} \frac{\sqrt{1+\nu}}{\pi} \sqrt{|e| - e_c}, \qquad \textbf{(2.6)}$$

where, $e_c = \frac{1}{4}\sqrt[3]{\left(\frac{3E_s}{E_f}\right)^2}$ is critical buckling strain, E_s and E_f are Young's moduli of the soft substrate and hard film respectively t_f is the thickness of the coats, ν Poisson's ratio of the substrate and e is the applied compressive strain (see Figure 2-18(d)). Wrinkle amplitude increases with thickness and modulus of the coating films and with a compression larger than the critical strain.

Figure 2-18 shows one such tunable diffuser made of polyimide (PI) film coated PDMS membrane substrate which forms submillimeter-sized wrinkles upon uniaxial compression [53]. While the polyimide film is 12.5μm thick with Young's modulus of 2.5GPa, the PDMS substrate is much softer with 1.3MPa Young's modulus. Hence, a 5% uniaxial compression buckles the hard PI surface into unidirectional large wrinkles

with ~680μm pitch and ~88μm amplitude (Figure 2-18(d-f)). This wrinkled surface diffuses the light passing through it and conceals the view behind the device (Figure 2-18(b)). The divergence angle of the diffused light is at most θ_{max}=12°. Hence, its effect of optical diffusion is only observable when the diffuser is spaced at a substantial distance from the image.

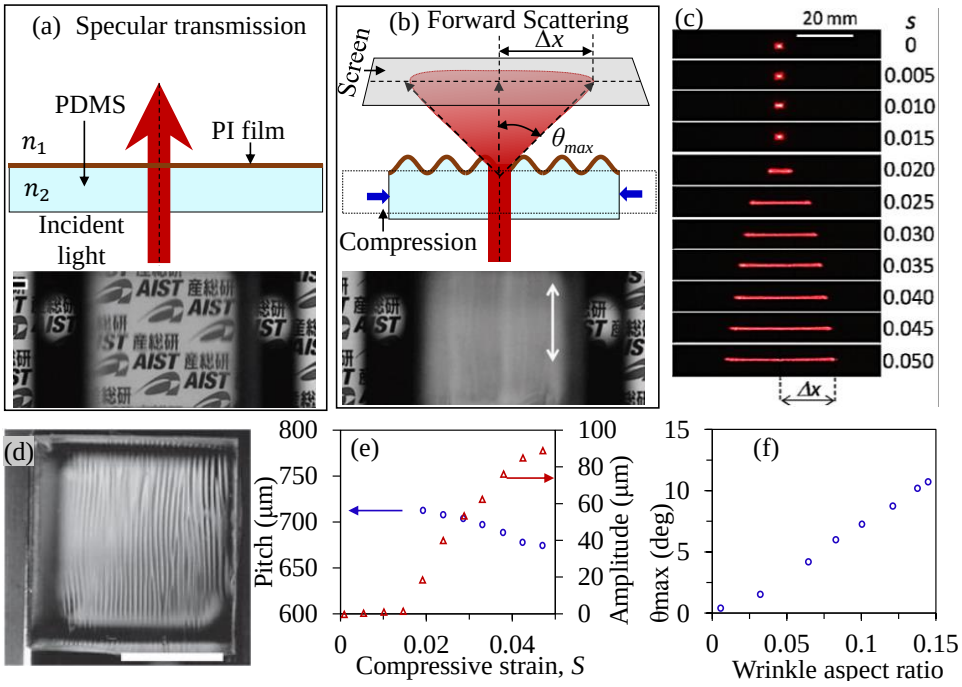

Figure 2-18. Mechanical wrinkling of a PI coated PDMS substrate to scatter light. Schematic and corresponding visibility through the device at: (a) flat state; (b) Wrinkled state; (c) Diffused pattern formed on a screen when a laser beam is shone through the device at various compression strain; (d) Photo of the wrinkled device; (e) Wrinkle pitch and amplitude with progression of compressive strain and (f) corresponding diffusion induced broadening angle with respect to wrinkle aspect ratio. (adapted from [53])

S. G. Lee et al. [51] developed a microwrinkling device consisting of a soft PDMS substrate with a hard silicate coating and an array of nano-pillars on its surfaces. When the pre-stretch of the device is released, the hard silicate layer forms microwrinkles. The nano-pillars were molded on the PDMS substrate and then stiff silicate surface layer was formed by plasma treatment of the pre-stretched PDMS substrate. The nano-pillars

behaved as anti-reflecting structures (see Figure 2-19) [51, 52]. The different aspect ratio of the nanopillars interfered differently with the incident light. The micro-molded nano-pillar had a 150nm top diameter and 300nm base diameter. The device with low aspect ratio nano-pillars (LNA) of 150nm height had reduced surface reflectance which made them highly transparent (~90% transmittance). But the devices with 700nm high aspect ratio nano-pillars (HNA) lowered the transmittance by light scattering (Figure 2-19(g-h)). Under 30% uniaxial compressive strain, the device with LNA formed unidirectional wrinkles of 31μm wavelength and 4.4μm amplitude. Consequently, it scattered light to lower its transmittance to 40%.

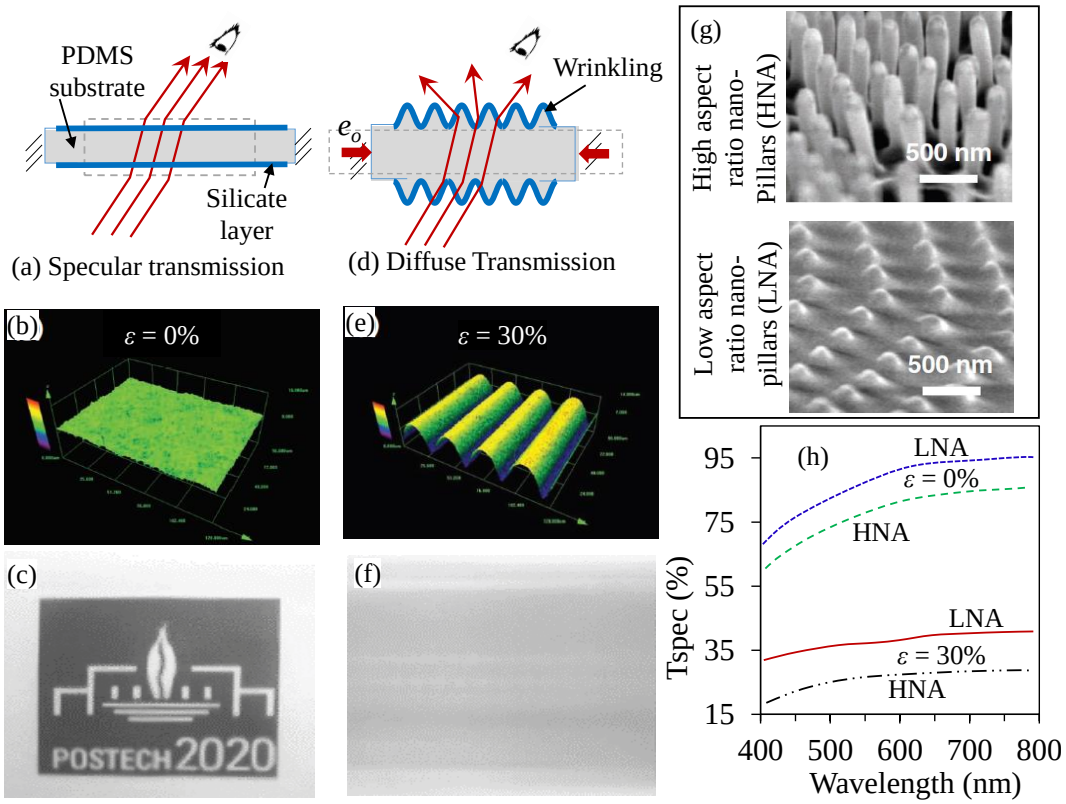

Figure 2-19. Mechanical wrinkling of a PDMS substrate with silicate coats to scatter light. (a), (b) and (c) are schematic of light transmission, confocal micrograph of the surface, and visibility through the membrane at flat state; (d) (e) and (f) are same at wrinkled state with a strain release of 30%; (g) SEM image of the device with low and high aspect ratio nano-pillar arrays; (h) Specular transmittance at 0% and 30% strain state for the device with nano-pillar arrays of different aspect ratio. (adapted from [51])

Though bulk metal is opaque, the nanometric metallic thin film can be transparent. A biaxially microwrinkled optical diffuser was made using a pre-stretched membrane (VHB 4910 tape) coated with a gold thin films [54]. The device with the flat gold film of 13nm thickness was almost transparent (transmittance 55%). Release of the biaxial pre-stretch in the dielectric membrane can buckle the surface coating of gold into ridges (see Figure 2-20(e)). Upon 70% biaxial compressive strain, the device formed ridges of 2-4μm amplitude and 8μm pitch. Consequently, it turns translucent almost 0% specular transmittance.

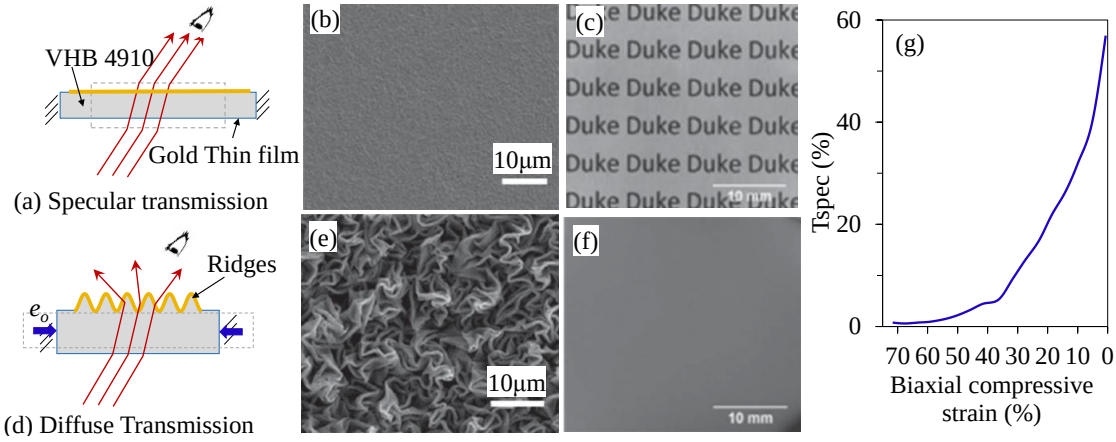

Figure 2-20. Biaxial compression of a gold thin film coated VHB elastomer to form ridges on the surface. Schematic diagram, SEM image, and visibility through the device at: (a), (b), and (c) 0% biaxial compressive strain; (d), (e), and (f) 67% biaxial compressive strain; (g) Change in specular transmittance upon biaxial compression. (adapted from [54])

Thomas et al. [24] used delamination buckling of the highly transparent graphene oxide (GO) thin films coated on a silicone rubber substrate to make a tunable diffuser. This GO film delaminated and buckled under biaxial compression while the silicone rubber substrate remained flat. The device consisted of a 100nm thick highly transparent coating of graphene oxide (GO) thin coated on pre-stretched silicone rubber substrates; it shows greater than 90% transmittance. Releasing the elastomer pre-stretch causes GO film detachment and buckling due to poor adhesion of the films to the substrate (see Figure 2-21(b)). Under a 400% uniaxially compressed states, the device formed delaminated

buckling patterns of 4–5μm amplitudes and 1–2μm pitch. The delaminated buckled films slightly absorb and mostly scatters the incident beam (see Figure 2-21(c)). Here high aspect ratio buckled patterns can significantly scatter light. A high biaxial compression strain of 400% can lower the transmittance to 10%.

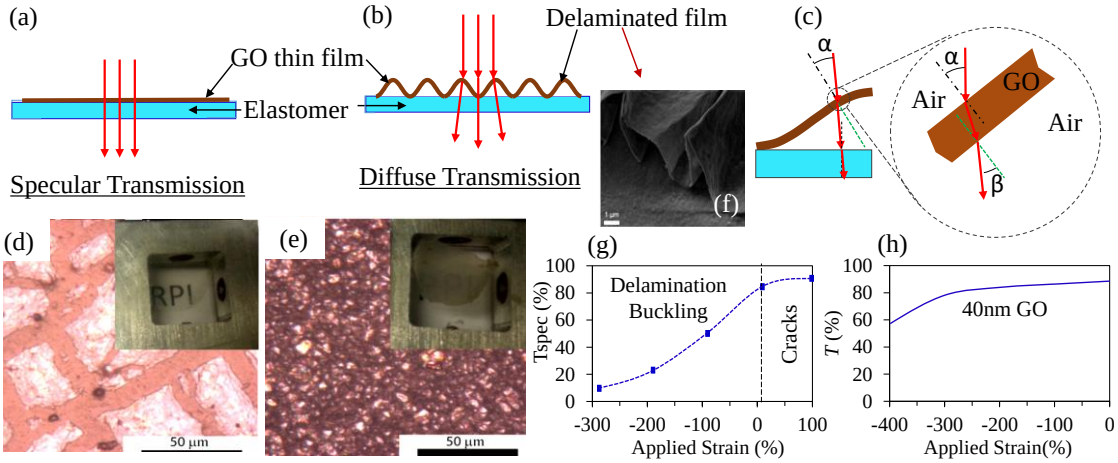

Figure 2-21. Graphene oxide (GO) film as it is strained from a crumpled with ≈300% biaxial pre-compression to a fully flat state. Schematic of (a) flat GO films; (b) delamination buckled GO films; (c) light refraction through delaminated buckled GO film. Micrograph of the GO surface with insets showing appearance of letters placed behind the membrane at biaxial compression release of: (d) ≈ 400%, at 400% strain the applied tensile strain exceeds the pre-compression of the GO film and hence cracks appear in the film and (e) ≈ 0%; (f) SEM image of the typical delamination buckling pattern of a GO on a silicon rubber; (g) Inline transmittance change and (h) Average diffuse transmittance change when releasing the delamination buckles. (adapted from [24])

Zang et al. [22] developed an electromechanically tunable optical diffuser using delamination buckling of a conductive few-layer graphene coated on an elastomer. The device made use of voltage-induced area expansion to unfold pre-microwrinkled electrodes. The device is a dielectric elastomer actuator which consists of a pair of graphene coating sandwiching a pre-stretched dielectric elastomer membrane (3M VHB 4905). The device is optically clear (80% transmittance) with a flat coating of 3-10 graphene layers, which was obtained by stamping on the 3-5 times biaxially pre-stretched elastomer substrate. Release of the elastomer pre-stretch causes delamination and

buckling of the graphene films. This yields random ridges of 0.2-2μm wavelength (see Figure 2-22) smaller or comparable to the visible light wavelength. Hence this device can only mildly scatter light. Even a 500% uniaxial mechanical compression merely lowers the transmittance of the device to 30%. A 100% areal expansion strain by DEA can unfold pre-ridges and increases transmittance to 60%.

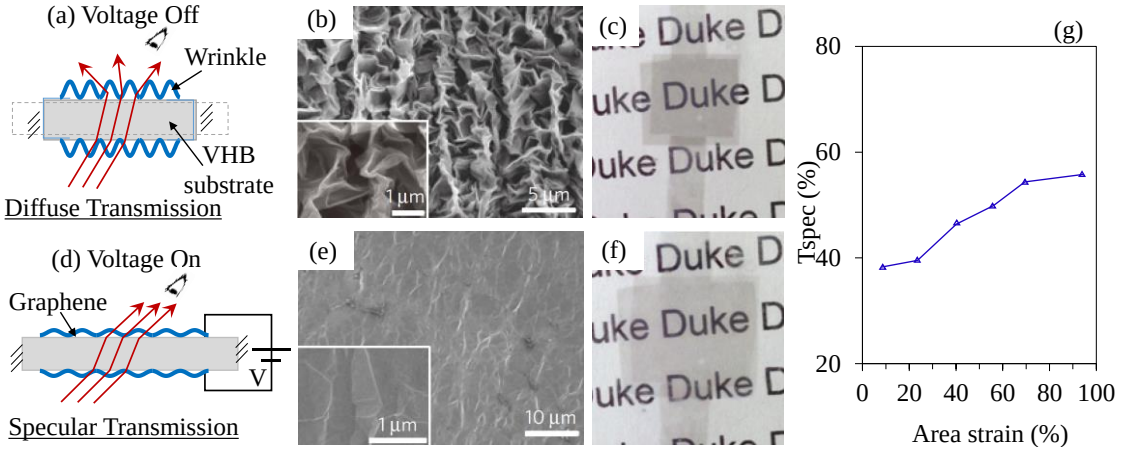

Figure 2-22. Wrinkling and unfolding of large-area graphene using DEA: (a) schematic of the DEA with wrinkled electrode; (b) SEM image of graphene sheet with delamination wrinkles (c) image behind the graphene film at the crumpled state; (d) schematic of flattening upon DEA activation; (e) SEM image of the flattened electrode; (f) image behind the graphene films at electrically flattened state; (g) The area actuation strain-induced change in transmittance. (adapted from [22])

Another DEA-based device used indium tin oxide (ITO) as a conductive coating on an elastomer to electrically unfold the microwrinkles. ITO is one of the few transparent conductive oxides commonly deposited on the glass to make transparent electrode of a touchscreen. But, physical vapor deposition of ITO on soft elastomeric substrate need proper optimization to achieve high clarity and low initial wrinkles. An initial attempt by H.-Y. Ong et al. [23] showed E-beam evaporation of nanometric ITO film (50nm) appears slightly brownish and is subjected to thermally induced microwrinkles on acrylic elastomer membrane. Hence, the initial wrinkles of as-deposited ITO nanometric films make this soft capacitor device slightly hazy (with only a 52% specular transmittance)

even without a radial compression. Upon radial compression of 14.2% strain, ITO nanometric on dielectric elastomer membrane is crumpled further to become hazier with the specular transmittance reduced to 39%. A 6kV activation induces a 37% areal expansion and thus restores the device clarity to 52% specular transmittance (see Figure 2-23).

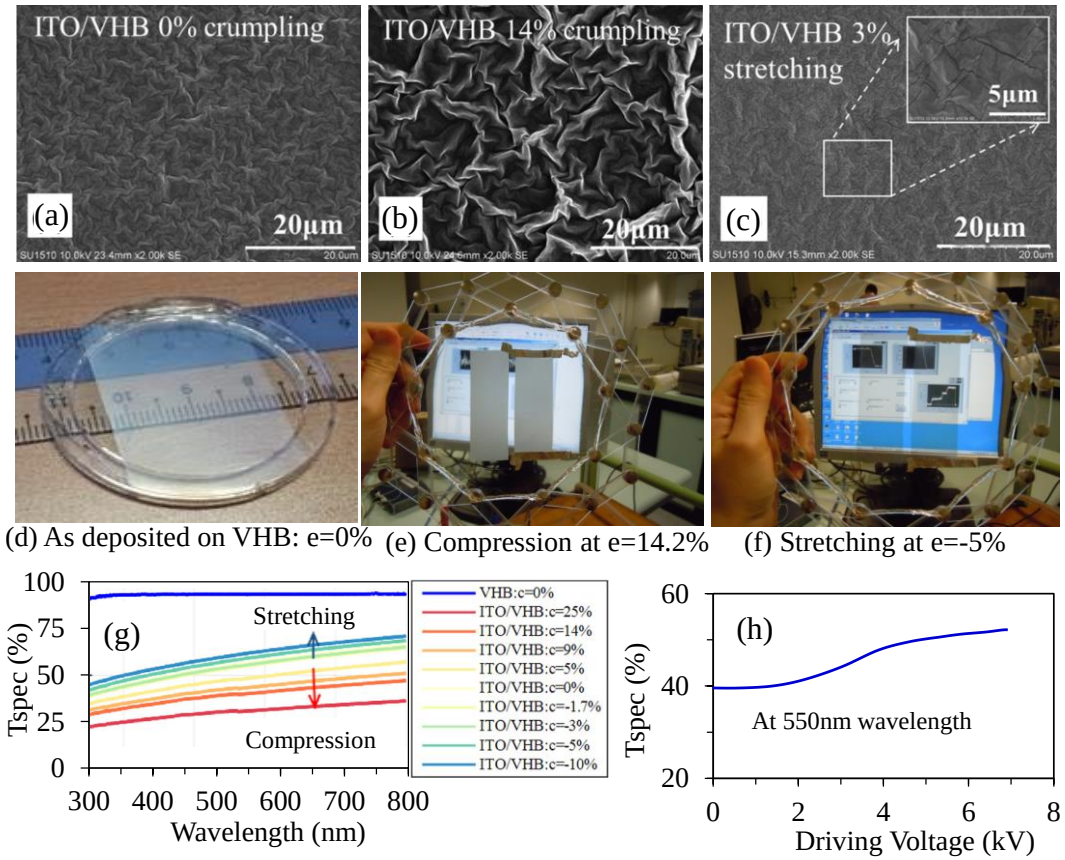

Figure 2-23. SEM image of the ITO at: (a) as deposited with thermally induced wrinkles; (b) 14.2% crumpled state; (c) 3% stretched state with crack formation; (d) An object behind ITO before crumpling can be seen clearly with slight haze appearance; (e) upon 14.2% biaxial compression it is able to conceal the image in the LCD screen; (f) Again upon reversible stretching back, the image in the LCD screen is clearly visible; (g) Transmittance of the ITO coated DEA at different compression strain; (e) Transmittance change through the DEA with 14% crumpled ITO upon step-wise increasing in voltage (adapted from[23]).

Indentation of Free DE membranes with Nanotube Electrodes. A dense coating of carbon nanotube network appears dark on an elastomer substrate; whereas, a sparse coating appears clearer with less light absorption. The biaxial areal expansion provides a means to tune the density of carbon nanotube network on the elastomer substrate and thus change the optical absorption. But, the voltage-induced indention of the elastomer by the nanotubes causes micro-bulging and thus roughen the elastomeric surface to cause the haziness.

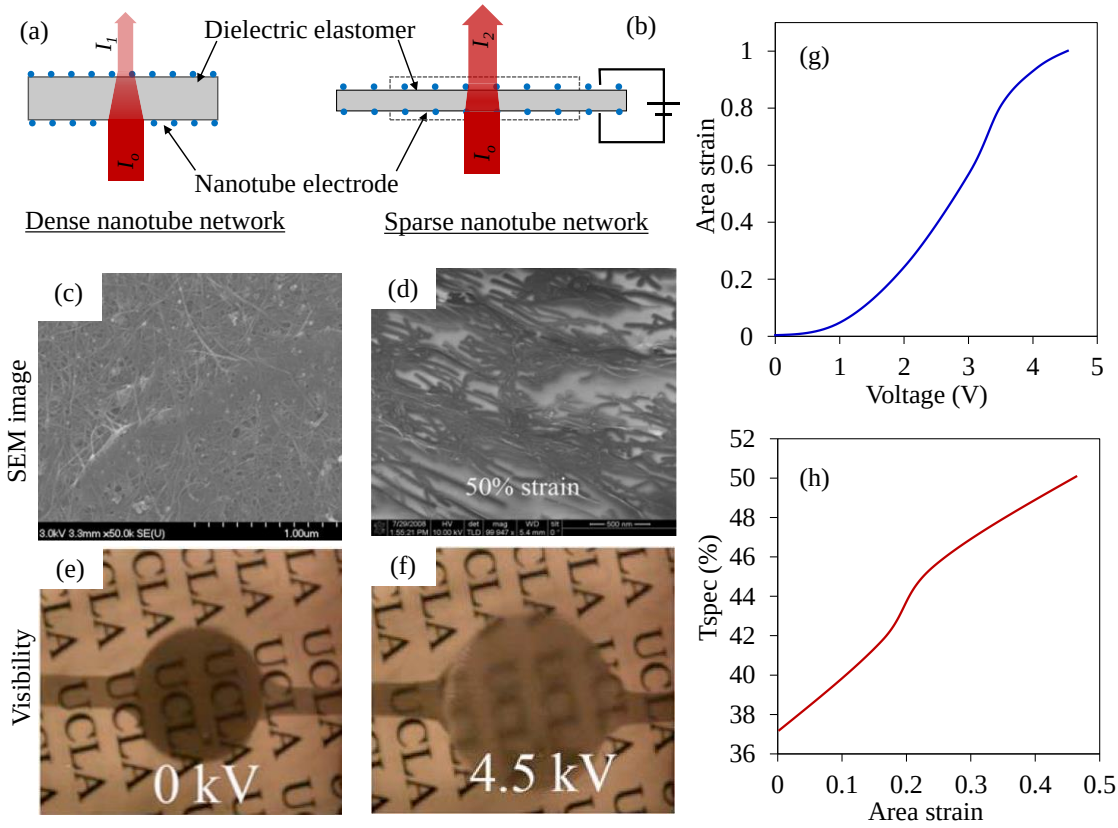

Figure 2-24. Changing density of the SWCNT network on a free elastomer membrane by DEA-induced area strain. Schematic: (a) at inactive state; (b) as the DEA is activated; SEM image of the surface at: (c) inactive state; (d) activated state; Visibility through the membrane: (e) at inactive state, (f) at activated state; (g) Area strain upon voltage activation and (h) corresponding change in transmittance (adapted from[59]).

Figure 2-24 shows that a dielectric elastomer actuator sandwiched by a pair of the 100nm thick coating of dense carbon nanotube network is dark and it can shadow a white

background. As expected, voltage induced areal expansion can reduce the network density and lighten the darkness [59]. But, to surprise, activation of DEA blurs out the logo image despite causing a sparse network of carbon nanotubes [59, 60]. In comparison, Figure 2-25 shows a sample with a 15nm thick coating of carbon nanotube network. The DEA is slightly dark but can clearly show a black-and-white logo, which was placed behind it. When activated at 5kV, the device undergoes 200% areal strain but blur out the logo and become hazy.

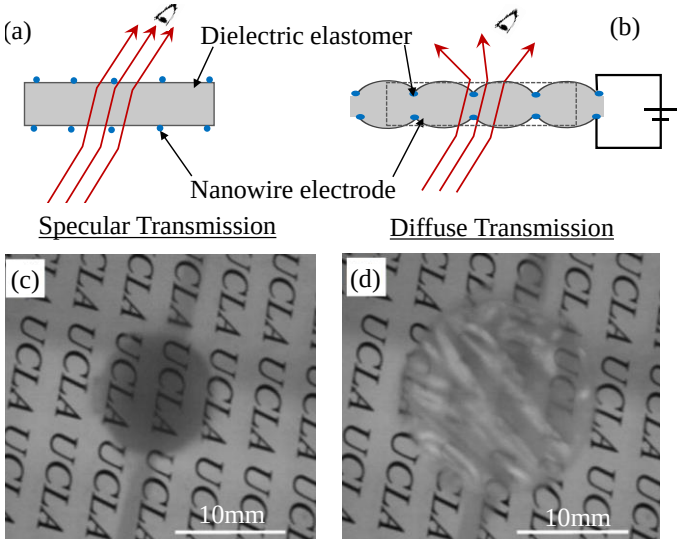

Figure 2-25. Light diffusion by the formation of an indented rough surface by activation of DEA with transparent single-walled carbon nanotube electrode on a free elastomer membrane. Schematic: (a) at inactive state; (b) as the DEA is activated; Visibility through the membrane: (c) at inactive state; (d) at activated state. (adapted from [60])

Voltage-induced Indentations and Surface Instability on Rigidly Bonded Rubber. Tunable roughness on the surface of a bonded rubber can make smart optical diffuser suitable for windows of fixed size. Such devices can be made either by using a thin film electrode or a nanowire-based electrode coated on a rigidly bonded rubber like a soft capacitor. First, the devices with conductive thin film form wrinkles by electromechanical instability upon high voltage activation. Second kind of device uses nanowire network to indent the elastomer substrate forming micro-bulges to roughen its surface upon high voltage activation [61, 62]. In addition to these micro-bulges, they can

form larger microroughness on the dielectric medium if they are activated up to the pull-in instability. Table 2-2 compares these devices in terms of elastomer material, electrodes materials, transparency tuning range and the applied electric field.

Table 2-2. Comparison of the smart windows based on voltage-induced surface instability and indentation of rigidly bonded elastomer.

Substrate (Shear Modulus)	Dielectric constant	Electrodes	Applied Electric field, E	Surface Property	T_{spec} @550nm Inactive	T_{spec} @550nm Active	Ref.
Acrylate elastomer (~380kPa)	20	Gold thin film (40nm) and ITO	14V/μm	2A~2μm p ~10-30μm	37%	33%	[20]
3M VHB4905 (600kPa)	4.7	AgNW (ϕ=90nm) /ITO	96V/μm	2A~0.6μm p ~3μm	70%	20%	[62]
3M VHBF9460PC (600kPa)	2.92	AgNW (ϕ=80nm)	125V/μm	N/A	62%	8%	[61]
PDMS-Sylgard 184;50:1 (2.7kPa)	2.68	CNT (ϕ=4-5nm) /ITO	33.3V/μm	2A~19μm p~250μm	80%	8%	[63] [64]

The tunable diffusers with flexible electrodes on a rigidly bonded elastomer exploits voltage-induced surface instability to induce microroughness. They consist of a soft transparent dielectric elastomer layer sandwiched by a flexible nanometric film or nanowire electrodes (see Figure 2-26). When a critically high voltage is applied across the two electrodes (one flexible and one rigid), the surface with flexible electrodes is subjected to electro-mechanical instability and thus forms microroughness and becomes hazy (see Figure 2-26(b)). The electromechanical instability occurs when the electrostatic pressure overcomes the elastic resistance stress of the elastomer layer. According to Ref. [65], the critical electrical field E_c leading to the electromechanical instability is

$$E_c = \sqrt{\frac{\xi_c Y}{\varepsilon_o \varepsilon_r}}, \tag{2.7}$$

where ε_o is the vacuum permittivity and ε_r is the dielectric constant of elastomer. The parameter ξ_c is a function of the Poisson ratio, and it is experimentally found to vary in the range between 0.256 to 0.667 for soft elastomers.

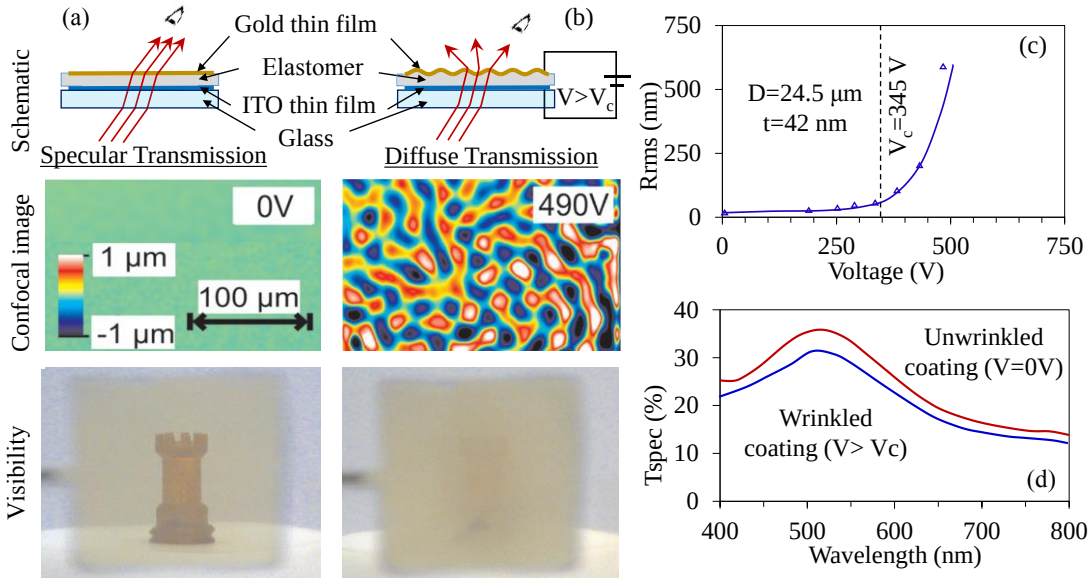

Figure 2-26. Schematic of the device, the corresponding surface topography of the device and visibility of the chess piece behind the device: (a) at voltage off state; (b) at activated state (light is scattered by roughened surface and the object is almost concealed); (c) Evolution of the surface roughness as voltage exceeds the critical voltage; (d) change in transmittance spectrum by voltage activation (adapted from [20]).

Van den Ende et al. [20] recently developed a device which induces wrinkles though surface instability on a thin film coated elastomer which is bonded to glass. The device consists of a 24.5μm thick dielectric elastomer layer (acrylate elastomer of low Young's modulus of 1.15MP, the high dielectric constant of 20) sandwiched by a gold nanometric film of 42nm thick and an ITO-coated glass. The surface of this dielectric elastomer is initially flat. But, its specular transmittance is only 37% due to light absorption and reflection by the gold thin film. A critical voltage activation above 345V (14V/μm) of the device causes surface microwrinkling with an average amplitude of up to 1μm and a

10-30μm pitch. A 500V activation of the device can roughen the surface up to the rms roughness of 600nm. This reduces the specular transmittance to 33 %, which is 11% lower than the off-and-flat state transmittance. This voltage-induced transmittance change is small because of mild wrinkle formation due to the lateral constraint by the rigid substrate and the gold thin film. A bonded elastomer layer becomes stiffen transversely across the thickness. Hence, such bonded rubber with metallic flexible electrode deforms little under electrostatic pressure.

Instead of a metallic thin film, a sparse network of conductive nanowires or nanotubes can make a clearer and more compliant electrode. Consider a nanowire of radius *R* on a bonded dielectric elastomer layer of thickness *H*, of permittivity ε on an ITO coated glass. Application of a voltage across the nanowire and the bottom flat electrode induces a 2-dimensional non-uniform electrostatic field across the bonded dielectric elastomer layer. Figure 2-27(b)) shows an electrostatic force per unit length of the nanowire acting along its normal direction follows $\frac{F_n}{l} = \frac{\pi\varepsilon}{4a^2}\frac{V^2}{\left[cosh^{-1}\left(\frac{H}{R}\right)\right]^2}$, [62] where $a = 1/2(H + \sqrt{H^2 - R^2})$.

This concentrated electrostatic force can locally indent the bonded rubber layer and causes elastomeric deformation to form surface micro-bulges. This roughens the elastomeric surface and thus diffuses the transmitting light.

Figure 2-27 shows one such device which used a single-dielectric layer capacitor with nanowire electrodes on one side to indent the elastomer surface upon high-voltage activation. It consists of a pre-stretched acrylic elastomer membrane tape of 4 by 4 times biaxially pre-stretched VHB 4905 (modulus 600kPa) sandwiched by a silver nanowire mat (of 78mg/m^2 areal density) and an ITO-coated glass. It is merely 70% clear at the inactive state because the mat of silver nanowires (90nm diameter and 20-60μm length) scatter light. When it is activated with 96V/μm, the silver nanowire network electrodes nano-indents into the elastomer surface and causes submicron bulging of 600nm peak-to-valley deformation. This activation turns the device to be translucent at a 20% specular transmittance.

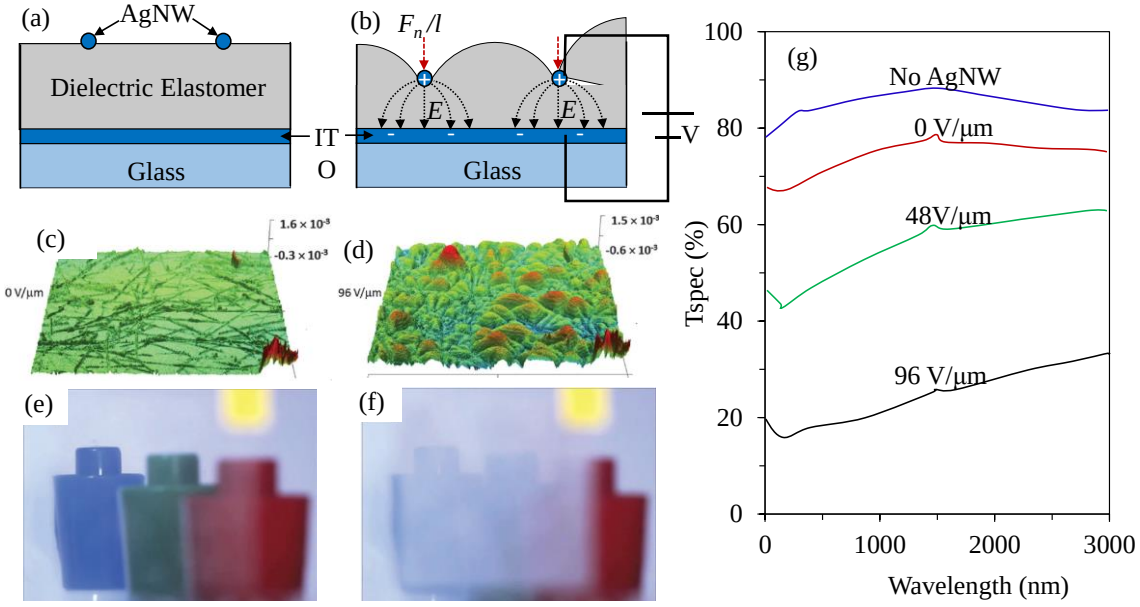

Figure 2-27. Smart window device made of a capacitor with single-dielectric layer sandwiched between dispersed AgNW and ITO coated glass. Schematic at: (a) off state; (b) on state showing bulging due to an electric field (*E*). Confocal images at (c) off state; (d) on state with 96MV/m electric field; Visibility through the device at (e) inactive and (f) when activated; (g) inline transmission at the different applied voltage. (adapted from [62])

Double variable roughness layers can obtain higher haze than using a single layer. Addition of a hard-dielectric layer between these soft layers allows this device to operate at higher electric-field without breakdown. Figure 2-28 shows such a device that used a triple-dielectric laminate soft capacitor which consists of a pair of nanowire electrode cladded acrylate elastomer films (of 3.1μm thick and 450kPa modulus) sandwiching a middle hard Mylar layer (13μm thick and 5.2GPa) [61]. Each of the elastomeric films was prepared from an acrylic adhesive tape (3M VHB F9460PC), which was biaxially pre-stretched 4 times. The electrode cladding is a sparse coating of the silver nanowire of 78mg/m^2 areal density. At inactive state, this laminate capacitive device is clear with 62% specular transmittance. A 2.4kV (125V/μm) dynamic activation at 3Hz can roughen the surface and reduce the specular transmittance down to 8% (see Figure 2-28(g)). This alternating-current (ac) high voltage activation is needed to prevent the drift in the activated transmittance. In comparison, a DC high-voltage activation of the device

cannot maintain a low transmittance. The DC-activated transmittance decays exponentially until it vanishes while the activation voltage is held constant (see Figure 2-28(h)). This decaying trend of transmittance appears similar to discharging of a soft capacitor, but the reason was not clear.

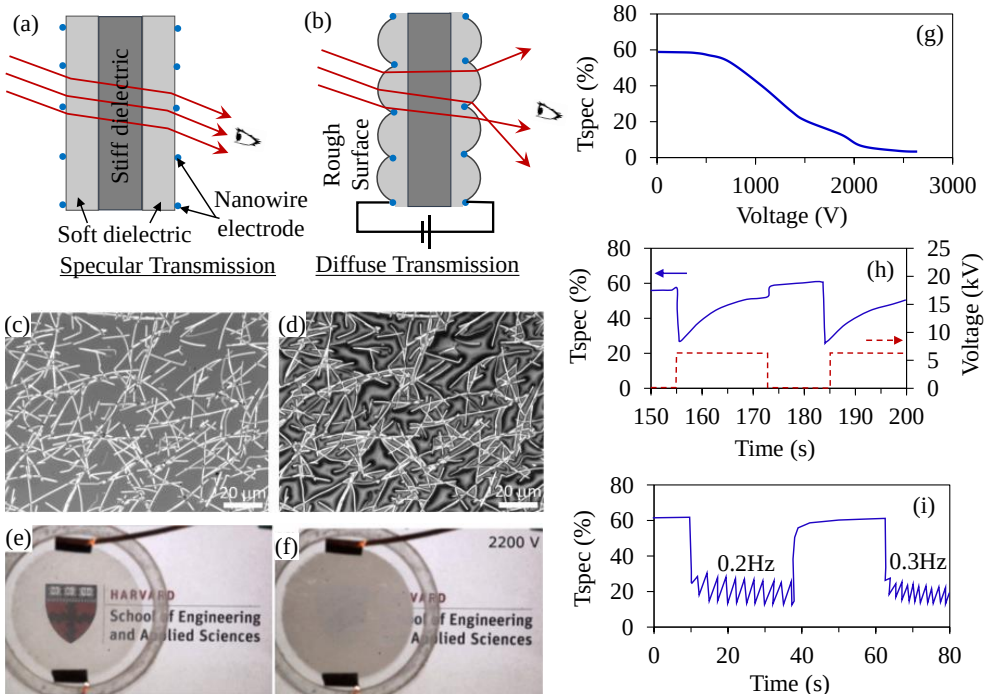

Figure 2-28. Smart window device made of double variable roughness layers with two dispersed AgNW as a compliant electrode. Schematic at: (a) off state; (b) on state. Micrograph at (c) off state; (d) on state with 125MV/m electric field; Visibility through the device (e) at 0V and (f) hazing at 2200V; (g) inline transmission at 550nm wavelength when gradually increasing the voltage; (h) Transmittance response with DC voltage activation;(i) Transmittance response with AC voltage activation. (adapted from [61])

Compared to the nano-indented surface, larger microroughness can be obtained on a very soft elastomer surface coated with nanotube electrodes through surface instabilities upon activation beyond a critical voltage. High-voltage activation of this device reduces the transmittance following an inverted sigmoid function. This transmittance change is characterized by 1) a gradual decrease due to nano-indentation and surface bulging under lower voltage, and 2) a sharp decrease due to surface instability at the critical voltage.

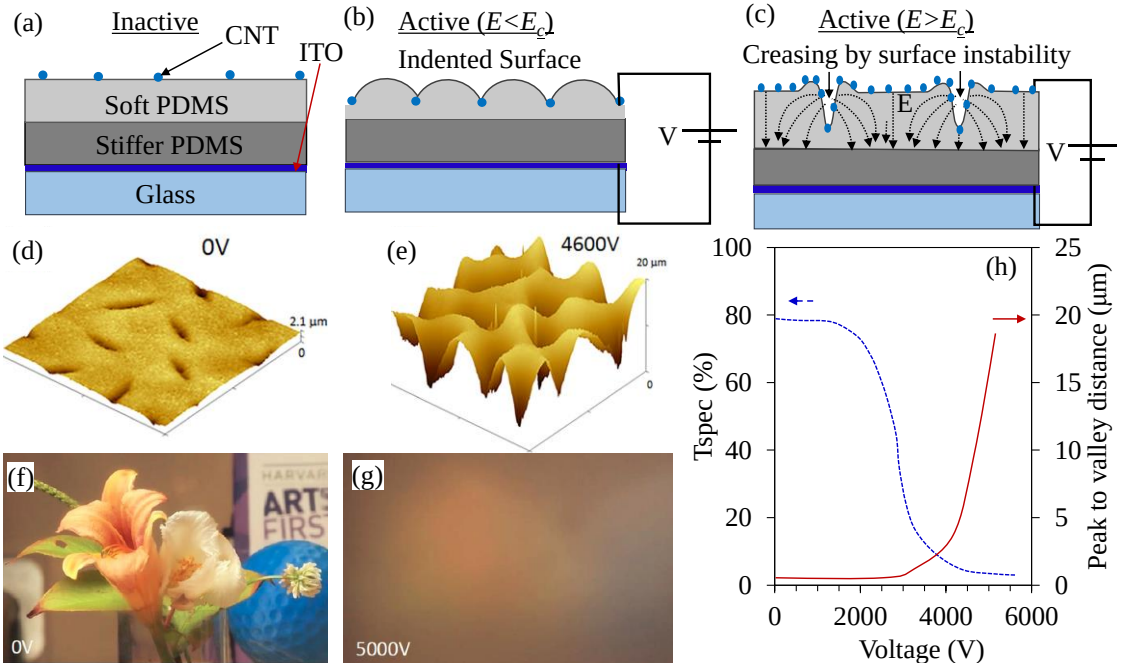

Figure 2-29. Smart window device working on surface instability induced roughness with CNT network as an electrode. Schematic of the device at: (a) Inactive state; (b) Indentation at low electric field; (c) Surface instability at electric field above E_c. Confocal micrograph at: (d) inactive state; (e) activated at $E>E_c$; Visibility through the device at: (c) inactive state; (d) activated state; (e) Change in inline transmittance obtained by corresponding voltage-induced roughness. (adapted from [63])

Figure 2-29 shows such a device which used a sparse mat of single-walled carbon nanotubes of 4-5nm diameter to make a much clearer device (80% specular transmittance) than silver nanowires coated ones in the inactive state [63]. It was made of a two-dielectric laminate soft capacitor, which consists of a top layer of sparsely electroded soft silicone (160μm thick, modulus 2.7 kPa)), and a middle layer of hard silicone (55μm thick) on an ITO-coated glass. The top layer of soft silicone was cured from a liquid mixture of 50-part prepolymer resin and 1 part of crosslinker (Sylgard 184); it was measured with a shear modulus of 7kPa. The middle layer of hard silicone was prepared from a liquid mixture of 10 parts of prepolymer resin and 1 part of cross-linker (also, Sylgard 184); it was measured with a shear modulus of 700kPa. The compliant electrode was prepared from an aqueous/isopropanol solution of carboxylic-acid

functionalized single-walled carbon nanotubes. This solution is optically clear, and it can absorb 10% of transmitted light. Filtration of 0.2-0.2ml through a Teflon filter (100nm pore size and 47 diameters, Omnipore) yields a clear mat of carbon nanotube network, which was later transferred to the surface of a silicone layer. As a result of critical voltage activation (at 4600V), the top surface becomes roughened with a 250μm pitch and a 19μm peak-to-valley height; this reduces specular transmittance to be only 8%. This device enables a wide range of transparency tuning from 80% to 8%. Deactivation is however subjected to substantial hysteresis. Compared to other nanowire-based smart windows, this device could obtain lower transmittance due to surface instabilities that induce high microroughness (refer to Table 2-2). Yet, due to the low aspect ratio of microtopography, the scattering angles is less than 10°.

2.5 Summary

Literature review shows commercial smart windows based on electrochromic and PDLC are still pricey for large area use (refer to Table A-1). The average-priced product of these smart windows can merely switch between low to moderate optical clarity (<65%). For some smart windows, a wide tunability up to high clarity is possible, but at a higher cost. To solve the above problems, many other new technologies have been developed for proof of concepts. Table 2-3 and Figure 2-30 summarizes their performance comparing their pros and cons. Among many demonstrations of the new active window, only a few can rival the commercial ones in terms of transparency tuning range. For example, optofluidic smart glass based on tunable total internal reflection can be 84% transparent when the prism-like corner compartments are filled with a liquid of matching refractive index; whereas it is only 8% transparent with the empty compartments. However, these devices involve pumping fluids in and out of the chambers which is difficult to handle and prone to leakage. Device-based on CNT indentation of a soft bonded rubber was reported to achieve a wide tunability from 8% to 80%. Yet, they are unable to obtain a highly frosted state (e.g. 1-2% transmittance) for privacy. Delamination buckling of graphene oxide thin film on silicon rubber seems to beat the obtainable range of transparency tuning (between 10% to 90%), but it requires areal

expansion of two to four times. This areal expansion to tune the optical diffusion cannot be applied to windows of nearly fixed size. This problem motivated this research work to create microwrinkle at low compression strain so that switching between clarity and frost can be obtained with small area change.

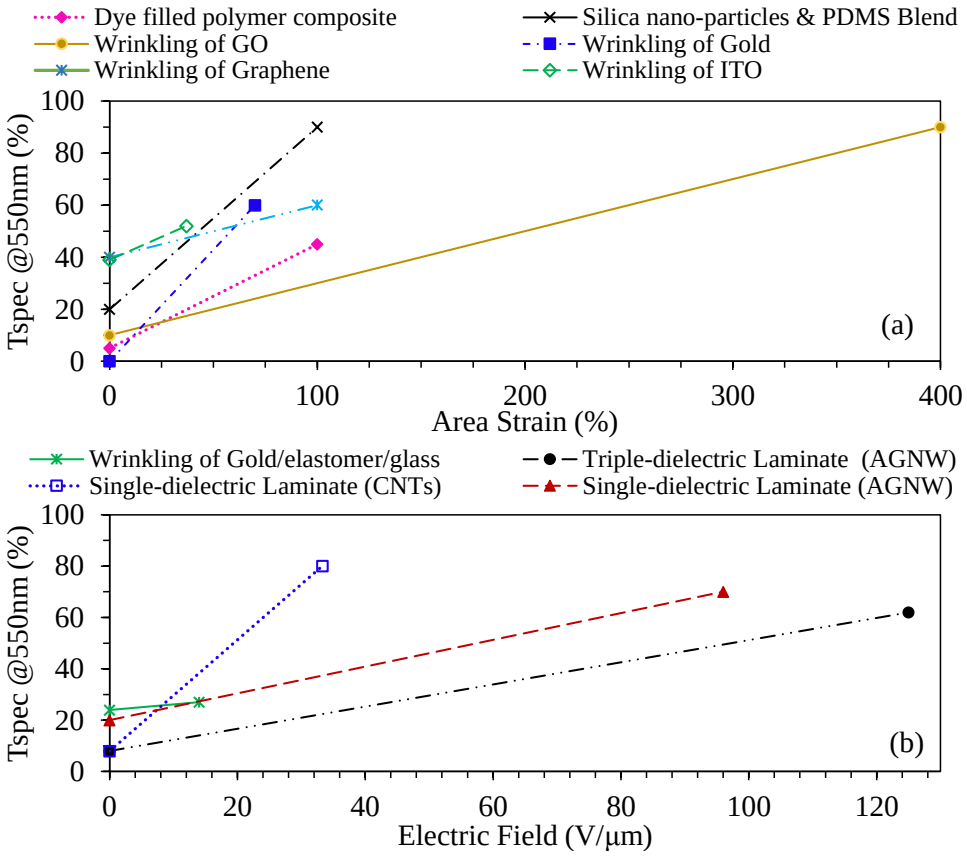

Figure 2-30. Comparison of various smart windows which (a) involves area strain; (b) are bonded to a rigid substrate.

Table 2-3. Performance comparison of the existing smart window technologies.

Smart window type [Ref]	Substrate material	Thin Film Electrode (Thickness)	Strain state (%)	T_{spec} @550nm Inactive	T_{spec} @550nm Active	Ref.
Electrochromic	Glass	-	-	5%	65%	[11, 14]

Polymer dispersed liquid crystal	Polymer composite	-	-	6%	62%	[14]
Suspended Particle Device	Glass	-	-	2.4%	59%	[14]
Dye suspended polymer composite	Polydimethyl siloxane (PDMS)	-	>100% (area strain)	5%	45%	[33]
Optofluidic smart glass	(Vero Clear)	(8.5mm)	0%	8%	84%	[35]
Micro-blinds array	Glass	ITO/Al	-	36%	53%	[34]
Wrinkling of thin film coated on a free elastomer substrate	PDMS (Nano-pillars)	Silicate (UVO & silane treated)	0%-30% (uniaxial mechanical stretch)	40%	90%	[51]
	Silicon Rubber	Graphene Oxide (20nm)	100% - 300% (areal mechanical stretch)	10%	90%	[24]
	Silicon Rubber	Graphene (3-10 layer)	0%-100% (DEA areal expansion)	40%	60%	[22]
	3M VHB 4910	Gold (13nm)	0%-70% (Biaxial mechanical stretch)	0%	60%	[54]
	3M VHB 4910	Indium Tin Oxide (ITO) (50nm)	0%-37% (DEA areal expansion)	39.14%	52.08 %	[23]
Wrinkling of thin film coated on bonded substrate	Acrylate elastomer on glass	Gold and ITO (42nm)	-	37%	33%	[20]
Nanowire indented elastomer	3M VHB F9460 PC and Mylar	Silver Nanowire	-	62%	8%	[61]
	3M VHB4905	AgNW (ϕ=90nm) /ITO	-	70%	20%	[62]
	3M VHB 4905	Carbon Nanotubes (10-100nm)	0-45% (areal expansion)	37%	50%	[59]

	PDMS (Sylgard 184)	Carbon Nanotubes (4-5 nm)	-	80%	8%	[63]

Chapter 3 Compliant Electrodes and Wrinkling Mechanics

A new kind of smart window has recently been developed based on microwrinkling of an optical thin film coated elastomer membrane. These coated elastomer membranes, which was optically clear with flat surface appears optically frosted when the coating forms microwrinkles (under mechanical compression). Mechanical compression and unfolding can tune the surface roughness and thus the degree of optical diffusion. Upon complete surface unfolding, the elastomer membrane will return to be optically clear. Such unfolding can be realized electromechanically by using a dielectric elastomer actuator (DEA). In such electrically tunable optical diffuser (based on DEA), the compliant electrodes are based on the microwrinkled thin film of high flexibility and electrical conductivity.

So far, there are some works using silver and gold thin film to form microwrinkled compliant electrodes. However, silver and gold are not inherently transparent; They need to be deposited at a nanometric thickness to be optically clear. However, the compression strain required to cause microwrinkles to nanometric Au/Ag films on elastomer is large above 50%. Optical oxides are harder than metals. So far, there are few works to show microwrinkling of optical oxides on elastomer. There was no report of their use as compliant wrinkled electrodes. This chapter shall investigate the mechanics and design of compliant wrinkled electrodes out of transparent conductive oxide thin films or multi-layered thin films.

3.1 Compliant Electrodes

A dielectric elastomer actuator consists of an elastomer membrane and a pair of compliant electrodes. Materials for the elastomeric membrane substrate are silicone or acrylate elastomers. Likewise, materials for the compliant electrodes include carbon grease, graphite or metal powders, composite of conductive powder and polymer, conductive polymers, metal thin films and so on. The electrodes for driving a dielectric

elastomer needs to be compliant to conform to large voltage-induced deformation of dielectric elastomer substrate [66, 67].

Conventionally, carbon black grease and graphite powder were used as the compliant electrodes for DEA. These electrodes have negligible stiffness with sheet resistivity in KΩ/□ range. But carbon grease and graphite poorly adhere to the elastomer and easily contaminate upon contact, causing shorting and DEA failure. In addition, carbon grease has poor stability over time because of the seeping and drying of the inherent solvent. In comparison, electrodes made of conductive polymer and metal thin films possess less of these issues. But, polymer and metal thin film electrodes are much stiffer with Young's modulus ranging from 0.9GPa (for PEDOT:PSS)[68] to 79GPa (for gold) compared to elastomer substrate like 3M VHB having Young's modulus of 1-2MPa.

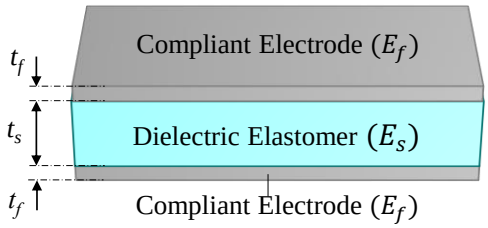

Figure 3-1. A dielectric elastomer actuator showing relative thickness and stiffness of the elastomer membrane and the compliant electrodes.

The thin film electrodes must be axially softer than the elastomer substrate; otherwise, they will limit the actuation strain of the DEA [69]. For instance, shown in Figure 3-1, if E_s is Young's modulus of the elastomer substrate with a thickness of t_s, to make a compliant electrode for the DEA, Young's modulus of the electrodes (E_f) with the thickness t_f must be lesser than

$$E_f = E_s \times \frac{t_s}{2t_f}. \quad \textbf{(3.1)}$$

However, based on Equation (3.1) even a pair of 55nm thin films of the soft polymeric electrode like PEDOT:PSS has a stiffness comparable to a 100μm thick VHB substrate.

Hence, DEAs made of these thin film electrodes in the flat forms hinders their expansive actuation strain.

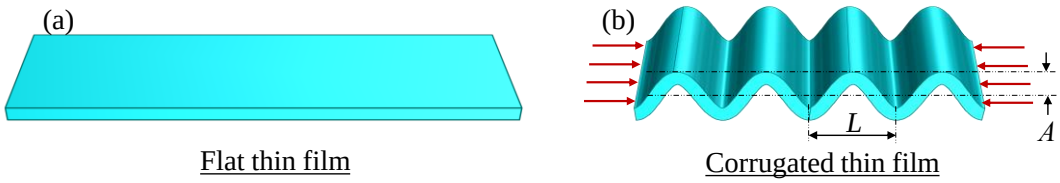

Figure 3-2. (a) Non-stretchable flat film; (b) Stretchable corrugated thin film.

Stiffness Analysis. Metals and metal-oxides in the form of flat thin films are non-stretchable. But, their corrugated film as shown in Figure 3-2(b) become compliant. Consider a uniaxially corrugated thin film with profiles represented by circular arc segments. In the limit of small deformation, the compliance factor which is a decrease in the stiffness of the corrugated electrode relative to the flat one of the same thickness (t_f) is given as [70-72],

$$f_c = 12\left(\frac{L}{s}\right)\left(\frac{A}{t_f}\right)^2. \tag{3.2}$$

where L is the spatial wavelength or the pitch, A is the amplitude and s is the are length along the full period. The effective Young's modulus ($E_{uniaxial}$) of the corrugate electrode is then given by:

$$E_{uniaxial} = {}^{E}/_{f_c} \tag{3.3}$$

where E is actual Young's modulus of the thin film. Uniaxially corrugated electrode is compliant in one direction. However, biaxially corrugated electrodes are needed to make radially compliant electrodes. Consider a biaxially corrugated plate in a sinusoidal profile:

$$h = A\sin\frac{2\pi}{L} \tag{3.4}$$

where *h* is the surface height, *A* is the amplitude and *L* is the spatial wavelength or the pitch. According to Timoshenko's plate theory for corrugation [73, 74], the effective axial modulus becomes only a fraction of the intrinsic modulus (for a flat plate) following:

$$E_{biaxial} = \left(\frac{\pi^2}{6(1+\nu)}\right)\left(\frac{2t_f}{L}\right)^2\left(\frac{1}{|e|}\right)E, \quad \textbf{(3.5)}$$

where *E* and *v* are actual Young's modulus and Poisson's ratio of the thin film, *L* is the corrugation pitch, and *e* is the biaxial compressive strain. Equation (3.5) shows a micro-corrugation can reduce the axial modulus of a film by approximately three orders. Consequently, micro-corrugation of metal or conductive oxide thin films can make compliant electrodes for DEA.

Fracture Limit. Bulk materials of metal-oxides are brittle. However, a nanometric thin film of metal-oxides can flex without exceeding the fracture limit. Here, we consider a flat nanometric thin film of thickness h_f. When it flex (or bend) into a radius of curvature *R*, it is subjected to a maximum strain on the surface following the beam bending theory:

$$\epsilon = \frac{t_f}{2R} \quad \textbf{(3.6)}$$

where, t_f is the thin film thickness.

The maximum tensile strain happens at the peak or valley of the corrugated surface where the radius of curvature becomes the smallest. Consider a flexing into the sinusoidal profile as described by Equation (3.4) with an amplitude *A* and a pitch *L*. The smallest radius of curvature is derived to be [75]:

$$R = \left.\frac{\left[1+\left(\frac{dt}{dx}\right)^2\right]^{3/2}}{\left|\frac{d^2t}{dx^2}\right|}\right|_{x=\lambda/4} = \frac{\lambda^2}{4\pi^2 A} \quad \textbf{(3.7)}$$

A finer-pitch wrinkling with a sharp bend may risk causing brittle fracture of metal-oxide thin films. To prevent fracture, the maximum strain of the flexing thin film as given by Equation (3.6) should not exceed the fracture limit of the material.

3.2 Microwrinkle Formation and Electrical Unfolding

As described before, a hard coating such as metal or conductive oxide in submicron thickness is axially stiffer and non-stretchable as compared to an elastomer substrate. But, under axial compression, it buckles into wrinkles. This microwrinkled thin film becomes stretchable as it is unfoldable. Hence, this microwrinkled thin films of metal or conductive oxides can make compliant electrodes for dielectric elastomer actuators.

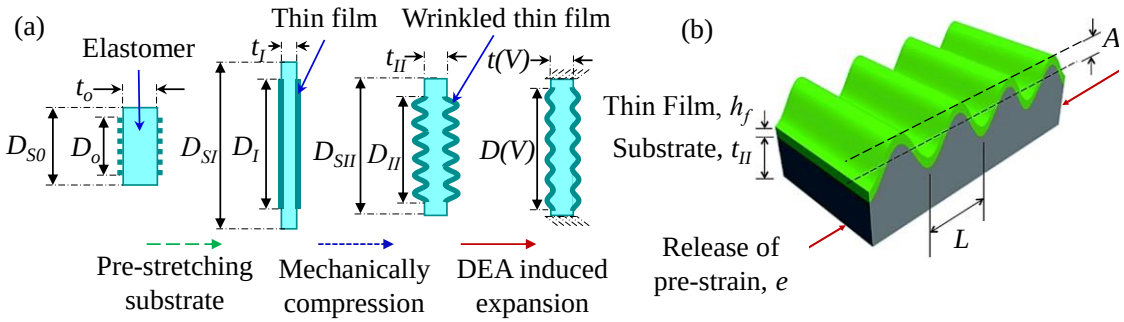

Figure 3-3. (a) Stretch states of a dielectric elastomer actuator during the wrinkle formation and unfolding; (b) Schematic of an isometric view of a wrinkled surface.

Microwrinkle Formation. Here, we show the fabrication of wrinkled compliant electrodes for a DEA or a soft capacitor. The fabrication is done in three steps (see Figure 3-3). First, a pristine elastomer membrane is radially pre-stretched. This enlarges the diameter of the elastomeric substrate from an initial value D_{S0} to be pre-stretched diameter D_{SI}. Meanwhile, this reduces the membrane thickness from an initial value of t_0 to t_I, which follows the relationship of volume incompressibility $t_0 D_{S0}^2 = t_I D_{SI}^2$.

Second, the thin films of metal or conductive oxides are deposited on both sides of the first pre-stretched elastomer substrate. The diameter of these as-deposited film is D_I.

Third, the thin films are subjected to a biaxial compression by relaxing the elastomer pre-stretch. This reduces the thin film diameter to D_{II} in proportion to the elastomer diameter D_{SII} following the relationship $D_{II}/D_I=D_{SII}/D_{SI.}$

The pre-compression strain in the thin films is

$$e_0 = \frac{D_{II}}{D_I} - 1. \tag{3.8}$$

Critical microwrinkling happens if the pre-compression strain is equal to the critical buckling strain given by (see Figure 3-3(b)) [57],

$$e_c = \frac{1}{4}\sqrt[3]{\left(\frac{3E_s}{E_f}\right)^2}, \tag{3.9}$$

which depends on the modulus mismatch between the film and the substrate. Here, E_s and E_f are Young's modulus of the substrate and thin film respectively.

Then, the critical pitch length L_c of the microwrinkle is [56, 57, 76-78]:

$$L_c = 2\pi t_f \sqrt[3]{\left(\frac{E_f}{3E_s}\right)} \tag{3.10}$$

where t_f is the thickness of thin film.

Post-buckling happens to the thin film when pre-compressive strain is greater than the critical strain e_c [57, 58, 74]. According to the Accordion bellow mechanics, the amplitude of the post buckled wrinkle is

$$A = L_c \frac{\sqrt{1+\nu}}{\pi}\sqrt{|e| - e_c}, \tag{3.11}$$

while the pitch length decreases with an increase in the compressive strain as

$$L = L_c \frac{(1-|e|)}{(1-e_c)}. \tag{3.12}$$

Equation (3.10), (3.11), and (3.12) suggests that a harder coating can form wrinkles of higher amplitude even under a smaller compressive strain. These equations have been experimentally verified in Chapter 5.

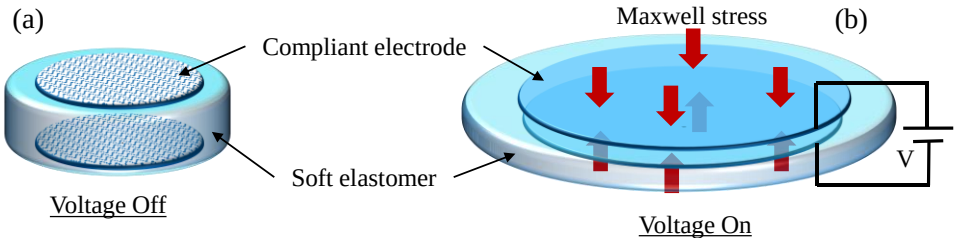

Figure 3-4. Schematic of a DEA at (a) in-active and (b) active states

Voltage-induced Unfolding of Microwrinkles. Voltage-induced activation strain can unfold the microwrinkled thin film electrodes of a DEA. Let us consider a circular DEA sandwiched by circular wrinkled thin film compliant electrode disks as shown in Figure 3-4. Maxwell stress is exerted on the dielectric elastomer upon application of a voltage. The electrostatic pressure (P_e) exerted on the elastomer membrane is expressed as [66, 79-81],

$$P_e = \frac{\epsilon_r \epsilon_o \left(\frac{V}{t}\right)^2}{2}, \tag{3.13}$$

Here V and t are the applied voltage and thickness of the membrane.

A high voltage (V) activation of the DEA induces a radial expansion with diameter increment $\Delta D(V) = D(V) - D_{II}$, relative to the diameter prior electrical activation D_{II} (see Figure 3-3). The voltage-induced net areal strain is simply the Poisson's ratio effect of Maxwell stress. The elastomer membrane is subjected to the following radial expansive strain:

$$\frac{\Delta D(V)}{D_{II}} = \frac{1}{2}\frac{\nu \varepsilon_r \varepsilon_0}{E_s}\left(\frac{V}{t_{II}}\right)^2, \tag{3.14}$$

where E_s is the Young modulus and v is the Poisson's ratio which has a value of 0.5 for the incompressible elastomer. In turn, the reduced compressive strain in the microwrinkled thin films relative to their as-deposited diameter (D_I) is given as:

$$e(V) = \frac{D(V)}{D_I} - 1 = e_0 + \frac{\Delta D(V)}{D_{II}}\left(\frac{D_{II}}{D_I}\right) = e_0 + \frac{\Delta D(V)}{D_{II}}(1 + e_0)$$
$$\approx e_0 + (1 + e_0)\frac{\varepsilon_r \varepsilon_0}{4Y_s}\left(\frac{V}{t_{II}}\right)^2. \quad \textbf{(3.15)}$$

This helps to unfold the microwrinkled electrodes. Such reversible microwrinkling and unfolding are useful to tune an optical diffuser.

3.3 Material Selection

Here, we review and select materials suitable to make compliant microwrinkled electrodes for the elastomeric tunable optical diffuser. This elastomeric tunable optical diffuser can be mechanically or electromechanically tuned with variable surface roughness and thus affect the optical diffusion. The selection of coating material is based on the following criteria:

- Being optically clear
- High refractive index
- Depositable near room temperature on an elastomer substrate
- Being conformal and smooth on the elastomer substrate
- Having uniform nanometric thickness distribution
- Good adhesion to the elastomer substrate
- High toughness
- Electrically conductive and stable
- Microwrinklable under a small compression strain

The clear state of this tunable optical diffuser depends on the inherent transparency and initial flatness of the deposited optical film on elastomer. A flat and smooth coating is only possible by room-temperature and low-stress deposition. Post-annealing process which was commonly used to improve the optical clarity and conductivity of transparent conductive oxide should be avoided because it introduces residual thermal stress and thus induces initial microwrinkles to the coating [23]. The initial microwrinkles results in hazy appearance which is harder to be tuned unless by a large stretch.

The frosted state of the diffuser requires mechanical compression to roughen the surface by microwrinkling. To fit into a window and remain tunable, activation strain requirements of the device needs to be small (say <5%) or it should involve only a small shrinkage of the active area. Otherwise, this device can only be operated like a curtain which folds under a large compression (greater than 50%) and will have a small window coverage. Equation (2.5) suggests, thin films with the higher refractive index can increase the light scattering power of these optical diffusers. Thus, these thin films enable transparency tuning using relatively smaller compression strain.

A thin film can form microwrinkles under a small compression (<5%) provided they are nanometric uniform thickness and have a high modulus mismatch with respect to the substrate. For example, a nanometric film of silicon was shown to form a wavy surface on silicon elastomer under 4.87% compressive strain [82]. But, due to optical opacity silicon nanofilm is not suitable for tunable optical devices. While optical oxide film is transparent, it risks fracture under bending. Fortunately, nanometer thickness and good adhesion to the adhesive elastomer substrate alleviates the fracture issues with small local tensile stress well below the fracture limit. Inherent toughness of other optical coatings should also further extend the lifetime of microwrinkled electrodes.

To make compliant electrodes out of the microwrinkled thin film, the thickness of the thin film must be several thousand times smaller than the soft substrate. While the flat optical coats are axially stiffer than the substrate, the microwrinkled coating could have comparable stiffness as the substrate, thanks to the axial stiffness reduction by microwrinkling.

Table 3-1. Comparison of mechanical, optical and electrical properties of various transparent thin films.

S. N	Coating Material	Processing technique (temperature)	Thin film modulus	Refractive Index	Tspec (%)	Sheet resistance/ Resistivity	Ref.

1.	Al_2O_3	Atomic layer deposition	(168-182) GPa (50 nm)	1.5-1.66	95%	10^6	[83, 84]
2.	ZnO	RF sputtering 25°C or (RT)	68-125 GPa (2-3 µm)	1.9-2	95%	$0.03\text{-}10^{-3}$ Ω.cm	[85, 86]
3.	AZO (2 % Al-doped)	RF sputtering (RT)	110 Gaps (500-800 nm)	1.87	87-93%	0.8×10^{-3} to $4.62\text{x}10^{-4}$ Ω.cm	[87, 88]
4.	FZO (5% F-doped)	RF sputtering (RT)	(300 nm)	1.5-1.6	80-85%	1.5×10^{-3} Ω.cm	[89]
5.	WO_3	sputtering (120°C)	150 GPa	1.9-2.3	75-88%	7.22 Ω/□	[90]
6.	TiO_2	E-beam evaporation/ low temp sol-gel (150 °C)	165GPa	2.5	88-95%	$2.3\text{x}10^4$ to 10^{10} Ω.cm	[91, 92]
7.	W-TiO_2 (4.5% W-doped)	Co-sputtering (650 °C) annealing/ CVD 500 °C	(150 nm)	-	50%	$1.5\text{x}10^{-2}$ Ω.cm/ 0.034 Ω.cm	[93]
8.	$Ti_{1-x}Nb_xO_2$ (TNO)	sputtering RT annealing (500 °C)	170 GPa (200 nm)	2.4	60-80%	$2\text{-}3\times10^{-4}$ Ω.cm	[94]
9.	ITO	DC magnetron sputtering	250 GPa	1.8	85%	30 Ω/□ (400 °C)	[95]
10.	FTO (5% F-doped)	DC magnetron sputtering (170 °C)	(400 nm)	2	82-85%	6.71×10^{-3} Ω.cm	[96]
11.	PEDOT:PSS	spin coating (RT)	0.9 GPa (90 nm)	1.44-1.6	71-95%	0.0012 Ω.cm / 40 Ω/□	[68]
12.	Poly N-vinyl carbazole/Ag / PEDOT:PSS	E-beam evaporation / spin coating	(50-60 nm)		85%	10 Ω/□	[97]

Table 3-1 lists various optical thin film materials which could be microwrinkled to make transparency tuning device and compares them in terms of their processing technique, elastic modulus, refractive index, optical transmittance, and sheet resistance. These thin

film materials can be classified into four groups for comparison; namely, electrically insulating optical oxides (ZnO, TiO_2), conductive oxides (ITO, AZO), conductive polymers (PEDOT:PSS), and metals (Ag, Au) (refer to Figure 3-5).

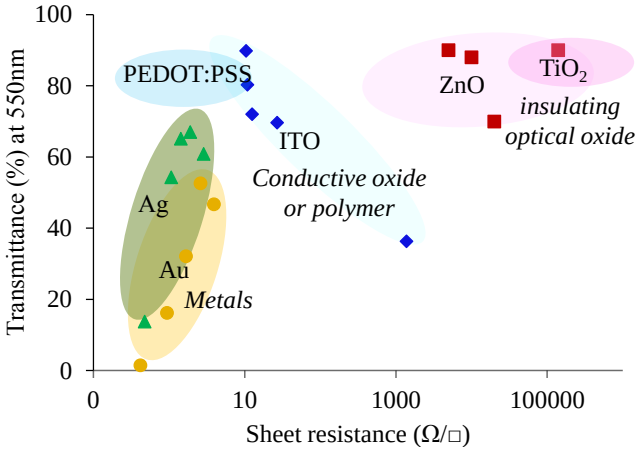

Figure 3-5. Comparison of thin film materials based on transparency and electrical conductivity.

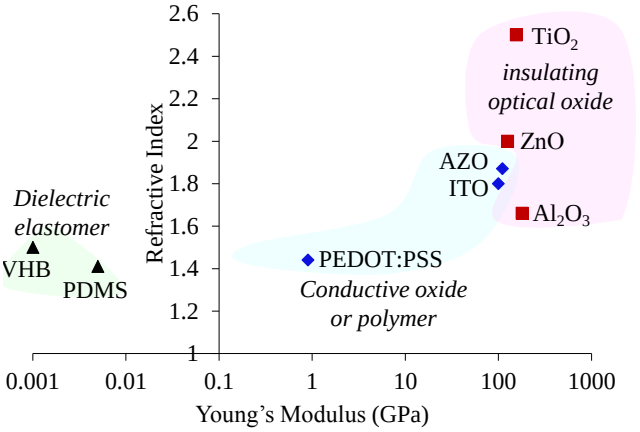

Figure 3-6. Comparison of thin film materials based on refractive index and elastic modulus.

Figure 3-5 shows the optical and electrical properties of the thin film materials under consideration. Among them, only a few are highly transparent and conductive, i.e. conductive polymer like PEDOT:PSS and conductive oxides like ITO, AZO. In comparison, metallic thin films are highly conductive but less transparent; insulating

optical coating like ZnO and TiO_2 are transparent but electrically insulating. Figure 3-6 compares Young's modulus and the refractive index of these thin film materials. Insulating optical coating have higher refractive index and modulus. In comparison, conductive polymer films have much lower stiffness and refractive index.

Figure 3-5 and Figure 3-6 suggests insulating optical oxides can easily form microwrinkles with small compression strain and also make better optical diffusers. But, they cannot be electrically tuned. Conductive transparent oxides like ITO thin film is ideal to make a microwrinkled compliant electrode. However, it needs post-annealing which forms residual wrinkles [23]. On the contrary, AZO nanometric thin films on dielectric elastomer have poor electrical conductivity. Moreover, conductive polymers merely have a small modulus mismatch with the elastomer substrate, thus they cannot form microwrinkles (see Figure 3-6).

There are only a few choices of conductive transparent thin films which can be processed at room temperature and sustain the microwrinkling without fracture. This motivates us to use tough insulating optical coating (ZnO, TiO_2) even though the coating may not be conductive. To achieve electrical conductivity, a conductive polymeric (PEDOT:PSS) overcoat can be applied to the insulating optical coating

3.4 Summary

Flat thin film electrodes of hard materials are non-stretchable, but they can make compliant electrodes upon microwrinkling. These compliant microwrinkled thin films can make electrodes for DEAs. Yet, the thin film materials to make DEAs for transparency tuning have additional requirements like high modulus, optically transparent, high refractive index, room-temperature processability and so on. Currently available thin film materials cannot individually meet these requirements. But, a combination of the multiple thin films made of insulating optical oxides and conductive thin film layer can make an appropriate DEA electrode for these transparency tuning devices.

Chapter 4 Tunable Window Device using ZnO Thin Film

A room temperature deposited ZnO thin film which can be coated conformally on an elastomer substrate is highly transparent. If the ZnO coated elastomer could form surface microwrinkles, it could be useful to tune the optical diffusion. However, it is not clear if ZnO thin film can sustain reversible microwrinkling and unfolding cycles without being subjected to fracture. This chapter will investigate the feasibility of inducing microwrinkles and unfolding ZnO nanometric film for the purpose of transparency tuning. In addition, we will try extra conductive coating on ZnO film to make compliant microwrinkled electrodes for dielectric elastomer actuators. This DEA with microwrinkled electrodes can make an electrically tunable window device. Results presented in this chapter has been published in Ref. [75, 98].

4.1 Introduction

Recent low-cost tunable window devices are developed based on elastomeric tunable optical diffusers [20, 23, 51, 54, 61]. They are made of deformable transparent elastomer substrate and nearly transparent electrodes. Their surface roughness changes with mechanical compression or electrical activation. With flat surfaces, they are transparent. But, with the surfaces roughened, they scatter light like an optical diffuser. Previously, gold thin films were used to induce electrical wrinkling on elastomer [20, 54], silver nanowires were used to electrically indent elastomer substrate [61]. These low-cost smart window devices have a moderate range of transparency tuning. For example, the clear state of 13-nm-thick gold coated elastomer has no better than 60% transmittance because the flat gold thin films are reflective and not so transparent [20, 54]. The transmittance of silver-nanowire coated elastomer is no better than 68%, because silver-nanowire networks are slightly hazy, scattering light even on the flat elastomer [61].

To improve on the clear state for transparency tuning, transparent conductive oxides (TCOs), such as indium tin oxides (ITO), could make a suitable transparent coating on

elastomer. Yet, preliminary experiments found that the evaporated ITO on the low-temperature elastomer substrate is brownish and not so transparent. Hence, this ITO-based electrically tunable window device [23] has merely a 52% transmittance as deposited. This low transparency is partly due to the thermally-induced initial wrinkles. Higher substrate temperature or post-annealing above 150°C [99] can improve transparency of the deposited ITO thin film but may risk melting the elastomer substrate and causing thermally induced wrinkles like the evaporated gold thin film on polydimethylsiloxane (PDMS) [100, 101]. Room-temperature deposited ZnO thin films reported to be flat with high transparency (of up to 95%) and good adhesion onto even a plastic substrate [102-104]. Hence, ZnO can possibly improve the range of transparency tuning if it could form wrinkles on the elastomer substrate.

This study investigates the microscopic wrinkling of transparent nanometric ZnO thin film on elastomer and its use for a smart window device. We will theoretically analyze the effect of microscopic wrinkles on diffuse refraction of light, and experimentally demonstrate that the microwrinkling and unfolding are reversible to tune the transparency over a nearly full range.

4.2 Theory

Figure 4-1 shows our tunable window device with a transparent elastomeric surface of variable roughness to diffuse light. It has a transparent coating of nanometric zinc oxide thin film on an elastomer substrate. The surface roughness of the device's top is tunable by diameter reduction, which induces microscopic wrinkle formation. At a flat state (see Figure 4-1(a)), an incident collimated ray of light is transmitted parallel in the same direction. When the same surface is roughened, it refracts the collimated rays of light in spatially varying directions (see Figure 4-1(b)).

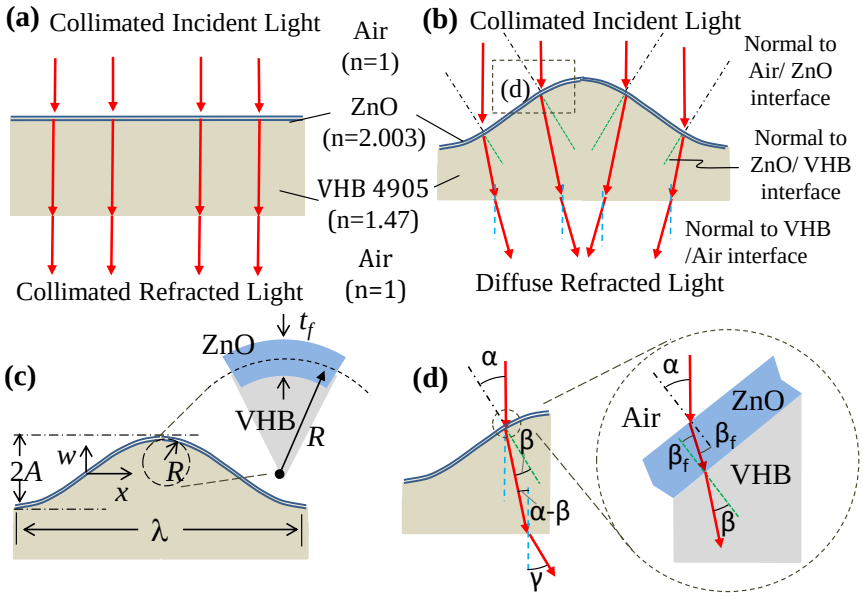

Figure 4-1. Principle of tunable window device based on surface roughness tuning: (a) a flat ZnO thin film on elastomer that in parallel transmits light (at an incident angle θ = 0°); (b) a wrinkled ZnO thin film on elastomer that scatters light; (c) a model of unidirectional wrinkles with sinusoidal profile; and (d) multiple refraction of a ray of light through the wrinkled surface.

For a simple analysis, consider unidirectional wrinkles in a sinusoidal surface profile (see Figure 4-1(c)) whose height w at the position x follows

$$w = A \sin 2\pi x/\lambda \tag{4.1}$$

where A and λ are the amplitude and wavelength, respectively. Consider a collimated beam of light, which was incident to the flat surface at an incident angle θ. As the surface becomes wrinkled, the incident angles of the same collimated light vary spatially, following

$$\alpha = \theta + \frac{dw}{dx} \tag{4.2}$$

where dw/dx varies spatially from $2\pi A/\lambda$ to $-2\pi A/\lambda$ over a half wavelength.

Consider a ray of light incident at a point tangent to the wrinkled surface (at an angle α as shown in (Figure 4-1(d)). The ray of light is subjected to refraction twice over the film

interfaces and once upon exiting the bottom of the elastomer substrate. The ZnO thin film is so thin that its two interfaces are parallel, and the refracted angle β_f at the first interface is equal to the incident angle at the second interface. Therefore, the angle of refraction into the VHB layer can be predicted by Snell's law, following

$$1.\sin\alpha_i = n\sin\beta, \tag{4.3}$$

This suggests that the refracted angle β in elastomer depends directly on the incident angle α in the air but is independent of the thin-film property. The refractive index of ZnO thin film is close to 2.0 [105], whereas the refractive index of elastomer used here (i.e., VHB 4910) ranges from 1.48 to 1.50 [61]. The third refraction occurs at the bottom interface of the elastomer substrate with air. The incident angle of $(\alpha - \beta)$ in the elastomer is refracted into an angle γ in the air following

$$n\sin(\alpha-\beta) = 1.\sin\gamma, \tag{4.4}$$

The exit refracted angle γ can be expressed only in terms of α upon substituting Equations (4.3) into Equation (4.4):

$$\gamma = \sin^{-1}\left(\sin(\alpha)\sqrt{n^2-\sin^2\alpha} - \frac{1}{2}\sin 2\alpha\right) \tag{4.5}$$

This analysis suggests a higher ratio of A/λ (i.e., a large amplitude) for microwrinkles means a higher spatial variation of incident angles and thus better for diffuse refraction of light. In comparison to the unidirectional microwrinkles, biaxial wrinkles (as induced by radial compression) will scatter light more effectively.

To increase the diffuse refraction, sharp wrinkles with few-micron-sized wavelength are desired. According to the mechanics for buckled thin films, the wavelength decreases, and the amplitude increases with increasing the compressive strain [58]. This means that a large compressive strain is needed to induce high amplitude wrinkles. Yet, the compression may cause delamination of the thin film off the substrate if adhesion is poor and the critical strain for delamination is exceeded [106]. A delaminated layer has the underlying substrate flattened and hence does not wrinkle much. The delamination even causes the amplitude reduction and wavelength increment to the neighboring wrinkles.

For example, a 100-nm thin film of radio frequency-sputtered ZnO with partial adhesion to the silicon substrate (polydimethylsiloxane) is subjected to buckle-delamination upon compression [107], and thus produces a rather long wavelength of 200μm at 5% compressive strain.

In addition, a sharp bend of microwrinkled ZnO thin film may risk causing a brittle fracture. ZnO thin film has a high Young's modulus of 110–137GPa [87, 108] relative to 1 MPa of acrylic elastomer [81]. A very small tensile fracture strain of 0.1% was reported for a 640-nm-thick ZnO free film, which was DC magnetron sputtered on a micro-bridge structure of 400-nm-thick silicon-nitride [108]. A higher crack onset strain of around 2% was reported from the controlled buckling test of a 75-nm-thick ZnO thin film DC-magnetron sputtered on a polyester sheet [102]. The buffer of submillimetre-thick polyester substrate greatly improves the fracture strain of ZnO. This finding of improved fracture strain is encouraging, but it is not clear if a ZnO thin film can be bent into a microscopic radius of curvature without fracture.

In this chapter, we will show that nanometric thin film of ZnO on an adhesive elastomer tape (VHB 4910) could meet this requirement for fine-pitch wrinkling. According to a 3M datasheet [109], 3M VHB 4910 is an elastomeric foam tape with a very high bond. It is reported to have a 90° peel adhesion of 26 N/cm, a dynamic overlap shear of 480 kPa to stainless steel, and a 690 kPa normal tensile adhesion to aluminum. Hence, its use as the elastomeric substrate can avoid delamination of the coated thin film.

Equations (3.6) and (3.7) leads to an estimate of 2.5μm radius of curvature for a sinusoidal wrinkle of 10-μm wavelength and 1μm amplitude. At this radius, a 50-nm thin film of ZnO is subjected to a calculated maximum tensile strain of 1%, less than the reported fracture strain of 2%. Hence, the 50nm thin film of ZnO could survive this sharp wrinkling to cause the diffuse refraction.

4.3 Method and Material

4.3.1 Device Fabrication

Figure 4-1(a)–(c) shows the procedure to reversibly form wrinkles of ZnO thin film on a VHB membrane (3M VHB 4910). First, the VHB elastomer membrane (initially 1mm thick) is radially pre-stretched to be three times larger in diameter compared to its original diameter using a custom-made radial stretcher [23, 74, 110]. Second, a 50-nm thick thin film of ZnO is deposited conformably by e-beam evaporation technique on the pre-stretched elastomer substrate through a Teflon film mask. Third, the radial pre-stretch of the elastomer substrate is partially released to apply the compressive stress on ZnO thin-film resulting in the formation of microwrinkles. The radial compressive strain is calculated to be $c=1-D_{II}/D_I$ where D_I is the initial diameter of flat coating and D_{II} is the reduced diameter of the wrinkled coating. A linear stage is used to manually drive the radial stretcher to achieve a controlled compression. Unfolding can restore the flat surface.

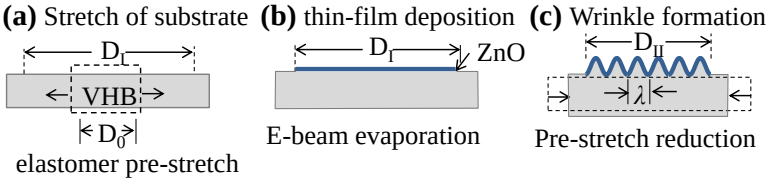

Figure 4-2. Process steps for device making: (a) pre-stretch of elastomer substrate (VHB 4910); (b) deposition of ZnO on the elastomer substrate and (c) wrinkle formation by partial release of the pre-stretched elastomer.

The evaporation material is 99.9% undoped ZnO pellets. The process parameters for the e-beam evaporator (Coaxial Power Systems) are: 4.2 × 10−5 torr pressure, 1.6-mA current, and 4.89-kV bias voltage. The deposited film thickness is monitored using a quartz crystal microbalance.

4.3.2 Experimental Setup

A scanning electron micrograph of the sample allows inspection of the morphology and wavelength of the microwrinkles, whereas a confocal micrograph of a 0.16μm spatial

sampling and 4nm RMS roughness repeatability (using a Sensofar PLμ 2300 confocal image profiler) provides a measure of the wrinkle heights. A spectrometer (AvaSpec-USB2 Fiber Optic) and halogen light source (AvaLight-Hal-S-Mini) were used in the experiment setup (see Figure A-4) to measure the in-line transmittance spectrum (of visible light range) through the sample of a ZnO/VHB-based device. To evaluate the repeatability of the transparency tuning cycles, a video capturing 30 cycles of transparency tuning was recorded. Relative Michelson contrast was used to quantitatively determine the perceived transparent state [111]. Gray values (intensity values) of a black logo in the captured video frames during transparency tuning cycles were extracted using the Image J software.

4.4 Results and Discussions

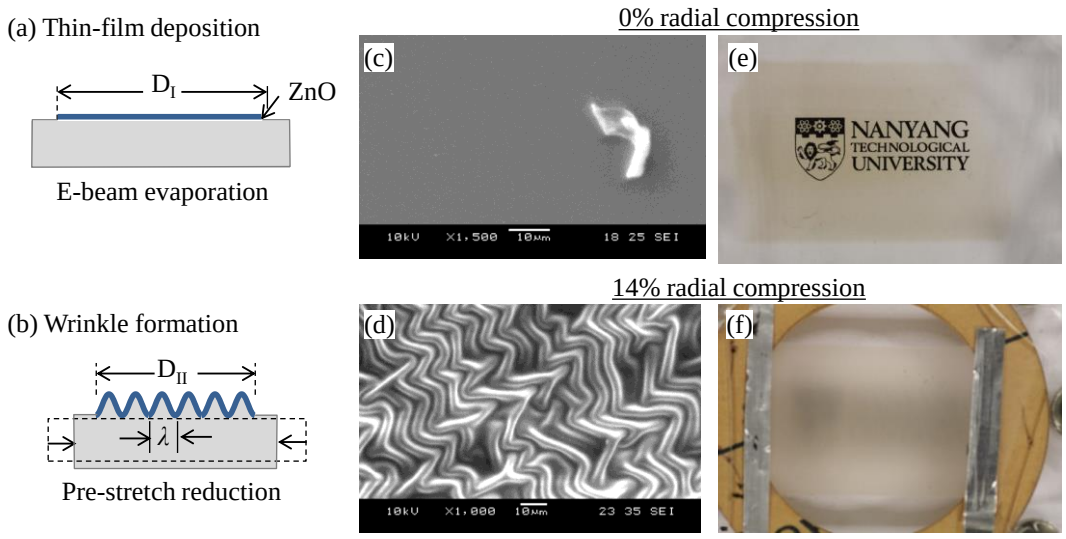

Figure 4-3. Schematic of a ZnO thin film coated on a VHB membrane at: (a) flat; and (b) wrinkled state. Scanning electron micrograph of the same (taken after 10 cycles of compression and unfolding) and optical appearance of a logo placed 10 mm beneath the same membrane: (c)–(e) the clear state at 0% radial compressive strain; and (d), (e) the translucent state at 14% radial compressive strain.

Figure 4-3(c) shows a flat ZnO thin film, deposited on a pre-stretched elastomer membrane (VHB 4910) by an e-beam evaporation technique. The flat surface

morphology suggests that the deposition of ZnO thin film occurred at room temperature. The flat ZnO thin film on VHB appears transparent, and a logo placed 10 mm beneath it can be clearly seen. Wrinkles form when the ZnO thin film is radially compressed by releasing the elastomer substrate's pre-stretch. Figure 4-3(d) shows that the ZnO wrinkles formed on VHB at 14% radial compression can fully obscure the logo beneath it (see Figure 4-3(f)). The wrinkle patterns are zig-zagged and irregular in orientation, with an average wavelength of approximately 7.6μm and an average amplitude of 1.78μm. No observable cracks are on this sharply bent ZnO even though the sample for scanning electron microscopy has undergone 10 cycles of compression and unfolding.

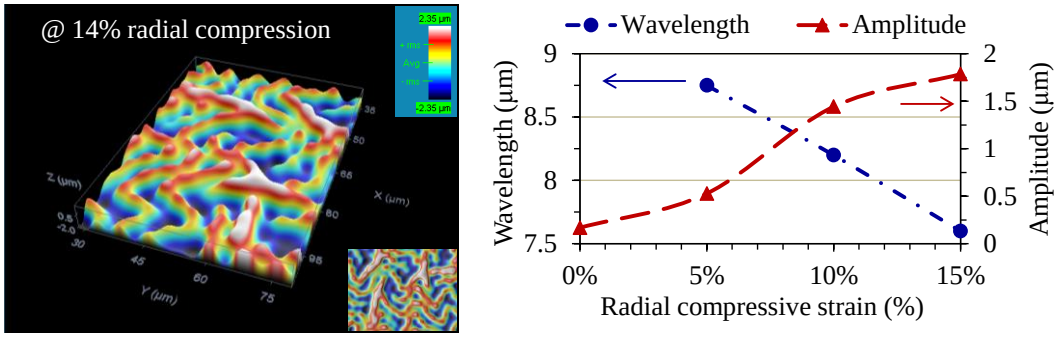

Figure 4-4. Confocal micrograph showing the surface morphology of ZnO thin film subjected to 14% radial compression (the inset is a top view of the same surface) (left); and the wavelength and amplitude plotted as a function of the radial compressive strain (right).

Figure 4-4 shows a confocal micrograph of ZnO wrinkles formed at 14% radial compression with the wrinkle heights measured. The wavelength of microscopic wrinkles decreases with increasing compression while the amplitude increases. As the ZnO/VHB surface roughens with increasing compression, its in-line transmittance decreases for broadband of visible light (see Figure 4-5). It demonstrated a nearly full range of transparency tuning, exceeding the performance of many reported devices based on other material systems [20, 23, 54]. For example, a clear state of 93% transmittance switches to a translucent state of 3% transmittance upon a 14% radial compression. This transparency tuning is reversible. Mechanical unfolding can flatten the transparent surface and restore high transparency.

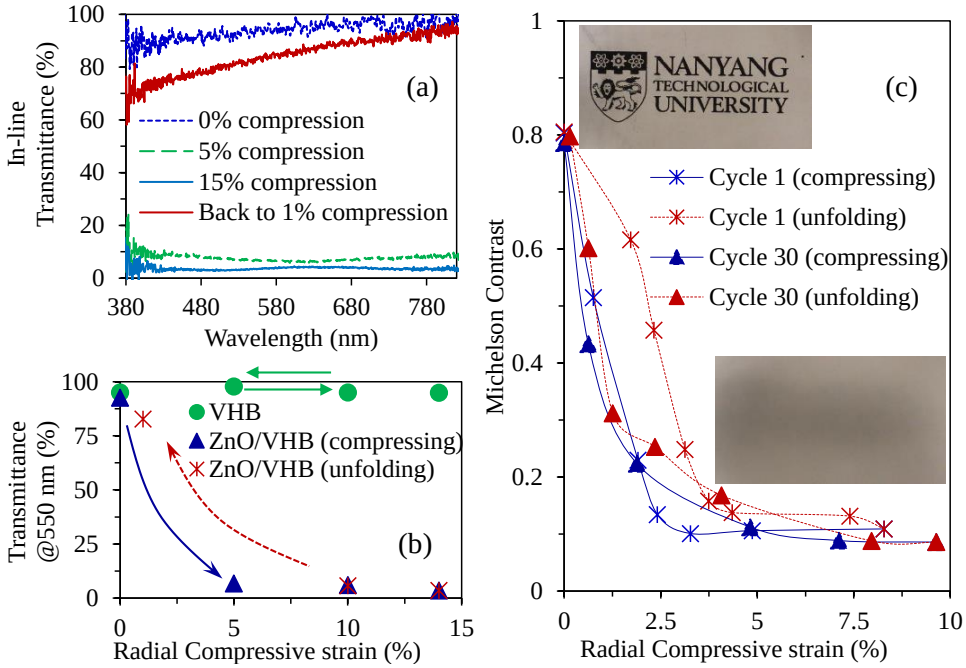

Figure 4-5. (a) In-line transmission spectra of visible light through ZnO/VHB at different radial compression; (b) the transmittance at 550nm wavelength as a function of the radial compression; (c) Michelson contrast over cycles of radial compression and unfolding.

For a reversibility test, the device is subjected to 30 cycles of compression of up to 10% strain and unfolding while a video records the visibility of a black logo beneath it. The perceived transmittance over the cycles is measured in terms of the relative Michelson contrast. Figure 4-5(c) shows that the transparent state at zero compression consistently shows a high contrast of 0.8 for 30 cycles. Similarly, the translucent state at 10% radial compression consistently shows a low contrast of 0.1. This initial test result shows that microwrinkling and unfolding of ZnO nanometric thin-film on acrylic elastomer substrate are reversible and repeatable over cycles. But, the transmittance at the intermediate states is inconsistent over cycles. This could be due to the viscoelastic nature of acrylic elastomer that delays the occurrence of wrinkling or unfolding relative to the radial diameter change over time.

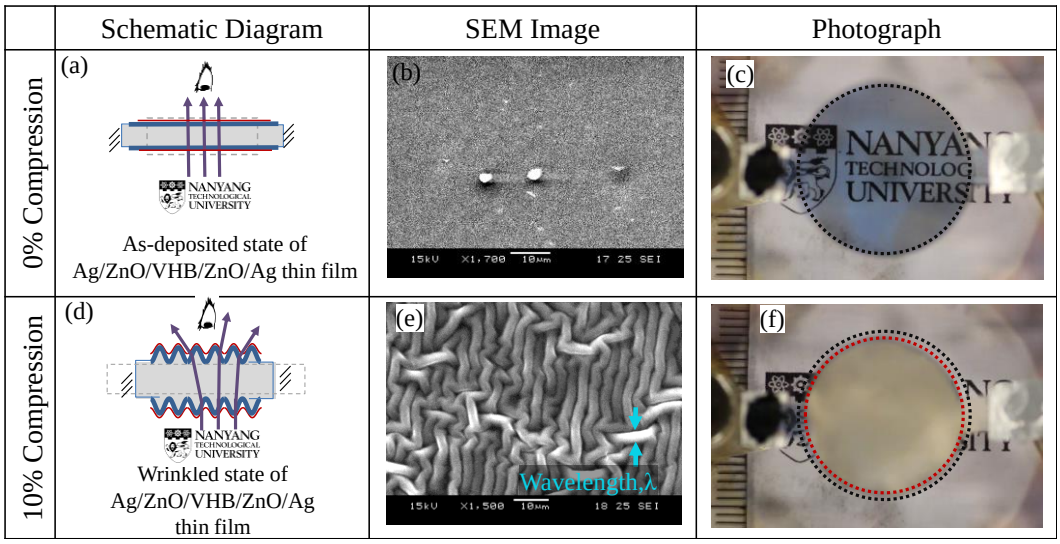

Figure 4-6: Schematic and SEM micrograph of the ZnO/Ag thin-films that sandwiches a VHB membrane and the visibility of the NTU logo placed 10 mm beneath the device: (a)–(c) the clear state at 0% radial compressive strain; and (d)-(f) the translucent state at 10% radial compressive strain.

To electrically tune transparency using a DEA, the coating layer must be a compliant electrode. Unlike ZnO thin films, a nanometric silver thin film is known to be transparent and conductive [112]. Hence, it is DC magnetron sputtered on a ZnO thin film coated VHB substrate to make a conductive electrode. Presented device is a DEA with a pair of 10nm-Ag/30nm-ZnO thin-film electrodes deposited on both sides of a three times pre-stretched DE membrane (VHB 4905). Surface morphology of the 70multilayer thin films and its effect on DEA's optical appearance is shown in Figure 4-6. Initially, the multi-layered thin films are equally flat as the elastomeric substrate. It has a roughness of approximately of 0.16μm. The device initially has a bluish appearance due to the plasmonic resonance effect [113] of the nanometric silver thin film which partially absorbs all visible light except the blue light. Figure 4-6(e) shows the multi-layer thin films wrinkled with ~3.35μm wavelength and maximum roughness of 1.443μm when subjected to 10% radial compression. At this state, the Ag/ZnO based device appears opaque and completely conceals the logo beneath it (see Figure 4-6(f)).

The DEA with the wrinkled Ag/ZnO thin film electrodes can electrically tune its transparency. Figure 4-7 shows it was opaque with 1% inline transmittance at 10% radially compressed state. It concealed a logo beneath it giving a Michelson contrast ratio of 0.05 (see Figure 4-7(b)). When activated with 6.5kV (i.e. 54MV/m), it produces an actuation expansion strain of 10%. This radial strain completely unfolds and flatten the electrodes restoring the initial transparency. At this activated state it has 47% in-line transmittance and the logo beneath it is clearly visible (at 0.72 Michelson contrast ratio. When the voltage off, the DEA gradually returns to its opaque state.

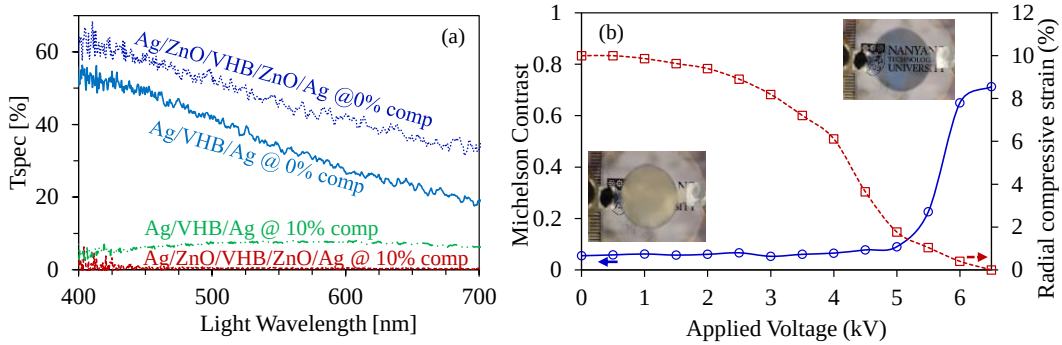

Figure 4-7: (a) Inline transmittance spectra of the visible light through the transparency tuning device; (b) Change in Michelson contrast of the image placed beneath Ag/ZnO/VHB/ZnO/Ag and radial compressive strain when activation voltage is increased.

A pulsed voltage activation (6kV, 50% duty cycle, and period of 2 seconds) can swiftly tune the device between opaque and transparent states. At on state, the electrode is radially expanded by ~10%. However, as the voltage is turned off, the dynamic recovery of Michelson contrast is incomplete (see Figure 4-8). VHB substrate's viscoelastic nature is responsible for this slow off response. The device's time constant can be determined by the visibility of a logo during its pulsed activation. While turning on the device, it takes 0.5 seconds to reach 90% of its transparent state (i.e. 0.72 Michelson contrast). For the few initial cycles, when the device is turned off, it returns to 0.3 Michelson contrast. Yet, the opaqueness during the off states decreases when activated more than 4000 cycles. However, it returns to its initial opaqueness if the device is turned off for more than 10 seconds. The pulsed resistive heating of the elastomer might be the cause of this

slow recovery response. Despite multiple activation cycles, the device was still operable with no major performance degradation. This proves it to be reliable for long-life operation.

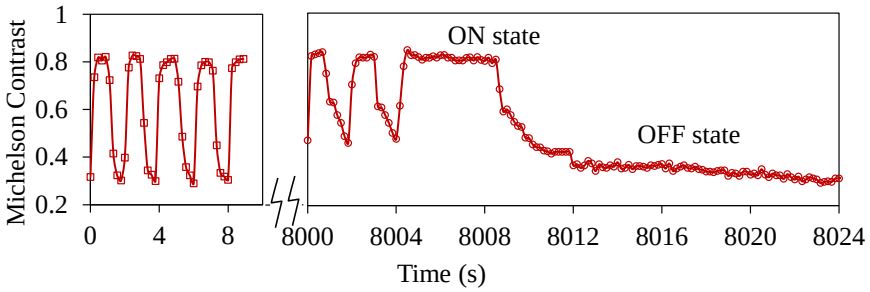

Figure 4-8: Response of the Ag/ZnO coated DEA when activated by a square pulse of 6kV at 0.5Hz. Plot of Michelson contrast for: (left) the first four cycles; (right) last three of the 4000 activation cycles.

4.5 Summary

This chapter developed a tunable window device capable of reversible tuning between the clear and translucent states upon wrinkling or unfolding of a transparent elastomeric surface. Its success lies with microscopic wrinkling of a zinc-oxide thin film on an adhesive elastomeric substrate. Analysis suggests that a large amplitude and aspect ratio of transparent microwrinkles are good for diffuse refraction of light. In addition, the use of nanometric thin film is essential to achieve the "crack-free" microwrinkling despite the brittle nature of zinc oxide. A conductive overcoat layer like Ag thin film on ZnO thin films can make a hybrid multi-layer electrode to tune transparency. However, the reflective and absorptive nature of Ag thin films reduces the transparency of the device. Moreover, the in-plane compression strain needed for the transparency switching is still too high to be used for a window device.

Chapter 5 Electrically Tunable Window Device using PEDOT:PSS/TiO_2 Thin Films

A microwrinkled surface of the transparent elastomer can diffuse light like frosted glass. Nanometric optical oxide films on an elastomer can form microwrinkles when compressed under a small compressive strain (<5% radial). However, only a few optical oxides are conductive. This chapter shows the use of an overcoat of transparent conductive polymer made of poly (3, 4-ethylene dioxythiophene)-poly styrene sulfonate (PEDOT-PSS) on high-refractive index coating of TiO_2 to form microwrinkled compliant electrodes. This microwrinkled compliant electrode is suitable to make a dielectric elastomer actuator as the electrically tunable optical diffuser. This chapter shall show such a DEA-based device with excellent tunability of optical diffusion, and low area-specific power consumption as compared to the commercial smart window based on polymer dispersed liquid crystal (PDLC). Results presented in this chapter is published in Ref. [114].

5.1 Introduction

Existing smart windows based on polymer dispersed liquid crystals (PDLCs) and electrochromes are still expensive for household use (see Table 1-1 for details), and they age under UV exposure [10, 14, 115-117]. In comparison, frosted glass is relatively cheap and reliable for window use to diffuse daylighting, to reduce sun glares, and to provide privacy. A frosted glass finish can be created by spraying aerosol of white paint on a transparent glass. Likewise, gel frost filters for theatrical lighting have a thin slurry of titanium dioxide (TiO_2) coating on a transparent plastic film [118]. TiO_2 is one of the few optical materials with the high refractive index [119]. TiO_2 nanoparticles are commonly used as a bright white pigment for high-opacity paint [120] that diffuses visible light by Mie scattering. The scattering power varies with the size of and separations between these transparent nanoparticles [120] in resin. Being 'dense packing' of nanoparticles, a nanometric thin film of TiO_2, however, becomes transparent [121]

due to the diminishing effect of Mie scattering. If the TiO_2 nanometric thin film can switch between clear and frosted (translucent) upon micro-topography change, it can be useful to make a smart window. This could also make a tunable optical diffuser handy for cinematography lighting, [122] removing the need for manual changing of lighting diffusion gels/filters.

Recent research and development [20, 22, 23, 34, 51, 53, 54, 61, 74] have witnessed various alternative technologies of the smart window. Among them, elastomeric tunable optical diffusers based on surface microwrinkling are one of the most promising and low-cost technologies. The window device based on microwrinkling of nanometric optical thin films works almost like a transparent shower curtain: it is clear when being flat, but it becomes translucent or frosted when its surfaces fold (or buckle) under axial compression. It required a large stretch to unfold the active area to be clear again, for example, a manual stretch of up to 30% for unfolding a sub-millimeter wrinkled silicone rubber [51, 53]. The electromechanical unfolding of the microwrinkled surface is possible by using a dielectric elastomer actuator [22, 23, 54, 74, 123, 124]. However, the microwrinkled transparent compliant electrodes for transparency tuning occupied only a small fraction of the actuator device as they need room for large-strain unfolding [54, 74].

While microwrinkled metallic thin film electrodes are commonly used in flexible and stretchable electronics,[124] nanometric metallic thin films with limited transparency are not perfect for transparency tuning [20, 125]. Recently, the nanometric optical coating was reported for tuning optical transmittance upon microwrinkle formation at a smaller strain down to 14.0% [23, 75]. Yet, few transparent and conductive oxides can make a long-life compliant microwrinkled electrodes without being prone to fatigue and fracture. A hybrid meta-material design [126-128] can potentially overcome the intrinsic material limits. Here, we shall consider this approach to design a tunable surface scatterer out of hybrid optical thin films for a smart window.

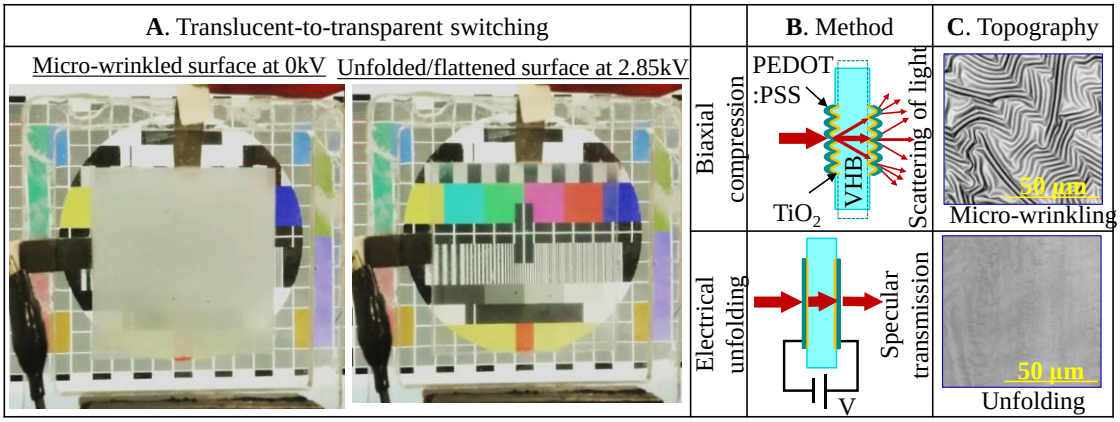

Figure 5-1. Smart window based on electric unfolding of microwrinkled TiO_2 nanometric films: (A) switch between hiding or revealing of a Philips pattern on a liquid crystal display; (B) working principle of tunable light scattering from microwrinkled surfaces and voltage-induced unfolding by a dielectric elastomer actuator (C) the topography change in the microwrinkles upon unfolding.

This chapter demonstrates a transparency tuning smart window based on small-strain microwrinkling/unfolding to switch between frosted and clear. This tunable window device is a dielectric elastomer actuator sandwiched by a pair of microwrinkled thin-film electrodes of hybrid optical materials (see Figure 5-1). Each compliant electrode consists of a nanometric optical interface of TiO_2, a nanometric conductive overcoat of poly (3,4-ethylene dioxythiophene) polystyrene sulfonate (PEDOT:PSS), both on a membrane substrate of pre-stretched acrylic elastomeric foam tape. As a tunable surface scatterer, this TiO_2 nanometric thin film readily forms crack-free microwrinkles under a smaller compression (e.g. 4-5%) despite the bulk nature of oxide being brittle and hard (Young's modulus of 165GPa [92]). A conductive, transparent and softer overcoat of PEDOT:PSS provides the necessary electrical conductivity, [129] missing from the TiO_2 nanometric thin film. Figure 5-1A (left) and Figure 5-1B-C (top row) shows the microwrinkled surfaces appearing highly translucent to conceal the color-bars like a yellowish white paint does. These hybrid microwrinkled thin films can be unfolded electrically by means of voltage-induced areal expansion of dielectric elastomer. Figure 5-1A (right) and

Figure 5-1B-C (bottom row) shows the unfolded surfaces turning highly transparent and making visible the color-bars beneath it.

5.2 Theory

This tunable optical diffuser consists of two tunable optical scatterer surfaces sandwiching a dielectric elastomer membrane. Its surface topography change can tune the scattering of forward visible light. Figure 5-1B shows a monochromatic light of wavelength λ incident normally (θ_i = 0°) onto a device's surface between the air (refractive index n_1) and dielectric elastomer (refractive index n_2). For a smooth surface, the total transmittance at normal incidence is: $T = 1 - R = \frac{4n_1 n_2}{(n_2+n_1)^2}$ according to Fresnel equations [36]. Consider a device with two identical Gaussian surfaces of voltage-tunable roughness σ (V) and finite electrical conductivity [47, 49, 50, 130]. The specular (non-diffuse) part of the total transmittance through the device is obtained as

$$T_{spec} = T^2 . \exp\left\{-2\left[\frac{2\pi\sigma(V)}{\lambda}(n_1 - n_2)\right]^2\right\} \quad \textbf{(5.1)}$$

where $n_1 = 1$ for air and n_2 being greater than 1 for elastomer substrate (refer to Appendix B). This relationship suggests that a TiO_2 coating of the higher refractive index (2.7) [119] can help achieve a stronger scattering effect (to visible light), more than other transparent materials do.

The surface roughens upon formation of microwrinkle under biaxial compression (see Figure 5-2A). Consider a pair of thin-film electrodes (of stress-free diameter D_I, thickness t_f, Young's modulus E_f) sandwiching a radially pre-stretched elastomer membrane (of thickness t_s and Young's modulus E_s). Releasing the radial pre-stretch in the elastomeric membrane reduces the thin-film electrode diameter to be D_{II}. When this radial compressive strain $e_0 = \frac{D_{II}}{D_I} - 1$ exceeds the critical buckling strain $e_c = \frac{1}{4}\sqrt[3]{\left(\frac{3E_s}{E_f}\right)^2}$ according to Ref. [58, 99], surface post-buckling happens to the radially compressed thin films.

Dielectric elastomer actuation can unfold this initially microwrinkled surfaces of compliant electrodes. High-voltage activation of dielectric elastomer actuator induces Maxwell stress between opposite electrodes [123, 131-134]. Due to Poisson's ratio effect, electrostatically squeezed membrane expands in area. Hence, this voltage-induced areal expansion can reduce the compressive strain in the thin-film electrodes to be

$$e(V) = \frac{D(V)}{D_I} = e_0 + (1 + e_0)\frac{\varepsilon_r \varepsilon_0}{4E_s}\left(\frac{V}{t_s}\right)^2. \quad \textbf{(5.2)}$$

by assuming the elastomer being incompressible (with Poisson's ratio of ν = 0.5). Refer to Equation (3.14)-(3.15) given in Chapter 4 for detailed derivation. The parameters used here for a VHB substrate are E_s = 200kPa according to Ref.[135, 136], t_s = 65.0μm, and a dielectric constant ε_r= 4.5-4.7 and a vacuum permittivity of 8.85 pF/m.

For a surface with a profile height h over a unit area (of lengths X and Y in the coordinates x and y respectively), the root mean square (rms) surface roughness is defined as [44]

$$\sigma = \sqrt{\frac{1}{XY}\iint \left(h(x,y) - \bar{h}\right)^2 dxdy}\,, \quad \textbf{(5.3)}$$

where $\bar{h}$ is the mean profile height. For a harmonic profile of $h = A\ sin\ 2\pi x/L$ with pitch length L and amplitude A, the rms surface roughness is calculated to be $\sigma = A/\sqrt{2}$, the same as that for a 45°-inclined harmonic profile of $h = A\ sin\ 2\pi(x + y)/\sqrt{2}L$.

According to the surface instability model,[57] the amplitude A of a harmonic or herringbone wrinkles depends on the biaxial compressive strain which is voltage-controllable here:

$$A = L_c \frac{\sqrt{1+\nu}}{\pi}\sqrt{|e| - e_c} \quad \textbf{(5.4)}$$

in which $L_c = 2\pi t_f \sqrt[3]{\left(\frac{E_f}{3E_s}\right)}$ is the wrinkle's critical spatial wavelength or the critical pitch length [57]. The parameters used here for the TiO_2 thin film are: E_f=165GPa, and t_f=19.79nm.

The relation of critical pitch length with moduli suggests that harder the coating modulus lesser the compressive strain required to induce the same microwrinkles. For example, a nanometric silicon film becomes wavy under 3.8% thermal pre-strain [137]. Yet, the harder coating may impede the voltage-induced areal expansion of dielectric elastomer. At the first sight, a hard nanometric coating of TiO_2 (with Young's modulus of up to 165GPa [138]) is almost inextensible to conform with the voltage-induced deformation of dielectric elastomer (e.g. VHB 4905 with a 0.2-1.0 MPa Young's modulus [132, 135, 136]). Fortunately, a microwrinkled form of the TiO_2 nanometric thin film becomes as stretchable and deformable as dielectric elastomer does due to the third-order reduction in effective axial stiffness (refer to Equation (3.5)) [74] by microwrinkling.

5.3 Materials and Methods

This tunable window device is a dielectric elastomer actuator with microwrinkled thin-film electrodes of hybrid optical materials. Fabrication of this tunable window device follows the same procedures as making a dielectric electrode actuator with microwrinkled electrodes, [74] except the special use of TiO_2 and PEDOT:PSS nanometric thin films as the surface scatterer. Fabrication steps include: 1) preparation of elastomer membrane substrate; 2) e-beam evaporation of TiO_2 film; 3) spin coating of PEDOT:PSS film. Completion of these steps and membrane transfer to rigid window frame yields a complete device, which has aluminum leads to the power supply and electronic instrumentation during testing. The device is subjected to various testing, which includes electromechanical activation, and measurement for morphology, transmittance and light scattering. Details of the materials and methods are elaborated below.

Elastomeric membrane substrate. The elastomeric membrane substrate is a pre-stretched tape of acrylate elastomer (3M VHB4905). The tape was pre-stretched for 3.0 times radially to have a 65μm thickness as measured by a micrometer. This measured membrane thickness is more than the estimated 500μm/(3x3) due to the release of the membrane’s free edges away from the sketcher's 9 contact points. The pre-stretched

elastomer membrane was left 24 hours to ensure that viscoelastic creeps settle down to a steady state. Subsequently, the pre-stretched membrane at steady state was deposited with optical thin films of higher modulus and elasticity. The optical thin films were radially compressed to form microwrinkles when the elastomer membrane has the pre-stretch partially released from 3.0 times to 2.7 times.

TiO_2 thin films. An amorphous TiO_2 thin film was e-beam evaporated on the elastomeric substrate. The evaporation material is 99.9% undoped TiO_2 pellets. An e-beam evaporator (Edwards) was used for the physical vapor deposition, with the process parameters being: $5x10^5$mbar pressure, 18mA current, and 5.01kV bias voltage. A built-in quartz crystal microbalance was used to monitor the deposited film thickness and it thus enables the controlled deposition to a target thickness. A surface profiler (Dektak 3ST Surface profilometer) was used to measure the actual thickness of the deposited film. Thickness measurement (see Figure 5-2B) shows the deposited film thickness is linearly proportional to the time of e-beam evaporation, at a measured deposition rate of 0.32nm/min.

The absence of thermally induced microwrinkles suggests that the substrate heating is minimal during this e-beam evaporation. Morphology of the deposited TiO_2 thin film appears rather smooth. In addition, we evaluated the crystallinity of the deposited thin film by using an X-Ray Diffractometer (Empyrean, PANalytical). The XRD analysis is carried out at a low incidence angle of 0.5° to isolate the signal of the nanometric thin film from that of the elastomeric substrate. XRD measurement (see Figure 5-2C) shows no spike of crystallinity. Hence, the deposited TiO_2 thin films are concluded to be amorphous.

Transparent compliant electrodes. A transparent compliant electrode was spin coated as an overcoat on a TiO_2 coated elastomer substrate. The conductive ink for spin coating is a water-based suspension, which was prepared by mixing one part by weight of as purchased PEDOT:PSS solution (Clevios P Jet HC V2, from Heraeus Deutschland GmbH &f Co. KG) with one part of deionized water. The static sessile drop method

(Optical Tensiometer, Attension Theta, KSV instruments) was used to measure the contact angle between a droplet of aqueous conductive ink and an elastomeric substrate.

Procedures of the spin coating are described as follow. First, the aqueous suspension of conductive ink was drop cast and spread on the elastomeric substrate. Second, the substrate with a puddle of aqueous ink was spun at 1000 rpm for 1 minute. Third, drying in an oven at 50-60°C yielded a 38.79nm thick uniform solid coating of PEDOT:PSS on the elastomeric substrate.

Measurement of surface topography. A confocal microscope (VK-X200 Series 3D Laser Scanning Confocal Microscope) was used to measure the three-dimensional (3D) morphology of a microwrinkled surface. This topography measurement yields the information about RMS roughness, wrinkle pitch and amplitude. This relevant roughness for Equation (5.1) was evaluated from the whole scan area by using a low pass filter with a 0.55μm cut-off spatial frequency.

Measurement of electro-mechanical activation. Figure A-3 shows the experimental setup for electromechanical activation. A high voltage power supply (TREK 610E) was used to electrically activate a dielectric elastomer device. It can generate a step voltage output for steady-state activation, or a square pulse for cyclic activation. By default, a manual knob was used to control steady voltage output from the supply. A function generator (Agilent 33120A) was used to trigger the high-voltage supply for generating a high-voltage pulse. The supply's voltage and current were logged continuously by using a National Instrument data logger and a LABVIEW software installed to a computer. Voltage monitor of the supply provides a signal voltage output, at a gain of one thousandth. Meanwhile, a multimeter (Agilent 34410A) was used to measure the current charging the capacitive device.

A digital single-lens reflex (DSLR) camera (Canon 550D) was used to take pictures or videos of dielectric elastomer actuation. A tracking software (Tracker) was used to track the electrode's diametral change from the pictures or videos. For the ease of image tracking of diameter change, the edge of a transparent/translucent compliant electrode was marked with two ink dots.

Measurement of transmittance spectra. Figure A-4 A shows a spectrometer from AvaSpec (USB2 Fiber Optic) used to measure the inline transmittance of a tunable optical diffuser. A halogen light source was used to generate a collimated light through a 6mm diameter collimator lens. An optical-fiber photodetector with a collimator lens was used to detect the specular light transmitted through the device, which is located at a distance of 70mm from the collimating lens. Forward scattering happens across the device's micro-rough surfaces. The in-line light transmittance at a wavelength λ is calculated as $T_{spec,\lambda} = \frac{I_\lambda}{I_{\lambda o}}$ where I_λ is the detected intensity of transmitted light in the presence of a diffuser and $I_{\lambda o}$ is a reference intensity of incident light (i.e. in the absence of the diffuser).

Figure A-4B shows an integrating sphere (Avasphere) used together with the spectrometer for a total reflectance measurement. A white reference standard was used to set the dark reference (i.e. 0% reflectance) and bright reference (i.e. 100% reflectance). The integrating sphere collects all the reflected light from the tunable window device so that the spectrometer can measure the homogenized light intensity.

Measurement of Light Scattering. Figure A-5 shows the experimental setup to measure the far-field patterns of forward light scattering. A red laser light source (635nm wavelength) with a 1mm-diameter aperture was used to shine a light beam through the tunable window device, and the transmitted light was projected on a planar image sensor (CMOS sensor of a digital camera, Sony 5100), which was placed at a distance of 20mm from the device. Software Image J is used to extract the intensity distribution from a monochrome image. This leads to the determination of the divergence angle and intensity profile of transmitted light. The intensity profile shows the light distribution as a function of angle; whereas, the divergence angle is measured as the width of the intensity profile at half the maximum (FWHM).

Measurement of LCR. This tunable window device is a non-ideal capacitor, which is subjected to a current leak during the high voltage activation. It can be modeled by a parallel circuit of a parallel capacitor and a parallel resistor (see Figure 5-4D). An impedance analyzer (Agilent 4294A Precision Impedance Analyzer) was used to

measure the capacitance C_p and resistance R_p of this soft capacitor. The dielectric constant is calculated from the relationship: $\epsilon_r = C_p \times t/(A\epsilon_o)$ where ϵ_o is the air permittivity, A and t is the cross section areal and thickness of the soft capacitor. Similarly, the dielectric resistivity is calculated from the Ohm's law: $\rho = R_p \times A/t$.

5.4 Results and Discussions

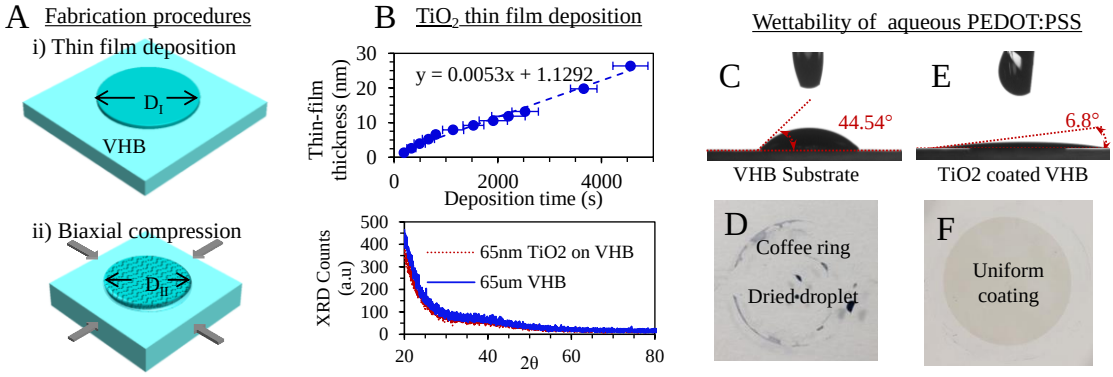

Figure 5-2. Fabrication procedures: (A) from thin-film deposition to compression-induced surface buckling; (B) the rate of TiO_2 thin-film deposition by e-beam evaporation; (C) X-ray diffraction (XRD) of surfaces; (D-E) droplet wettability and coating uniformity of PEDOT:PSS on VHB substrate; (F-G) droplet wettability and coating uniformity of PEDOT:PSS on TiO_2 coated VHB substrate.

Figure 5-2 shows the creation of this tunable optical diffuser following the same procedures for making a dielectric elastomer actuator with microwrinkled compliant electrodes, except the extra interfaces of the TiO_2 thin films. Brief process steps are outlined here. The substrate of the device is an acrylic adhesive membrane (3M very high bond tape, VHB 4905), which was pre-stretched radially 3.0 times and measured with a 65μm pre-stretched membrane thickness. A 19.8 nm thick thin film of TiO_2 was deposited onto each side of the substrate through a Teflon stencil mask. Figure 5-2(B-C) show the rate of thin-film deposition by e-beam evaporation and the evaporated thin film is amorphous. Second, we spin coated a uniform nanometric coating of PEDOT:PSS (e.g., 38.79 nm thick) on top of a TiO_2-coated VHB substrate. Figure 5-2(F-G) show that an aqueous droplet of PEDOT:PSS ink spreads well on the TiO_2-coated VHB substrate

at a low contact angle of 6.8°. In contrast, the contact angle of an aqueous droplet is higher at 44.5° on the slightly hydrophobic surface of an uncoated pristine VHB. In the absence of a hydrophilic interface, spin coating of the aqueous solution yields coffee rings and segregated stains on the VHB substrate. Third, we partially released the elastomer's radial pre-stretch from 3.0 times to 2.7 times and thus buckled the hybrid multilayer thin films into microwrinkles. The active area of TiO_2/PEDOT:PSS was merely compressed to 4−5% radial strain, while the mechanical stretcher (with nine rivet caps for adhesive mounting) partially released the pre-stretch in the dielectric elastomer membrane for an 11.0% radial strain.

The basic device under test is a 45 mm diameter circular dielectric elastomer actuator with 20.0 mm diameter microwrinkled electrodes. Figure 5-3 shows this microwrinkled TiO_2/PEDOT:PSS electrodes being crack free in a herringbone pattern under a low pre-compression of 4-5% strain (D_{II}/D_I=0.96). Then, the average amplitude of the microwrinkles is 0.585±0.085μm while the whole-field rms roughness is 0.525μm. Complete unfolding ($D(V)/D_I$ =1.0) of the microwrinkled surface can reduce the rms roughness down to approximately 0.036μm. The analysis shows the microwrinkling of this nanometric oxide is within the fracture limit (see Equation (3.6) and (3.7)) [75].

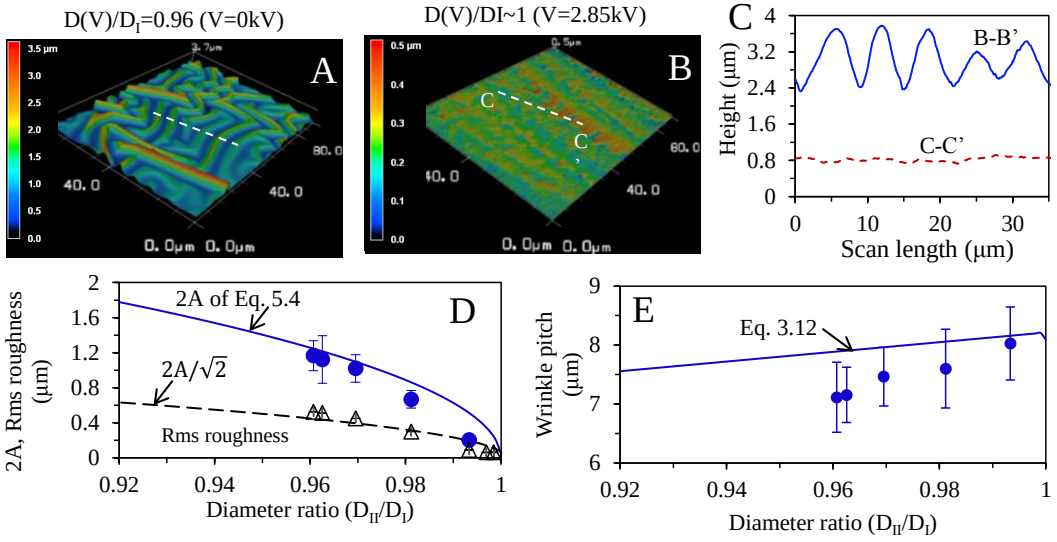

Figure 5-3. Topography of a microwrinkled optical surface: (A-B) confocal micrographs showing the topography of microwrinkles and the effect of voltage-controllable unfolding;

(C) profile heights of microwrinkles upon unfolding; (D) wrinkle amplitude and surface roughness with respect to voltage-induced unfolding; (F) wrinkle pitch with respect to voltage-induced unfolding.

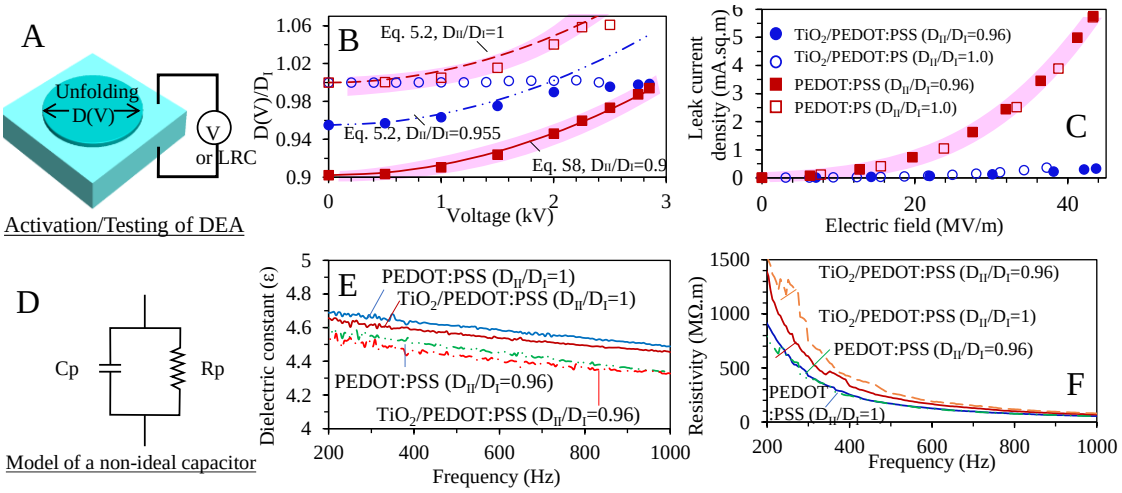

Figure 5-4. Activation and testing of a dielectric elastomer actuator, with microwrinkled TiO_2/PEDOT:PSS compliant electrodes: (A) schematic showing the setup for electrical activation; (B, C) voltage-induced diametral expansion and leakage current across the soft capacitor; (D − F) non-ideal capacitor model and LCR measurement.

Figure 5-4 shows the voltage controllable areal expansion (i.e. unfolding) of the microwrinkled electrodes agreeing to Equation (5.2). The 2.85kV activation (approximately 43.8MV/m) of dielectric elastomer almost completely unfold the microwrinkled surfaces. Towards complete unfolding, this flattened TiO_2 becomes increasingly stiff in the biaxial direction; the actuation is thus tapered off despite increasing the applied voltage (see Figure 5-4B). Similarly, the same high-voltage activation cannot stretch the flat surfaces (with DII/DI = 1.0) at all due to high axial stiffness[69]. Interestingly, TiO_2 interfaces greatly reduce the leakage current across the device during high-voltage activation (see Figure 5-4C). In comparison, the window device using PEDOT:PSS-only compliant electrodes consumes higher power during high voltage activation, although the PEDOT:PSS electrodes are softer (with a 0.5−1GPa Young's modulus [129, 139]) and more stretchable than the TiO_2 film (see Figure 5-4(B-

C)). The PEDOT:PSS-only compliant electrodes of 38.79nm thickness can neither make a strong surface scatterer nor readily form microwrinkles under a small compression (refer to Appendix D and Figure A-2).

In addition, we measured the capacitance and dielectric resistance of the tunable window device with TiO_2/PEDOT:PSS thin-film compliant electrodes. For comparison, a reference device with PEDOT:PSS-only compliant electrodes were also tested. LCR measurements (see Figure 5-4(D-F)) show that the parallel capacitance does not change much with the types of compliant electrodes used. As measured from the soft capacitors of the same dielectric elastomer, the dielectric constant decreases slightly with the addition of TiO_2 interfaces. Yet, the additional nanometric insulation interface of TiO_2 increases the dielectric resistivity.

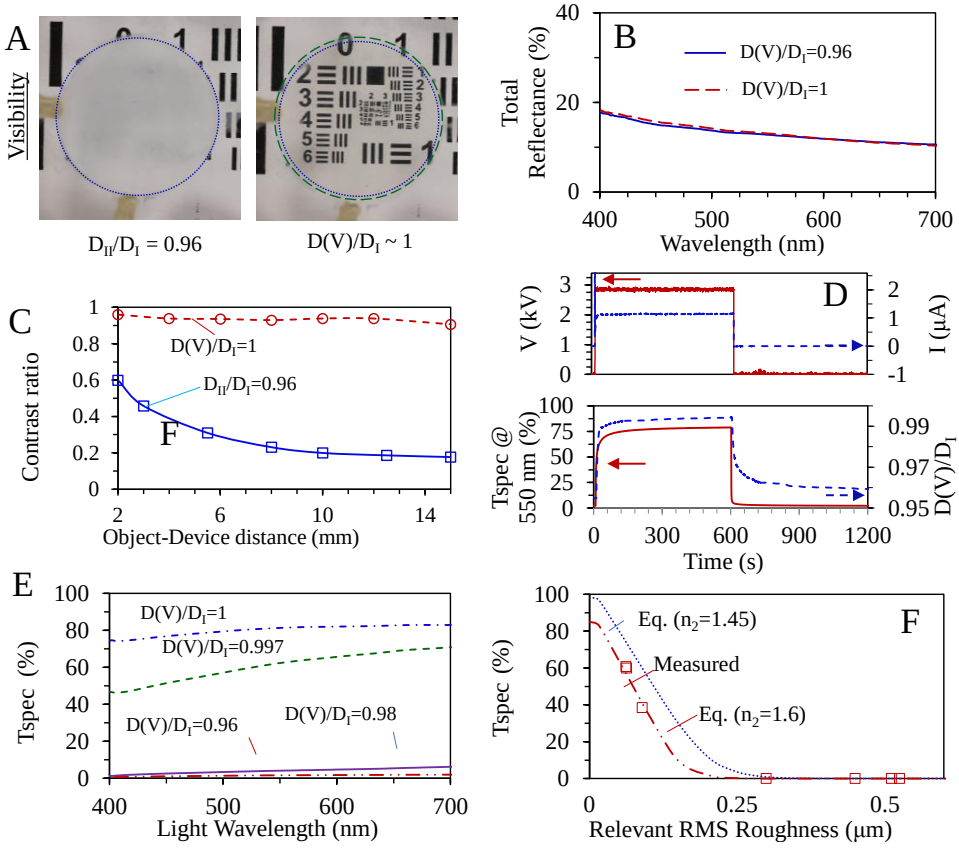

Figure 5-5. Tuning of visibility, total reflectance and specular transmittance by voltage-controlled surface unfolding: (A) from hiding to revealing of a black-and-white logo placed beneath the diffuser; (B) total reflectance spectra being independent of topography change;

(C) Dependence of Michelson contrast ratio on the logo to diffuser distance; (D-E) specular transmittance change due to voltage-induced unfolding; (F) correlation between specular transmittance and RMS surface roughness.

Figure 5-5A shows this tunable window device can electrically vary the visibility of a black and white logo (i.e. a laser-printed USAF resolution test chart) which was behind the device under front lighting. The device was activated with a square pulse (10 minutes on at 2.85kV and 10 minutes off). When being turned on, the device appears transparent with a contrast ratio close to 1.0. When being switched off, it becomes translucent and the contrast ratio becomes much lesser than 1.0 (see Figure 5-5B). The off-state contrast ratio decreases with increasing the distance between the device and the logo, for example, 0.2 at a 10mm distance.

When this tunable device is switched on from 0kV to 2.85kV, the diameter ratio increases from $D_{II}/D_I \sim 0.96$ towards 1.0 (see Figure 5-5D) and thus the microwrinkled surfaces are unfolded. While creeps happen to dielectric elastomer actuation, they taper off and eventually settle to a steady state. While the total reflectance (R = 1 - T) does not change with the surface unfolding (see Figure 5-5C), the specular (in-line) transmittance (T_{spec}) does change. The in-line transmittance (for the green light of 550nm wavelength) increases from 1.85-3.0% to 78-81%. In terms of speed, the switch to clarity takes 60 seconds (90% rise time); whereas, the return to translucence takes 2 seconds. This suggests that a faster elastic recoil (wrinkling back) takes place at the thin-film-coated surface while a slow deactivated creep happens to the bulk viscoelastic elastomer.

After all, the unfolding shows a broadband effect on increasing specular (in-line) transmittance (see Figure 5-5E). The measured specular transmittance is closely correlated to the rms surface roughness (see Figure 5-5F). Best fit by Equation (5.1) to the measurement yields the determination of an effective refractive index being $n_2 = 1.6$, higher than $n_2 = 1.47$ of VHB acrylic elastomer [140]. This enhanced light diffusion confirms a TiO_2 nanometric film being a stronger surface scatterer than the elastomer substrate.

In addition, we measured the angle of light scattering by shining a collimated light beam (of a 635nm wavelength laser) through this tunable optical diffuser. Figure 5-6 shows a scattering angle of 44.77-degree (full width at half maximum) at the device's frosted state but almost no scattering at the device's clear state.

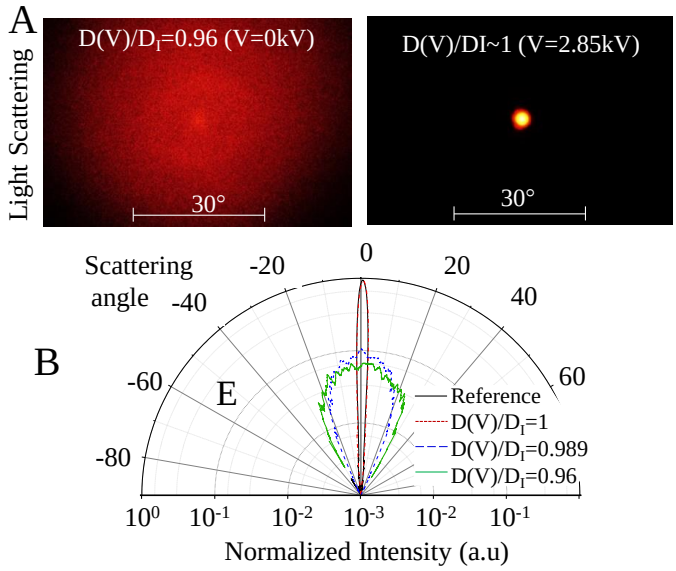

Figure 5-6. Tunable light scattering by unfolding of microwrinkled surfaces: (A) CMOS images showing the switch from diffuse to non-diffuse light scattering; (B) light scattering angle change with respect to voltage-induced unfolding.

In addition, we tested a larger squarish window device to diffuse lighting and provide privacy (see Figure 5-7). This device is a dielectric elastomeric membrane actuator of a total 80 × 80mm^2 area, of which the active area covers 60 × 60mm^2. Two color blocks were separately placed in front and behind a tunable diffuser device, while they are backlighted by a LED torchlight. When being inactive, this window device appears translucent to diffuse the backlighting (see Figure 5-7(c)top), and to hide the color blocks behind it (see Figure 5-7(b)left). When being activated, the device turns transparent to show the backlight source glaring (see Figure 5-7(c) bottom) and the color blocks behind it (see Figure 5-7(b) right). Such tunable light diffusion can vary the shadows from blurred to defined (see Figure 5-7 (d)). In addition, it can be useful as a tunable sun-visor against sun-glare.

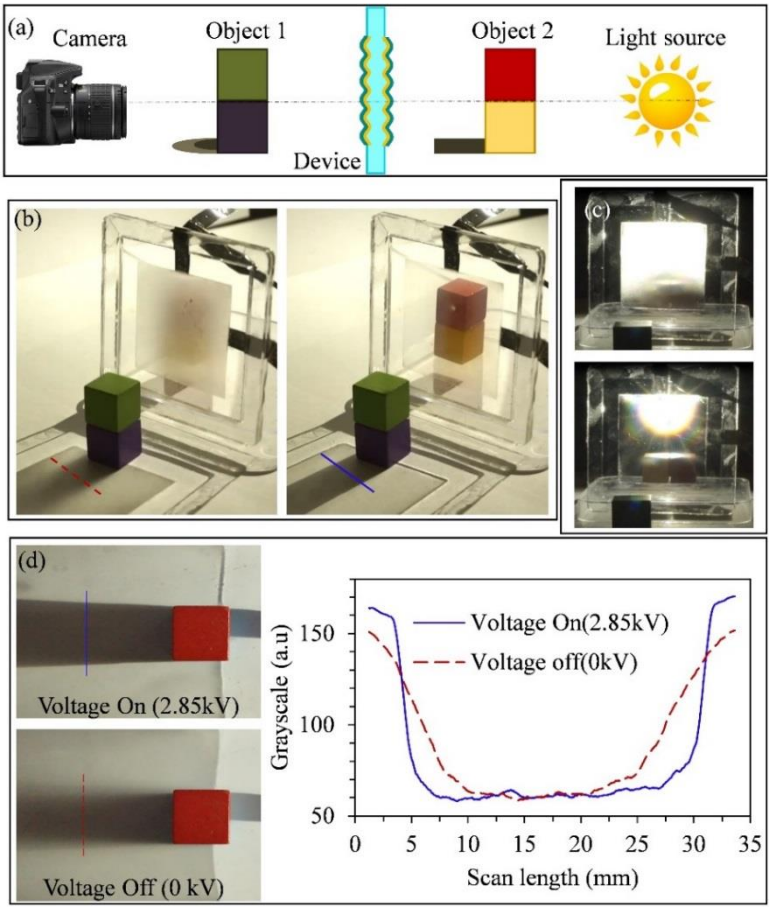

Figure 5-7. Demonstration of the applications of the tunable optical diffuser. (a) Schematic of the experimental setup used for the demonstration of tunable light diffusion; Demonstration as (b) a privacy glass; (c) as an anti-glaring glass; (d) as an optical diffuser to produce different sharpness of shades (graph shows the sharpness of the shadow at on and off state of the device).

To demonstrate life-long cyclic switching (see Figure 5-8(c)), we activated and deactivated the window device with a train of high-voltage square pulses (2.85kV amplitude, 50% duty cycle, and a pulse-on width of 1 minute). This accelerated test for one thousand cycles confirms that the TiO_2 interfaces remain intact over repeated cycles of unfolding and wrinkling. At the activated clear state, this window device consumes merely a 0.831W/m^2 area-specific electrical power despite high-voltage activation. In comparison, a polymer-dispersed-liquid crystal (PDLC) smart window, [10, 115] typically consumes 5-20W/m^2 by alternating current (a.c.) activation to be clear. Since it

was first prepared four months ago, this tunable window device can still function for long-hour activation. The device remains stable and clear when being activated continuously for example 6 hours (see Figure 5-8(b)). There was no electrical breakdown observed during the hour-long activation. For practical application, the device needs to be cladded between the two protective glasses with an air-gap. The protective cladding glasses prevents possible damage upon physical contact and electrically isolates it to eliminate any possible electrical hazard.

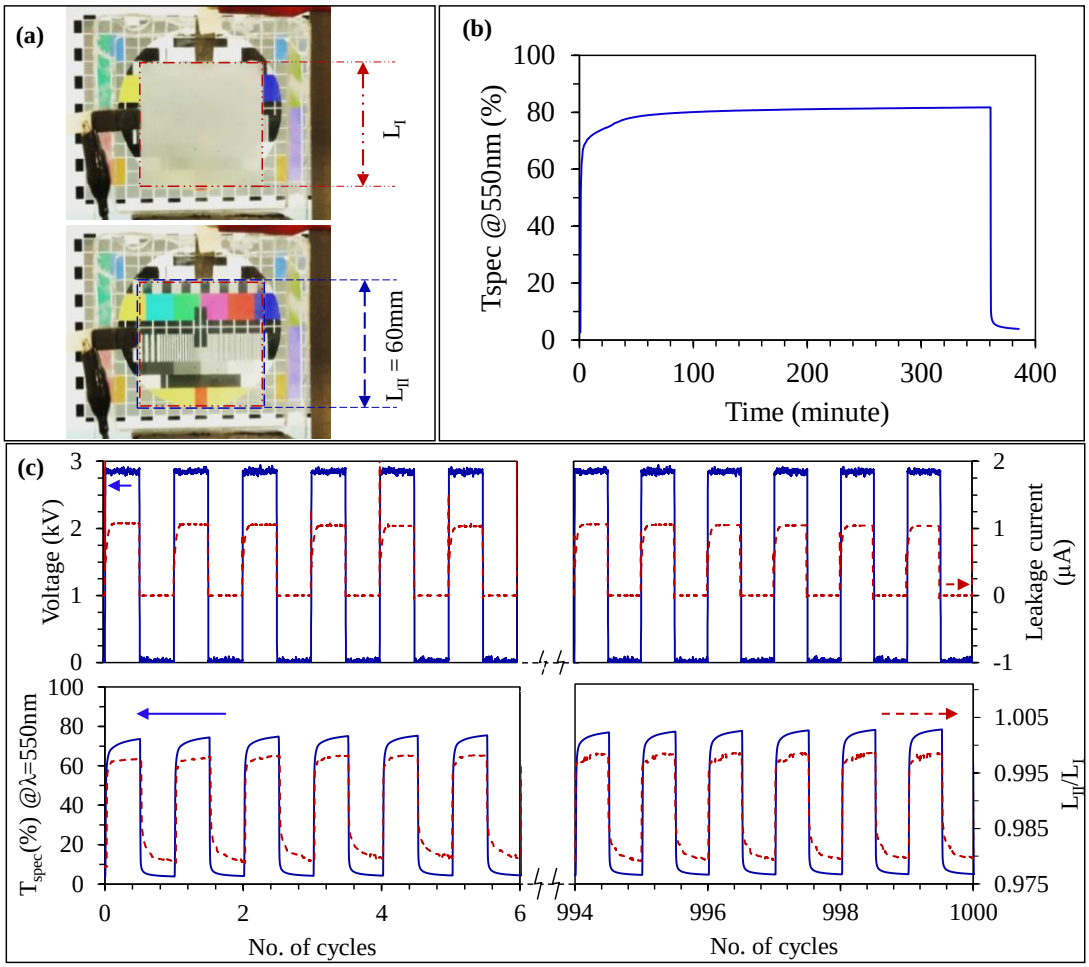

Figure 5-8. Squarish transparency tuning device (60mm length): (a) Visibility of the Phillips pattern in a liquid crystal display at voltage off and on states; (b) Consistent transparent state maintained when kept activated for 6 hours (c) Cyclic activation at 8.334mHz for more than 1000 cycles showed consistent performance.

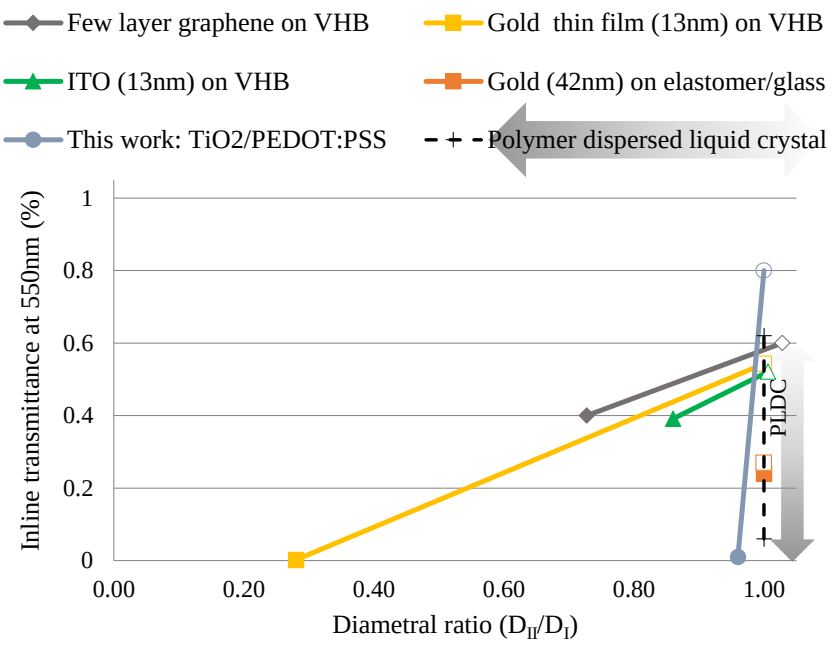

Figure 5-9. Benchmarking among various dielectric elastomer window devices in terms of the range of transmittance tuning and the actuation strain requirement.

In comparison to our previous Ag/ZnO thin films based tunable optical diffuser, the device based on PEDOT:PSS/TiO_2 thin film is clearer as the overcoat of PEDOT:PSS is more transparent that Ag films. In addition, TiO_2 has a refractive index of 2.8 which is much higher than that of ZnO (refractive index of 2). Therefore, microwrinkled TiO_2 thin films make better optical scatterer than ZnO thin films. Hence, a device using PEDOT:PSS/TiO_2 films requires comparatively lower area strain for transparency tuning.

For benchmarking, tunability of various dielectric elastomer optical diffusers reported so far are compared. Figure 5-9 shows the tuning range attained by these optical diffusers, as marked by the most translucent state (at which the diffuser is compressed with a diameter ratio $D_{II}=D_I < 1$) and the clearest state (at which the compression to diffuser is removed or reduced). In general, the tunable devices based on the metallic nanometric thin film, e.g. gold, show a limited range of transparency tuning. The nanometric gold thin film is moderately transparent with a smooth surface; it needs to be highly crumpled (by large compression of up to 70%) to become highly opaque [54]. In comparison, the

TiO_2-based surfaces of high transparency attain a much wider range of transparency tuning between 81% to 1.85% transmittance at the least actuation (of not more than 5% strain). This excellent tunability even exceeds the reported tuning range (e.g. 6% and 62% in-line transmittance) of a commercial PDLC window [14]. Furthermore, making this TiO_2 based smart window costs low as compared to the existing smart window (see Table A-1 and Table A-2).

5.5 Summary

This chapter presented a tunable optical diffuser to make a durable and high-performance smart window at low cost, low power, in all solid state. We showed that the TiO_2 nanometric thin film of high transparency and higher refractive index turns to be a strong surface scatterer to visible light when being microwrinkled on dielectric elastomer under low radial compression. This hybrid design of optical surfaces overcomes the material limits to achieve unprecedentedly high electric tunability of optical diffusion. It also promises to greatly reduce the power consumption by the transparent dielectric elastomer actuator, useful for soft tunable optics and acoustics [141-143]. Moreover, these devices can easily be mass produced using currently available manufacturing technologies. Commercial membrane stretching machines [144, 145] are already available in the market. In addition, the thin film coating machines used for large area displays can easily be used to coat thin films in these stretched membranes [146], which makes these devices easily manufacturable at industrial scale.

Part II Tunable Acoustic Absorption

Chapter 6 Technology Review for Indoor Acoustic Treatment and Tunable Absorption

This chapter reviews recent advances of acoustic absorbers and tunable acoustics which are used for sound attenuation. The sound that we hear is a mixture of directly transmitting sound and indirect reflection from the surfaces. Indoor and outdoor sources of noise like vehicles, loudspeaker, air conditioning systems and so on can produce noise of various audible frequency. The dominant frequency of the noise being produced by these sources also varies based on their types and state of operation. For instance, vehicles noise dominant frequencies changes with engine speed and even loading (see Figure 6-1). Hence, a lighter vehicle produces noise of higher frequencies that the heavier vehicles. In addition, traffic noise during off-peak hours is skewed towards higher frequencies than during traffic jams [147].

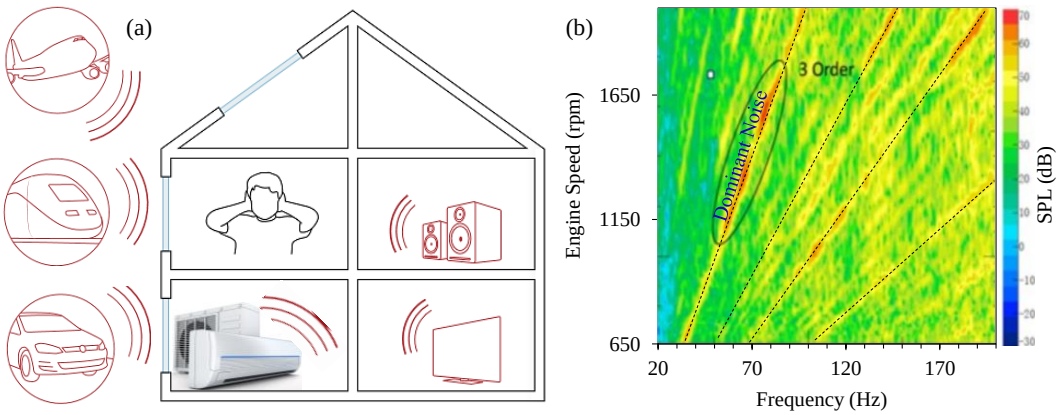

Figure 6-1. (a) Various sources of noises; (b) Variation of dominant noise frequencies with engine speed (adapted from [148]).

Hard and dense structures like concrete walls, ceilings, and window glasses reflect most of the incident sound. On the contrary, soft, pliable, or porous materials like foams and fiberglass absorb most of the incident sound. High acoustic reflection by concrete walls and window glasses causes echoes within an enclosed space (see Figure 6-2(a)). This indoor sound reverberation can degrade intelligibility of speech. It usually occurs in enclosed spaces like living rooms, auditoriums, and studios. Hence, various sound

absorbers are usually installed on the walls, ceilings and window glasses to attenuate the echo (see Figure 6-2(b-d)) [6].

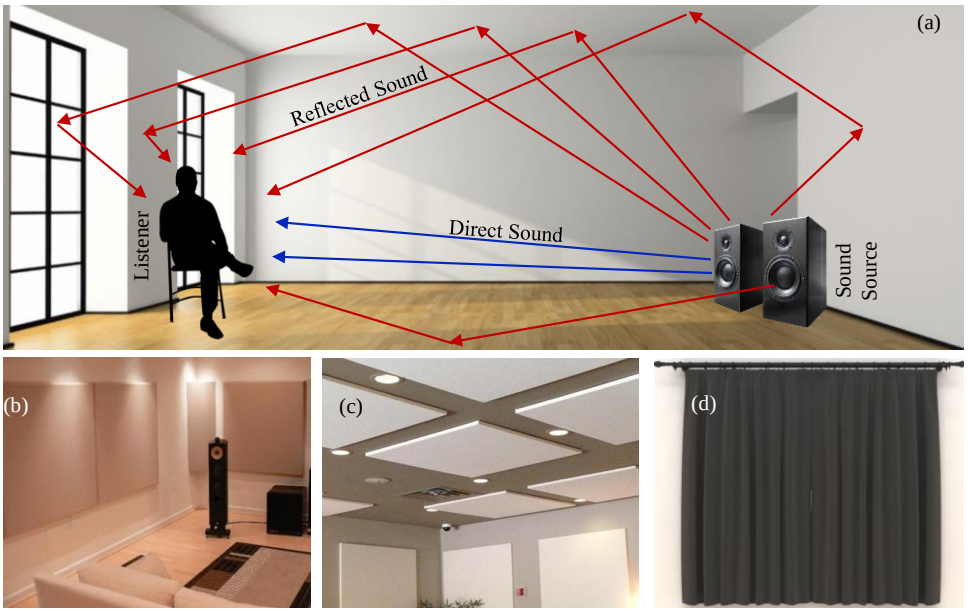

Figure 6-2. (a) Schematic showing sound reflection in a room causing reverberation; Acoustic absorbers used in front of a hard surface like (b) walls; (c) ceiling and (d) windows (thick curtains serve as absorbers).

Figure 6-3 classifies three categories of acoustic attenuation systems: (a) passive absorbers, (b) tunable absorbers and (c) active noise control (ANC) systems. Firstly, there are two kinds of passive acoustic absorbers namely, porous absorbers and resonant absorbers. Porous absorbents include foams, fiberglass; Resonant absorbers include panel absorbers, Helmholtz resonators and micro-perforated panels (MPPs). They work without the need for external power. Passive absorbers can have various working frequency and absorption bandwidth. For example, a porous absorber is good for broadband absorption, but only from mid-to-high audible frequency range. Meanwhile, resonant absorbers can be designed to absorb the sound of a specific low-frequency but only over a narrow frequency bandwidth. Their absorption coefficient peak at resonant frequency but drops substantially outside the bandwidth. Secondly, tunable acoustic absorbers are recently developed to shift and target their absorption spectrum to the noise dominant frequency. These are in principle resonant absorbers with tunable resonant

frequencies. Hence, their resonant frequency can be adjusted to target noise spectrum of varying dominant frequency, like engine noise which varies with speed and loading. In this way, the working frequency range of the tunable resonant absorber is widened more than that of a non-tunable one. Finally, ANC systems cancel the noise by generating a counter sound; but it is power hungry and so far, its application is limited to small enclosures.

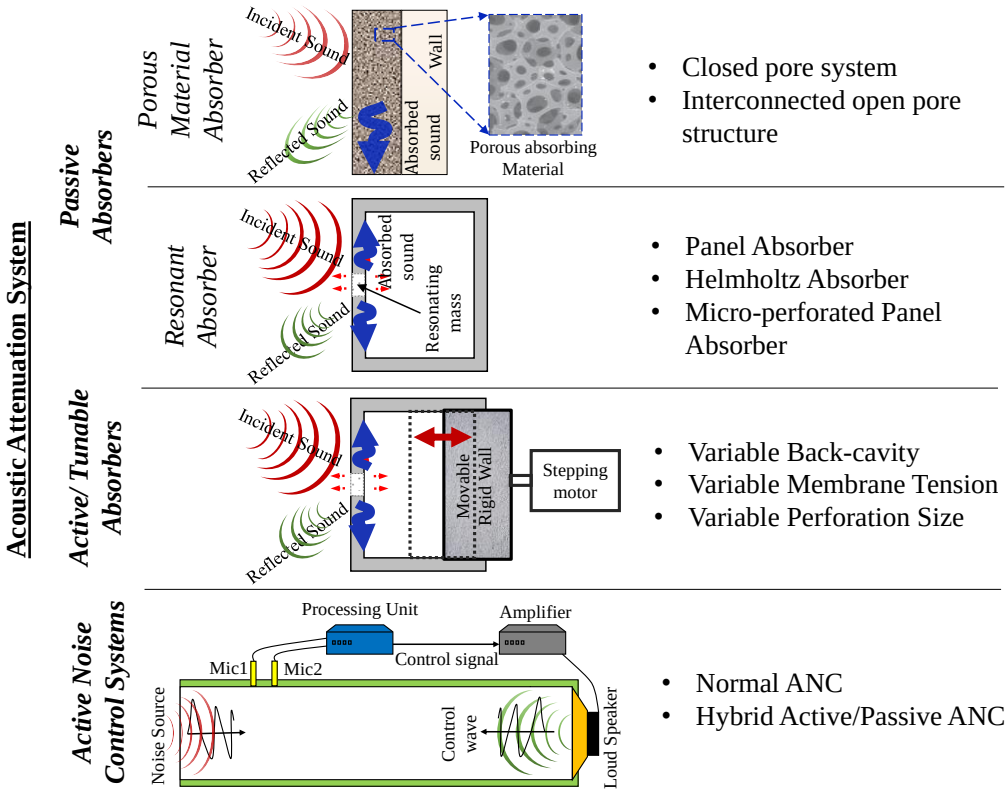

Figure 6-3. Classification of the existing acoustic absorbers.

Sound propagates through gas, liquid, and solids in form of a longitudinal pressure wave. But, in solids, it can also propagate as transverse waves. When a sound impinges on a surface, it is partially reflected, absorbed and transmitted through the surface (see Figure 6-4). Acoustic absorbers dissipate sound energy to heat. Their acoustic absorption coefficient *(α)* is measured as the ratio of absorbed intensity to the source intensity of the sound. The absorption coefficient varies with the sound frequency and angle of the incidence. It ranges between 0 and 1, where 0 means no absorption and 1 means complete

absorption. Direct experimental measurement of sound absorption is difficult. Instead, the reflected and transmitted sound energies are measured. The absorption coefficient (α) is calculated from the relationship:

$$\alpha = 1 - \frac{E_r}{E_i} - \frac{E_t}{E_i} \quad \textbf{(6.1)}$$

where E_r and E_t are the reflected and transmitted portion of the incident acoustic power E_i.

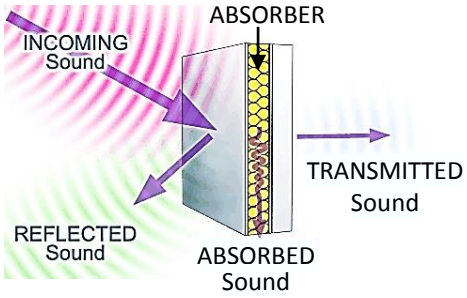

Figure 6-4 Illustration of absorption, transmission, and reflection of sound incident on an acoustical material.

6.1 Passive Acoustic Absorbers

There are two types of passive acoustic absorbers, namely: (1) porous absorber and (2) resonant absorber.

6.1.1 Porous Absorber

Porous absorbers consist of porous or fibrous materials. Examples of porous acoustic absorbers include curtain's textiles, acoustic foams, aerated plasters, cushions, cotton, and fiberglass. The porous absorbers are largely filled with air, as high as 90% (see Figure 6-5(b-c)). These soft porous absorbers are usually mounted to a rigid backing like walls and ceilings (see Figure 6-5(a)). They effectively absorb the sound of moderate to high frequency. Mechanisms of sound absorption in the porous medium are due to viscous loss and momentum loss. When sound impinges on the porous absorber the air in the pores is driven to oscillate at the sound's frequency. Viscous friction loss happens

at the submillimeter viscous boundary layer [6] next to the pore's walls [149]. In addition, momentum loss happens when the sound wave propagates in pores of irregular shape. Therefore, interconnected open pore structure can better absorb sound than a closed pore structure (see Figure 6-5 (e) and (f)) [150].

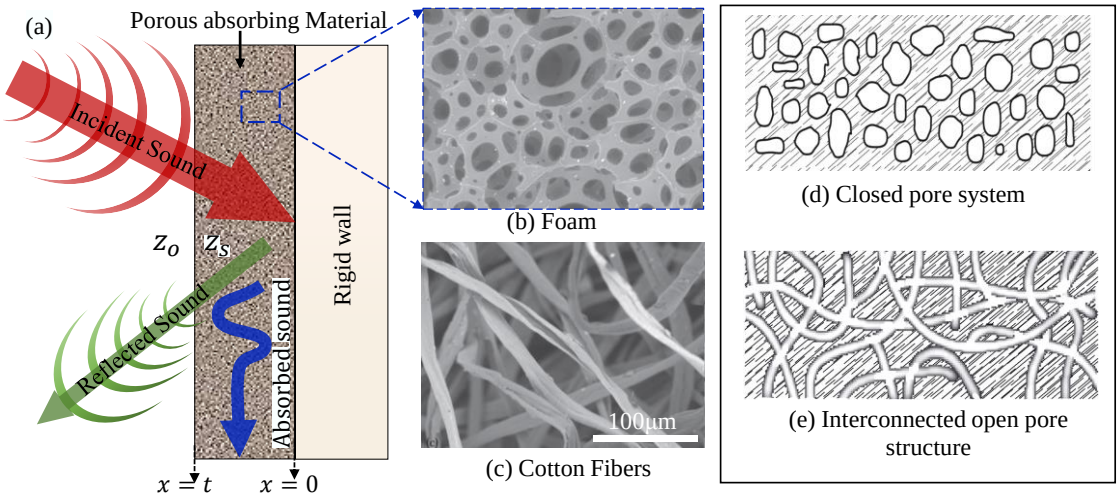

Figure 6-5. (a) Schematic of sound absorption by a porous absorber. SEM images of porous material: (b) white foam; (c) Cotton fibers; Type of porous absorbers based on pore morphology: (d) closed and (e) open pore structures. (adapted from [6])

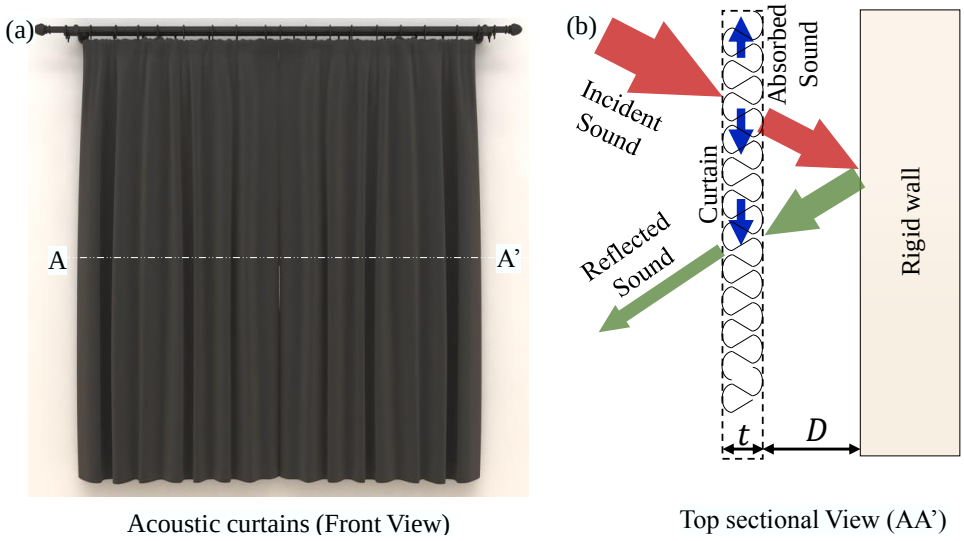

Figure 6-6. (a) Use of curtains place at a distance from the rigid walls as acoustic absorber; (b) Top view showing the effect of placing an absorber at a distance from the rigid wall.

The absorption coefficient of porous materials varies with material thickness *(t)* and the distance (*D*) from the rigid wall. The porous absorbers are more effective to attenuate sound traveling with high particle speed. The air particle speed is maximum at a quarter sound wavelength from the walls (i.e. at $D=\lambda/4$) but is zero upon at the wall (i.e. at $D=0$). Hence, the maximum absorption occurs when the porous absorber is placed at a distance of quarter wavelength from the rigid wall [151]. This suggests that absorption of the bass sound of low-frequency requires very thick porous absorbers (see Figure 6-7).

Curtains and drapes can address the thickness limitation of the porous absorbers. They can be positioned at a distance (*D*) from the rigid wall for optimal absorption of low-frequency sound (see Figure 6-6 and Figure 6-7) [152]. Maximum absorption occurs when the air gap is a quarter of the sound wavelength (i.e. at $D=\lambda/4$). A curtain with a deep fold presents more acoustic resistance and this can better absorb sound. But, thick curtains cannot be fitted in a small space. Recently, translucent curtains with micro-slits are developed to provide 0.5-0.6 absorption coefficient for sound frequency greater than 500Hz [5, 6].

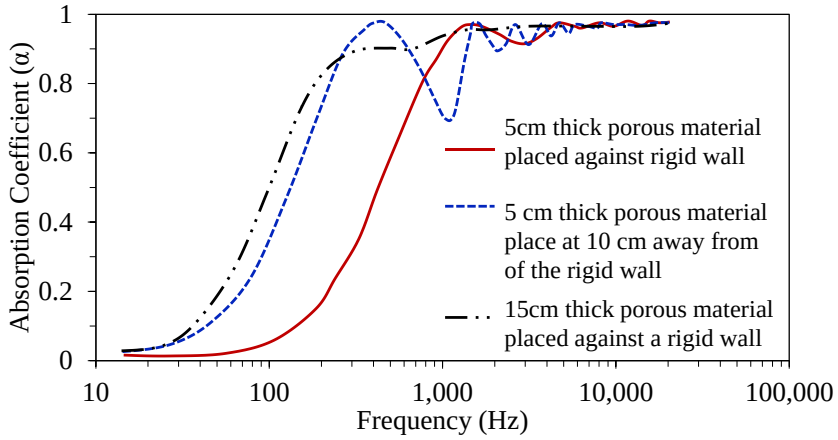

Figure 6-7. Typical sound absorption coefficient curves of porous sound absorbers with flow resistivities of 10,000 Nsm^{-4}. (adapted from [16])

6.1.2 Resonant Absorber

Resonant absorbers are mass-spring systems under excitation by a sound pressure wave [153-155]. The maximum acoustic absorption happens at the resonant frequency of the

damped forced vibration. They perform best when being placed closer to the rigid walls, ceilings, and corners where the sound pressure is the highest. Hence, they can easily be fitted even in small rooms. There are three kinds of resonant absorbers, namely panel absorber, Helmholtz absorbers, and micro-perforated panel absorbers.

Panel Absorbers. Panel absorbers are flexible panels/membranes backed by an air cavity in front of a rigid wall. The panels are often made of rubber, mass loaded vinyl and plywood. They are compact to be placed in front of rigid walls, ceilings, and window glazing (see Figure 6-8). The panel absorbers behave as a spring-mass system with a mass of panel and spring of partially the enclosed air and flexible panel. The system vibrates in response to incident sound pressure. The vibration-induced deformation of the panel transfers sound energy to mechanical energy [16]. The air cavity also helps to dissipate mechanical energy into heat.

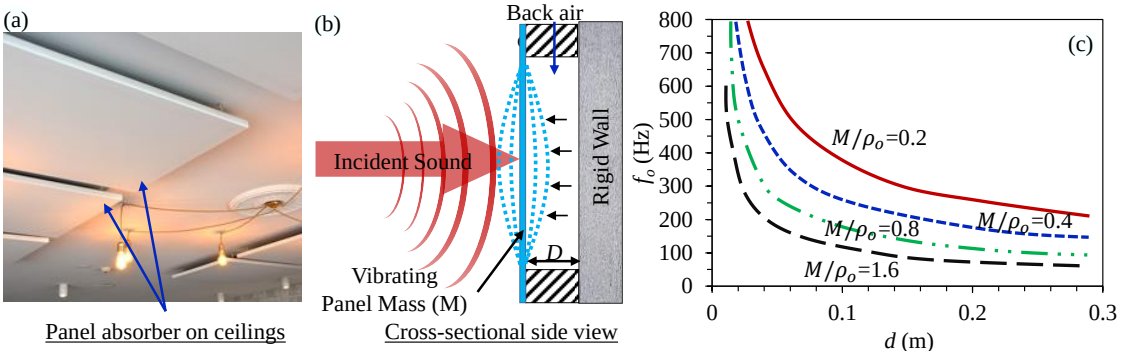

Figure 6-8. (a) Panel absorbers on ceiling of a room; (b) Schematic representation of a panel absorber backed by an air cavity and a rigid wall; (c) Resonant frequencies of a panel absorber predicted by Equation ((6.2)) for a panel with different surface mass density (adapted from [156]).

The resonant frequency of a panel absorber is given by, [156]

$$f_o \approx \frac{60}{\sqrt{MD}} \qquad \textbf{(6.2)}$$

where M is mass per unit area of the panel and D is the depth of the back-cavity (see Figure 6-8(b)). Usually, panel absorbers can be designed with a low resonant frequency to absorb bass sound by proper selection of panel mass (M) and the cavity-depth (D)(see

Figure 6-8(c)). Yet, their acoustic absorption bandwidth is narrow. To broaden the absorption spectrum, porous materials can be added to partially fill their air cavity (see Figure 6-9). This reduces the resonant frequency to be,[6]

$$f_o \approx \frac{50}{\sqrt{MD}} \tag{6.3}$$

In this hybrid absorber, porous materials absorb the sound of high to the medium frequency, while the panel absorber absorbs the low-frequency sound. Yet, the porous materials are opaque and unsuitable for installation to window glazing.

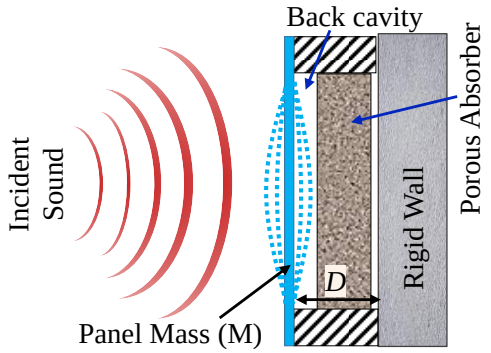

Figure 6-9. Schematic of a panel absorber with a back cavity filled with porous materials.

Helmholtz Absorbers. A Helmholtz resonator consists of an enclosed air-cavity with a small opening or hole (see Figure 6-10(a)). This unit can be repeated in an array for large area coverage. The air in the hole neck serves as the resonating mass, while, the air in the enclosed chamber acts as a spring. When sound impinges the resonator surface, the air-plug in the hole neck oscillates. The friction between the oscillating air and neck wall dissipates sound energy into heat.

Helmholtz absorber is best placed near the room boundaries where the sound pressure is maximum. A higher sound pressure increases the oscillation amplitude of the air plug and thus, increases the acoustic absorption. Maximum sound absorption by a Helmholtz absorber occurs at the resonant frequency given by,[157]

$$f_o = \frac{c_o}{2\pi}\sqrt{\frac{S}{Vt}} \tag{6.4}$$

where (V) is the volume of the cavity, (S) is the area of the opening holes and (t) is the thickness of the holes. A bigger hole size (S) increases the absorber's resonant frequency by allowing a faster rush of air through it. A larger cavity volume decreases the resonant frequency because of the increased compliance of the air cavity. A deeper hole increases the viscous friction but decreases the resonant frequency. According to Equation (6.4), a Helmholtz absorber for bass sound should have a large cavity volume and a smaller and deeper hole.

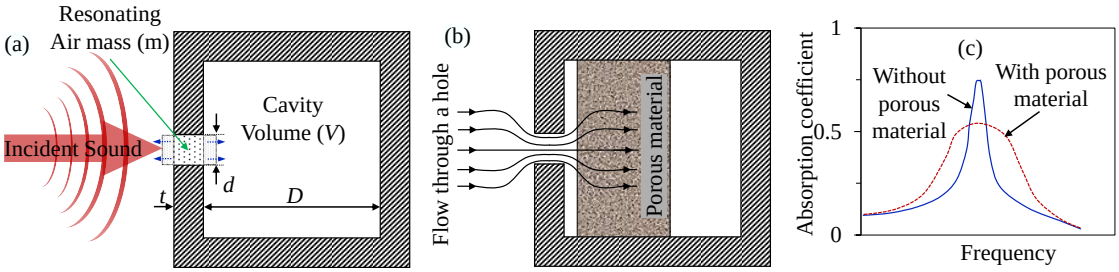

Figure 6-10. Schematic diagram of a Helmholtz resonator (a) indicating the resonating air mass plug at the holes; (b) indicating the air particle velocity at the opening which suggests the best position to place a dissipative porous absorbent for a hybrid system; (c) Typical absorption spectrum of a Helmholtz absorber with and without porous absorbent in the cavity. (adapted from [158])

In a Helmholtz resonator, a hole in the panel helps convert high acoustic pressure into high particle speed. This leads to high absorption peaks over a narrow bandwidth (see Figure 6-10(c)). To broaden the bandwidth of Helmholtz resonator, porous absorbent can be added to fill part of the air cavity next to the hole (see Figure 6-10(b)) [158]. This, however, slows down the particle speed and slightly reduces the peak absorption (see Figure 6-10(c)).

Micro-perforated panel absorbers. Micro-perforated panel (MPP) absorbers are a type of Helmholtz absorbers. They consist of a panel with an array of sub-millimeter diameter holes. Usually, for fabrication ease, MPP absorbers have MPPs backed by a non-partitioned common air cavity for all the holes (see Figure 6-12(a)). MPP absorber can absorb the sound of a broader bandwidth than a simple Helmholtz resonator or a panel

absorber. Yet, it is still narrower than porous absorber's absorption bandwidth (Figure 6-11) [149, 155, 159]. It is generally used for absorption of mid-range frequency sound.

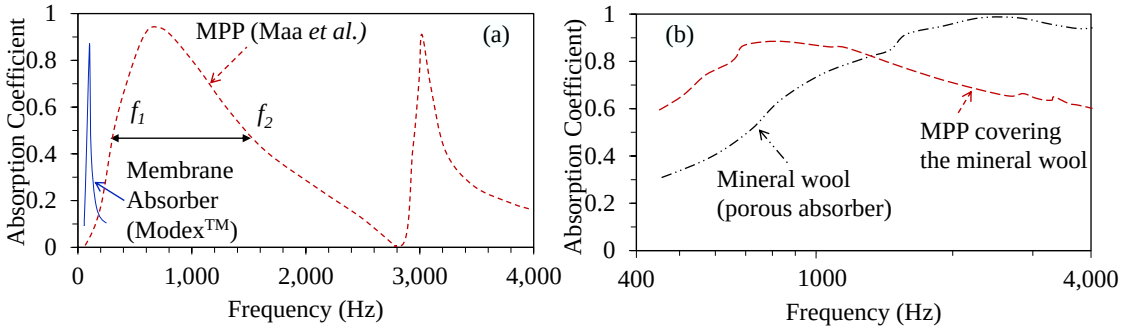

Figure 6-11. Comparison of normal incidence absorption coefficient between: (a) a membrane absorber and an MPP absorber; (b) a porous absorber and an MPP with porous absorber placed at the back cavity (adapted from [6]).

Like Helmholtz resonator, sound absorption mechanism of MPP absorbers is attributed to the viscous friction of air plugs. To enhance the viscous friction, the holes are sized comparably to the thickness of the viscous boundary layer of air. A broader absorption bandwidth of MPP absorber is achieved by a design with high acoustic resistance and a low acoustic mass reactance. For the aesthetic reason, micro-perforated glass panel can be made from glass. To ease the fabrication, micro-slots can be formed to the glass instead of micro-holes to serve the same function of comparable performance (see Figure 6-12(b)) [160].

Consider a unit cell of MPP absorber with a square panel of width $2b$ and a hole of diameter d and depth t. Back-cavity for this absorber has a depth D. Resonant frequency of an MPP absorber can be estimated using a modified model from Helmholtz resonator (i.e. Equation (6.4)) as [6, 161]:

$$f_o = \frac{c}{2\pi}\sqrt{\frac{\varepsilon}{Dt}} \qquad \textbf{(6.5)}$$

where $\varepsilon = \frac{\pi(d/2)^2}{(2b)^2}$ is the fraction of the open area of the perforated plate provided that the holes are on a square lattice. A more elaborate acoustic model of an MPP absorbers is presented below.

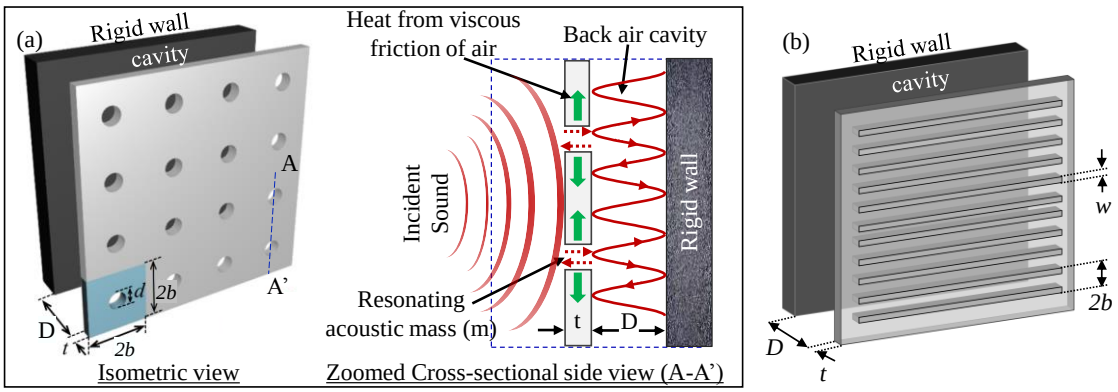

Figure 6-12. Schematic representation of cavity backed (a) micro-perforated panel absorber; (b) magnified view showing a sound absorption mechanism; (c) micro-slotted panel absorber.

Acoustic Model for a Rigid Micro-perforated Panel Absorber

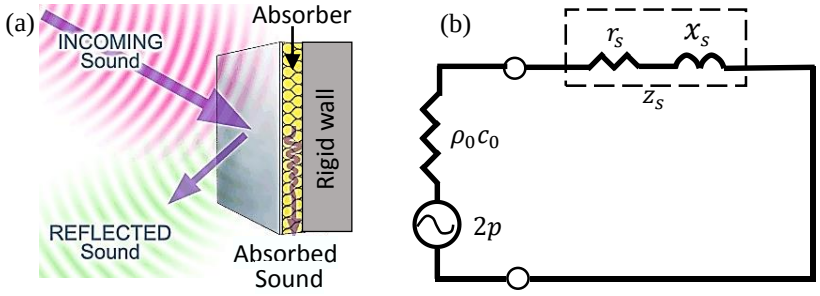

Figure 6-13. (a)Illustration of absorption and reflection of sound incident on an acoustic absorber placed on a rigid wall; (b) electro-acoustic model of the same absorber.

The acoustic absorption coefficient of an absorber can be calculated from its acoustic impedance. Acoustic impedance z_s is defined as the ratio of the acoustic pressure (p) in the medium to the particle velocity (v). It is the sum of the acoustic resistance r_s that accounts for sound energy loss and acoustic reactance x_s that changes phase between pressure wave and particle velocity. Figure 6-13 shows an electro-acoustic model for an

acoustic absorber with the prescribed acoustic impedance z_s. According to Ref. [162], its absorption coefficient is given as

$$\alpha = 1 - \left|\frac{z_s - \rho_o c_o}{z_s + \rho_o c_o}\right|^2 = \frac{4r_s/\rho_o c_o}{(r_s/\rho_o c_o + 1)^2 + (x_s/\rho_o c_o)^2} \quad \textbf{(6.6)}$$

where $z_o = \rho_o c_o$ is the acoustic impedance of the air, ρ_o is the air density, and c_o is the sound speed in air. Impedance mismatch between air and medium leads to increased sound reflection. Maximum absorption happens at zero reactance (i.e. $x_s = 0$) (refer to Equation (6.6)).

Maa et al. [163] estimated the absorption coefficient of an MPP absorber was by using an electro-acoustic circuit model shown in Figure 6-14(b). This model assumes a rigid panel (i.e. no panel vibration) and a no-slip condition which assumes air particle velocity is zero at the hole-wall. Hence. the effect of MPP absorber is modeled by two acoustic impedance in series, i.e. one of MPP-holes and another of back cavity. The MPP-hole impedance is attributed to the in-phase resonance of air plugs.

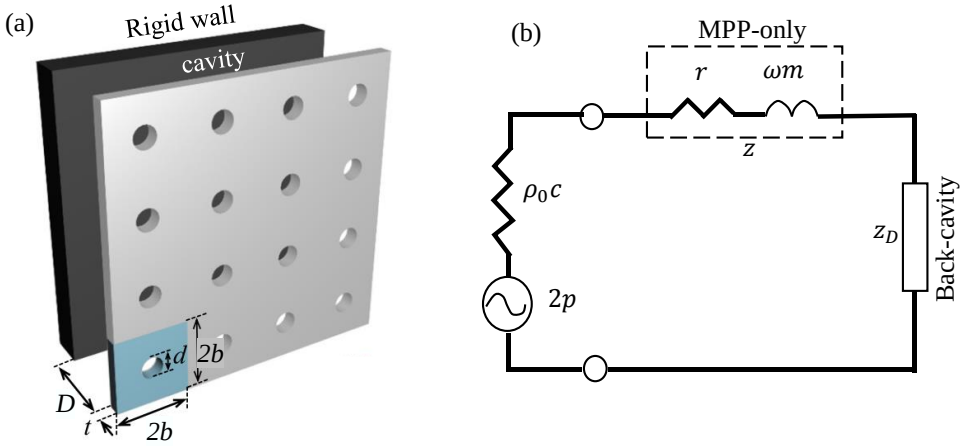

Figure 6-14. Schematic showing (a) an isometric view of an MPP absorber; (b) an electro-acoustical model of an MPP absorber.

The acoustic impedance of MPP-hole (z) is [163]:

$$z = r + j\omega m, \quad \textbf{(6.7)}$$

where r is the acoustic resistance and ωm is the mass reactance following:

$$r = \frac{32\eta t}{\sigma \rho_o c d^2}\left[\left(1 + \frac{k^2}{32}\right)^2 + \frac{\sqrt{2}}{32} k \frac{d}{t}\right], \quad \textbf{(6.8)}$$

$$\omega m = \frac{\omega t}{\sigma c}\left[1 + \left(1 + \frac{k^2}{2}\right)^{-1/2} + 0.85\frac{d}{t}\right], \quad \textbf{(6.9)}$$

where k is the perforate-constant, σ is the porosity, t is the thickness of the panel, $\omega = 2\pi f$ is the angular frequency of the incident sound with c velocity, η and ρ_o are the coefficient of viscosity and density of air respectively. The perforate-constant k is a function of the ratio of hole radius to the viscous boundary layer thickness [163]. It is given by $k = d\sqrt{\omega\rho_o/4\eta}$. The porosity of a unit panel is given by $\sigma = \pi d^2/4S$, where d is the hole diameter and S is the surface area of a unit panel. The back-cavity only presents a reactance $z_D = j\frac{\omega D}{c}$, where D is the back-cavity depth. The electro-acoustic circuit for this cavity-backed MPP absorber produces the following absorption coefficient (see Figure 6-14(b)) [163]

$$\alpha = \frac{4r}{(1+r)^2 + (\omega m - \cot(\frac{\omega D}{c}))^2} \quad \textbf{(6.10)}$$

when driven by a pressure source.

Maximum sound absorption occurs when the driving frequency of sound waves match with the system's resonant frequency. At the resonance the system's mass reactance vanishes which mean $(\omega m - \cot(\frac{\omega D}{c})) = 0$. As such, the maximum absorption coefficient is derived to be $\alpha_{max} = 4r/(1+r)^2$. The bandwidth of an acoustic absorber is calculated as the full width $(f_2 - f_1)$ for half maximum absorption coefficient (see Figure 6-11(a)). Lower and upper frequencies of the bandwidth, f_1 and f_2 can be obtained from the derived equation $(\omega m - \cot(\frac{\omega D}{c})) = \pm(1+r)$. The ratio of upper-bound frequency to lower-bound frequency is given by:

$$\frac{f_2}{f_1} = \frac{\pi}{\cot^{-1}(1+r)} - 1, \quad \textbf{(6.11)}$$

This suggests that the absorption bandwidth $(f_2 - f_1)$ is proportional to the relative acoustic resistance (r).

We expect that an MPP with smaller and deeper holes can achieve a broader bandwidth (from Equation (6.8)), but it lowers the maximum absorption coefficient (from Equation (6.10) [163]. Smaller hole diameter (*d*) relative to the panel thickness (at d/t<1) helps maximize the absorption of sound at a lower frequency. More holes (or increased porosity) in the MPP can help broaden the absorption bandwidth [164]. However, the porosity above 8% can compromise the absorption of low-frequency sound.

Performance of MPP absorber is not perfect for the whole range of sound frequency. While MPP has a broader absorption bandwidth as compared to panel absorber, a rigid MPP absorber is not good at absorbing bass sound. Furthermore, its absorption bandwidth is still not as broad as porous absorbers.

A few methods were proposed to improve the performance of MPP absorbers without using a deep back-cavity (see Figure 6-15). The first method makes use of a flexible micro-perforated membrane absorber in replacement of rigid MPP that broadens the absorption bandwidth by lowering the lower-bound for the full-width half-maximum [165, 166]. The enhanced performance is a coupled effect of membrane resonance and air-plug resonance in holes as predicted by Chen Xi et al. [167]. The second method simply makes use of multiple MPPs arranged in series (see Figure 6-15(a)) [168, 169]. The third method uses a partitioned back-cavity using honeycomb structures (see Figure 6-15(c)) [170]. Random distribution of hole size and cavity depth further helps to broaden the absorption bandwidth [171, 172]. For example, irregular cavity depth in each cell of back-cavity partitions help broaden the absorption bandwidth of MPP absorber (refer to Figure 6-15(c)) [173]. In another novel design, the back-cavity of a Helmholtz resonator or MPP is partitioned into connected channels in a shape similar to a coplanar spiral coil to help sound trapping and enhance sound absorption (refer to Figure 6-15(d)) [155]. Despite all these modifications to MPP absorbers, their absorption bandwidth is not as broad as porous absorbers absorption bandwidth.

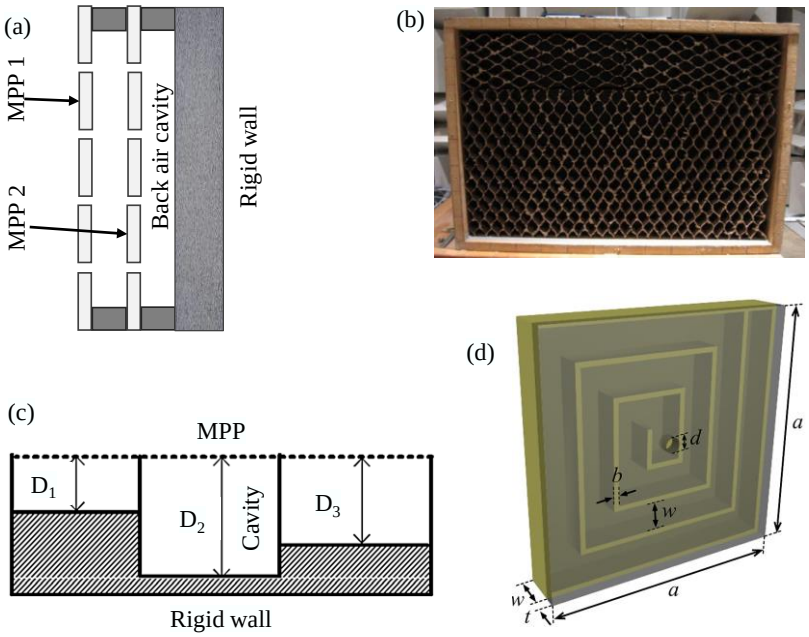

Figure 6-15. Innovative modification to micro-perforated panel absorbers (a) Double layered MPP; (b) Honeycomb shaped partitions to the back cavity of the MPP (adapted from [170]); (c) non-uniform cavity depth of individual cells of the MPP (adapted from [173]) and (d) unit cell of a metasurface made of a perforated plate and individual coplanar coiled air chamber (adapted from [155]).

6.2 Tunable Acoustic Absorber

The resonant absorber is only good at absorbing sound that matches its resonant frequency. While the use of MPP-based resonant absorber helps to broaden the absorption bandwidth, the peak absorption occurs only at the fixed resonant frequency. As a solution, a tunable resonant absorber can timely or continuously shift the resonant frequency to match the varying noise frequency. This tuning is achieved by changing the geometry and material property of these absorbers, such as varying back cavity depth, hole size, and even membrane stiffness. Various actuators were used to actively tune the absorber's geometric parameters, such as mechanical screw adjustments, stepping motors, electrostatic microactuators, electromagnets, dielectric elastomer actuators and so on. These tunable acoustic absorbers are compared in Table 6-1 in terms of tuning mechanism and frequency tuning range.

Table 6-1. Comparison of various tunable acoustic absorbers.

S. N	Tunable acoustic absorbers	Driving mechanism	Acoustic peak-frequency tuning range	Ref.
1.	Variable back-cavity (Helmholtz absorber)	Screw adjustment	60Hz - 700Hz	[158]
2.	Variable back-cavity (MPP absorber)	Stepping motor	1050Hz - 800Hz	[174]
3.		Electromechanical microactuators	600Hz - 875Hz	[174-176]
4.	Variable Hole Size (MPP absorber)	Mechanical linear stages	1350Hz -2150Hz	[177]
5.	Variable membrane tension (Membrane absorber)	Electromagnets	-	[178]
6.		Electromagnets (magnetorheological membrane)	238Hz-394Hz	[179]
7.		Electric-field (parallel-plate air capacitor)	180Hz-110Hz	[180]
8.		DEA	~400Hz-310Hz	[181]

6.2.1 Tunable Resonant Absorbers with Variable Back-Cavity

A simplest tunable resonant absorber is realized by adjustment of the back-cavity depth of Helmholtz or MPP absorber. Equation (6.5) dictates the dependence of absorber's resonant frequency on the back-cavity depth (D). Figure 6-16 shows the construction of such tunable absorbers. A screw adjustment (see Figure 6-16(a)) can slide the rigid back wall of the absorber to change its back-cavity volume. Such Helmholtz resonators were installed in the Royal Festival Hall in London to cover the frequency range from 60Hz to 700Hz [158]. In a similar design by S. Konishi et al. [174-176], a stepping motor was used to change the back-cavity depth (D) of an MPP absorber (see Figure 6-16 (b)). The MPP consisted of a plate of 40mm diameter and 1mm thickness with 400 holes of 100μm diameter arranged orthogonally in a square of 28mm. A cavity depth adjustment from 6mm to 12mm can lower the MPP absorber's resonant frequency from ~1050Hz to

800Hz respectively (see Figure 6-16(c)). However, this mechanical or electromechanical drive of a sliding back-wall is subjected to some issues. A mechanical sliding risks producing screeching noise; whereas the drive by the stepping motor is costly and requires power. Hence, such tunable absorber is limited in use for discrete adjustment, but not for real-time tuning.

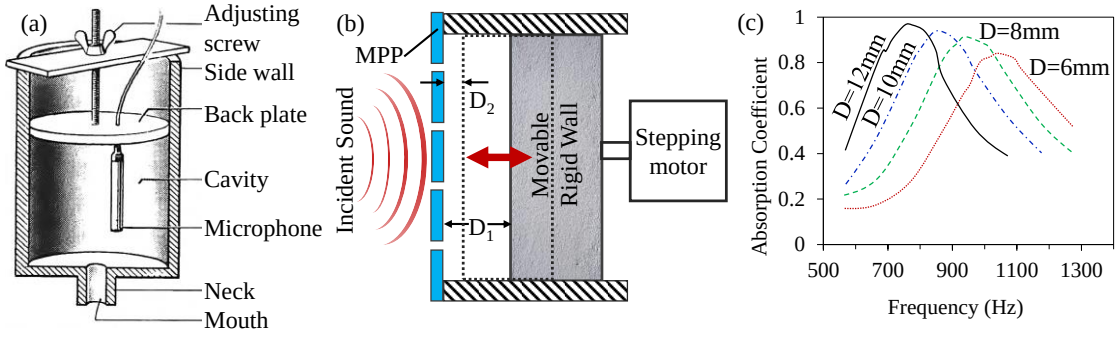

Figure 6-16. (a) Schematic showing setup for changing cavity depth of (a) a Helmholtz resonator (adapted from [158]); (b) an MPP absorber; (c) shifting of the peak absorption frequency by cavity depth variation of an MPP absorber. (adapted from [175, 176])

In another of tunable MPP absorber developed by Konishi et al. [174], electrostatic microactuators were proposed to close the holes of MPP absorber. The proposed absorber device consisted of two MPPs placed at a 10 mm spacing and a 20mm deep back cavity (see Figure 6-17(a)). The first MPP is a 1mm thick PMMA plate with 400 holes of 100μm diameter. The second MPP is integrated with an array of electrostatic C-shaped microactuators, each housing the holes of 1mm diameter (see Figure 6-17(a-b)). The microactuators can close the holes upon application of an electric field, and thus shift the absorption spectrum. At the open state of the second MPP, this absorber has a resonant frequency at ~600Hz. To experimentally simulate the closed state without the use of micro-actuators, a 7.5μm thick polyimide film is bonded to the second MPP. This closing of the second MPP holes raised the resonance to ~875Hz (see Figure 6-17(c)).

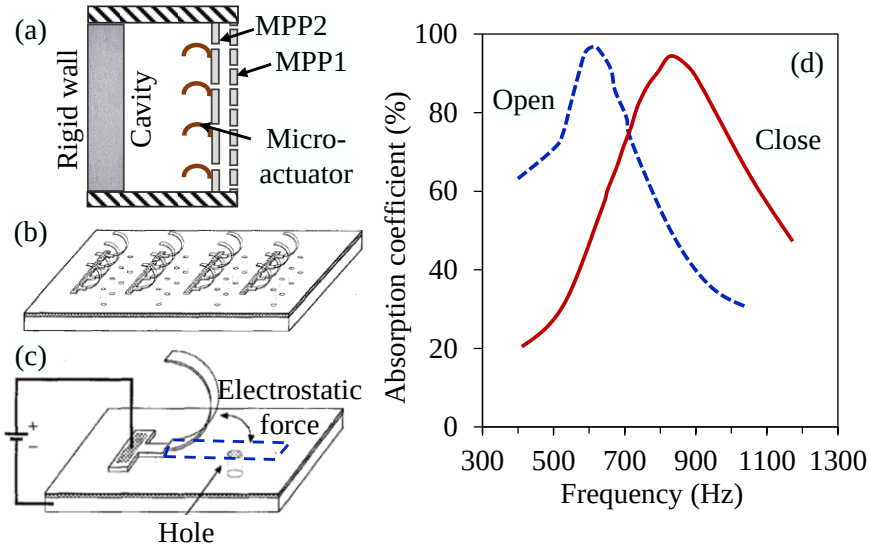

Figure 6-17. A conceptual MPPs setup with C-shaped microactuators to open and close the perforation holes of one of the MPP. (a) Schematic of the whole setup; (b) Schematic of the second MPP; (c) Magnified view of a single hole and actuator; (d) shifting the absorption spectrum by opening and closing the holes of the second MPP. (adapted from [174])

6.2.2 Tunable MPP Absorber of Variable Hole Size

A tunable MPP absorber can be based on the hole size change. In a tunable MPP developed by Cherrier et al. [177], the hole size change is effected by the variable overlap of identical holes in two MPPs, one front and another rear (see Figure 6-18(a-c)). The through hole area is maximum when the front and rear holes are aligned and overlapped. But, the through hole area is reduced when the front and rear holes are partially offset by sliding the front MPP. The front movable MPP is slid relative to the rear fixed MPP by using a manual linear stage. A prototype of tunable MPP developed by Cherrier et al. consists of two 1mm thick MPPs with 1mm diameter holes and 5% porosity. The MPPs were backed by 10mm deep air-cavity. When the holes in the two MPPs are aligned, the resonant frequency of the tunable absorber is approximately 2150Hz. The resonant frequency is reduced to ~1350Hz when the front holes are offset by 0.9mm relative to the rear holes. This means of mechanical tuning of MPP, however, requires a complex drive which includes sliding rails, link rods, and translation stages. Moreover, the drive of two overlapped MPPs is subjected to high friction and noise generation.

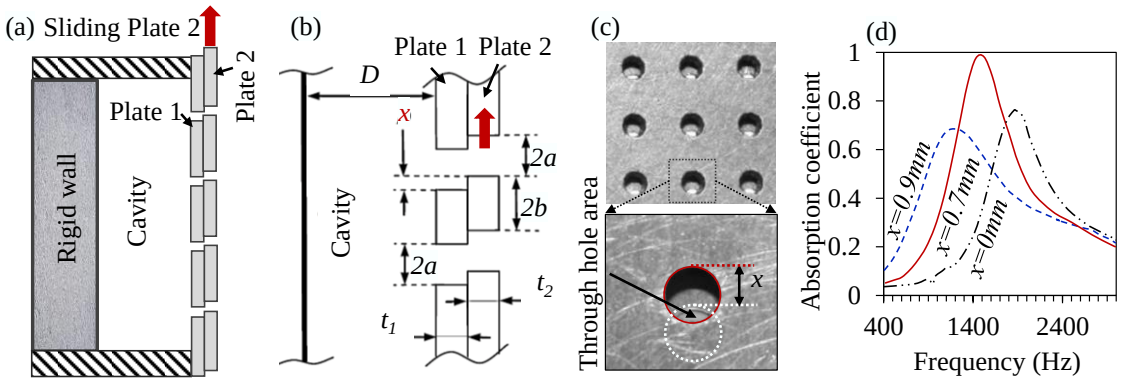

Figure 6-18. Variation of the perforation size and shape of an MPP. Schematic: (a) showing two MPP plates, one of the plate slides to change the through hole area; (b) magnified view of the same; (c) Photograph showing top views of the same; (d) shifting of the absorption spectrum by sliding Plate 2. (adapted from [177])

6.2.3 Tunable Membrane Resonator

A tunable membrane resonator's resonant frequency is shifted by adjustment of membrane tension (T) and stiffness following the relation $f_1 = \frac{2.405}{2\pi a}\sqrt{\frac{T}{\rho h}}$ [179], where ρ, h and a are mass density, thickness and radius of the membrane respectively [182, 183] (see Figure 6-19).

In a membrane resonator with variable tension developed by Chen et al. [178], electromagnets were used to exert extra stress on a pre-stretched membrane. The pre-stretched membrane of circular shape is placed in a tube with side holes in a periodic array. A DC electromagnet was activated to exert pressure at the outer annulus of the membrane. The pressure on the outer annulus radially stretches the circular membrane by sliding relative to the inner ring support (see Figure 6-19(a-c)). In this way, the membrane was stiffened from 1275N/m to 2047N/m (see Figure 6-19(d)) and thus shifted the transmission spectrum to higher frequencies (see Figure 6-19(e)). Drive of this tunable absorber by using electromagnets can be costly and limited to a small area.

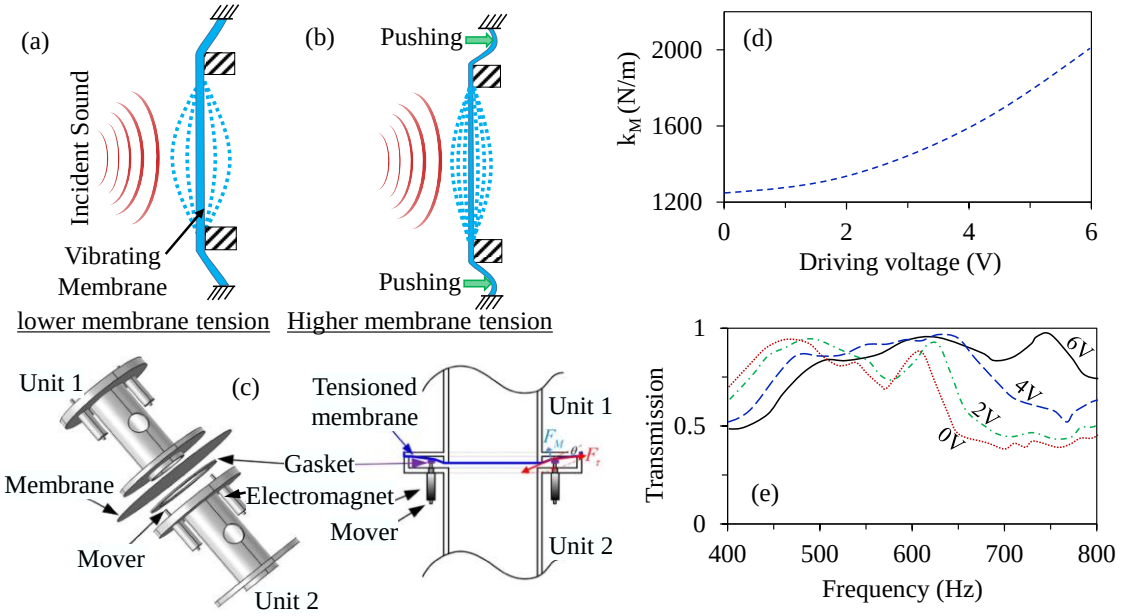

Figure 6-19. Controlling membrane tension by using electromagnets. Schematic of: (a) a membrane at a small pre-tension; (b) a stretched membrane with increased tension; (c) Setup to electromagnetically add tension to the membrane; (d) Electromagnetically induced change in the membrane's effective stiffness; (e) corresponding shifting in acoustic transmissions. (adapted from [178])

In a membrane resonator with variable resonant frequency developed by Chen et al. [179], an external magnetic field was applied to vary the stiffness of a magnetorheological elastomer membrane (see Figure 6-20(a)). The magnetorheological membrane was a silicone rubber filled with Fe3O4 particles. It was pre-stretched and fixed on rigid ring support (see Figure 6-20(b)). A permanent magnet is placed at a distance to induce a magnetic field gradient across the magnetorheological membrane. It exerts a uniform magnetic force $P_o = h\mu_o M\nabla H$ to the membrane, where, h and M are the thickness and magnetization of the magnetorheological membrane, μ_o is vacuum permeability, and H is the magnetic field intensity. In turn, this increase the membrane tension following the relationship $\Delta T = \left[\frac{Eha^2P_o^2}{24(1-\nu)}\right]^{1/3}$, where E, ν and a are Young's modulus, Poisson's ratio and radius of the membrane respectively. A 50mm shift of the magnet closer towards the membrane can raise the membrane's resonant frequency from

238 Hz to 394 Hz (see Figure 6-20(d)). Drive of this tunable absorber requires a linear actuator or a manual stage for moving the magnet closer or away from the magnetorheological membrane.

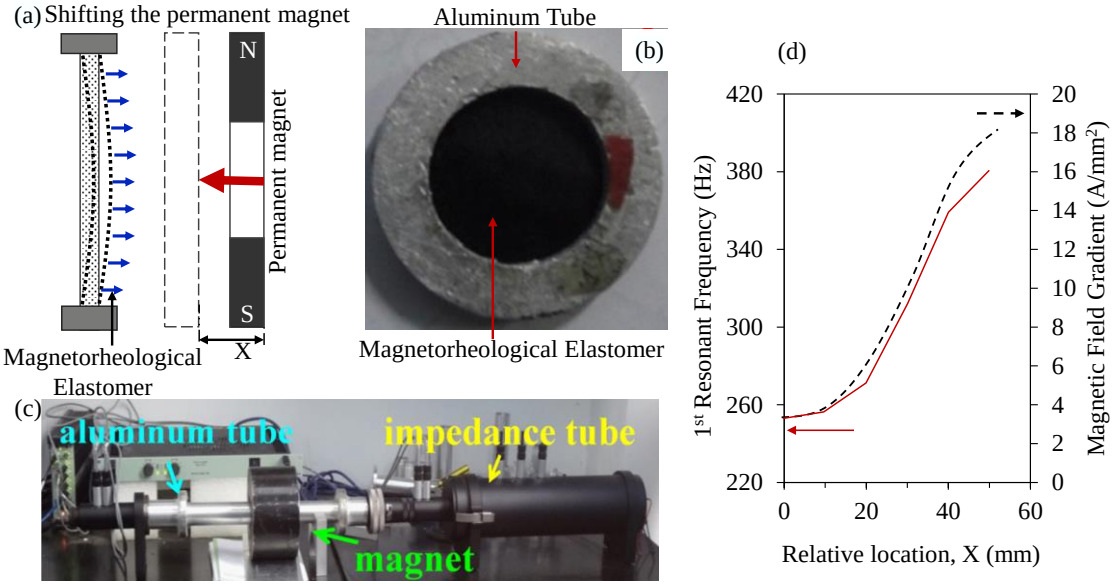

Figure 6-20. (a) Schematic showing effect of a magnetic field on a magnetorheological membrane; (b) photo of a magnetorheological membrane; (c) Impedance tube setup with a changeable permanent magnet to membrane distance; (d) Variation in the resonant frequency of the membrane with magnetic field gradient due to change in position of the permanent magnet.(adapted from [179])

In a novel tunable membrane absorber developed by Xiao et al. [180], a parallel-plate air capacitor is used to change the tension in an annular membrane surrounding a movable back plate. The air capacitor cum membrane absorber consists of a top fixed electrode in the form of a rigid fishnet and a bottom movable electrode in the form of a gold-coated disk of area *S* which was suspended by a ring of the pre-stretched membrane. The top conductive mesh electrode is placed at a distance *d* from the bottom disk. The mesh is transparent to sound propagation (see Figure 6-21(a)).

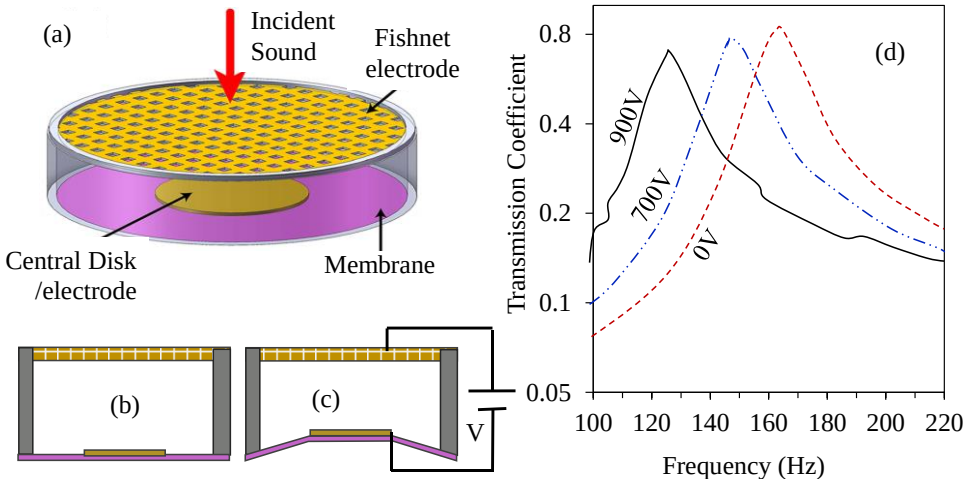

Figure 6-21. Membrane resonant frequency is tuned by an electric field. Schematic: (a) of the device; (b) at an inactive state; (c) when activated; (d) shift in acoustic transmission spectrum by an electric field. (adapted from [180])

Electrostatic activation of the parallel-plate capacitor can electrically dampen the membrane spring. A DC voltage-induce electrostatic force is $F_{DC} = -F_o + \bar{K}\Delta z$, where F_o is a static attractive force, $\bar{K}\Delta z$ is the dynamic attractive force which is proportional to the dynamic displacement Δz of the membrane, and $\bar{K} = \varepsilon S V^2/d^3$ is the electrostatic force constant. This extra force acting on the deformable electroded elastomer membrane can modulate the membrane tension and thus shift the membrane resonant frequency to be $f_1 = \frac{1}{2\pi}\sqrt{\frac{K_o - \bar{K}}{m}}$, where K_o is force constant due to membrane's pre-stress and m is effective membrane mass. A 900V activation of the air-gap capacitor can reduce the membrane resonant frequency by 70Hz (see Figure 6-21(b)).

6.2.4 Tunable Membrane Absorber based on Dielectric Elastomer Actuator

In a novel membrane absorber, a dielectric elastomer actuator is used to vary the tension in the pre-stretched membrane. The dielectric elastomer actuator is a pre-stretched dielectric elastomer membrane sandwiched by a pair of compliant electrodes based on carbon grease. High-voltage activation of the dielectric elastomer can induce Maxwell stress which squeezes the membrane and thus reduces the membrane tension by $\Delta T =$

$\varepsilon\left(\frac{V}{t}\right)^2$, where ε is the dielectric permittivity, and t is the thickness of the dielectric membrane (see Figure 6-22(a-b)) [182, 184].

Dubios et al. [182] demonstrated that the application of voltage can reduce the resonant frequency of a circular membrane of DEA. The first resonant frequency (f_r^{01}) for this DEA is voltage (V) dependent following the relationship, [182, 185]

$$f_r^{01} = \frac{1}{2\pi d\sqrt{\rho}}\sqrt{23.13\left(T_o - \frac{\varepsilon V^2}{t^2}\right) + \frac{1657D}{4td^2}} \qquad \textbf{(6.12)}$$

where d is the membrane diameter, ρ and t are mass density and thickness of the membrane, and T_o is the pre-stress in the membrane. Flexural rigidity of the membrane is the given by, $D = \frac{Yt^3}{12(1-\nu^2)}$, where Y and ν are the Young's modulus and the Poisson ratio of the dielectric elastomer. For example, 1.8kV activation of a silicone rubber DEA with 4mm diameter and 20-35μm thick gold thin film electrodes can shift the resonant frequency from 1670Hz to 535Hz.

Lu et al. [181, 184] first developed a tunable DEA-based membrane absorber as shown in Figure 6-22. The membrane absorber consists of a pre-stretched dielectric elastomer membrane of 100mm diameter (3M VHB4910) and an air-back cavity of 70mm depth. The pre-stretched membrane absorber can resonate in multiple modes under excitation by sound pressure wave and shows a peak acoustic absorption coefficient at resonance (see Figure 6-22(c)). Absorption bandwidth of the membrane absorber is narrow. While peak absorption coefficient can be as high as 1, the coefficient outside the bandwidth is merely 0.2. A 5kV activation can lower the resonant frequency by 87.2Hz (see Figure 6-22(c-d)). An array of multiple DEA-based membrane absorbers can be applied to the large area (540mm by 160mm) to achieve a 90Hz shift in resonant frequency [186].

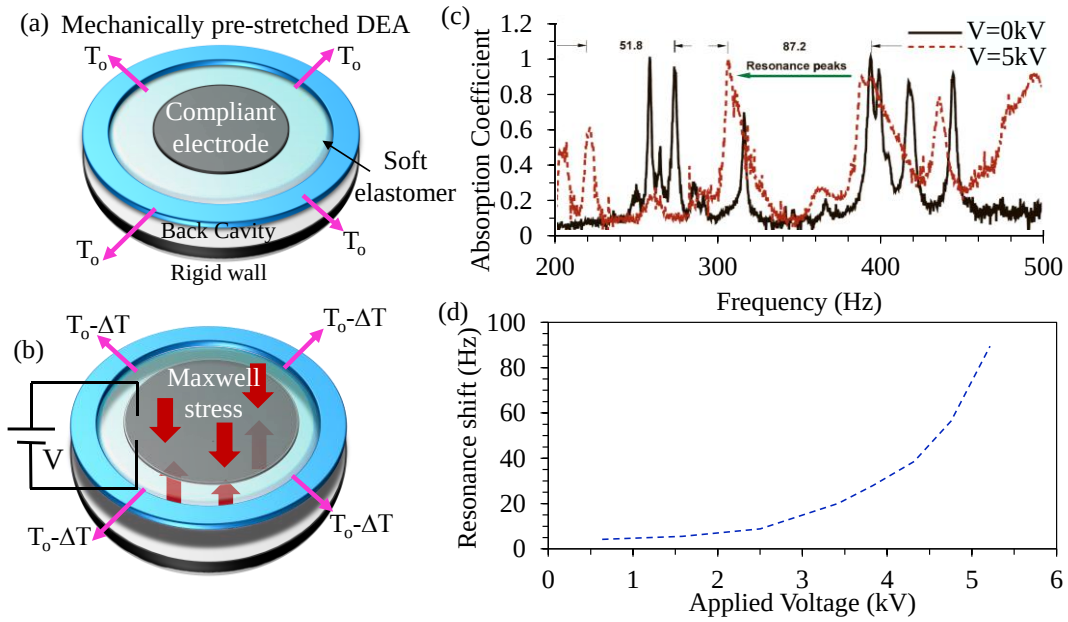

Figure 6-22. A DEA-based tunable membrane absorber. Schematic of the absorbers (a) at inactive state; (b) at activated state; (c) absorption peak frequency shift by DEA activation with 5kV; (d) resonance shift by increasing activation voltage of the DEAs. (adapted from [181])

6.3 Active Noise Control Systems

Active noise control (ANC) systems overcome the low-frequency limitation of the passive absorbers [187-189]. It actively introduces a counter sound field to destruct the unwanted sound field by interference [190]. The introduced canceling sound wave is the mirror image in terms of phase and amplitude of the unwanted sound waves. Hence, it enables the system to selectively attenuate the incoming sound waves [191].

ANC systems are suitable to dampen bass sound and resonating standing waves in an enclosed space like ducts and small rooms. Often, they are used as exhaust muffler to treat acoustic instabilities in an industrial combustor. Though ANC systems are usually limited to small enclosed spaces, multiple canceling sound sources can simultaneously be applied for larger rooms [192, 193]. However, they are more sophisticated systems and their performance drops with broadband and/or diffuse sound fields. This kind of the active system also consumes high power.

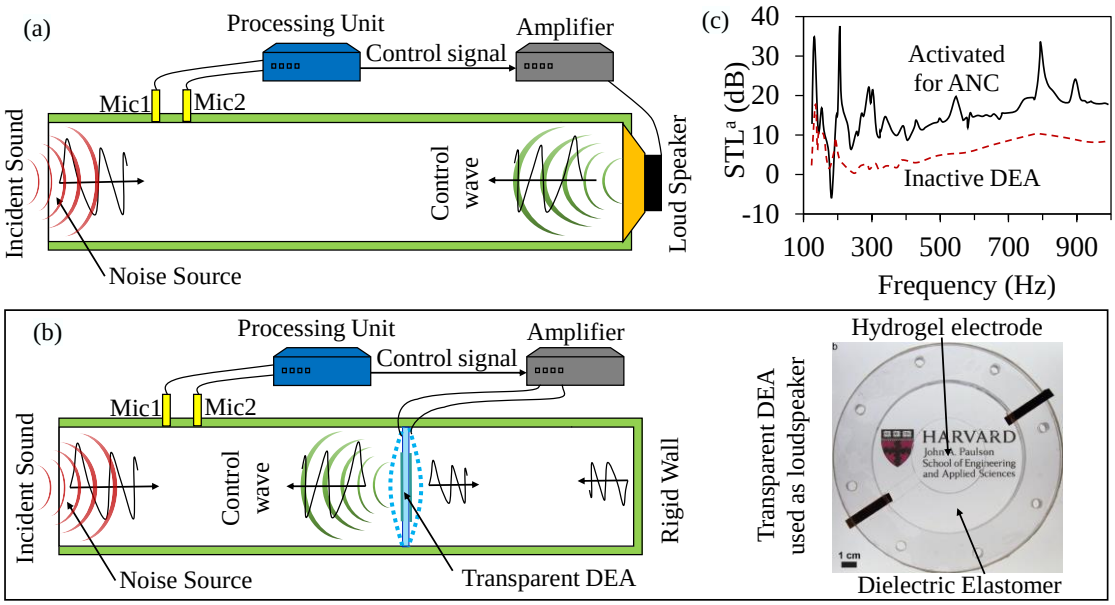

Figure 6-23. Sound absorption by ANC systems. Schematic of: (a) a general ANC system in an enclosed duct-like environment; (b) an ANC system with a transparent DEA (right) used as the loudspeaker; (c) Comparison of the sound transmission loss (STL) of an incident sound of 80dB by an inactive DEA membrane and the same in the ANC mode with excitation amplitude of 645V. (adapted from [189])

Active noise control (ANC) systems use a loudspeaker for sound cancellation. ANC systems also include a feedback loop to generate the canceling signal in response to the noise signal sensed by error microphones placed in the noise field. Figure 6-23(a) shows the canceling signal controls the loudspeaker's output in real-time [191]. Recently, a loudspeaker made of transparent DEA membrane was used in replacement to voice coil motor to make a transparent ANC system. Figure 6-23(c) shows the ANC system using the DEA-based loudspeaker attenuates sound in the frequency range from 100 to 900Hz. Recently, a transparent loudspeaker based on hydrogel-electroded DEA was developed for active noise cancellation [189] (see Figure 6-23(b)).

Hybrid active/passive absorber system combines an ANC system and a passive absorber. The passive absorber is placed in front of the control loudspeaker [194-197]. The control loudspeaker is used to tune the absorption characteristics of the passive absorbers to maintain optimal performance. Hybrid active/passive absorber systems can obtain

optimal acoustic absorption by using two control methods. First is by active "pressure releasing" on the back of the passive absorbers. Second is by active "impedance matching" of the passive absorber.

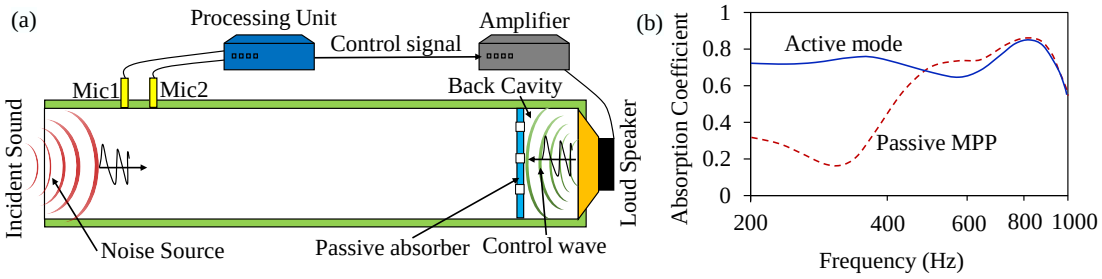

Figure 6-24. An MPP based hybrid passive-active absorber operating in the pressure release condition. (a) Schematic of the same; (b) comparison of the absorption performance in the active and the passive mode of operation. (adapted from [192])

In the pressure releasing mode, the loudspeaker maintains a zero pressure at the air cavity between the passive absorber and the loudspeaker. Then, the low-frequency impedance of the system is matched to the flow resistance of the passive absorber in order to obtain maximum absorption.

Meanwhile, in the impedance matching mode, the system's impedance is actively controlled [198]. The loudspeaker is used to control particle velocity near the wall of the back cavity. Through the tuning of the back-cavity impedance, the system acoustic impedance is actively matched with the air-impedance.

The passive component of a hybrid active/passive absorber system includes porous materials or resonant absorbers. For example, a hybrid system with a 3cm porous layer and a back-cavity of 7cm can achieve an absorption coefficient up to 0.95 over a frequency range of 90-850Hz using the pressure release strategy [195]. Recently, an MPP was used as the passive unit in a hybrid absorption system with a 5cm back cavity (see Figure 6-24) [192, 194, 198] and the system realized an absorption coefficient up to 0.82 over a frequency range of 100-1600 Hz [198].

6.4 Summary

To attenuate the reverberating indoor sound, acoustic absorbers are needed at walls, ceiling, and windows. Transparent acoustic absorbers are needed at windows. Existing porous absorbers are optically opaque or translucent. In addition, they require an impractically thick layer of porous materials to absorb low-frequency sound. Passive resonant absorbers like a panel or MPP absorbers can address these issues. Panel absorbers are can absorb low-frequency noise, but only over a narrow frequency bandwidth. Meanwhile, MPP absorbers have slightly broader absorption bandwidth in the mid-low frequency range. Consequently, these resonant absorbers cannot effectively absorb the noise of widely varying frequencies like traffic noise. The ANC systems can resolve this limitation of the passive absorbers. They use a feedback system to selectively absorb the noise of varying frequencies. But they are bulky, power hungry, limited to the small enclosed environments. Tunable acoustic absorbers can be an alternative to passive absorbers and ANC systems. They can actively target a varying dominant noise frequency. But existing tunable absorbers use impractical and noisy tuning mechanisms. For example, some use stepping motors to change back-cavity depth or to slide the metal plates. Moreover, tunable absorbers based on panel/membrane absorbers have a narrow absorption bandwidth, hence they are unable to absorb a broadband noise. This motivates us to develop tunable absorbers with relatively broader absorption bandwidth. In addition, such absorbers must use silent mechanisms which are also feasible for large-area absorbers like DEA.

Chapter 7 Mechanics of DEA-based Tunable Acoustic Devices

Recently, few acoustic absorbers are capable of actively tuning their absorption spectrum. This tunable acoustic absorber can be driven silently by using dielectric elastomer actuators. For example, a circular DEA was used to adjust the membrane tension in an acoustic absorber [181]. Previously, an annular DEA was used to relax the membrane tension that stretched a deformable lens of oil capsule at its centre [141, 199, 200]. Here, this chapter first presents the mechanics of tuning the hole size of a membrane using such annular DEAs which can make a tunable microperforated panel absorber. These tunable devices are purposely designed to work under small strain activation (<5%). Hence, analysis of electrostatically induced deformation can assume small strain, and thus simple elastic models can be used instead of nonlinear models which were previously used for analysis of DEA induced large deformation (>100%) [81, 131].

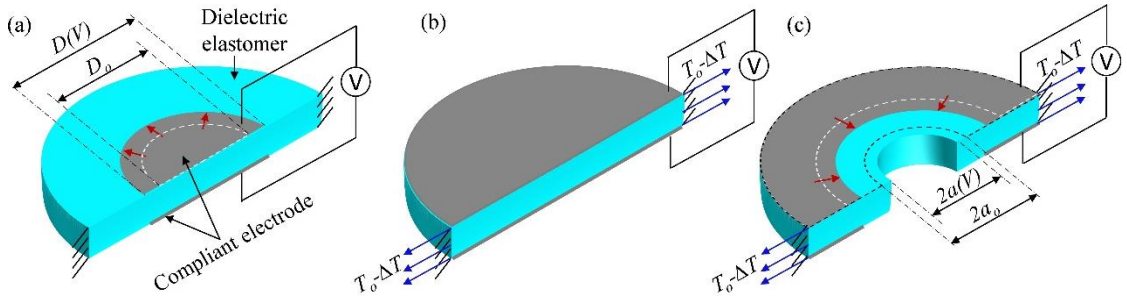

Figure 7-1. Isometric cross-sectional view of the various designs of the DEAs. Schematic of (a) circular DEA for radial actuation under isotonic condition; (b) circular DEA for tension change under the isometric condition, (c) annular DEA for controlling the hole size in a passive membrane.

A dielectric elastomer actuator is a soft capacitor that undergoes an areal expansion when being compressed by Maxwell stress [66, 67]. The Maxwell stress (electrostatic pressure) can modulate the membrane tension, which greatly helps to enhance the voltage-induced areal expansion. However, the level of actuation varies substantially with the boundary

and loading conditions, even when ideally compliant electrodes were used to drive the dielectric elastomer actuators. This chapter presented the analyses of three designs of dielectric elastomer actuators which are used to make tunable membrane absorber. They are shown in Figure 7-1, and includes (1) a circular DEA for radial actuation under isotonic condition; (2) a circular DEA for tension change under the isometric condition, (3) an annular DEA for controlling the hole size in a passive membrane.

7.1 Circular DEA for Radial Actuation under Isotonic Condition

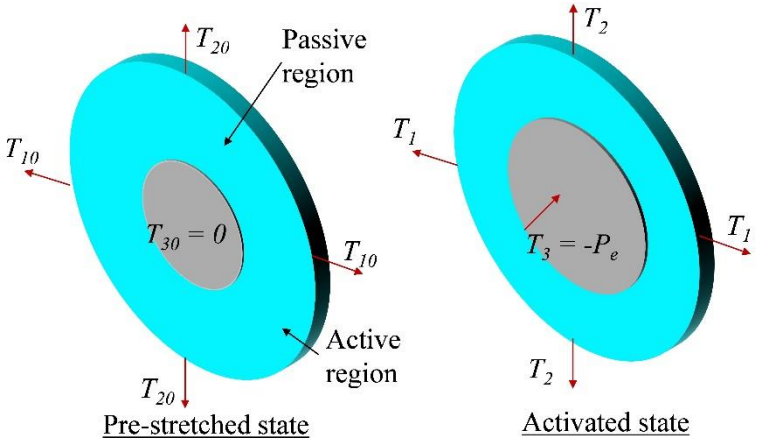

Figure 7-2. DEA with circular disc electrodes at (left) inactivated state; (right) activated state.

Let us consider a circular DEA sandwiched by small compliant electrode disks as shown in Figure 7-2. While being surrounded by a large passive pre-stretched membrane, the electroded membrane can maintain a constant pre-stress even during DEA activation. Under this biaxial isotonic condition, the voltage-induced net biaxial strains (ΔS_1 and ΔS_2) is simply the Poisson's ratio effect of Maxwell stress and is given as:

$$\Delta S_1 = S_1 - S_{10} = \frac{\nu P_e}{E},$$
$$\Delta S_2 = S_2 - S_{20} = \frac{\nu P_e}{E}. \qquad \textbf{(7.1)}$$

where E and v are the Young modulus and Poisson's ratio of dielectric elastomer membrane, respectively. The biaxial pre-strains (S_{10} and S_{20}) due to initially applied biaxial pre-stress T_{10} and T_{20} is given by [201]

$$S_{10} = \frac{T_{10}}{E} - \frac{\nu T_{20}}{E}, \qquad S_{20} = \frac{T_{20}}{E} - \frac{\nu T_{10}}{E}, \tag{7.2}$$

and the total biaxial strains under voltage activation are given by constitutive equations

$$S_1 = \frac{T_1}{E} - \frac{\nu T_2}{E} - \frac{\nu T_3}{E}, \qquad S_2 = \frac{T_2}{E} - \frac{\nu T_1}{E} - \frac{\nu T_3}{E}. \tag{7.3}$$

where T_3 is the normal traction due to the electrostatic pressure (P_e) expressed as [66, 79-81],

$$T_3 = -P_e = -\frac{\epsilon_r \epsilon_o \left(\frac{V}{t}\right)^2}{2}, \tag{7.4}$$

and $T_1 = T_{10}$ and $T_2 = T_{20}$ for the isotonic condition. Here V and t are the applied voltage and thickness of the membrane.

7.2 Circular DEA for Tension Change under Isometric Condition

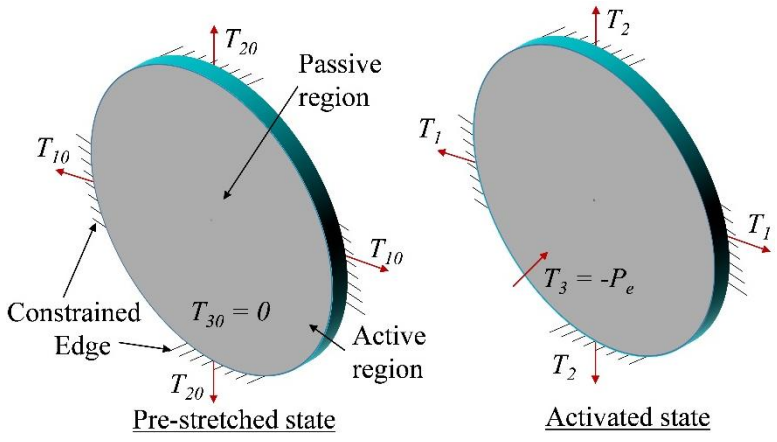

Figure 7-3. DEA with annular electrodes at (left) inactivated state; (right) activated state.

Next, we consider a circular DEA sandwiched fully by compliant electrodes as shown in Figure 7-3. There is no passive membrane and the whole DEA is surrounded by a fixed boundary. Under this isometric condition, activation of the DEA cannot produce any areal expansion, but it can reduce the membrane tension. Based on the constitutive equation for a biaxially pre-stretched membrane given in Equation (7.3) and isometric boundary condition $S_1 = S_{10}$ and $S_2 = S_{20}$, the membrane's biaxial tensions under voltage activation of the DEA are derived to be

$$T_1 = T_{10} - \frac{\nu P_e}{1-\nu}, \qquad T_2 = T_{20} - \frac{\nu P_e}{1-\nu}. \tag{7.5}$$

using the isometric identity, $S_1 + \nu S_2 = S_{10} + \nu S_{20}\ or, \nu S_1 + S_2 = \nu S_{10} + S_{20}$.

Under equibiaxial pre-tension, i.e. $T_1 = T_2$ and $T_{10} = T_{20}$, the membrane stress change $\Delta T = T_1 - T_{10} = T_2 - T_{20}$ is solely due to the electrostatic pressure following,

$$\Delta T = -\frac{\nu P_e}{1-\nu}. \tag{7.6}$$

7.3 Annular DEA for Controlling the Hole Size in a Passive Membrane

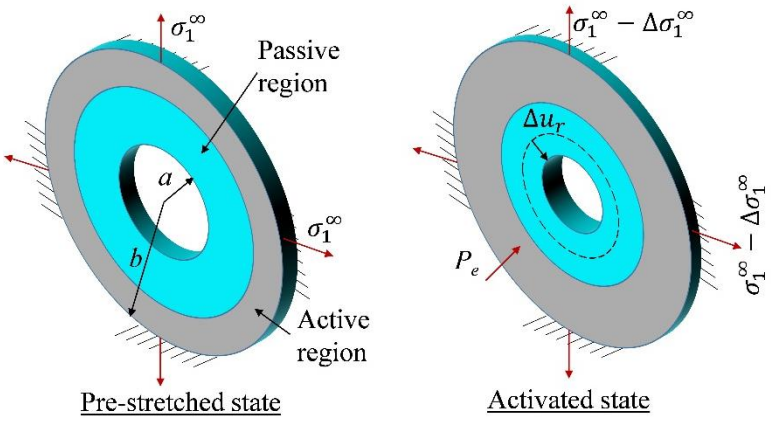

Figure 7-4. Schematic of a DEA with an annular electrode surrounding a hole at: (left) inactivated state; (right) activated state.

Next, we consider a DEA of annular shape which is used to control the size of a hole through the central passive membrane (see Figure 7-4). The external annular DEA and the inner passive annulus are made of the same piece of pre-stretched dielectric elastomer membrane. The difference lies with the electrode coverage of the former. The diameter of through-hole at the center of the passive annular membrane is moderated by DEA. Voltage activation of the DEA can control membrane tension. In turn, this distant membrane tension change tunes the hole diameter of the passive inner annulus.

Let's consider an annular DEA of radius *b* with the through-hole of *a* radius, and an initial radial pre-stress σ_1^∞ (see Figure 7-4). In the case that DEA is much larger than the passive annulus, the voltage induced stress change ($\Delta\sigma_1^\infty$) can be approximated as that induced under the isometric condition (refer to Equation (7.6)) as

$$\Delta\sigma_1^\infty = -\frac{\nu P_e}{1-\nu}. \tag{7.7}$$

Stress distribution in the DEA and passive annulus follows the general solution for stress surrounding a hole under radial loading, which is given as:

$$\begin{aligned}
\sigma_{rr} &= \left(\frac{\sigma_1^\infty+\sigma_2^\infty}{2}\right)\left(1-\frac{a^2}{r^2}\right)+\left(\frac{\sigma_1^\infty-\sigma_2^\infty}{2}\right)\left(1-\frac{4a^2}{r^2}+\frac{3a^4}{r^4}\right)cos(2\theta),\\
\sigma_{r\theta} &= -\left(\frac{\sigma_1^\infty-\sigma_2^\infty}{2}\right)\left(1+\frac{2a^2}{r^2}-\frac{3a^4}{r^4}\right)sin(2\theta),\\
\sigma_{\theta\theta} &= \left(\frac{\sigma_1^\infty+\sigma_2^\infty}{2}\right)\left(1+\frac{a^2}{r^2}\right)-\left(\frac{\sigma_1^\infty-\sigma_2^\infty}{2}\right)\left(1+\frac{3a^4}{r^4}\right)cos(2\theta),
\end{aligned} \tag{7.8}$$

where $\sigma_1^\infty \; and \; \sigma_2^\infty$ are the applied bi-axial pre-stress far away from the hole. For the case of radial pre-stretching i.e. $\sigma_1^\infty = \sigma_2^\infty$, according to the plane stress analysis [202, 203], the stress distribution reduces to:

$$\begin{aligned}
\sigma_{rr} &= (\sigma_1^\infty)\left(1-\frac{a^2}{r^2}\right),\\
\sigma_{r\theta} &= 0,\\
\sigma_{\theta\theta} &= (\sigma_1^\infty)\left(1+\frac{a^2}{r^2}\right).
\end{aligned} \tag{7.9}$$

Similarly, the change in stress distribution ($\Delta\sigma_{rr}, \Delta\sigma_{r\theta} \; and \; \Delta\sigma_{\theta\theta}$) are obtained by substituting Equation (7.7) in Equation (7.9) as,

$$\Delta\sigma_{rr} = (\Delta\sigma_1^{\infty})\left(1-\frac{a^2}{r^2}\right) = -\frac{\nu P_e}{1-\nu}\left(1-\frac{a^2}{r^2}\right),$$

$$\Delta\sigma_{r\theta} = 0 \tag{7.10}$$

$$\Delta\sigma_{\theta\theta} = (\Delta\sigma_1^{\infty})\left(1+\frac{a^2}{r^2}\right) = -\frac{\nu P_e}{1-\nu}\left(1+\frac{a^2}{r^2}\right).$$

Since there is no electrode near the holes, the stress along thickness direction near the perforation holes does not change. The radial strain can be calculated from the equivalent radial stress using these constitutive equations as,

$$\begin{aligned}\Delta\varepsilon_{rr} &= \frac{1}{E}(\Delta\sigma_{rr} - \nu\Delta\sigma_{\theta\theta} - \nu\Delta\sigma_{zz}),\\ &= \frac{1}{E}\left(-\frac{\nu P_e}{1-\nu}\left(1-\frac{a^2}{r^2}\right) + \nu\left(\frac{\nu P_e}{1-\nu}\right)\left(1+\frac{a^2}{r^2}\right)\right).\end{aligned} \tag{7.11}$$

Integration of this radial strain with respect to the radius yields the radial displacement as,

$$\Delta u_r = \int \Delta\varepsilon_{rr}dr = -\frac{\nu}{1-\nu}\frac{P_e}{E}\left[\left(r+\frac{a^2}{r}\right) - \nu\left(r-\frac{a^2}{r}\right)\right] + c(\theta,z), \tag{7.12}$$

The unknown constant $c(\theta,z)$ can be solved by using the isometric boundary condition that applies the outer edge of the DEA does not move, i.e.$\Delta u_r = 0$ at r=b as,

$$c(\theta,z) = \frac{\nu}{1-\nu}\frac{P_e}{E}\left[\left(b+\frac{a^2}{b}\right) - \nu\left(b-\frac{a^2}{b}\right)\right]. \tag{7.13}$$

In turn, the radial displacement takes the following form,

$$\Delta u_r = -\frac{\nu}{1-\nu}\frac{P_e}{E}\left[\left(r+\frac{a^2}{r}\right) - \nu\left(r-\frac{a^2}{r}\right) - \left(b+\frac{a^2}{b}\right) + \nu\left(b-\frac{a^2}{b}\right)\right] \tag{7.14}$$

As such, the reduction of the hole radius (i.e. Δu_r at r=a) by voltage activation is given by

$$|\Delta u_r|_{r=a} = \Delta a(V) = \frac{\nu}{1-\nu}\frac{P_e}{E}\left[b+\frac{a^2}{b} - 2a - \nu\left(b-\frac{a^2}{b}\right)\right] \tag{7.15}$$

This equation is used to predict the hole size change of a tunable micro-perforated membrane absorber and is experimentally verified in Chapter 8.

7.4 Summary

This chapter discussed and analyzed three designs of dielectric elastomer actuators, (1) a circular DEA for radial actuation under isotonic condition; (2) a circular DEA for tension change under the isometric condition, (3) an annular DEA for controlling the hole size in a passive membrane. The models were developed with the small strain assumptions, hence simple linear elastic models were applied. The model for the hole size change in an annular DEA given by Equation (7.15) will later be used to predict the hole size change of a tunable micro-perforated membrane absorber. The experimental validation of the Equation (7.7) for the voltage induced stress change and Equation (7.15) for the hole size change is also present in the following chapter.

Chapter 8 Tunable Acoustic Absorber using Micro-Perforated Dielectric Elastomer Actuator (MPDEA)

Most membrane-type acoustic absorbers for low-frequency sound attenuation are applicable only at a fixed resonant frequency for a narrow bandwidth. Tuning of the acoustic absorption spectrum is desired to match the varying noise's dominant frequency. This chapter presents a micro-perforated dielectric elastomer actuator (MPDEA) to make an electrically tunable broader-band acoustic absorber. These MPDEAs use patterned wrinkled gold thin films as compliant electrodes. Voltage activation of the MPDEA reduces the membrane tension and hole size and thus enables the active shifting of the acoustic absorption spectrum. Such a membrane tuning method does not require discrete mechanical parts as for the cavity tuning method. Also presented are the analytical models to predict the voltage-induced hole size change and acoustic characteristics of MPDEA. Results presented in this chapter is published in Ref. [143].

8.1 Introduction

Acoustic metamaterials are man-made sub-wavelength structures to control and manipulate sound waves [204]. Examples of them include periodic resonators/scatterers,[205-207] sonic crystals, [208-210] and resonant membrane absorbers [211-215]. Among them, membrane-type absorbers with a subwavelength air cavity can absorb the noises in the low to medium frequency range, eliminating the need for thick porous absorbers. However, most of these metamaterials have a narrow absorption band around a fixed resonant frequency;[155, 216, 217] they cannot be actively tuned to match the varying noise conditions. Recently, tunable membrane absorbers have been developed using a biaxially pre-stretched dielectric elastomer actuator (DEA) with a back-cavity of fixed depth [181, 186, 218, 219]. Voltage activation of the DEA reduces the membrane tension (by applying the Maxwell stress [220]) and thus enables the shift (reduction) of the absorber's resonant frequency [182, 218]. Yet,

the absorption bandwidth of such a DEA acoustic absorber remains narrow, around the tunable resonant frequency.

A broader band of sound absorption is possible using a micro-perforated panel (MPP),[159, 163, 167] a type of Helmholtz resonator, due to periodic resonance. The MPP consists of a rigid panel with submillimetre perforations (holes) and a back cavity. Its resonant frequency depends on the pore sizes (i.e., diameter and depth) and the back-cavity volume [158, 163]. A screw adjustment [158] of the cavity volume provides a simple mechanical means to tune the resonant frequency of a Helmholtz resonator. Similarly, a stepper motor [175, 221] was previously used to change the back-cavity volume of the MPP absorber, moving the back-cavity plate from 6mm to 12mm. These cavity tuning methods are however impractical and costly for large-area MPP. These MPPs with negligible panel vibration work only for medium frequencies, ranging from 600Hz to 1000Hz, despite being capable of cavity tuning. In contrary, the recently developed membrane-type acoustic absorber can better attenuate noises at a low frequency (below 500Hz).

This chapter presents an electrically tunable acoustic absorber based on a micro-perforated dielectric elastomer actuator (MPDEA) (see Figure 8-1). It is capable of broader band attenuation of low-to-medium frequency sound and electrical tuning of the peak absorption frequency and bandwidth. This is achieved by voltage activation that reduces the membrane tension and thus hole size. Such a membrane tuning method does not require discrete mechanical parts as for the reported cavity tuning method [158, 175, 221].

This MPDEA has a circular dielectric elastomer (DE) membrane which is radially pre-stretched and has its outer edge fixed to a rigid cylindrical tube of radius R_0. The membrane was laser drilled with an orthogonal array of holes at a pitch of $2b$. The perforated DE membrane is initially subjected to a pre-stress σ_0^{∞}. Figure 8-1(b) shows a unit cell of MPDEA which consists of a hole of a radius a, a passive annulus, and an active part in the pre-stretched dielectric elastomer membrane. The passive annulus is

non-coated and has a hole at its centre, while the surrounding active membrane is sandwiched by wrinkled gold compliant electrodes [74, 222, 223]. The laser-drilled holes have the edges thickened upon membrane stress relief. Multi-layer MPDEAs, for example, a two-layer device, are thicker to make deeper holes to improve the sound absorption but reduces the membrane flexibility, as compared to a single-layer MPDEA.

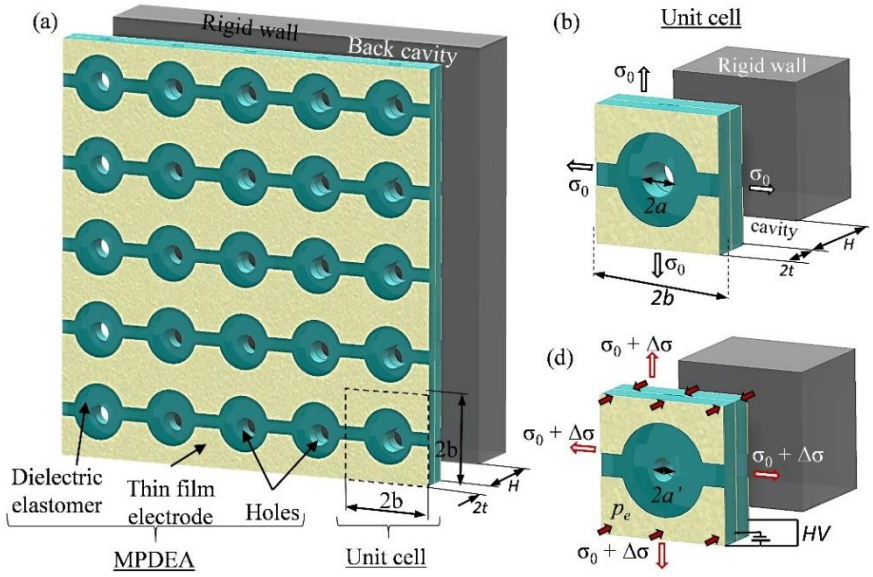

Figure 8-1. A broadband tunable acoustic absorber using micro-perforated dielectric elastomer actuators (MPDEA): (a) an array of electrically tunable holes in DEA; (b) its unit cell with a hole at either passive or active states;

8.2 Theory

Activation of the MPDEA at a voltage V induces a Maxwell stress $P_e = \frac{\epsilon_r \epsilon_o E^2}{2}$ across the active dielectric elastomer membrane of thickness t and relative permittivity $\epsilon_r = 4.7$, where $\epsilon_o = 8.85 \times 10^{-12}$ F/m is the vacuum permittivity. This isometric loading on the DE membrane with the Poisson ratio $\nu = 0.5$ reduces the distant equi-biaxial stresses in the passive annular membrane by $\sigma^{\infty} = -\frac{\nu P_e}{1-\nu}$. Hence, the passive annular membrane with a hole radius a is subjected to the voltage-induced stress changes in the cylindrical coordinates r, θ, and z as given by Equations (7.10). As such, the voltage-induced reduction of the hole radius is given by

$$\Delta a(V) = \frac{\nu}{1-\nu}\frac{P_e}{E}\left[b + \frac{a^2}{b} - 2a - \nu\left(b - \frac{a^2}{b}\right)\right] \quad \textbf{(8.1)}$$

where E is the tangent of Young's modulus of the pre-stretched perforated dielectric elastomer membrane (refer to Section 7.3 for details of derivation).

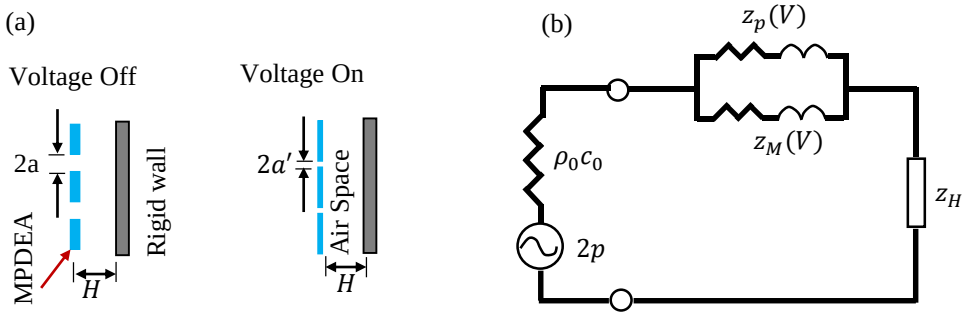

Figure 8-2. (a) Schematic showing the perforation size change by voltage activation of the MPDEA; (b) An equivalent electro-acoustic circuit representing the MPDEA backed by an air cavity. (retrieved from [143])

This resonant acoustic absorber consists of an MPDEA and a back cavity. The air-filled back cavity has a depth H from a rigid back plate. Consider a sound wave of a frequency f that travels at the sound speed c_0 in the air. Upon normally impinging on the rigid wall (normal incidence), the sound reflects and produces an equivalent source pressure $2p$. The sound absorption coefficient $\alpha(V)$ of this MPDEA has a similar expression as derived for the perforated membrane absorber,[167] except the voltage dependence

$$\alpha(V) = \frac{4Re(z(V))}{\left(1+Re(z(V))\right)^2 + Im(z(V))^2}, \quad \textbf{(8.2)}$$

Where z is the total acoustic impedance of the resonant absorber as presented in the electro-acoustic model in Figure 8-2(b). The model has a mass-impedance element in series with a cavity reactance $z_H = -jcot\left(\frac{\omega H}{c_0}\right)$, where $\omega = 2\pi f$, f is the frequency (Hz). The mass-impedance is voltage tunable. It consists of a parallel connection of a membrane impedance $z_M = \frac{1}{\rho_0 c_0}(R_M + jM_M)$, and a perforation impedance $z_P =$

$\frac{1}{\rho_0 c_0}(R_P + jM_P)$. Here, R and M denotes the acoustic resistance and reactance respectively. Based on the electro-acoustic model, the total acoustic impedance is

$$z = \frac{z_M z_P}{z_M + z_P} + z_H, \tag{8.3}$$

The pre-tensioned micro-perforated membrane vibrates like a string when it is subjected to a sound pressure wave Δp in the air of density ρ_o and the viscosity μ. Applying a voltage to the MPDEA reduces the membrane tension. This modulated membrane tension *T(V)* also tunes the membrane's resonant frequency [218]. Consider a pre-tensioned circular membrane with an outer radius R_o with material properties as: membrane surface density (ρ_m) and internal damping (η). Its membrane acoustic impedance z_M is given by [167]:

$$z_M(U) = \frac{\omega \rho_p}{j \rho_0 c_0}\left[\frac{2}{K_{mem}(U) R_0}\frac{J_1(K_{mem}(U)R_0)}{J_0(K_{mem}(U)R_0)} - 1\right]^{-1} \tag{8.4}$$

where $K'_{mem} = \frac{\omega^2 \rho_m}{T(V) + 2j\omega\eta}$ is voltage dependent (as indicated with a prime symbol), J_1 is the Bessel function of the first kind and first order, and J_0 is the same of zeroth order. This shows the dependence of membrane impedance on the electrically controllable tension.

The acoustic impedance of the array of *N* perforations in the MPDEA with the circular membrane of outer radius R_o is a sum of contribution by individual holes of *a'*, given by

$$z_P(V) = \sum_{n=1}^{N} \frac{R_o^2}{a'^2} z_{hole(R,V)} \tag{8.5}$$

where $a' = a - \Delta a(V)$ is the activated hole size.

The acoustic impedance $z_{hole(R,V)}$ of individual holes at the radial coordinate R in the circular flexible membrane is given by [155]

$$z_{hole}(R,V) = \left[\frac{j2\rho_0 c_0}{\omega \rho_m K_{air} a'}\frac{J_1(K_{air}a')}{J_0(K_{air}a')}\left[\frac{J_0(K_{mem}R)}{J_0(K_{mem}R_0)} - 1\right] + \frac{1}{z'_{Maa}\delta'}\right]^{-1}, \tag{8.6}$$

where $K_{air} = -j\frac{\rho_0\omega}{\mu}$, $\delta' = Na'^2/R_o^2$ is the perforation ratio of the membrane with N number of holes.

Maa's estimated acoustic impedance z'_{Maa} of a hole in the rigid panel is given by[155, 163]

$$z'_{Maa} = 36.75\times10^{-3}\frac{t}{a'^2\delta'}\left(\sqrt{1+\frac{x'^2}{32}}+\frac{\sqrt{2}}{4}\frac{x'a'}{t}\right)+j0.294\times10^{-3}\frac{\omega t}{\delta'}\left(1+\frac{1}{\sqrt{9+x'^2/2}}+1.70\frac{a'}{t}\right), \quad \textbf{(8.7)}$$

where $x' = a'\sqrt{2f/5}$ is the perforation constant. These equations show the dependence of perforation impedance on both hole size and tension which are electrically controllable.

8.3 Experiment

Figure 8-3 shows the fabrication processes of the proposed MPDEA. First, a 1-mm thick polyacrylate elastomer membrane (3M VHB 4910, a 3M trademark for very high bond (VHB) adhesive tape) is radially stretched for $\lambda = 3.15$ times using a custom-made stretcher. The pre-stretch ratio is $\lambda = R_o/R_i$, where R_i is the initial dimension of the membrane and R_o is the pre-stretched dimension. The pre-stretched membranes are left undisturbed for 48 hours to allow the membranes to slowly relax and reach a stable pre-stretched state.[224] Second, a 1.5mm thick Teflon mask, which is laser cut (Epilog Helix 24) into the designed pattern, is applied and aligned on each side of an elastomer substrate. Third, a 10 nm gold thin film is DC magnetron sputtered on each side of the exposed elastomer substrate. Fourth, the Teflon mask is lifted off to yield the electrode patterns. Next, the electrode patterning steps are repeated on the other side. A pair of such patterned electrodes sandwich the membrane to make dielectric elastomer actuators. Electrical leads to each sputtered electrode are formed each by a copper foil with conductive grease contact. Fifth, the membrane is laser drilled into *N*=325 submillimetre holes (perforations) at an initial pitch of *2b*=5mm over the non-electrode parts. The

passive annulus is 2mm radial wide from the hole to avoid electric arcing through the hole and air. Sixth, the perforated membrane is partially released to have a 2.9-time radial pre-stretch such that the gold thin films wrinkle under a 6.5% radial compressive strain and make stretchable compliant electrodes. As a result, the hole pitch reduces to *2b*=4.5mm approximately and the hole radius reduces to be close to 0.15 mm. Next, this MPDEA is adhesively fixed to a cylindrical tube with an inner radius of $R_o = 50.5$ mm. A multilayer MPDEA is fabricated using the same steps but requires the extra steps of alignment, stacking, and degassing before the steps of laser drilling. Degassing at -85 kPa (lower than atmospheric pressure) for 3–4 h helps remove the trapped air and improve the adhesion at the interfaces of multilayer DEA. Finally, a device of a two-layer MPDEA is completed on a circular rim as shown in the photograph in Figure 8-3(b), while Figure 8-3(c) and (d) show its unit cell and a part of the wrinkled gold electrode, respectively.

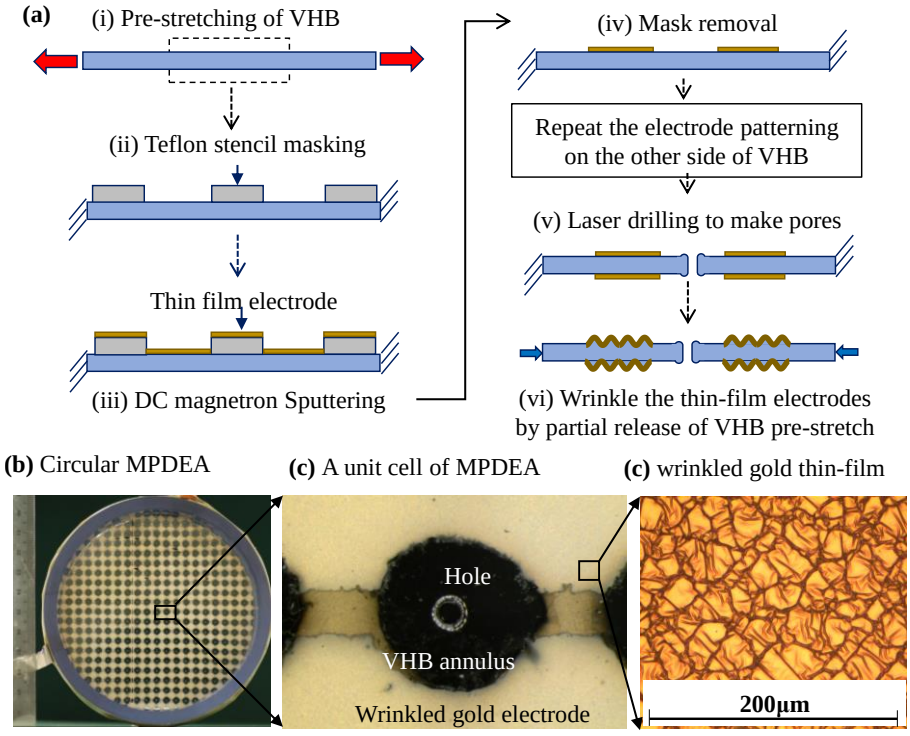

Figure 8-3. Fabrication of an MPDEA acoustic absorber: (a) the fabrication steps for a single-layer MPDEA; (b) photograph of a two-layer MPDEA device; (c) optical micrograph of an MPDEA unit cell; and (d) the photograph of the wrinkled gold electrode.

Three kinds of acoustic absorbers were fabricated, namely, a single-layer perforated one, a double-layer perforated one, and a single-layer non-perforated one for reference. Each layer is a 2.9 time radially pre-stretched VHB4910 tape, with a pre-stretched membrane thickness of 125.0 μm. The Young's modulus of these radially pre-stretched membranes averages at 1.14 MPa (curve fitted to Equation (8.1), comparable to supplier's data). The parameters affecting the acoustic behavior of the fabricated MPDEAs are shown below.

Table 8-1. Design parameters for the MPDEAs.

Sample	Pre-stretch ratio λ	Initial hole's diameter $2a$ (μm)	Thickness t (μm)	Perforation ratio δ (%)
One-layer MPDEA	2.90	315	125.0	0.309
Two-layer MPDEA	2.90	308	2×125.0	0.296

The parameters used for theoretical modeling of the two-layer MPDEA are $T(V = 0kV) = 57.69N/m$ and $T(V = 5kV) = 49.29N/m$ (Measured, refer to Figure A-8 for the measurement setup used), $\mu = 1.846 \times 10^{-5} kg/(m \cdot s)$, $R_0 = 0.0505m$ $c_0 = 346m/s$ $\rho_0 = 1.184kg/m^3$, $\rho_m = 0.1904kg/m^2$ (surface density) and $\eta = 0.02$. The cavity depth $H = 0.08m$ is chosen so that it can fit inside a window frame of ~0.1m thickness.

Non-contact measurement techniques were used to observe the actuation of MPDEA: (1) optical microscope or camera to measure the hole diameter and (2) a confocal image profiler (sensofar PLμ 2300) to measure the membrane topography. A tensile tester (Instron) and a custom-made radial stretcher with elastic torsional joints were used to measure the membrane tension as a ratio of the total radial forces to the circumferential cross-sectional area (see Figure A-8). Setup of the acoustic impedance tube [218, 219] with normally incident sound waves were used to characterize the MPDEA absorber's acoustic performance (see Figure A-9). It has a loudspeaker installed as the sound source at one end of a 770mm long and 100mm diameter tube, while the MPDEA absorber was

installed at the other end of the tube. Two electret array microphones (PCB Piezotronics, model 130E20), i.e., "Mic" 1 and "Mic" 2 spaced for a 30mm distance, were used to measure the sound pressure in the tube (see Figure A-11 and Figure A-12). A high voltage (HV) amplifier/supply (Trek 10/40A) was used to activate the MPDEA absorber. Meanwhile, data (NI PCI-6251) were used to acquire the measured signals and send the control signals to the measurement instruments (see Figure A-7). The absorption coefficient α of a 20mm thick-rigid-acrylic circular plate was measured to calibrate this acoustic measurement system (see Figure A-10).

8.4 Results and Discussion

Voltage activation of the MPDEA reduces its membrane tension and thus reduces the hole size (see Figure 8-4). For example, the membrane tension in two-layer MPDEA reduces from 215kPa at 0kV to 195kPa at 5 kV. This 5kV voltage activation reduces the hole diameter from 307.6μm to 263μm, a 14.5% reduction. In comparison, a single-layer MPDEA shows a limited electrical tunability due to higher susceptibility to air breakdown near the exposed high voltage electrode (see Figure 8-5).

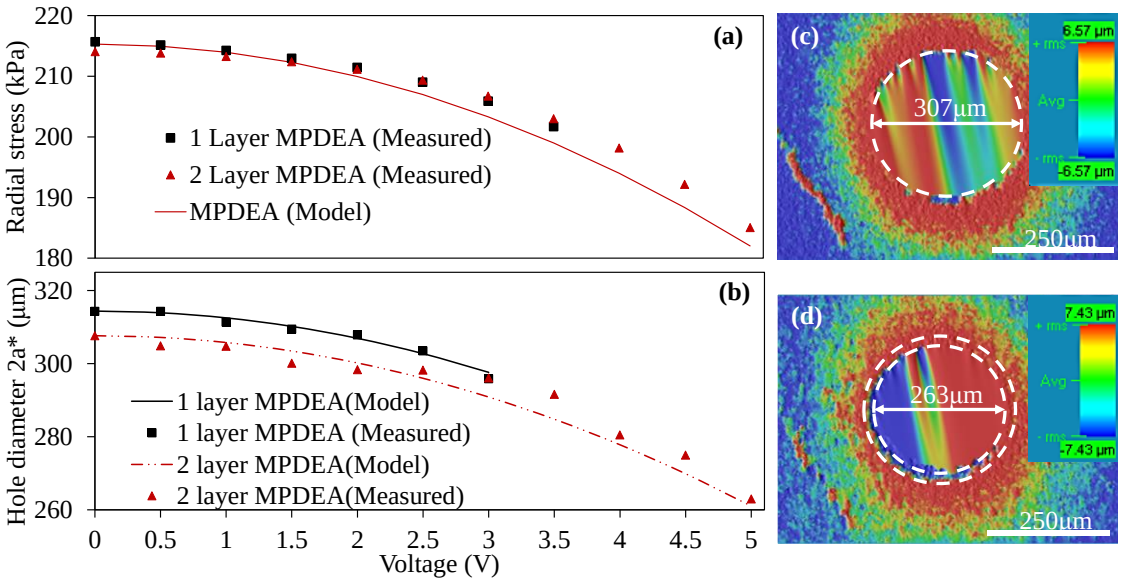

Figure 8-4. Changes in the membrane stress and micro-perforation size by voltage activation of the MPDEAs with single and double layers: (a) change in membrane stress

(Model data is obtained using Equation (7.7)); (b) change in perforation's diameter (Model data is obtained using Equation (8.1); (c) and (d) are confocal micrographs of a hole of the two-layer MPDEA at 0 kV or 5 kV respectively.

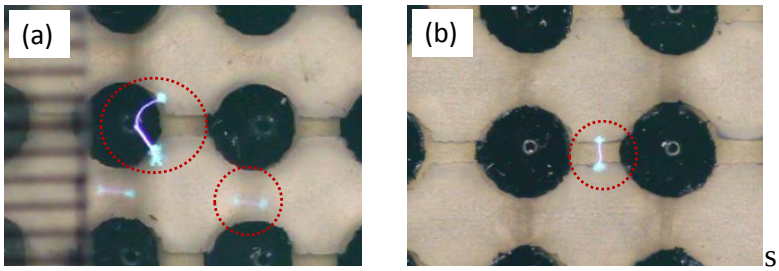

Figure 8-5. Air breakdown at high voltage on a one-layer MPDEA causing sparking (highlighted with red-dotted circles): (a) between the electrode at the opposite sides of the membrane through the perforation hole; (b) between the two electrodes of the same side which were split due to the limitation of the Teflon stencils used for electrode patterning.

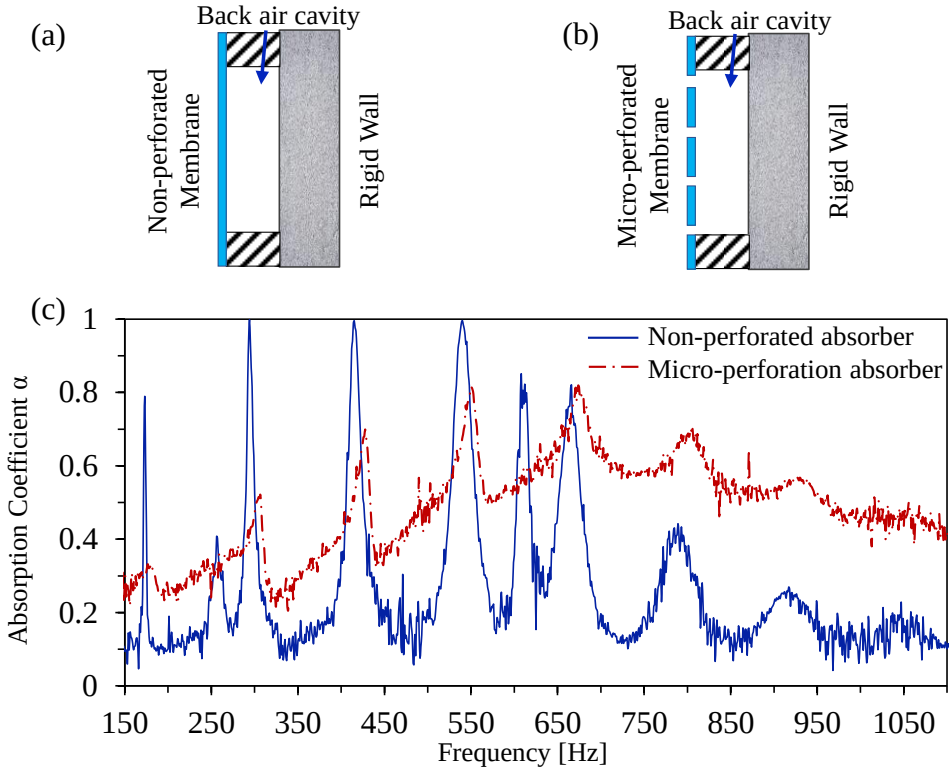

Figure 8-6. Demonstration of inclusion of micro-perforations in a resonating membrane type acoustic absorber: Schematic of (a) cavity backed membrane type acoustic absorber;

(b) cavity backed micro-perforated membrane type acoustic absorber; (c) comparison of their acoustic absorption spectrum.

Figure 8-6 shows the spectrums of sound absorption for DE acoustic absorbers with and without perforations. Perforations in the DE membrane absorber greatly broaden the absorption band at the expense of peak absorption coefficient value, as compared to the non-perforated one. Increasing the number of MPDEA layers helps raise the absorption coefficient as compared to a single layered MPDEA because deeper holes in the thicker membrane increase the amount of damping to resonating air plug. Figure 8-7 shows that the two-layer MPDEA has a 560 Hz bandwidth to absorb the low-to-medium frequency sound (300 to 900 Hz) for more than 50% ($a > 0.5$). The major peak of sound absorption is as much as 90% at around 500 Hz, while minor absorption peaks happen to correspond to those of nonperforated MPDEA given the same back cavity.

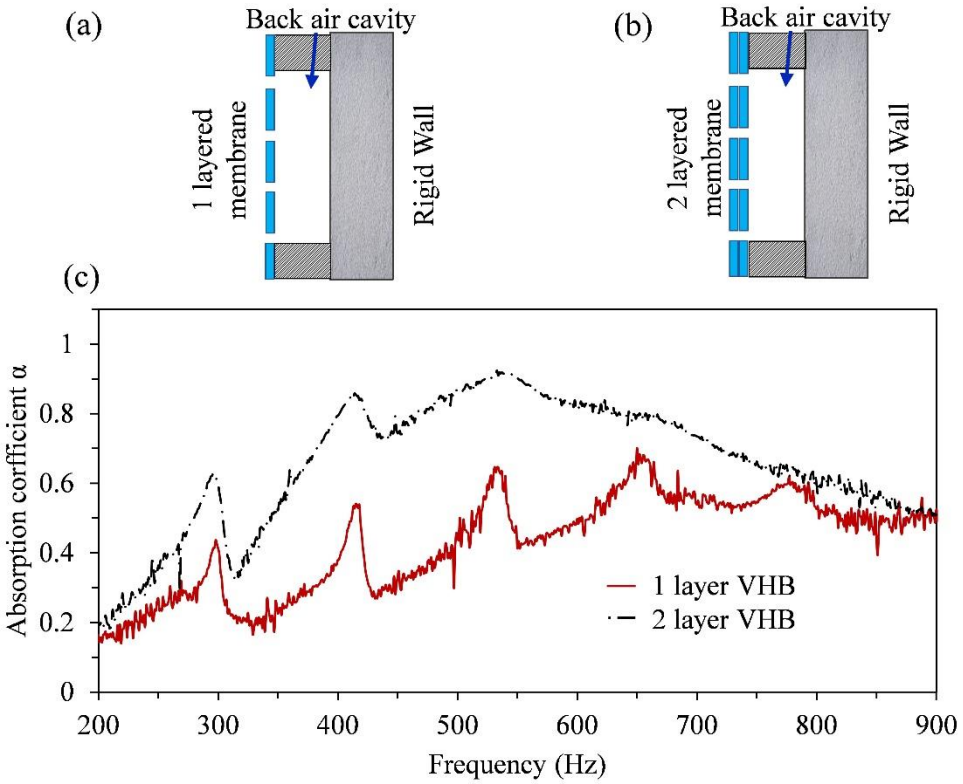

Figure 8-7. Demonstration of the effect of micro-perforated membrane thickness on the acoustic absorption: Schematic of cavity backed absorbers with (a) 1-layered (thinner)

micro-perforated membrane; (b) 2-layered (thicker) micro-perforated membrane; (c) comparison of their acoustic absorption spectrum.

Figure 8-8 shows the effect of electrical tuning on the double-layer MPDEA's absorption spectrum. At zero voltage, its peak absorption frequency is 538.5 Hz, while the lower bound of the absorption band ($\alpha > 0.5$) is 345.3 Hz. At the 5kV activation, its peak absorption is shifted lower by 13.1% (to 467.8 Hz), while the lower bound of the absorption band is lowered by 11.2% (to 306.4 Hz). Our theoretical model also predicts such acoustic characteristics and the electrical tuning of the bandwidth and frequency.

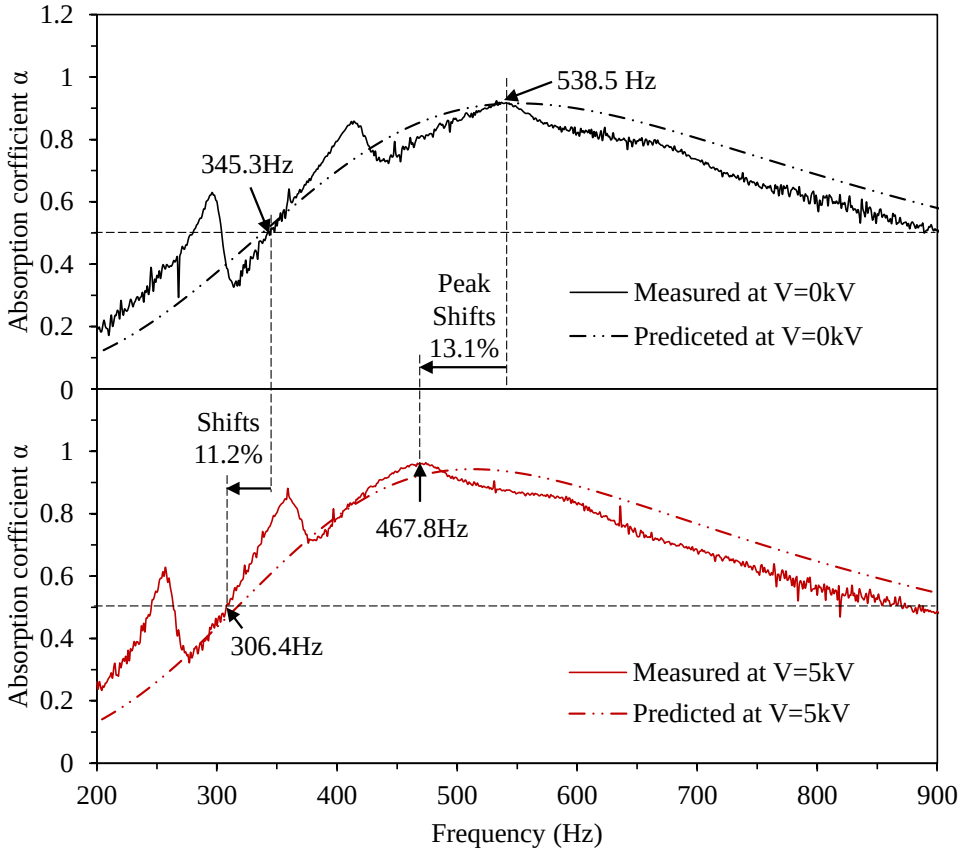

Figure 8-8. Tuning of the acoustic absorption spectrum by voltage activation of the two-layered MPDEA absorber: the passive state at 0kV and the activated state at 5kV are measured and theoretically predicted as well using Equation (8.2)-(8.7) and parameters in Table 8-1.

This MPDEA absorber shows superb performance for low-frequency sound absorption, thanks to the viscoelastic effect [225] of the DE membrane (VHB 4910) and the acoustic effect of perforations [163]. Its peak absorption and bandwidth are comparable to if not better than the dark acoustic metamaterial [226] made of silicone rubber membrane (Silastic 3133) and iron platelets. In addition, this MPDEA with electrically tunable resonances of air can be readily scaled up to make a large-area acoustic absorber.

In the future, such MPDEA can be loaded with point masses to make an electrically tunable super-absorbing metasurface [155, 216] to absorb even lower frequency sound. Besides, VHB membranes are known to have slow viscous relaxation over time. This could cause the membrane tension to release and the acoustic characteristic of the absorber might drift. However, this issues of viscoelastic drift of membrane tension can be tackled by applying a closed-loop operation of DEAs [227].

8.5 Summary

In conclusion, this chapter presented MPDEA acoustic absorber capable of broad-band attenuation of low-to-medium frequency sound. This absorption performance is due to the viscoelastic effect of the VHB tape-based DE membrane and the acoustic effects of the micro-perforations. Electrical tuning of their membrane tension and perforation size enabled active control of the acoustic absorption spectrum. An analytical model is developed for the proposed MPDEA. The model can predict an electrically induced reduction of both the aperture's size d and the membrane tension T. When it is coupled with the electro-acoustic model of the MPDEA, it can predict corresponding change on the absorption spectrum of the system. The proposed model shows good agreement with the experimental results. Later we show transparent MPDEA absorber can be made with the use of transparent compliant electrodes.

Chapter 9 Transparent MPDEA using Ink-jet Printed PEDOT:PSS Electrodes

When large windows are closed, the indoor noise level and echo can hamper speech intelligibility. To reduce the echo, transparent sound absorbers must be installed on these large windows as well. This chapter developed a transparent tunable acoustic absorber based on a micro-perforated dielectric elastomer actuator (MPDEA) with inkjet-printed transparent polymeric electrodes. A single-layer MPDEA remains optically clear (of up to 78.64% optical transmittance) with a 349 Hz bandwidth for above 80% acoustic absorption. Its 5kV activation can shift the maximum acoustic absorption frequency from 1055 Hz to 860 Hz (an 18.5% shift) by the 9%-hole contraction. This high tunability and optical clarity of MPDEA is possible by using an inkjet-printed nanometric thin film of PEDOT:PSS as a transparent compliant electrode. Here, we design the modulus of PEDOT:PSS coating to be at least 2-times softer than the elastomer substrate, by adding a surfactant to the conductive ink for printing. Such transparent compliant electrodes are self-clearable and they will also be useful to other transparent DEA based devices.

9.1 Introduction

Glass panels are widely used in windows for shops and offices. They are optically transparent to allow daylighting, but they reverberate sound within a large indoor space. When large windows were closed, the noise level in a restaurant can increase to badly affect proper conversation among diners [1]. Curtains can be used for interior acoustic absorption, but they are usually opaque. A translucent fabric Absorber Light is recently developed by Gerriets GmbH [5] for sound absorption by using micro perforations within the fabric weave, yet it is not optically clear. Meanwhile, micro-perforated glass panels [7, 8, 153, 171, 173] were proposed to be installed to the window; their acoustic absorption spectrum is however fixed and not as broad as fabric absorber [159, 163].

Active tuning of the panel absorber can help shift the absorption spectrum to target a varying noise. Electroactive polymers [66, 123, 131, 134, 228-230] provide a silent

means of distributed actuation, being much lighter than conventional servo motors. Recently, dielectric elastomer actuators (DEAs) have been used to make for tunable acoustic absorbers [181, 218, 219]. A dielectric elastomer actuator is a soft capacitor which consists of a pre-stretched dielectric elastomer membrane sandwiched by a pair of compliant electrodes. It was used to reduce the membrane tension and thus shifts the acoustic resonant frequency of the membrane absorbers [182, 218, 219]. In addition, the same actuation principle can tune the hole size of a micro-perforated dielectric elastomer membrane and thus makes for a tunable micro-perforated acoustic absorber [143]. These tunable acoustic absorbers developed so far are opaque due to the use of carbon-based [218, 219] or gold-thin film compliant electrodes [74, 143] for dielectric elastomer actuators. For window use, a tunable absorber based on DEA requires transparent compliant electrodes.

Common electrode materials for dielectric elastomer actuator include conductive grease (such as carbon grease or silver grease) [66, 131], conductive powders (such as carbon black or graphite powder) [201], and conductive nanometric networks (such as carbon nanotubes or silver nanowires) [60, 231]. Among them, a sparse and smooth coverage of the conductive nanometric network,[231] such as carbon nanotube, is transparent on a dielectric elastomer actuator. However, this initially transparent DEA turns hazy upon activation [60, 61]. The haze happens because the surface of the dielectric elastomer roughened when it is electrostatically squeezed (or indented) by the networks of conductive nanotubes or nanowires [61]. Few electrode materials can remain transparent [124] during large-strain activation and deactivation of dielectric elastomer actuator. Only hydrogel or ionic gel (which was swollen by ionic liquids) [142] can make for always-transparent compliant electrodes. Yet, the gel is prone to dry up [232-234]. Hence, hydrogel-based compliant electrodes are not lasting [233] without liquid encapsulation [141, 234, 235].

Poly(3,4-ethylenedioxythiophene) polystyrene sulfonate (PEDOT:PSS) have been widely used as a transparent conductive coating of antistatic shielding bag [236], and a transparent polymeric conductor for all-polymer capacitors [237], transistors [238, 239]

or solar cells [240]. Nanometric film of PEDOT:PSS also makes a stretchable electrode on a hyperelastic substrate of elastomer membrane [68, 129]. Conductivity of PEDOT:PSS film is higher than that required by compliant electrodes for dielectric elastomer actuators. Yet, the stretched film of PEDOT:PSS is prone to plastic yielding beyond 2% strain [139]. When being stretched uniaxially beyond 30% strain [129], a PEDOT:PSS film is prone to crack and lose conductivity.

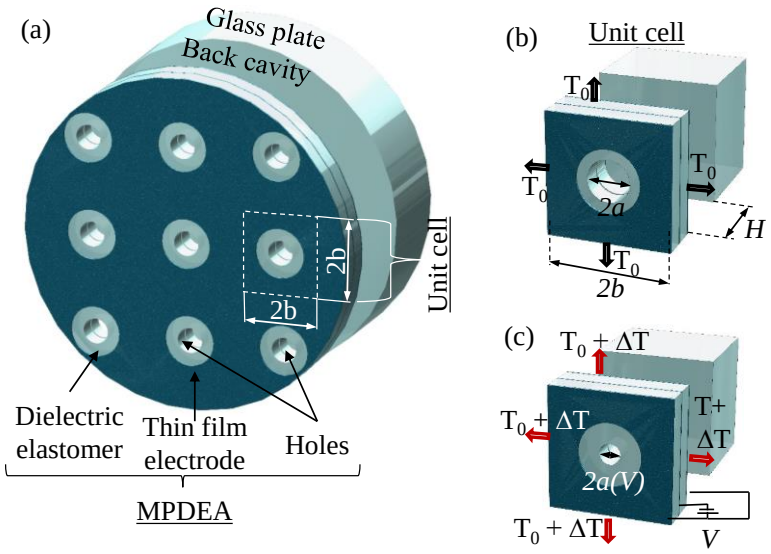

Figure 9-1. Transparent tunable acoustic absorber based on micro-perforated dielectric elastomer actuator (MPDEA): (a) schematic showing the device components; (b)-(c) a unit cell at inactivated and activated states.

Being moderately stretchable, nanometric films of PEDOT:PSS are good enough as compliant electrodes for moderate-strain actuation of dielectric elastomer. Previously, pristine PEDOT:PSS was not applied as compliant electrodes because its modulus of 2GPa [129, 139] is 2-order higher than that of acrylate dielectric elastomer, i.e. 0.2-0.5MPa modulus [135, 225]. This suggests that even a submicron thin film of PEDOT:PSS is axially stiffer than a hundred-micron membrane of acrylate elastomer (e.g. VHB4910). Furthermore, the aqueous ink of pristine PEDOT:PSS does not spread well on the slightly hydrophobic surface of acrylate dielectric elastomer. Recently, Yoon et al. [241] reported the addition of surfactant Triton-x100 improving the wettability of

aqueous suspension of PEDOT:PSS on a polydimethylsiloxane elastomer substrate while acting as a plasticizer to soften the obtained solid film of PEDOT:PSS. Motivated by this recent finding, the feasibility, and formulation of PEDOT:PSS for making compliant electrodes of dielectric elastomer actuators are re-examined.

This chapter developed a transparent tunable acoustic absorber (see Figure 9-1) based on a micro-perforated dielectric elastomer actuator with inkjet-printed transparent polymer electrodes. The inkjet printing parameters to form a uniform PEDOT:PSS thin films in various pattern on acrylate dielectric elastomer is optimized. Such inkjet-printed transparent polymeric thin films can make compliant electrodes for driving a dielectric elastomer actuator for up to 20.6% strain. A micro-perforated dielectric elastomer actuator (MPDEA) with the inkjet-printed compliant electrode can tune the acoustic absorption spectrum while transmitting light. Such transparent acoustic absorber is suitable for use to the glass window.

9.2 Methods and Materials

Figure 9-1 shows a transparent tunable acoustic absorber consisting of a micro-perforated dielectric elastomer actuator (MPDEA), a rigid ring frame, and a back-cavity plate, all in a circular outer profile. Back cavity of this acoustic absorber is 40mm deep which is within the space for installation to window glass. The MPDEA consists of a micro-perforated membrane of dielectric elastomer sandwiched by a pair of transparent polymeric compliant electrodes. Stacking of multiple MPDEAs can increase the total membrane thickness and thus increases the hole depth for a broader acoustic absorption effect [143]. Here, a single-layer MPDEA and a double-layer MPDEA is prepared for performance comparison. In addition, a standard circular DEA is prepared for stretchability test. Presented below are the design and analysis of devices, device fabrication, inkjet printing of conductive ink, and experimental setup for measurement.

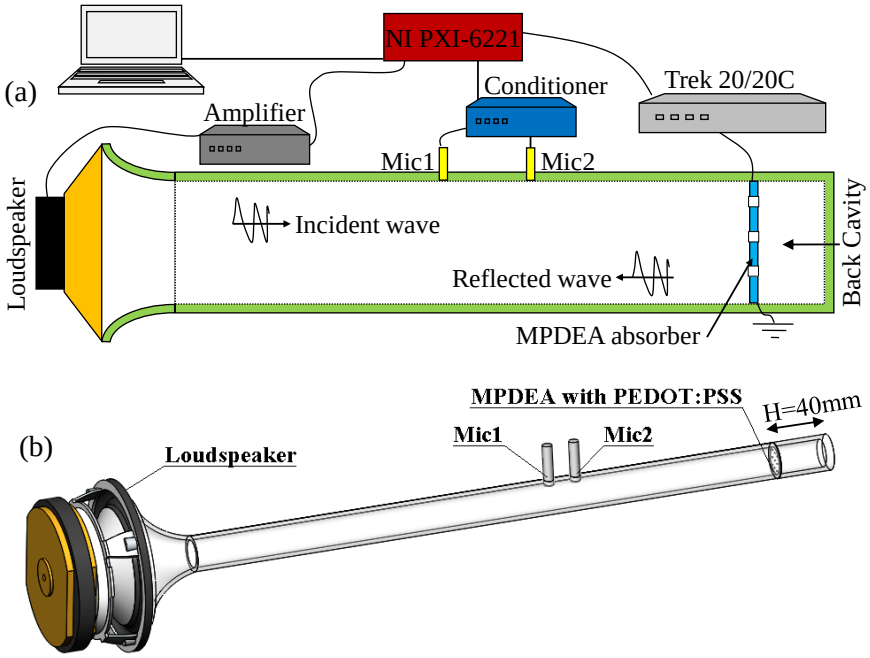

Figure 9-2. Measurement setup with an acoustic impedance tube.

Dielectric Elastomer Actuator. Application of high voltage V across the dielectric membrane of thickness t_s induces a compressive electrostatic pressure $P_e = \epsilon_r \epsilon_o (V/t_s)^2$, where ϵ_r is the dielectric constant and ϵ_o is the permittivity of vacuum [139, 142]. This activation reduces the bi-axial pre-stress T_0 in the membrane by $\Delta T(V)$ such that the remaining tension becomes

$$T = T_0 - \Delta T(V) = T_0 - \frac{\nu}{1-\nu} P_e, \qquad \textbf{(9.1)}$$

where ν is the Poisson's ratio of dielectric elastomer membrane according to Ref.[242] on the assumption of small elastic strain.

Micro-perforation or puncturing a hole can locally release the pre-tension in a membrane, which was not perforated. This leads to enlargement of initial puncture size (more than that initially drilled by laser). Activation of the annular dielectric elastomer that surrounds the passive hole can reduce the hole radius by $\Delta a(V)$ (refer Section 7.3 for details of the derivation):

$$\Delta a(V) = \frac{\nu}{1-\nu}\frac{P_e}{E}\left[b + \frac{a^2}{b} - 2a - \nu\left(b - \frac{a^2}{b}\right)\right] \quad \textbf{(9.2)}$$

where b is the half pitch between holes (see Figure 9-1).

Helmholtz Resonator Design. As a quick estimate, a micro-perforated membrane acoustic absorber can be represented by unit cells of Helmholtz resonators [158, 159, 163]. A Helmholtz resonator is a container of air with a neck-like open hole. When disturbed by sound, the air in the container or the open hole can vibrate and bounces at a fixed resonant frequency (like a spring-mass system does) to dissipate acoustic energy into heat. According to Ref. [158], this resonant frequency of air vibration is determined from the formula

$$f = \frac{c}{2\pi}\sqrt{\frac{A}{SL}}, \quad \textbf{(9.3)}$$

where c is the sound speed, A and L are the cross-sectional area and length of the neck-like open hole, and S is the volume space of the air container. Here, the hole size, i.e. $A = A(V) = \pi a^2(V)$ and $L = L(V)$ are electrically tunable by a dielectric elastomer actuator. For exact expression for the acoustic resonance and absorption of a micro-perforated panel absorber, please refer to the analysis of acoustic impedance as presented in Section 8.2 [61, 124].

Device Fabrication. Figure 9-3 shows the fabrication steps for making an MPDEA. First, an adhesive tape of acrylate dielectric elastomer (VHB 4910) was pre-stretched radially 3 times to have a 125.0μm membrane thickness as measured by a micrometer. The measured membrane thickness is thicker than the calculated thickness of 1000μm/(3x3) because the membrane free edges relax and are stretched lesser from the stretcher's 9 contact points. Later the pre-stretched membrane was transferred and adhesively bonded to a rigid ring frame of a 20.5mm internal diameter and a 28mm external diameter. The pre-stretched elastomer membrane was left 24 hours to relax and let the viscoelastic creep settle to a steady state of deformation.

Second, the aqueous conductive ink of PEDOT:PSS suspension was inkjet printed on the substrate of pre-stretched membrane. Printing twice and subsequent drying yield a pair

of transparent polymeric compliant electrodes sandwiching the dielectric elastomer membrane. Figure 9-1(a) shows a circular electrode of 20mm diameter printed on a VHB substrate, except 9 uncoated minor disk areas within it. These 9 uncoated disk areas were arranged in an orthogonal array with an equal spacing of 2*b*=5mm. This membrane DEA can be stacked up readily to another to make a multi-layered membrane DEA. Finally, a laser cutting machine (Epilog Helix 24) was used to laser drill through the uncoated membrane areas to produce a micro-perforated DEA (MPDEA). The average diameter of the laser drilled holes are 2*a* = 447.5±30.78μm for 1-layer MPDEA, and 2*a* = 541.0 ± 25.39μm for 2-layer MPDEA.

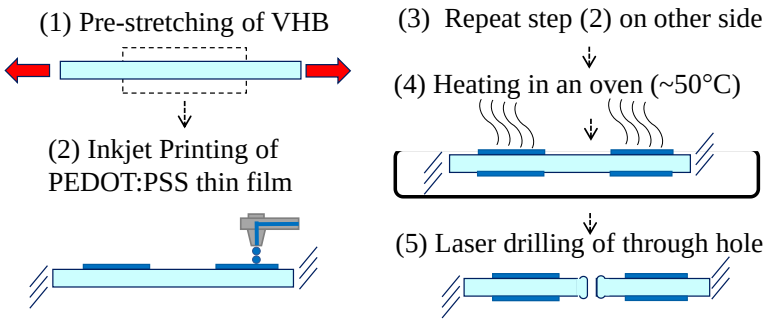

Figure 9-3. Schematic showing the fabrication steps for making a MPDEA: (1) substrate preparation by pre-stretching a VHB tape; (2) inkjet printing of PEDO:PSS thin film on the substrate; (3) inkjet printing on the other side; (4) Laser drilling to make holes through the substrate membrane.

Design of Compliant Electrodes. The electrodes for driving a dielectric elastomer needs to be compliant to conform to large voltage-induced deformation of dielectric elastomer substrate. The compliant electrodes must be axially softer than the elastomer substrate; otherwise, they will limit the deformation [69]. Nanometric thickness control of inkjet-printed film is difficult due to the coffee ring effect. To mitigate the impact of thickness variation, we proposed to formulate the ink recipe to yield a softer solid conductive film at submicron thickness. The modulus of plasticizer-added conductive ink is designed to be at least 2-times softer than the elastomer substrate. Consider an acrylate elastomer substrate (3M VHB 4910) with Young's modulus E_s=220kPa and membrane thickness

t_s=125μm, a conductive film of thickness t_f =0.3μm needs to have Young's modulus E_f lesser than

$$E_f = E_f \times \frac{t_s}{2t_f} = 220kPa \times \frac{125\mu m}{0.3\mu m} = 45.84MPa. \quad \textbf{(9.4)}$$

A solid film with 2% Triton-x100/98% PEDOT:PSS was reported [241] with Young's modulus of 80-92 MPa, which is twice stiffer than the required. To make a compliant electrode to the calculated axial stiffness, more than 3% Triton-x100 (as a plasticizer) must be added to the conductive ink of PEDOT:PSS while ensuring the uniformity of printed film on VHB substrate.

Inkjet Printing of Conductive Ink. Here, the conductive ink used for inkjet printing is an aqueous suspension of PEDOT:PSS. The pristine ink of PEDOT:PSS, as purchased (from Clevios P Jet HC V2 from Heraeus Deutschland GmbH & Co. KG), cannot properly wet a slightly hydrophobic surface of elastomer [68, 241]. O_2 plasma treatment does not make the substrate of acrylate dielectric elastomer more hydrophilic as it does to that of silicone dielectric elastomer [68, 129]. Hence, the ink needs to be formulated by adding a surfactant (Triton-x100)[241] to improve the wettability on an elastomeric substrate. The ink was also diluted with deionized water to yield a thinner solid coating upon drying up.

A commercial material printer (Dimatrix 2381) [243, 244] was used to inkjet print the aqueous conductive ink. The printhead (cartridge) has 16 nozzles (see Figure A-6); each nozzle can eject an ink droplet of 10pL. The material printer can eject conductive ink droplets to form an isolated dot, a line out of sequential dots with partial overlaps, or an area out of sequential lines with partial overlaps. To form a continuous film, the print drop of diameter *D* needs to be properly spaced with partial overlap. Figure 9-4 shows that a proper overlap during printing can merge wet ink droplets by reflow into a thin puddle. However, an insufficient overlap leads to a void area uncoated by the wet film; too much overlap yields a thicker puddle. Baking of the printed wet film in an oven at 50°C evaporates the water content of the ink and left a solid nanometric film on the

substrate. Transparency of the solid film of PEDOT:PSS decreases with increasing film thickness.

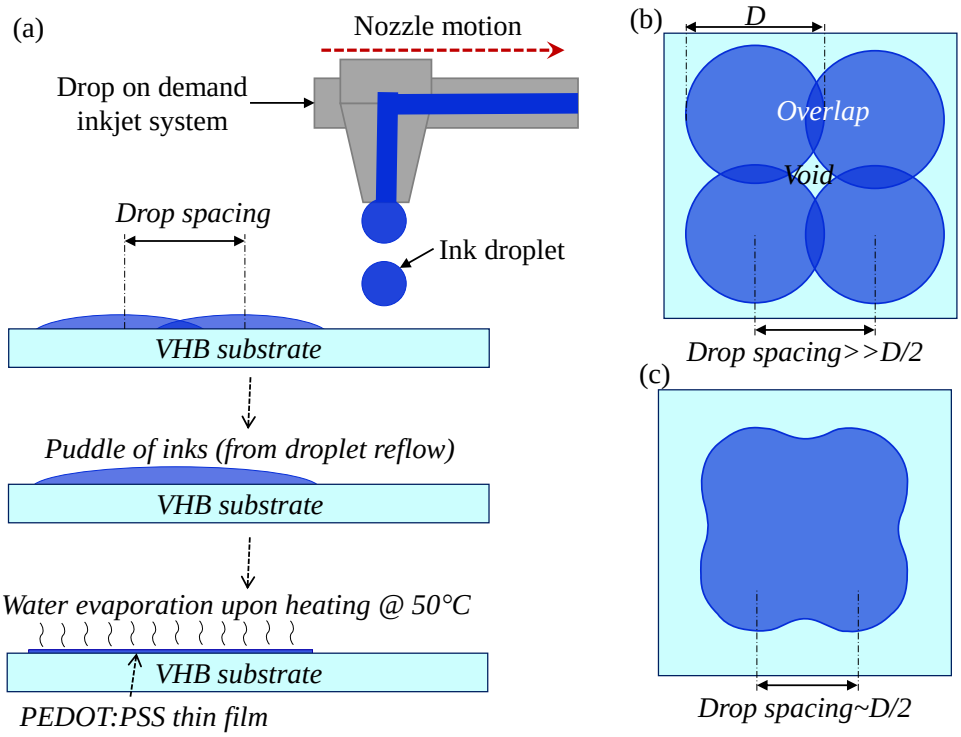

Figure 9-4. Optimization of drop spacing for printing a continuous and uniform wet film on a VHB substrate.

To save printing time, all 16 nozzles of the printhead were selected for droplet ejection. Typically, inkjet printing of a 20mm diameter PEDOT:PSS takes 15-20 minutes with all 16 nozzles selected. Continuity of a printed line/film may be disrupted when some of the nozzles incidentally clog despite automated nozzle cleaning once for every printing of 5 lines. Discontinuity in printed line can be mitigated by using a closer drop spacing. A print drop spacing is controlled by tilting the printhead relative to the print direction. According to the printer manual [243], a 10μm drop spacing is achieved by a tilt angle of 2.3 degrees; while 15μm and 20μm drop spacings can be done at the angles of 3.4 and 4.5 degrees respectively.

Experimental Setup. Figure A-7 shows a high voltage supply (Trek 610E) being used to activate dielectric elastomer actuators. A computer and a NI data logger were used to

monitor the voltage and current supplied during the device activation. Voltage monitor of the supply provides a signal voltage output, at a gain of one thousandth. Meanwhile, a multimeter (Agilent 34410A) was used to measure the current leaking through the DEAs and resistance of the electrode.

A camera was used to take the video or pictures of the device in action, i.e. voltage induced diameter expansion. A stereoscopic microscope (Olympus SZX7) was used to have a zoom-in view of the voltage induced hole contraction. Images were taken at increasing voltage steps. Image J software was used to extract the size change from the images captured.

A confocal microscope (VK-X200 Series 3D Laser Scanning Confocal Microscope) was used to measure the three-dimensional (3D) morphology of printed thin films. This topography measurement yields the information about the ink dot thickness and line width.

Figure 9-2 shows an acoustic impedance tube being used to measure the acoustic absorption spectrum of a tunable absorber at normal incidence. The 500mm long and 20mm diameter tube has a loudspeaker installed at one end and the tunable absorber mounted at the other end. Two electret array microphones (PCB piezotronic, model 130E20), which were spaced at a 20mm distance, were used to measure the sound pressure in the tube. In this setup for acoustic testing, a data logger NI PXI 6221 was used for data recording; while a high voltage amplifier (Trek model 20/20C) was used for driving a device of MPDEA.

Figure A-4 shows a spectrometer from AvaSpec (USB2 Fiber Optic) being used to measure the inline transmittance of a transparent MPDEA. A halogen light source was used to generate a collimated light through a 6mm diameter collimator lens. An optical-fiber photodetector with a collimator lens was used to detect the specular light transmitted through the device, which is located at a distance of 70mm from the collimating lens.

9.3 Results and Discussions

Figure 9-5. (a) (second column) shows that an aqueous droplet of pristine PEDOT:PSS ink does not spread well on a VHB substrate, at a 44.54° contact angle. Inkjet printing of the pristine aqueous ink cannot form a continuous wet film, but forms separated ink puddles on VHB substrate. Here, the ink in an optimized weight ratio of 40.78% PEDOT:PSS ink, 4.5% Triton-X100, and 54.72% deionized water (see Table in Figure 9-5(b)) are formulated. This optimized ink spread well (at an 11.5° contact angle) on the VHB substrate, and it can be inkjet-printed to form a continuous wet film which eventually evaporated to make a nanometric solid coating of PEDOT:PSS (see Figure 9-5(a) (third column)).

(a) Sessile drop test and print film uniformity

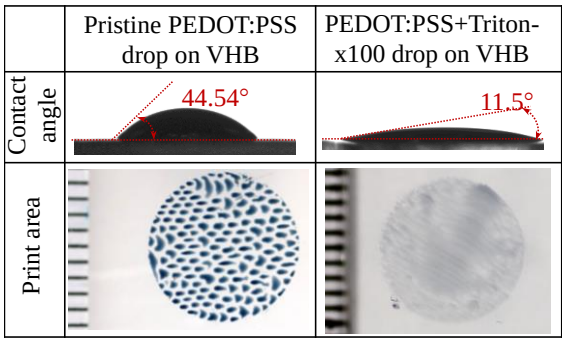

(b) Effects of aqueous conductive ink formulation

PEDOT:PSS /Triton-x /Water (wt%)	90% / 10% / 0%	61.3% / 6.8% / 31.8%	40.78% / 4.5% / 54.72%	26.75% / 3% / 70.25%
Resistance (kΩ)	1.15	2.37	4.44	5.54
Film uniformity (on VHB)	Yes	Yes	Yes	Yes
Transmittance @550nm (%)	83.9	89.2	89.4	91.0

Figure 9-5. Formulation of aqueous PEDOT:PSS ink for improved wettability and formation of uniform and clear film on VHB substrate: (a) wettability of ink droplet and uniformity of wet film printed (at 10μm drop spacing) on VHB substrate; (b) effect of ink formulation on electrical resistance, uniform film formation, and optical transmittance (at 10μm print drop spacing).

Figure 9-6 shows a printed dot of PEDOT:PSS ink with D=38.10µm diameter and 0.27µm thick on the VHB substrate. Figure 9-7 shows a continuous line can be formed by printing at the following drop spacing: 10µm, 15µm, 20µm. A closer print drop yields a thicker and wider line, but too much ink droplets may reflow to distort the straightness of line edges. Figure 9-8 shows a printed film obtained by printing multiple lines with overlaps. A closer drop spacing, for example, 10μm or 15μm, is required to obtain a

continuous film by allowing the reflow between a freshly printed wet drop and a previously printed wet line that could have dried up a bit. A thicker film obtained by printing at a closer drop spacing is electrically more conductive but optically less clear (see Figure 9-8(c-d)).

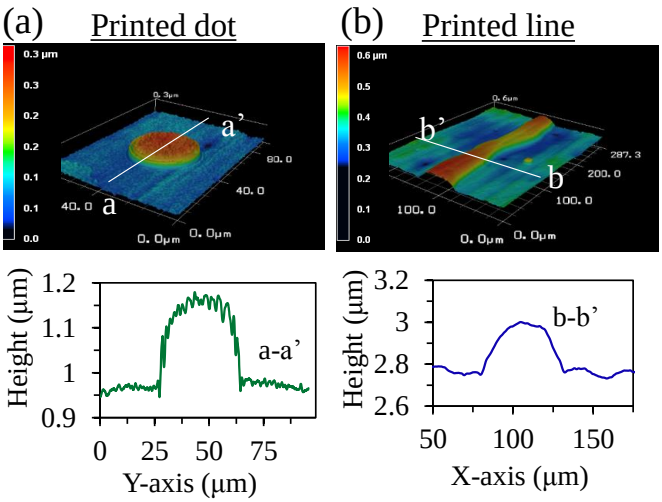

Figure 9-6. Topography and height measurement for (a) a dot and (b) a line (printed at 10μm drop spacing).

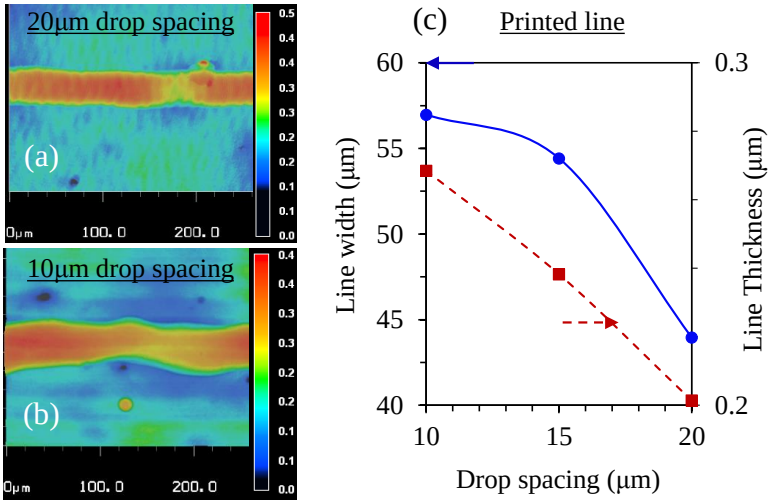

Figure 9-7. Optimization of drop spacing for printing a line: (a)-(b) contour plot showing the topography of a printed line at the drop spacing of 20μm and 10μm respectively; (c) effect on the line width and thickness.

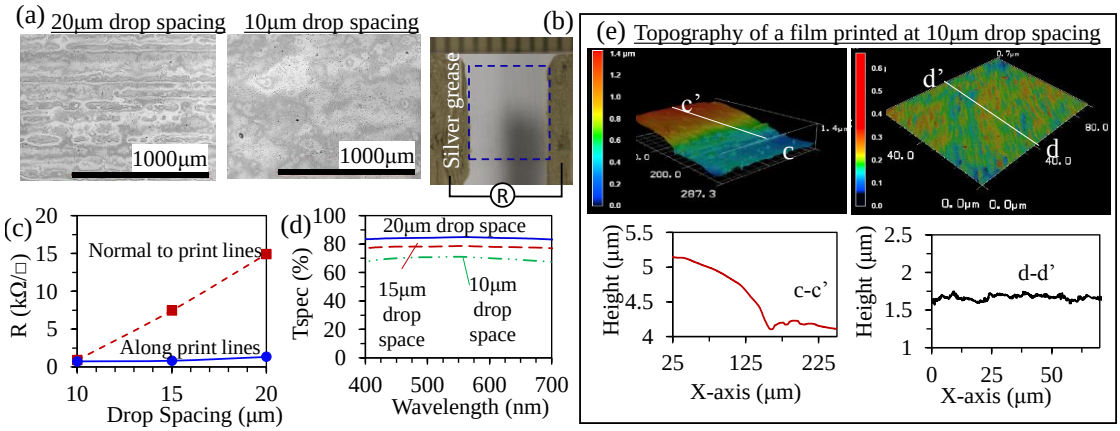

Figure 9-8. Inkjet-printed films of PEDOT:PSS on VHB substrate: (a) top-view micrographs showing the effect of print drop spacing; (b) a photograph showing a setup for resistance measurement; (c)-(d) Effect of drop spacing on electrical sheet resistance and specular optical transmission (Tspec) (f) topography and height measurement of a film of PEDOT:PSS printed at 10μm drop spacing.

Figure 9-8(e) shows a patch of the printed film which was measured with thicker edges due to the coffee ring effect [245] that happens during the drying of an ink puddle. The measured sheet resistance of a film printed at 20μm drop spacing is less than 14.92kΩ/□ measured normal to the print direction and less than 1.34kΩ/□ measured along the print direction. This suggests a poorer electrical contact at the interface between the print lines. After all, these films of printed PEDOT:PSS are conductive enough to make for compliant electrodes of DEAs.

Stretchability of the inkjet-printed PEDOT:PSS thin film can be tested on a standard dielectric elastomer actuator. This dielectric elastomer actuator device consists of a pre-stretched dielectric elastomer membrane (a VHB4910 tape with 3-times radial pre-stretches) sandwiched by a pair of circular PEDOT:PSS electrodes. Two types of inkjet-printed PEDOT:PSS compliant electrodes are tested, namely a thicker film as obtained by printing at 15μm drop spacing, and a thinner film as obtained by printing at 20μm drop spacing. A thicker film of inkjet-printed PEDOT:PSS is axially stiffer than a thinner film.

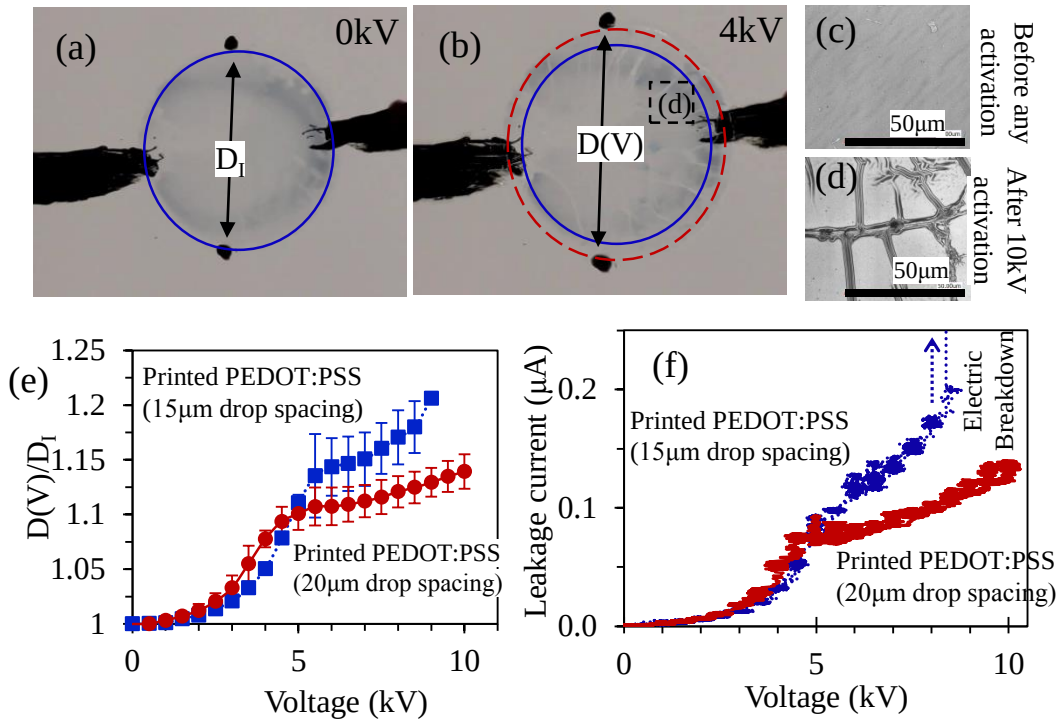

Figure 9-9. Effect of print drop spacing on dielectric elastomer activation (DEA) and electrode stretchability: (a) photographs showing deactivation and activation of a DEA with PEDOT:PSS electrodes printed at the 15μm drop spacing ; (b) Surface topography transition from smooth (prior activation) to micro-ridged (upon release from 10kV activation) (c) voltage-induced areal expansion ; (d) Leakage current across the dielectric elastomer upon activation by a step-wise voltage ramp.

Figure 9-9 shows the voltage induced electrode areal expansion of an activated dielectric elastomer actuator. It is found that the thicker PEDOT:PSS electrodes expand slightly lesser than the thinner electrodes at a lower voltage range at which the voltage-induced actuation rises in a quadratic trend. Beyond the limit of quadratic rise, further actuation tapers with increasing voltage. In comparison, the thicker PEDOT:PSS compliant electrodes undergo a higher actuation, for the quadratic limit and ultimate voltage-induced expansion of D(V)/DI=1.21 at 9kV, as compared to the thinner electrodes that expand ultimately for D(V)/DI=1.14. This difference can be explained by the fact that a thicker film of inkjet-printed PEDOT:PSS can elongate plastically more by necking longer [129]. Figure 9-9(d) shows that such plastic deformation results in the formation

of micro-ridges after the release from 10kV activation. The ultimate breakdown is marked by a crack in PEDOT:PSS thin-film electrodes and puncture through the membrane. This is accompanied by a current surge as shown in Figure 9-9(f).

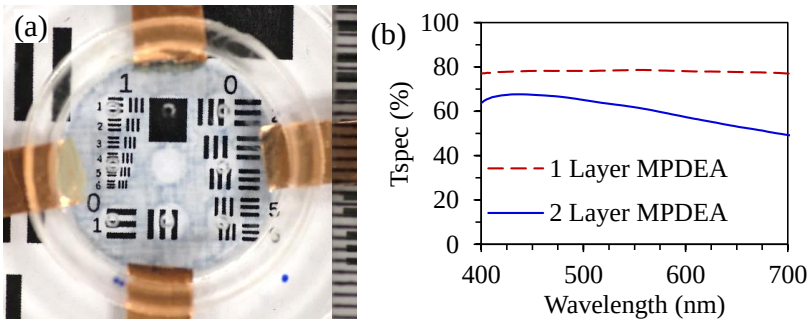

Figure 9-10. Optical clarity of micro-perforated dielectric elastomer actuators (with PEDOT:PSS electrodes printed at the 15m drop spacing): (a) a photograph of a 2-layer MPDEA which is placed in front of a black-and-white printed USAF target; (b) effect of the number of layer on specular optical transmittance T_{spec}.

In view of higher stretchability, the thicker PEDOT:PSS films (as obtained from 15μm drop-space printing) were adopted as the compliant electrodes for the tunable devices of the transparent acoustic absorber. Figure 9-10 shows that MPDEAs with inkjet-printed PEDOT:PSS electrodes are slightly bluish. While a single-layer MPDEA is optically clear with close to 78.64% optical transmittance, a two-layer MPDEAs with doubling the number of electrodes is less clear (of 61.8% transmittance for 550nm wavelength). The alternate color tone, between dark and light blues, suggests thickness variation in the printed film.

Figure 9-11 shows electrical activation of MPDEAs reducing the perforation hole from an inactivated diameter $2a_o$ to a smaller activated diameter *2a(V).* Two-layer MPDEA can sustain a higher driving voltage up to 5.5kV and thus reduces the hole diameter (from 541.04±25.36μm to 459.53±20.40μm) by close to 15%. As the electric field for activation of this MPDEA is relatively low (of up to 44MV/m nominal field), the power consumed is kept less than 1.14mW (or 3.62W/m^2). On the other hand, the single-layer MPDEA can only be driven up to 4kV for 10% hole reduce due to the premature electrical breakdown of the air across the shallower holes between opposite electrodes.

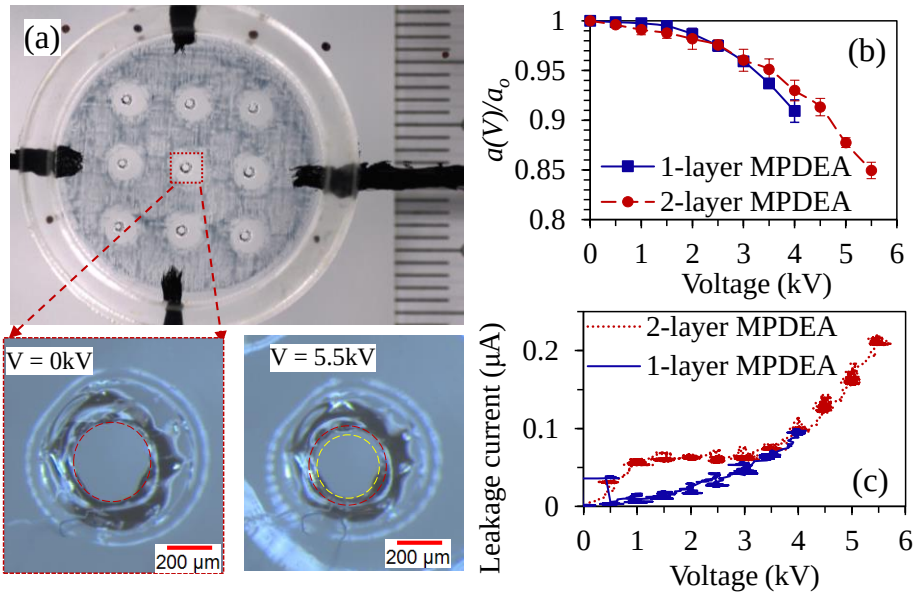

Figure 9-11. High-voltage activation of MPDEAs for reducing the hole size: (a) a photograph of a 2-layer MPDEA prototype and micrographs showing the hole contraction upon activation; (b) A stepwise voltage ramp for activating an MPDEA and the current leak across it; (c) the voltage induced contraction of the through holes in an MPDEA

The device is self-clearable and can survive a pre-mature breakdown upon voltage removal. As a result, it can sustain a higher driving voltage up to 5kV for next cycle of actuation (as shown in the acoustic testing of the same device). This self-healing of the device happens because the PEDOT:PSS electrodes surrounding the holes are self-cleared to be further apart from the opposite electrodes. This is similar to those observed from other self-clearable compliant electrodes [60, 74, 246].

Figure 9-12 shows the absorption spectrum of MPDEA-based tunable acoustic absorbers. A two-layer MPDEA with deeper holes show a broader bandwidth in the absorption spectrum as compared to a single-layer MPDEA. In the inactivated state, the bandwidth for above acoustic absorption coefficient 0.8 is 444 Hz (from 836 Hz to 1290 Hz) for the two-layer MPDEA, but 349 Hz (from 831 Hz to 1180 Hz) for the single-layer MPDEA. For the two-layer MPDEA, the peak absorption frequency happens to be 1170 Hz upon inactivation (0kV) but shifted by 15.2% to 992 Hz upon 6kV activation. For the

single-layer MPDEA, the peak absorption happens at 1055 Hz upon inactivation (0kV) but shifted by 18.5% to 860 Hz upon 5.0kV activation.

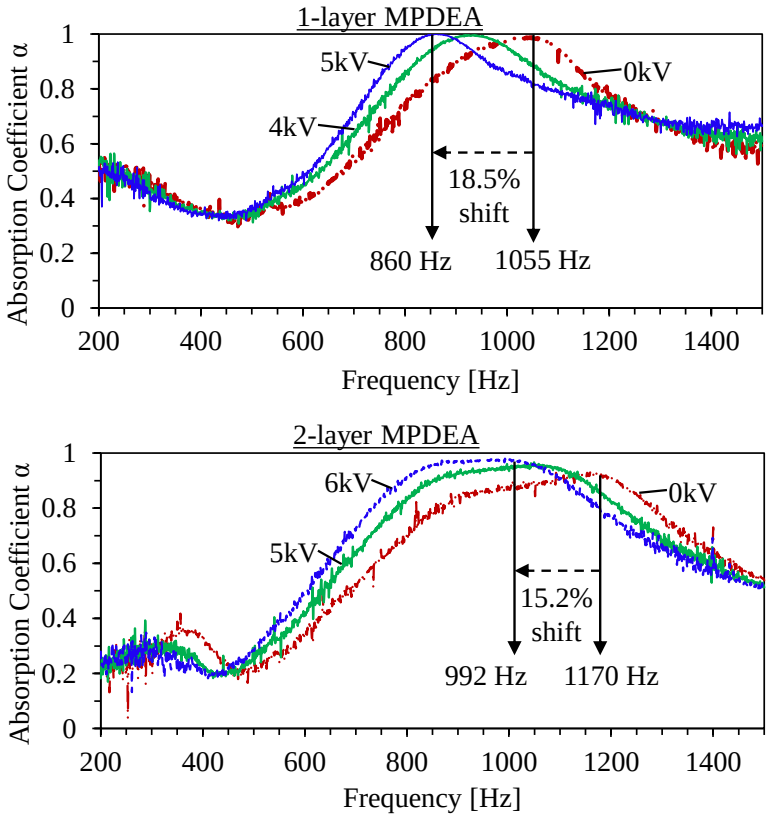

Figure 9-12. Acoustic absorption spectrum of MPDEAs: (a) tunable spectrums for a 1-layer MPDEA; (b) tunable spectrums for a 2-layer MPDEA.

In comparison, the previous MPDEA developed shown in Chapter 7 using microwrinkled gold thin-film compliant electrodes was opaque [143] while having a larger perforated membrane of 100mm diameter. It can only be operated up to a maximum voltage of 5kV (less than 40MV/m nominal field) and reduce the hole size by 14.5%. This larger and opaque tunable acoustic absorber shows a more complex absorption spectrum. It was better for low-frequency sound absorption, with a peak amplitude of 0.85 happening at 538.5 Hz. The peak absorption frequency of the previously MPDEA can be shifted lower by 13.1% upon the maximum voltage-induced hole contraction.

9.4 Summary

This chapter developed a transparent tunable acoustic absorber suitable for window use. This device based on micro-perforated dielectric elastomer actuator can absorb mid-frequency sound while being optically clear (up to 78.64% light transmission). Such tunable acoustic absorbers can be arranged in an array for large-area mounting to window glass. Advances of such transparent tunable acoustic absorbers are anticipated to bring good quality acoustics and natural lighting to the indoor space. This high tunability and optical clarity of MPDEA is possible by material design and inkjet printing of an aqueous suspension of surfactant-added PEDOT:PSS. Such transparent compliant electrodes are self-clearable, and they will also be useful to other tunable optics [141, 200] based on dielectric elastomer actuators.

Chapter 10 Conclusion and Future Works

10.1 Conclusion

Glass has been used widely in urban buildings as the window panel, roof, and indoor partitions to admit natural light and isolate sound. As a complement to the glass window, curtains are used to control privacy (visibility) and improve the indoor acoustic ambiance. Opaque curtains can block the sunlight while translucent curtain diffusively admits light. Switch between opacity and clarity is done by drawing and closing the curtains. Commercial smart windows can replace glass and curtains to provide controllable privacy as desired, but they cannot absorb sound. The quiet glass that absorbs sound is in need; it will be even better if it can be tuned to maximize the sound absorption at the dominant frequency of the noise which can vary with time. Here, we proposed and developed a solution for tunable optical and acoustic window based on dielectric elastomer actuators and transparent wrinklable compliant electrodes.

A membrane with tunable transparency is not new. In principle, they are tunable optical surface scatters which turns transparent with smooth surfaces like a flat glass; but it turns 'opaque' (translucent) with the micro-rough surface. The surface roughness is varied by means of surface micro-wrinkling or unfolding. But, to effectively diffuse light, they needed large compressive strain to induce surface wrinkles and large stretch to reduce the surface wrinkles. This operation is more like a curtain's which is not suitable for a window glass of fixed size. Small strain induced microwrinkling and unfolding is wished to make smart glasses. For the first time, this work showed microwrinkling of nanometric films of optical oxides such as ZnO and TiO_2 of high refractive index being effective to diffuse light down to 1-2% inline transmittance (very frosted) upon less than 5% axial compressive strain. Interestingly, these oxide thin films can sustain thousands of cyclic microwrinkling and unfolding. A conductive overcoat on the oxide film made of conductive polymer or metal provides electrical conductivity. Such multilayer thin film can make microwrinkled compliant electrode suitable for activating DEA and thus generates voltage induced unfolding. Moreover, this device also showed prominent

improvements in terms of power consumption. The TiO_2 layer helped to significantly reduce the power consumption of the transparent DEAs by reducing the leakage current (consumes merely ~0.831W/m^2).

Glass does not absorb sound but reflects it. The only way to make a glass sound trap is by making glass resonant cavities like Helmholtz resonators. A microperforated glass with an air cavity backed by a glass plate can make such resonant acoustic absorbers. This transparent acoustic absorber can have an absorption coefficient >90%, but they have fixed resonant frequency and bandwidth. The need for tuning the resonant frequency to match the noise dominant frequency can only be addressed using our microperforated DEA. We first devised a mechanism of tuning hole-diameter by activation of an MPDEA. Also, we developed an elastic model to predict the voltage-induced hole-diameter change. These MPDEA can shrink hole size by applying Maxwell stress that reduces the membrane's tension. Unlike other actuators such as electric motor or mechanical switches, MPDEA provides a distributed and quiet actuation. Moreover, we show our multilayer MPDEA can suppress the air breakdown under high voltage and also improve the acoustic dampening effect.

Previously, PEDOT:PSS was used as a flexible electrode on a plastic sheet and a slightly stretchable electrode on an elastomer membrane. However, it has not been used as a compliant electrode for DEAs because its modulus of 1-2GPa is two to three orders higher than the VHB membrane's. This work first showed a submicron thickness of PEDOT:PSS which is compliant enough to produce a moderate dielectric elastomer deformation (<15%). Also, we formulated an aqueous ink of PEDOT:PSS which can be inkjet-printed on a hydrophobic dielectric elastomer substrate to make transparent compliant electrodes for transparent MPDEA absorber. Such novel smart windows can be made as cheap as glass due to its simple all-solid-state construction. They can be used in green smart buildings and could potentially enhance the urban livability.

10.2 Suggestions for Future Works

This work presented smart tunable devices for windows. Yet, there are a few areas where it requires improvements. They are pointed out as follows:

- The major challenge of the presented smart window is their limited lifetime. The VHB elastomer under stress can creep and tear over time. In addition, they can degrade over prolonged exposure to sunlight. 3M VHB has been guaranteed to last for more than 10 years. But, based on window standards, we desire a lifetime of 20 to 25 years [247]. This presents a need to replace the VHB based dielectric elastomer with another weatherproof elastomer material that can survive tear and long-term exposure to UV and moisture change.
- The presented devices have been lab tested for over a thousand cycle and for six months. But, for commercialization of these devices, proper field tests and validation of their performance and lifetime in the actual environment over a longer duration needs to be done.
- The response speed of the presented device is in few seconds to a minute range. This slow response is mainly because of the viscoelastic nature of the VHB material. Therefore, we can further investigate the use of less viscous elastomer like PDMS, natural rubber and so on as a substrate for the faster DEAs.
- Despite consuming low power, these devices are still activated with a high voltage (i.e. 2.85kV). The high voltage requirement can be lowered by thinning down the dielectric membrane and further reducing their actuation strain. Use of softer elastomer with a higher dielectric constant can lead to larger actuation strain at a lower voltage. Hence, various elastomer materials can also be investigated for activation-voltage reduction.
- The tunable acoustic absorber developed under this study needs a large back air-cavity (40-70mm) for effective sound absorption. This additional space requirement limits its use in small spaces, like vehicles windows. Meta-surface backed resonant absorber has been reported to reduce the back-cavity depth requirements [155]. A similar 3D printed meta-surface base can be used along

with the tunable MPDEA absorber to reduce the thickness of the air cavity needed for efficient acoustic noise absorption.

- Current tunable MPDEA absorber is working in the low-to-medium frequency range. It remains a challenge for it to absorb bass noise of low-frequency. Recently, resonant absorbers whose membranes are loaded with point masses have shown lowered resonant frequency by an increase in the membrane effective mass density [248, 249]. We can further investigate into similar decorated tunable acoustic absorbers for low-frequency applications.

Appendix

Appendix A. Comparison with Existing Smart Window

The metrics that affect the user adoption of a smart window include the following: 1) transmittance change, 2) response time, 3) power consumption, and finally 4) device cost. According to recent reviews by Baetens et al. [14] and Granqvist et al. [11], the smart window based on liquid crystals or electrochromic is still expensive, with the device cost more than US dollar \$200/m^2. Their clear state is not very clear (less than 65%) and thus this limits daylighting when required.

In comparison, our tunable window device can be tuned for high opacity (1% in-line transmittance) and high transparency (81% in-line transmittance). Furthermore, Table A-2 lists the material cost to make our window device, not more than US\$16/m2. The sale price is estimated to be \$65.6/m^2.

Table A-1. Performance comparison of our smart window with commercial devices.

Smart window [Ref]	**Substrate**	**T_{spec} @550nm**	**Response time**	**Power**	**Sale price on 2016 (brand)**
Electrochromic (WO3 and NiO) [11, 14]	Glass	5%-65%	300sec (5x20 cm^2)	0.1-0.5 Whr/sq.m	\$1000/sq.m (View glass)
Polymer dispersed liquid crystal [14]	Polymer composite	6%-62%	500 ms	5-20 W/sq.m	\$396/sq.m (sonte) \$100-300 (Alibaba)
Suspended Particle Device [14]	Glass	2.4%- 59%	100-200 ms	1.9-16 W/sq.m	-
This work	**VHB 4905**	**1%-81%**	**<60sec**	**0.831 W/sq.m**	**~\$65.6/sq.m**

Table A-2. Cost estimate for this tunable window device based on PEDOT:PSS/TiO_2.

Estimate for product cost and sale price		
Material cost	**Price for sq.m**	**[Ref]**

VHB4905	23in x 72-yard x 0.5mm at $3283	$3283/(40.13m^2)/(3x3) = $9.46 /sq.m	[250]
TiO_2 pellet	$155/kg	$155/kg×2×1m^2×19.8nm×4230kg/m^3 =$0.026/sq.m	[251]
PEDOT:PSS	$163/250gm (1wt % resin in suspension)	$163/0.25kg/1%×2x1m^2×38.7nm×1000kg/m^3 =$5.05/sq.m	[252]
Sub-Total of material costs		$14.546/sq.m	
Estimate of Process Cost		×3 the material costs	
Saving from bulk purchase and batch production		25%	
Total manufacturing cost		$14.546/sq.m × 4 × 0.75 = $43.64/m^2	
Sale price (50% profit margin)		$43.64/m^2 × 1.5=$65.567/m^2	

Appendix B. Scattering of Light by an Optically Rough Surface

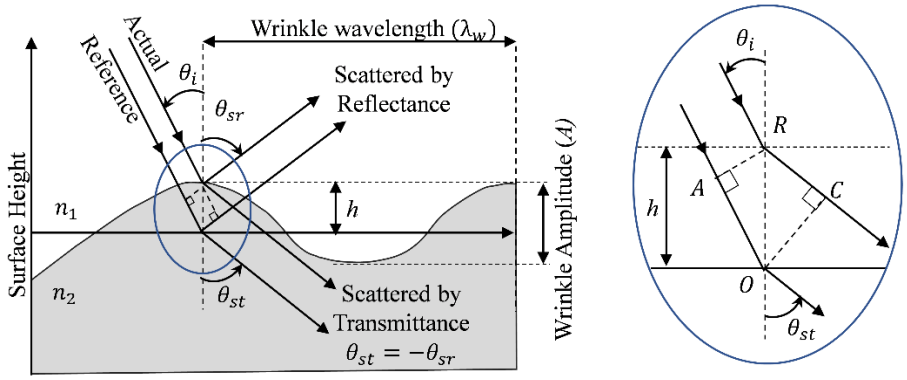

Figure A-1. Schematic of a magnified cross-sectional view of a roughened surface and an incident beam showing how it generates an optical path difference between different transmitting rays of the incident beam (adapted from [46]).

Scattering of the light by an optically rough surface can be described based on diffraction. In Figure 2-17, parallel monochromatic rays form a single beam is an incident on a rough surface at an angle θ_i. These rays are partially scattered backward at an angle θ_{sr} and most of it is diffracted forward at an angle -θ_{st}. We are concerned with forward scattering only; hence, forward scattering angle will be noted as θ_s. To conceptualize, let's assume two rays. The actual ray is transmitted from surface deviated at height (h) and the reference

ray is transmitted from the surface-mean. The actual ray travels a shorter distance compared to reference ray. The overall optical path difference can be computed by the difference of the travel length of these two rays.

The optical path difference (*OPD*) between two rays is given by

$$OPD = -(n_1 AO - n_2 RC) = -h(n_1 \cos\theta_i - n_2 \cos\theta_s) \qquad \textbf{(A.1)}$$

Here n_1 and n_2 are refractive indices of the medium where incident and the transmitting rays lies. The surface has a random roughness which leads to random *OPD*. This *OPD* leads to the random phase difference ($\varphi(\hat{x}, \hat{y})$),

$$\varphi(x, y) = \left(\frac{2\pi}{\lambda}\right) OPD = -\frac{2\pi}{\lambda}(n_1 \cos\ \theta_i - n_2 \cos\ \theta_s)\ h(x, y) \qquad \textbf{(A.2)}$$

Here *x, y,* and *h* are spatial coordinates and deviated surface heights, and λ is the wavelength of the monochromatic light. This phase difference between the two rays cause them to interfere and diffract. In large scale at the far-field, this random diffraction is observed as a scattering of the light.

Adapting the diffraction principle, the scattering of scalar waves by a randomly rough surface was theoretically treated by Beckman and Spizzichino [47, 48]. With paraxial approximations, the scalar theory in its simplest form can predict the specular transmission from a rough surface. Meanwhile, with information on the autocorrelation function of the rough surface, the scalar theory can evaluate the angular dependence of light scattering [253-255]. Linear systems formulation of surface scatter theory based on scalar diffraction analysis has been developed for non-paraxial cases as well [45, 46, 255]. However, evaluating the angular dependence of the light scattering from multiple rough surfaces using scalar theories are complicated. Meanwhile, transparency of film has a stronger dependence on specular transmission. Hence, our study is more focused on the specular component of the total transmission through the rough surface.

Beckman and Spizzichino's [47, 48] formulations for optical scattering by rough surface are based on Helmholtz-Kirchhoff diffraction integral. It is limited to the surface whose rms roughness (σ) is smaller compared to its autocorrelation length (*S*). It also assumes

the scattering is observed at the far-field in the Fraunhofer zone of the rough surface. Based on this formulation, provided a Gaussian surface, the specular (non-diffuse) part T_{spec} of the total transmittance through the device is obtained as [47, 49, 50]:

$$T_{spec} = T.\exp\left\{-\left[\frac{2\pi\sigma}{\lambda}(n_1\cos\ \theta_i - n_2\cos\ \theta_s)\right]^2\right\} \quad \textbf{(A.3)}$$

Here total transmittance T is obtained from the Fresnel Equation. In case of multi-layer material like our tunable optical diffuser, the refractive index of the transmitting medium n_2 is not the same as the substrate index. It is an effective refractive index, which is a weighted spatial average of multilayer materials and is also influenced by the surface profile [256]. If the coating layers are too thin, then the effective refractive index will be closer to the substrate's refractive index.

The optical diffuser reported in this thesis consists of two voltage-dependent rough surfaces at two sides of the substrate. Although uncorrelated, these rough surfaces have approximately the same roughness and spatial distribution. For the case of scattering from two uncorrelated rough surfaces in sequence, provided normal incidence, the inline transmittance is given by:

$$T_{spec} = T^2.\exp\left\{-2\left[\frac{2\pi\sigma(V)}{\lambda}(n_1 - n_2)\right]^2\right\} \quad \textbf{(A.4)}$$

where $\sigma(V)$ is the voltage dependent rms roughness of the wrinkled surface.

Beckman and Spizzichino's formulation can approximate the diffuse transmitted scattered light $D(\theta_i, \theta_s)$ without knowing the autocorrelation function of the surface. This approximation uses correlation length (S) and applies to small scattering angle which is deviated less than $\varepsilon = \lambda/2S\cos\theta_i$ from the specular direction. It is given by [49]:

$$D(\theta_i, \theta_s) \propto \left(\frac{n_2\cos\ \theta_s}{n_1\cos\ \theta_i}\right)\left(\frac{S}{L}\right)D_o \quad \textbf{(A.5)}$$

where D_o is the diffuse transmittance given by $D_o \cong T.\left[\frac{2\pi\sigma}{\lambda}(n_1 \cos\ \theta_i - n_2 \cos\ \theta_s)\right]^2$. $2L$ is the one-dimensional length of the rough surface. It can be evaluated from half angular extent ε_s of the beam transmitted by a smooth surface given approximately by $\varepsilon_s \cong \lambda/2L \cos\theta_i$.

Appendix C. Calculation of the Inline Transmittance (Tspec)

Consider two identical interfaces for a tunable optical diffuser device. The interfaces are between the air (n_1=1) and dielectric elastomer (n_2=1.47 for VHB 4905) on the device's top and bottom surfaces. The TiO_2 nanometric thin film helps to increase the effective refractive index to be 1.6 based on the experimental correlation. For normal incidence by a 550nm wavelength beam of light, the simulated in-line transmittance is worked out as below.

For a smooth surface of 0.036μm rms roughness:

$$T_{spec} = \left(\frac{4\times1\times1.6}{(1+1.6)^2}\right) e^{-2\left\{2\pi(1-1.6)\frac{0.036\mu m}{0.55\mu m}\right\}^2} = 0.838$$

For a rough surface of 0.525μm rms roughness:

$$T_{spec} = \left(\frac{4\times1\times1.6}{(1+1.6)^2}\right) e^{-2\left\{2\pi(1-1.6)\frac{0.525\mu m}{0.55\mu m}\right\}^2} \approx 0$$

Appendix D. Tunable Diffuser with PEDOT:PSS Coating

In the absence of TiO_2 meta-surface, a conductive-polymer coated dielectric elastomer actuator does not make a good tunable optical diffuser. To confirm this, we prepared a device with only overcoats of PEDOT:PSS. An aqueous suspension of the conductive ink does not wet and spread well on the non-treated surface of the elastomer substrate (VHB 4905). To improve the latter's wettability on the elastomer substrate, 1 weight% of surfactant Triton-x100 was added to the aqueous conductive ink. Spin coating of the mixture at 1000 rpm for 1-minute results in an even spread of aqueous ink droplet and subsequent a uniform coating of treated PEDOT:PSS on the elastomeric surface. After drying of water, we obtained a ~45.5nm thick solid coating of conductive polymer on

the substrate of acrylate elastomer. The surfactant residual acts as a plasticizer that reduces the effective modulus and electrical conductivity.

This softened coating of conductive polymer barely wrinkles under the same radial compression as applied to the coating with TiO_2 interface. For example, the surface remains smooth (at 200nm rms roughness) when the overcoats being subjected to 4% radial compression (i.e. D_{II}/D_I = 0.96). This smooth surface does not scatter light much. Hence, the device remains clear and does not conceal the logo behind it. To properly conceal the logo, the device requires a much larger compression (e.g. 33% to induce rougher surfaces to the conductive-polymer overcoats). This large actuation requirement, however, does not allow enough areal coverage to a window.

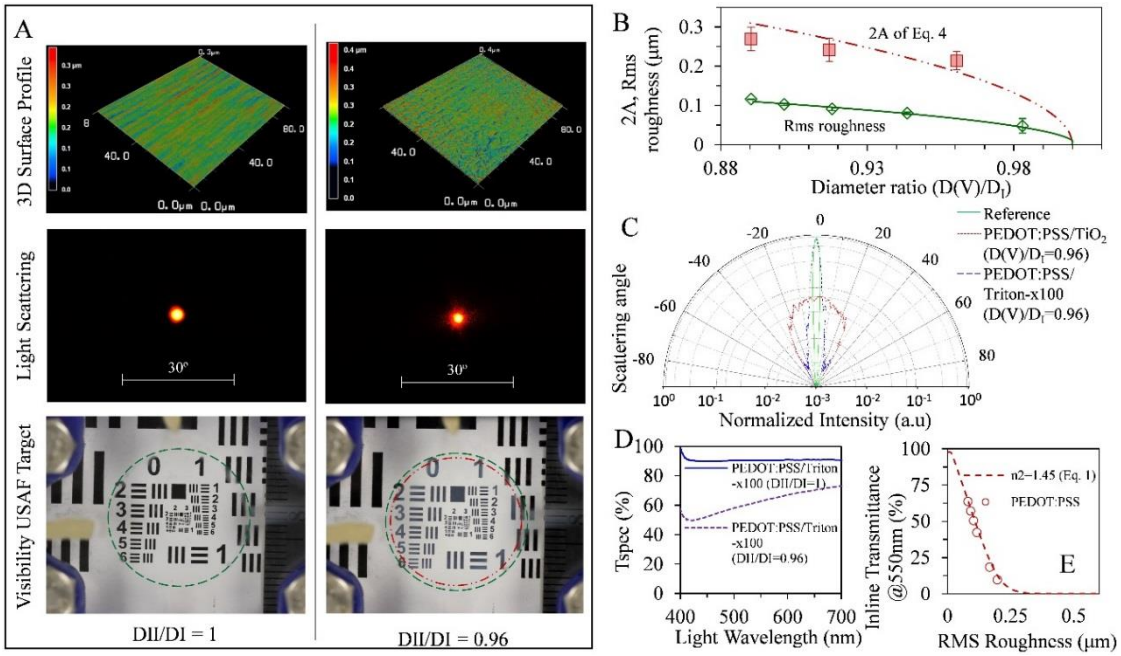

Figure A-2. Microwrinkling of PEDOT:PSS nanometric thin films for tunable window: (a) effect of small radial compression (4% radial strain) on surface morphology (top row), light scattering (middle row) and visibility (bottom row) through the device; dependence of (b) surface roughness light scattering on radial compression; (c) difference between scattering angle of different surface wrinkling under the same radial compression; change of transmittance spectra (d) and in-line transmittance (e) with respect to radial compression.

Appendix E. Measurement Setup for Transparency Tuning Device

Electro-mechanical activation. A high voltage power supply (TREK 610E) was used to electrically activate a dielectric elastomer device. It can generate a step voltage output for steady-state activation, or a square pulse for cyclic activation. By default, a manual knob is used to control steady voltage output from the supply. For pulse generation, this high-voltage supply needs to be triggered by a low-voltage pulse, for example, a 4V square pulse from a function generator (Agilent 33120A). The supply's voltage and current are logged continuously during the activation. Here, the data logging is done by using a computer installed with a National Instrument data logger and the LABVIEW software. Voltage monitor of the supply provides a signal voltage output, at a gain of one thousandth. Meanwhile, a multimeter (Agilent 34410A) was used to measure the current charging the capacitive device.

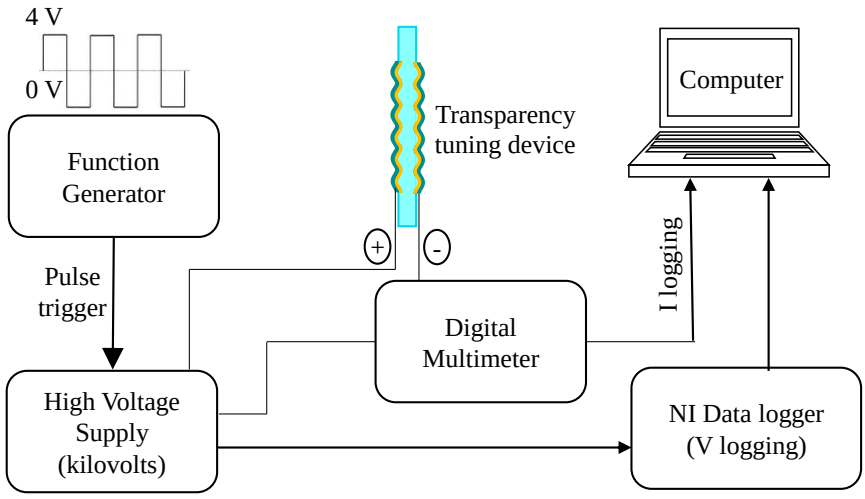

Figure A-3. Experimental setup for electromechanical activation.

A digital single-lens reflex (DSLR) camera (Canon 550D) was used to take pictures or a video of dielectric elastomer actuation. The dynamic or cyclic response of the dielectric elastomer actuator is obtained by software tracking (Tracker) of the electrode's diametral change. To improve the point tracking from the video, two ink dots were marked on the edge of the transparent/translucent compliant electrode to define the electrode diameter.

A. Inline transmittance

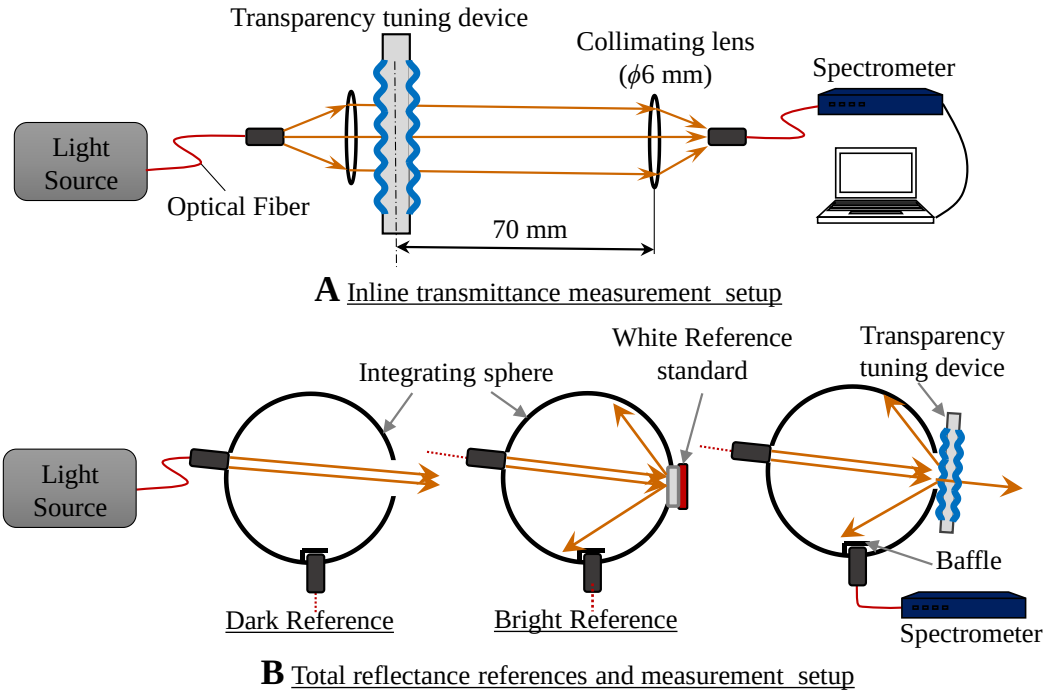

Figure A-4. Setup to measure: A. in-line transmission; B. Total reflectance through a diffuser device.

A spectrometer from AvaSpec (USB2 Fiber Optic) was used to measure the inline transmittance through a tunable optical diffuser. A halogen light source was used to generate a collimated light through a 6mm-diameter collimator lens. An optical-fiber photodetector with a collimator lens was used to detect the in-line light transmission through the device. It is located at a distance of 70mm from the device and aligned normally to the collimated light. Forward scattering happens across the device's micro-rough surfaces. A fraction of the transmitted beam remains in-line and gets detected by the photodetector. The in-line light transmittance at a wavelength λ is calculated as:

$$T_{\perp\lambda} = \frac{I_\lambda}{I_{\lambda o}} \qquad \textbf{(A.6)}$$

where I_λ is the detected intensity of transmitted light in the presence of a diffuser and $I_{\lambda o}$ is a reference intensity of incident light (i.e. in the absence of the diffuser).

Similarly, an integrating sphere (Avasphere) and a reference white standard were used to measure the total reflectance of the tunable optical diffuser. Before the measurements, the dark reference (i.e. 0% reflectance) and bright reference (i.e. 100% reflectance) were set using the white reference standard. As shown in Figure A-4A, the collimated light strikes the diffuser sample and all the reflected light is collected by the integrating sphere. The homogenized intensity is measured by the spectrometer. The total reflectance is then obtained as $R_{\mathrm{Total},\lambda} = \frac{R_\lambda}{R_{\lambda o}}$, where R_λ is the total intensity reflected by the sample and $R_{\lambda o}$ is the total intensity reflected by the reference white standard.

B. Light Scattering

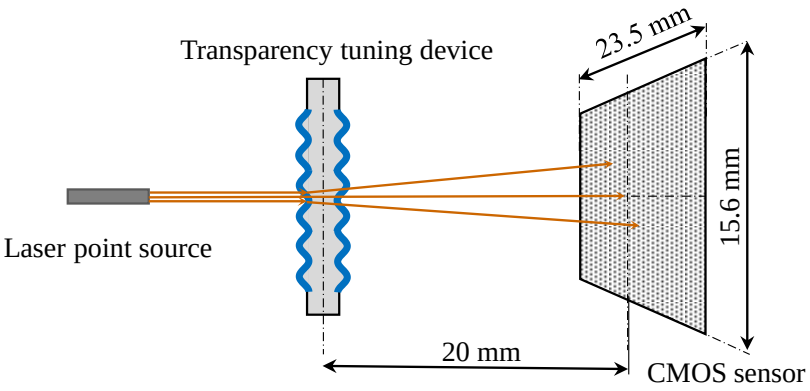

Figure A-5. Setup to measure the intensity distribution of light scattered through a tunable diffuser device.

This window device is a tunable optical diffuser, which can be characterized in terms of divergence angle and intensity profile of transmitted light. The intensity profile shows the light distribution as a function of angle; whereas, the divergence angle is measured as the width of the intensity profile at half the maximum (FWHM). Figure A-5 shows the experimental setup to measure the intensity profile on a planar image sensor placed at a 20mm distance away from the tunable diffuser. The light source is a red laser (635nm wavelength) with a 1mm-diameter aperture. The image sensor is a CMOS sensor of a digital camera (Sony α5100). Software Image J is used to extract the intensity distribution from a monochrome image of the far-field patterns of forward light scattering.

Appendix F. Dimatrix Material Cartridge and Nozzle Information

DMP 2800 allows manual adjustment of the nozzle or cartridge angle. This feature enables the user to manually set the drop spacing in the y-axis. This also allows adjustment of printing resolution or density. The drop spacing is set while feeding the printing patterns. But the nozzles are in a single row, hence, this only sets the drop-spacing along the printing direction. To set the drop spacing along normal to the print direction the cartridge is set to various angles which adjust the effective spacing of the nozzles for printing. When they are perpendicular to the printing direction they are at their maximum spacing in the y-axis of 254 microns nozzle to nozzle. When you adjust the cartridge to an angle lower than 90°, it decreases the y-axis nozzle spacing for higher resolution printing.[243]

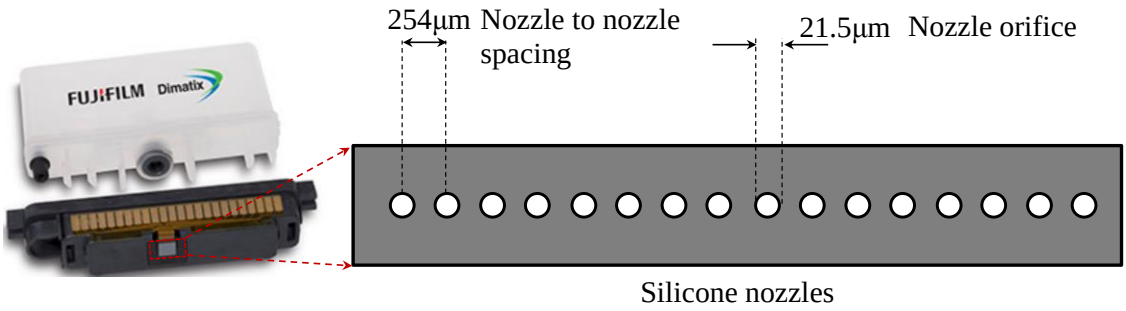

Figure A-6. Dimatrix material cartridge for 10pL droplet ejection. Nozzle arrangement size and spacing is shown in the schematic view.

Appendix G. Measurement Setup for Tunable Acoustic Absorbers

To completely characterize the acoustic performance of MPDEA and it's frequency tuning capabilities various tests were performed. They were electrically activated using the setup shown in the figure below. Meanwhile, the loss of membrane tension during activation, a corresponding change in perforation radius and corresponding acoustic absorption coefficient were measured.

Setup for Electromechanical Activation of the MPDEAs

This setup is used to supply high voltage to the MPDEAs while measuring the applied voltage and the leakage current. Digital multimeter Agilent 34410A is used to measure

the leakage current. Meanwhile, the voltage monitor of the Trek 610E high voltage power supply provides a signal voltage output at a gain of one thousandth. This signal is logged using the NI data logger. Camera or microscopes are used to observe the perforation holes during the activations.

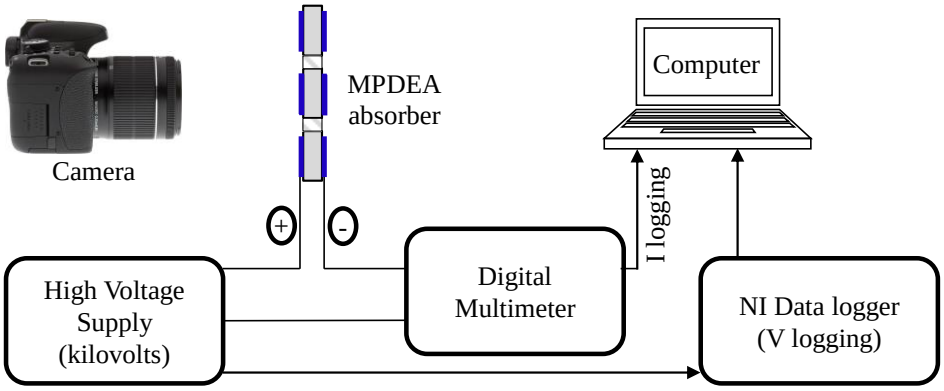

Figure A-7. Setup for electrical activation of the MPDEAs while applied voltage and leakage current are simultaneously measured.

Membrane tension measurement setup

The pre-stretched MPDEA membrane initially has a pretension. As the voltage is applied between the electrodes, induced Maxwell stress causes a loss in the membrane tension. These lose in membrane tension is one of the driving factors for a shift in the absorption spectrum. Trek 610E is used to supply a high voltage to the MPDEA. A custom-made setup consisting of a nine contact-point radial stretcher with elastic torsional joints, and a tensile tester (Instron) with a 500N load cell was used to measure any fluctuation in the membrane tension.

The MPDEA under pre-tension is attached to nine contacting points of the custom-made stretching device. They are kept under tension by two diametrically placed hinges of the stretching device, which is clamped using jaws of the tensile testing machine. Any change of the membrane tension will cause a change in pulling force between these hinges. The MPDEA is activated using TREK 610E high voltage power supply. The force *(F)* in the hinge is simultaneously measured and logged to a computer by the load cells of the tensile testing machine. It is later used to calculate the membrane tension as

a ratio of the total radial forces to the circumferential cross-sectional area as $\Delta T = (F_o - F_V)/(2\pi R_o t)$. Here F_o and F_V are the force measured by the load cells at the initial and activated states respectively, R_o and t is the radius and thickness of the MPDEA.

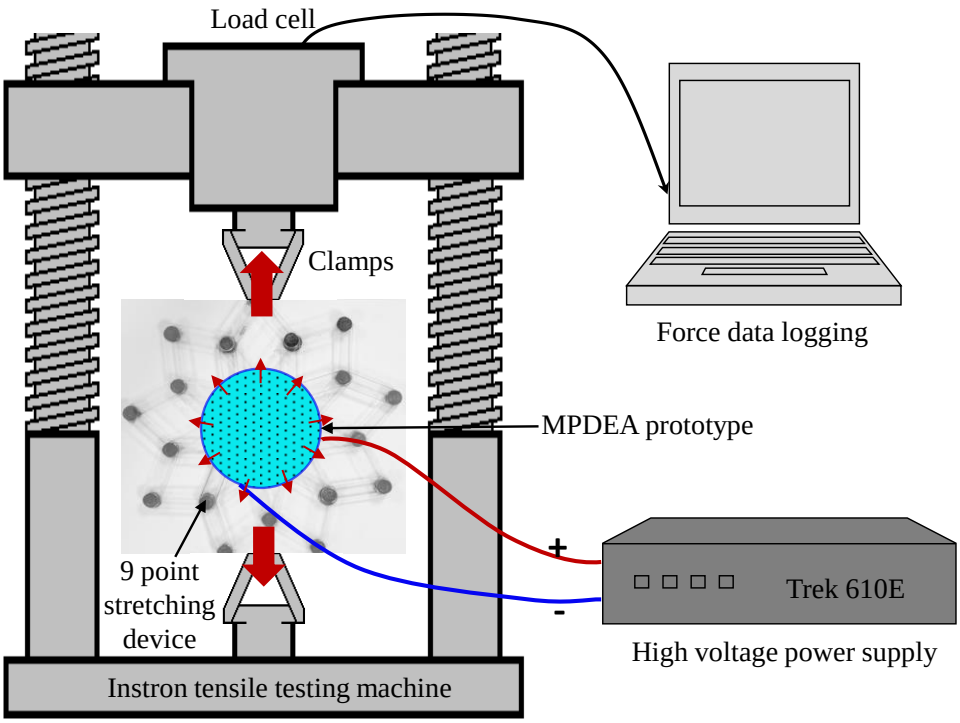

Figure A-8. Setup for the measurement of loss in membrane tension during electrical activation of the MPDEA.

Perforation size measurement

Non-contact measurement techniques were used to observe the change in perforation by actuation of MPDEA: (1) optical microscope or camera to measure the hole diameter and (2) a confocal image profiler (sensofar PLl 2300) to measure the membrane topography. The image obtained from cameras or the optical microscope was analyzed using the software Image J to measure perforation diameters.

Acoustic absorption coefficient measurement setup

The acoustic absorption performance of an absorber is evaluated by their absorption coefficient at the designed audible spectrum. The absorption coefficient is measured in

the range of 0 to 1. In this range, 0 indicates no absorption and 1 indicates full absorption of the sound of that frequency.

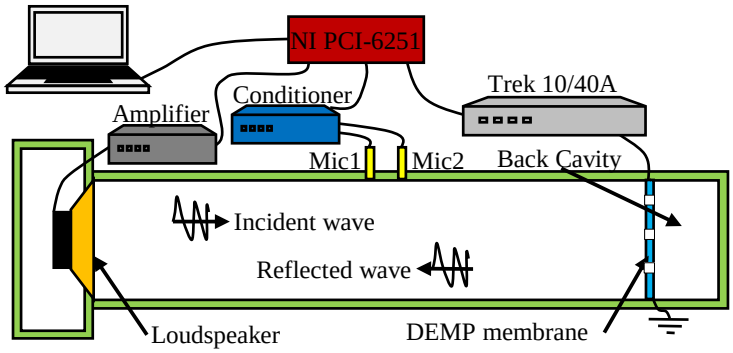

Figure A-9. The test setup for measurement of the acoustic absorption coefficient of the MPDEA backed by an air cavity.

Two microphone method was used for the measurement of the absorption coefficient of the MPDEA absorbers. Setup of the acoustic impedance tube [143, 181] with normally incident sound waves were used to characterize their acoustic performance (see Figure A-9). It has a loudspeaker installed as the sound source at one end of a 700mm long and 100mm diameter tube, while the MPDEA absorber was installed at the other end of the tube. The MPDEA consisted and extra back cavity of 70mm depth. The back of the tube is closed using rigid acrylic plates. Two electret array microphones (PCB Piezotronics, model 130E20), i.e., “Mic” 1 and “Mic” 2 spaced for a 30mm distance, were used to measure the sound pressure in the tube. The microphone measures the sound pressure levels in decibels, (p_1, p_2). These pressure levels are manipulated to evaluate the incident and reflected waves. Incident and reflected pressure waves are used to evaluate reflection coefficient and eventually the absorption coefficient is calculated at the frequency range from 120 Hz to 1400 Hz [181]. In order to address the error due to microphone mismatch, microphone switch method is used to evaluate the phase and amplitude corrections and hence pressure and phase difference are evaluated with the addition of the corresponding correction factors. A high voltage (HV) amplifier/ supply (Trek 10/40A) was used to activate the MPDEA absorber. Meanwhile, data (NI PCI-6251) were used to acquire the measured signals and send the control signals to the measurement instruments.

In the presented experiments, the sampling frequency is set to 40 kHz. The sound pressures measured by the microphones are then processed with a calculation program based on the two-microphone method [257] to calculate the absorption coefficient α. The absorption coefficient α of a 20mm thick-rigid-acrylic circular plate was measured to calibrate this acoustic measurement system. The result is shown in Figure A-10. From 120Hz to 1400Hz, the absorption coefficient α of the circular plate is close to zero which agrees to the theory for the rigid wall.

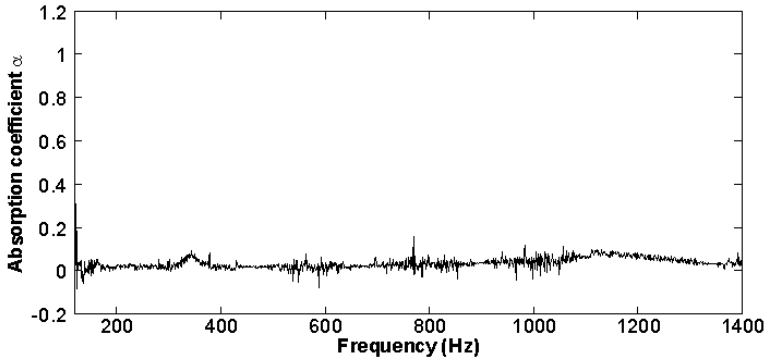

Figure A-10. The absorption coefficient α of a 20mm thick-rigid-acrylic circular plate.

Appendix H. Two-Microphone Method for Acoustic Absorption Measurement

The measurement of the absorption coefficient is done using an impedance tube [258]. This device uses the incident sound pressure and reflected sound pressure to evaluate the impedance and the absorption coefficient of the absorber. As shown in the schematic in Figure A-11, the sound pressure at the two microphones is (p_1, ϕ_1) and (p_2, ϕ_2) where p and ϕ denote the sound pressure and the phase, and the subscripts 1 and 2 denote the two microphones at two measurement positions, respectively. Note that the sound pressure is measured by decibels. The absorption coefficient is evaluated by finding the reflection coefficient. As two microphones are never exactly the same, they are switched to compensate for their differences.

The derivation of the reflection coefficient

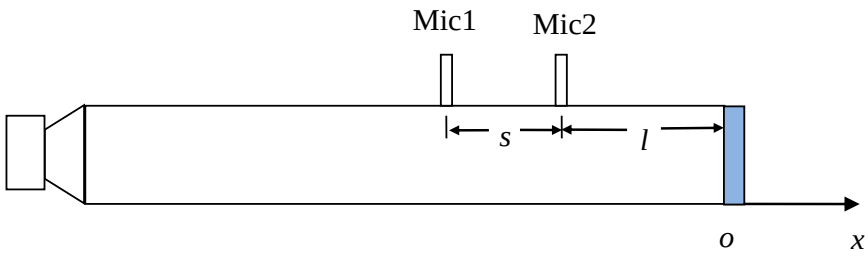

Figure A-11. The schematic of the experimental setup.

One dimensional wave equation is:

$$\hat{p}_1 = \hat{p}_i \exp(-ikx_1) + \hat{p}_r \exp(ikx_1) \quad \textbf{(A.7)}$$

$$\hat{p}_2 = \hat{p}_i \exp(-ikx_2) + \hat{p}_r \exp(ikx_2) \quad \textbf{(A.8)}$$

The reflected waves are represented as:

$$\hat{p}_1 \exp(ikx_1) = \hat{p}_i + \hat{p}_r \exp(2ikx_1) \quad \textbf{(A.9)}$$

$$\hat{p}_1 \exp(ikx_1) = \hat{p}_i + \hat{p}_r \exp(2ikx_1) \quad \textbf{(A.10)}$$

$$\hat{p}_r = \frac{\hat{p}_1 \exp(ikx_1) - \hat{p}_2 \exp(ikx_2)}{\exp(2ikx_1) - \exp(2ikx_2)} = \frac{\hat{p}_2 \exp(-ikx_2) - \hat{p}_1 \exp[ik(x_1 - 2x_2)]}{1 - \exp[2ik(x_1 - x_2)]} \quad \textbf{(A.11)}$$

The incident waves are represented as:

$$\hat{p}_1 \exp(-ikx_1) = \hat{p}_i \exp(-2ikx_1) + \hat{p}_r \quad \textbf{(A.12)}$$

$$\hat{p}_2 \exp(-ikx_2) = \hat{p}_i \exp(-2ikx_2) + \hat{p}_r \quad \textbf{(A.13)}$$

$$\hat{p}_i = \frac{\hat{p}_1 \exp(-ikx_1) - \hat{p}_2 \exp(-ikx_2)}{\exp(-2ikx_1) - \exp(-2ikx_2)} = \frac{\hat{p}_1 \exp(ikx_1) - \hat{p}_2 \exp[ik(2x_1 - x_2)]}{1 - \exp[2ik(x_1 - x_2)]} \quad \textbf{(A.14)}$$

The reflection coefficient is hence given by:

$$R = \frac{\hat{p}_r}{\hat{p}_i} = \frac{\hat{p}_2 \exp(-ikx_2) - \hat{p}_1 \exp[ik(x_1 - 2x_2)]}{\hat{p}_1 \exp(ikx_1) - \hat{p}_2 \exp[ik(2x_1 - x_2)]} = \exp[2ik(l+s)] \frac{\hat{p}_1 - \hat{p}_2 \exp(iks)}{\hat{p}_2 \exp(-iks) - \hat{p}_1} \quad \textbf{(A.15)}$$

where $x_1 = -(l+s)$ and $x_2 - x_1 = s$.

Taking $H = \hat{p}_2 / \hat{p}_1 = (p_2 / p_1)\exp[i(\phi_2 - \phi_1)]$, then

$$R = \exp[2ik(l+s)]\frac{H - \exp(-iks)}{\exp(iks) - H} \qquad \textbf{(A.16)}$$

The absorption coefficient can be calculated by using the following expression:

$$\alpha = 1 - |R|^2 \qquad \textbf{(A.17)}$$

Elimination of the microphone mismatch by switch method

The two microphones have inherent measurement errors in both amplitude and phase which are $(\delta p_{m1}, \delta\phi_{m1})$ and $(\delta p_{m2}, \delta\phi_{m2})$ where the subscripts m1 and m2 denote microphone number 1 and 2, respectively. To compensate for the mismatch, the microphones are switched, and measurements are taken again.

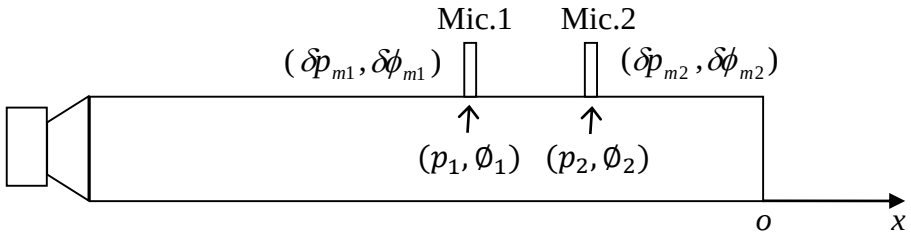

Figure A-12. The mismatch between the two microphones.

Then, the sound pressure measured by the two microphones in the standard configuration is,

$$\begin{cases} p_{m1}^{I} = p_1 + \delta p_{m1} \\ \phi_{m1}^{I} = \phi_1 + \delta\phi_{m1} \end{cases} \qquad \begin{cases} p_{m2}^{I} = p_2 + \delta p_{m2} \\ \phi_{m2}^{I} = \phi_2 + \delta\phi_{m2} \end{cases} \qquad \textbf{(A.18)}$$

And in the switch configuration,

$$\begin{cases} p_{m1}^{II} = p_2 + \delta p_{m1} \\ \phi_{m1}^{II} = \phi_2 + \delta\phi_{m1} \end{cases} \qquad \begin{cases} p_{m2}^{II} = p_1 + \delta p_{m2} \\ \phi_{m2}^{II} = \phi_1 + \delta\phi_{m2} \end{cases} \qquad \textbf{(A.19)}$$

Let $p^{I} = p_{m2}^{I} - p_{m1}^{I}$, $p^{II} = p_{m2}^{II} - p_{m1}^{II}$, $\phi^{I} = \phi_{m2}^{I} - \phi_{m1}^{I}$, $\phi^{II} = \phi_{m2}^{II} - \phi_{m1}^{II}$

Then, by combing Equations (A.18) and (A.19), we obtain the amplitude and phase corrections $p_c = \delta p_{m2} - \delta p_{m1}$ and $\phi_c = \delta\phi_{m2} - \delta\phi_{m1}$ as follows:

$$\begin{cases} p_c = \frac{1}{2}(p^I + p^{II}) \\ \phi_c = \frac{1}{2}(\phi^I + \phi^{II}) \end{cases} \quad \textbf{(A.20)}$$

And the exact results are as follows,

$$\begin{cases} p_2 - p_1 = (p^I_{m2} - p^I_{m1}) - p_c \\ \phi_2 - \phi_1 = (\phi^I_{m2} - \phi^I_{m1}) - \phi_c \end{cases} \quad \textbf{(A.21)}$$

$$\begin{cases} p_2 - p_1 = (p^{II}_{m1} - p^{II}_{m2}) + p_c \\ \phi_2 - \phi_1 = (\phi^{II}_{m1} - \phi^{II}_{m2}) + \phi_c \end{cases} \quad \textbf{(A.22)}$$

References

[1] P. Hernandez. (2014). *For restaurant owners, striking the right noise level is key*. Available: https://www.bostonglobe.com/lifestyle/food-dining/2014/04/22/what-can-hear-you/uJGdqtAwATBLlxAKDxV0wK/story.html

[2] M^{C} Squared System Design Group. Inc. (2018). *So why does reverberation affect speech intelligibility?* Available: http://www.mcsquared.com/y-reverb.htm

[3] T. Arai, K. Kinoshita, N. Hodoshima, A. Kusumoto, and T. Kitamura, "Effects of suppressing steady-state portions of speech on intelligibility in reverberant environments," *Acoustical science and technology*, vol. 23, pp. 229-232, 2002.

[4] N. Hodoshima, T. Arai, and A. Kusumoto, "Enhancing temporal dynamics of speech to improve intelligibility in reverberant environments," in *Proc. Forum Acusticum, Sevilla*, 2002.

[5] Gerriets-GmbH. (2018). *Absorber Light*. Available: https://www.gerriets.com/us/absorber-light-8172

[6] T. J. Cox and P. D'antonio, *Acoustic absorbers and diffusers: theory, design and application*: Crc Press, 2009.

[7] J. Kang, "An acoustic window system with optimum ventilation and daylighting performance," *Noise & Vibration Worldwide*, vol. 37, pp. 9-17, 2006.

[8] F. Asdrubali and G. Pispola, "Properties of transparent sound-absorbing panels for use in noise barriers," *The Journal of the Acoustical Society of America*, vol. 121, pp. 214-221, 2007.

[9] A. Struiksma, M. Tenpierik, A. Snijder, F. Veer, B. Botterman, M. Hornikx, *et al.*, "Sound absorbing glass: transparent solution for poor acoustics of monumental spaces," *SPOOL*, vol. 4, pp. 53-58, 2017.

[10] C. M. Lampert, "Chromogenic smart materials," *Materials today*, vol. 7, pp. 28-35, 2004.

[11] C. G. Granqvist, "Electrochromics for smart windows: Oxide-based thin films and devices," *Thin Solid Films*, vol. 564, pp. 1-38, 2014.

[12] J. W. Doane, N. A. Vaz, B. G. Wu, and S. Žumer, "Field controlled light scattering from nematic microdroplets," *Applied Physics Letters*, vol. 48, pp. 269-271, 1986.

[13] P. S. Drzaic, "Polymer dispersed nematic liquid crystal for large area displays and light valves," *Journal of applied physics*, vol. 60, pp. 2142-2148, 1986.

[14] R. Baetens, B. P. Jelle, and A. Gustavsen, "Properties, requirements and possibilities of smart windows for dynamic daylight and solar energy control in buildings: A state-of-the-art review," *Solar Energy Materials and Solar Cells*, vol. 94, pp. 87-105, 2010.

[15] E. S. Lee and D. DiBartolomeo, "Application issues for large-area electrochromic windows in commercial buildings," *Solar Energy Materials and Solar Cells*, vol. 71, pp. 465-491, 2002.

[16] X. Qiu, "Principles of Sound Absorbers," in *Acoustic Textiles*, ed: Springer, 2016, pp. 43-72.

[17] 4TU.Federation. (2016). *Sound Absorbing Glass*. Available: https://www.4tu.nl/bouw/en/LHP2016/Sound%20Absorbing%20Glass/

[18] Soundproofing-windows.net. (2016). *Soundproofing Windows with Double and Triple Glazing*. Available: http://soundproofing-windows.net/index.php/soundproofing-windows-with-double-and-triple-glazing

[19] N. B. SAS. (2016). *MICROSORBER®* Available: http://www.archiexpo.com/prod/barrisol/product-1797-1592310.html

[20] D. van den Ende, J. D. Kamminga, A. Boersma, T. Andritsch, and P. G. Steeneken, "Voltage-controlled surface wrinkling of elastomeric coatings," *Adv Mater*, vol. 25, pp. 3438-42, Jul 5 2013.

[21] P. Görrn, W. Cao, and S. Wagner, "Isotropically stretchable gold conductors on elastomeric substrates," *Soft Matter*, vol. 7, p. 7177, 2011.

[22] J. Zang, S. Ryu, N. Pugno, Q. Wang, Q. Tu, M. J. Buehler, *et al.*, "Multifunctionality and control of the crumpling and unfolding of large-area graphene," *Nat Mater,* vol. 12, pp. 321-5, Apr 2013.

[23] H.-Y. Ong, M. Shrestha, and G.-K. Lau, "Microscopically crumpled indium-tin-oxide thin films as compliant electrodes with tunable transmittance," *Applied Physics Letters,* vol. 107, p. 132902, 2015.

[24] A. V. Thomas, B. C. Andow, S. Suresh, O. Eksik, J. Yin, A. H. Dyson, *et al.*, "Controlled crumpling of graphene oxide films for tunable optical transmittance," *Adv Mater,* vol. 27, pp. 3256-65, Jun 3 2015.

[25] S. D. Rezaei, S. Shannigrahi, and S. Ramakrishna, "A review of conventional, advanced, and smart glazing technologies and materials for improving indoor environment," *Solar Energy Materials and Solar Cells,* vol. 159, pp. 26-51, 2017.

[26] J. Scarminio, A. Urbano, and B. Gardes, "The Beer-Lambert law for electrochromic tungsten oxide thin films," *Materials chemistry and physics,* vol. 61, pp. 143-146, 1999.

[27] J. M. Palmer, "The measurement of transmission, absorption, emission, and reflection," *Handbook of optics,* vol. 2, pp. 251-255, 1995.

[28] E. C. Fest and S. o. P.-o. I. Engineers, *Stray light analysis and control*: SPIE Press Bellingham, 2013.

[29] J. Flammer, M. Mozaffarieh, and H. Bebie, "The Interaction Between Light and Matter," pp. 21-39, 2013.

[30] C. M. Lampert, "Optical switching technology for glazings," *Thin Solid Films,* vol. 236, pp. 6-13, 1993.

[31] L. Jun, W. Chien-Hui, S. Gauza, R. Lu, and W. Shin-Tson, "Refractive indices of liquid crystals for display applications," *Journal of Display Technology,* vol. 1, pp. 51-61, 2005.

[32] J. W. Doane, "Polymer-Dispersed Liquid Crystals: Boojums at Work," *MRS Bulletin,* vol. 16, pp. 22-28, 2013.

[33] F. López Jiménez, S. Kumar, and P. M. Reis, "Soft Color Composites with Tunable Optical Transmittance," *Advanced Optical Materials,* vol. 4, pp. 620-626, 2016.

[34] K. Mori, K. Misawa, S. Ihida, T. Takahashi, H. Fujita, and H. Toshiyoshi, "A MEMS electrostatic roll-up window shade array for house energy management system," *IEEE Photon. Technol. Lett.,* vol. 28, pp. 593-596, 2016.

[35] D. Wolfe and K. W. Goossen, "Evaluation of 3D printed optofluidic smart glass prototypes," *Optics Express,* vol. 26, p. A85, 2017.

[36] E. Hecht, *Optics*: Pearson Education, 2016.

[37] E. J. McCartney, "Optics of the atmosphere: scattering by molecules and particles," *New York, John Wiley and Sons, Inc., 1976. 421 p.,* 1976.

[38] S. M. Mahpeykar, Q. Xiong, J. Wei, L. Meng, B. K. Russell, P. Hermansen, *et al.*, "Stretchable Hexagonal Diffraction Gratings as Optical Diffusers for In Situ Tunable Broadband Photon Management," *Advanced Optical Materials,* vol. 4, pp. 1106-1114, 2016.

[39] X. Ma, J. Q. Lu, R. S. Brock, K. M. Jacobs, P. Yang, and X.-H. Hu, "Determination of complex refractive index of polystyrene microspheres from 370 to 1610 nm," *Physics in Medicine & Biology,* vol. 48, p. 4165, 2003.

[40] D. Ge, E. Lee, L. Yang, Y. Cho, M. Li, D. S. Gianola, *et al.*, "A robust smart window: reversibly switching from high transparency to angle-independent structural color display," *Adv Mater,* vol. 27, pp. 2489-95, Apr 17 2015.

[41] H. N. Apostoleris, M. Chiesa, and M. Stefancich, "Improved transparency switching in paraffin–PDMS composites," *J. Mater. Chem. C,* vol. 3, pp. 1371-1377, 2015.

[42] J. Zhang, G. Pu, M. R. Dubay, Y. Zhao, and S. J. Severtson, "Repositionable pressure-sensitive adhesive possessing thermal-stimuli switchable transparency," *Journal of Materials Chemistry C*, vol. 1, p. 1080, 2013.

[43] J. Y. Park, H. Song, T. Kim, J. W. Suk, T. J. Kang, D. Jung, *et al.*, "PDMS-paraffin/graphene laminated films with electrothermally switchable haze," *Carbon*, vol. 96, pp. 805-811, 2016.

[44] J. C. Stover, *Optical scattering: measurement and analysis* vol. 2. Bellingham: SPIE optical engineering press 1995.

[45] A. Krywonos, "Predicting surface scatter using a linear systems formulation of non-paraxial scalar diffraction," Ph.D. Dissertation, University of Central Florida, 2006.

[46] A. Krywonos, J. E. Harvey, and N. Choi, "Linear systems formulation of scattering theory for rough surfaces with arbitrary incident and scattering angles," *JOSA A*, vol. 28, pp. 1121-1138, 2011.

[47] P. Beckmann and A. Spizzichino, "The scattering of electromagnetic waves from rough surfaces," *Norwood, MA, Artech House, Inc., 1987, 511 p.*, 1987.

[48] A. Spizzichino, *The Scattering of Electromagnetic Waves from Rough Surfaces. By P. Beckmann... and André Spizzichino*: Pergamon Press, 1963.

[49] C. Carniglia, "Scalar scattering theory for multilayer optical coatings," *Optical Engineering*, vol. 18, p. 182104, 1979.

[50] J. Eastman, "Surface scattering in optical interference coatings," 1974.

[51] S. G. Lee, D. Y. Lee, H. S. Lim, D. H. Lee, S. Lee, and K. Cho, "Switchable transparency and wetting of elastomeric smart windows," *Adv Mater*, vol. 22, pp. 5013-7, Nov 24 2010.

[52] E. Lee, M. Zhang, Y. Cho, Y. Cui, J. Van der Spiegel, N. Engheta, *et al.*, "Tilted pillars on wrinkled elastomers as a reversibly tunable optical window," *Adv Mater*, vol. 26, pp. 4127-33, Jun 25 2014.

[53] T. Ohzono, K. Suzuki, T. Yamaguchi, and N. Fukuda, "Tunable Optical Diffuser Based on Deformable Wrinkles," *Advanced Optical Materials,* vol. 1, pp. 374-380, 2013.

[54] C. Cao, H. F. Chan, J. Zang, K. W. Leong, and X. Zhao, "Harnessing localized ridges for high-aspect-ratio hierarchical patterns with dynamic tunability and multifunctionality," *Adv Mater,* vol. 26, pp. 1763-70, Mar 19 2014.

[55] D.-Y. Khang, J. A. Rogers, and H. H. Lee, "Mechanical Buckling: Mechanics, Metrology, and Stretchable Electronics," *Advanced Functional Materials,* vol. 19, pp. 1526-1536, 2009.

[56] A. L. Volynskii, S. Bazhenov, O. V. Lebedeva, and N. F. Bakeev, "Mechanical buckling instability of thin coatings deposited on soft polymer substrates," *Journal of Materials Science,* vol. 35, pp. 547– 554, 2000.

[57] P. Kim, M. Abkarian, and H. A. Stone, "Hierarchical folding of elastic membranes under biaxial compressive stress," *Nat Mater,* vol. 10, pp. 952-7, Dec 2011.

[58] H. Jiang, D. Y. Khang, J. Song, Y. Sun, Y. Huang, and J. A. Rogers, "Finite deformation mechanics in buckled thin films on compliant supports," *Proc Natl Acad Sci U S A,* vol. 104, pp. 15607-12, Oct 2007.

[59] L. Hu, W. Yuan, P. Brochu, G. Gruner, and Q. Pei, "Highly stretchable, conductive, and transparent nanotube thin films," *Applied Physics Letters,* vol. 94, p. 161108, 2009.

[60] W. Yuan, L. B. Hu, Z. B. Yu, T. Lam, J. Biggs, S. M. Ha, *et al.*, "Fault-Tolerant Dielectric Elastomer Actuators using Single-Walled Carbon Nanotube Electrodes," *Advanced Materials,* vol. 20, pp. 621-625, 2008.

[61] S. Shian and D. R. Clarke, "Electrically tunable window device," *Opt Lett,* vol. 41, pp. 1289-92, Mar 15 2016.

[62] S. Shian and D. R. Clarke, "Electrically-tunable surface deformation of a soft elastomer," *Soft Matter,* vol. 12, pp. 3137-41, Apr 7 2016.

[63] S. Shian, P. Kjeer, and D. R. Clarke, "Electric-field induced surface instabilities of soft dielectrics and their effects on optical transmittance and scattering," *Journal of Applied Physics,* vol. 123, p. 113105, 2018.

[64] M. Ochsner, M. R. Dusseiller, H. M. Grandin, S. Luna-Morris, M. Textor, V. Vogel, *et al.*, "Micro-well arrays for 3D shape control and high resolution analysis of single cells," *Lab Chip,* vol. 7, pp. 1074-7, Aug 2007.

[65] R. Huang, "Electrically induced surface instability of a conductive thin film on a dielectric substrate," *Applied Physics Letters,* vol. 87, p. 151911, 2005.

[66] Ronald E. Pelrine, Roy D. Kornbluh , and Jose P. Joseph, "Electrostriction of polymer dielectrics with compliant electrodes as a means of actuation," *Sensors and Actuators A: Physical,* vol. 64, pp. 77-85, 1998.

[67] M. Kollosche, J. Zhu, Z. Suo, and G. Kofod, "Complex interplay of nonlinear processes in dielectric elastomers," *Physical Review E,* vol. 85, 2012.

[68] M. Vosgueritchian, D. J. Lipomi, and Z. Bao, "Highly conductive and transparent PEDOT: PSS films with a fluorosurfactant for stretchable and flexible transparent electrodes," *Advanced functional materials,* vol. 22, pp. 421-428, 2012.

[69] A. Pimpin, Y. Suzuki, and N. Kasagi, "Micro electrostrictive actuator with metal compliant electrodes for flow control applications," *MEMES'04,* 2004.

[70] R. Jones, P. Wang, B. Lassen, and R. Sarban, "Dielectric elastomers and compliant metal electrode technology," in *MELECON 2010-2010 15th IEEE Mediterranean Electrotechnical Conference*, 2010, pp. 368-373.

[71] G. Kofod and P. Sommer-Larsen, "Compliant electrodes: solutions, materials and technologies," 2011.

[72] M. Benslimane and P. Gravesen, "ARTMUS Status Report 2000," 2000.

[73] S. Timoshenko, "Strength of Materials," in *Strength of Materials*. vol. 1, 2nd ed New York: D. Van Nostrand Company, Inc., 1955, pp. 88-90.

[74] S. H. Low and G. K. Lau, "Bi-axially crumpled silver thin-film electrodes for dielectric elastomer actuators," *Smart Materials and Structures,* vol. 23, p. 125021, 2014.

[75] M. Shrestha and G.-K. Lau, "Tunable window device based on micro-wrinkling of nanometric zinc-oxide thin film on elastomer," *Optics Letters,* vol. 41, p. 4433, 2016.

[76] J. Genzer and J. Groenewold, "Soft matter with hard skin: From skin wrinkles to templating and material characterization," *Soft Matter,* vol. 2, p. 310, 2006.

[77] M. D. Casper, A. Ö. Gözen, M. D. Dickey, J. Genzer, and J.-P. Maria, "Surface wrinkling by chemical modification of poly(dimethylsiloxane)-based networks during sputtering," *Soft Matter,* vol. 9, p. 7797, 2013.

[78] Dan Wu, Huimin Xie, and Yajun Yin, "Fracture behavior of thin aluminum films on soft substrate," presented at the International Conference on Fracture, China, 2013.

[79] M. Wissler and E. Mazza, "Electromechanical coupling in dielectric elastomer actuators," *Sensors and Actuators A: Physical,* vol. 138, pp. 384-393, 2007.

[80] Z. Suo, "Theory of dielectric elastomers," *Acta Mechanica Solida Sinica,* vol. 23, pp. 549-578, 2010.

[81] G. Kofod, P. Sommer-Larsen, R. Kornbluh, and R. Pelrine, "Actuation Response of Polyacrylate Dielectric Elastomers," *Journal of Intelligent Materials Systems and Structures,* vol. 14, pp. 787-793, 2003.

[82] Q. Guo, M. Zhang, Z. Xue, L. Ye, G. Wang, G. Huang, *et al.*, "Three dimensional strain distribution of wrinkled silicon nanomembranes fabricated by rolling-transfer technique," *Applied Physics Letters,* vol. 103, p. 264102, 2013.

[83] M. K. Tripp, C. Stampfer, D. C. Miller, T. Helbling, C. F. Herrmann, C. Hierold, *et al.*, "The mechanical properties of atomic layer deposited alumina for use in

micro-and nano-electromechanical systems," *Sensors and Actuators A: Physical*, vol. 130, pp. 419-429, 2006.

[84] J. Houska, J. Blazek, J. Rezek, and S. Proksova, "Overview of optical properties of Al2O3 films prepared by various techniques," *Thin Solid Films*, vol. 520, pp. 5405-5408, 2012.

[85] A. Ismail and M. J. Abdullah, "The structural and optical properties of ZnO thin films prepared at different RF sputtering power," *Journal of King Saud University - Science*, vol. 25, pp. 209-215, 2013.

[86] T.-H. Fang, W.-J. Chang, and C.-M. Lin, "Nanoindentation characterization of ZnO thin films," *Materials Science and Engineering: A*, vol. 452-453, pp. 715-720, 2007.

[87] S.-Y. Chang, Y.-C. Hsiao, and Y.-C. Huang, "Preparation and mechanical properties of aluminum-doped zinc oxide transparent conducting films," *Surface and Coatings Technology*, vol. 202, pp. 5416-5420, 2008.

[88] W. Yang, Z. Liu, D.-L. Peng, F. Zhang, H. Huang, Y. Xie, *et al.*, "Room-temperature deposition of transparent conducting Al-doped ZnO films by RF magnetron sputtering method," *Applied Surface Science*, vol. 255, pp. 5669-5673, 2009.

[89] H. S. Yoon, K. S. Lee, T. S. Lee, B. Cheong, D. K. Choi, D. H. Kim, *et al.*, "Properties of fluorine doped ZnO thin films deposited by magnetron sputtering," *Solar Energy Materials and Solar Cells*, vol. 92, pp. 1366-1372, 2008.

[90] G. A. Niklasson and C. G. Granqvist, "Electrochromics for smart windows: thin films of tungsten oxide and nickel oxide, and devices based on these," *J. Mater. Chem.*, vol. 17, pp. 127-156, 2007.

[91] Y. Gaillard, V. J. Rico, E. Jimenez-Pique, and A. R. González-Elipe, "Nanoindentation of TiO2thin films with different microstructures," *Journal of Physics D: Applied Physics*, vol. 42, p. 145305, 2009.

[92] A. Bendavid, P. Martin, and H. Takikawa, "Deposition and modification of titanium dioxide thin films by filtered arc deposition," *Thin Solid Films*, vol. 360, pp. 241-249, 2000.

[93] S. Sathasivam, D. S. Bhachu, Y. Lu, N. Chadwick, S. A. Althabaiti, A. O. Alyoubi, *et al.*, "Tungsten Doped TiO2 with Enhanced Photocatalytic and Optoelectrical Properties via Aerosol Assisted Chemical Vapor Deposition," *Sci Rep*, vol. 5, p. 10952, 2015.

[94] T. Hitosugi, "TiO2-based Transparent Conducting Oxide."

[95] H. Askari, H. Fallah, M. Askari, and M. C. Mohmmadieyh, "Electrical and optical properties of ITO thin films prepared by DC magnetron sputtering for low-emitting coatings," *arXiv preprint arXiv:1409.5293*, 2014.

[96] Z. Banyamin, P. Kelly, G. West, and J. Boardman, "Electrical and Optical Properties of Fluorine Doped Tin Oxide Thin Films Prepared by Magnetron Sputtering," *Coatings*, vol. 4, pp. 732-746, 2014.

[97] H. Kang, S. Jung, S. Jeong, G. Kim, and K. Lee, "Polymer-metal hybrid transparent electrodes for flexible electronics," *Nat Commun*, vol. 6, p. 6503, 2015.

[98] M. Shrestha, A. K. Asundi, and G. K. Lau, "Electrically tunable window based on wrinkled ZnO/Ag thin film," presented at the SPIE Smart Structures/NDE Portland, USA, 2017.

[99] N. Bowden, S. Brittain, A. G. Evans, J. W. Hutchinson, and G. M. Whitesides, "Spontaneous formation of ordered structures in thin films of metals supported on an elastomeric polymer," *Nature*, vol. 393, p. 146, 1998.

[100] O. Oyewole, D. Yu, J. Du, J. Asare, D. Oyewole, V. Anye, *et al.*, "Micro-wrinkling and delamination-induced buckling of stretchable electronic structures," *Journal of Applied Physics*, vol. 117, p. 235501, 2015.

[101] J. George and C. Menon, "Electrical and optical properties of electron beam evaporated ITO thin films," *Surface and Coatings Technology*, vol. 132, pp. 45-48, 2000.

[102] K. A. Sierros, D. A. Banerjee, N. J. Morris, D. R. Cairns, I. Kortidis, and G. Kiriakidis, "Mechanical properties of ZnO thin films deposited on polyester substrates used in flexible device applications," *Thin Solid Films*, vol. 519, pp. 325-330, 2010.

[103] K. Park, D.-K. Lee, B.-S. Kim, H. Jeon, N.-E. Lee, D. Whang, *et al.*, "Stretchable, Transparent Zinc Oxide Thin Film Transistors," *Advanced Functional Materials*, vol. 20, pp. 3577-3582, 2010.

[104] K. Ellmer, "Magnetron sputtering of transparent conductive zinc oxide: relation between the sputtering parameters and the electronic properties," *Journal of Physics D: Applied Physics*, vol. 33, p. R17, 2000.

[105] R. Heideman, P. Lambeck, and J. G. Gardeniers, "High quality ZnO layers with adjustable refractive indices for integrated optics applications," *Optical materials*, vol. 4, pp. 741-755, 1995.

[106] Y. Ebata, A. B. Croll, and A. J. Crosby, "Wrinkling and strain localizations in polymer thin films," *Soft Matter*, vol. 8, pp. 9086-9091, 2012.

[107] K. G. Lee, K. J. Park, S. Seok, S. Shin, D. H. Kim, J. Y. Park, *et al.*, "3D printed modules for integrated microfluidic devices," *RSC Advances*, vol. 4, p. 32876, 2014.

[108] C. Ong, D. Zong, M. Aravind, C. Choy, and D. Lu, "Tensile strength of zinc oxide films measured by a microbridge method," *Journal of materials research*, vol. 18, pp. 2464-2472, 2003.

[109] M. Company. (2015). *3M VHB Tape Speciality Tapes*. Available: http://multimedia.3m.com/mws/media/986695O/3m-vhb-tape-specialty-tapes.pdf

[110] X. Li, L. Wei, R. H. Poelma, S. Vollebregt, J. Wei, H. P. Urbach, *et al.*, "Stretchable binary fresnel lens for focus tuning," *Scientific reports*, vol. 6, p. 25348, 2016.

[111] M. Singh and B. L. Anderson, "Toward a perceptual theory of transparency," *Psychological review*, vol. 109, p. 492, 2002.

[112] D. Sahu and J.-L. Huang, "Design of ZnO/Ag/ZnO multilayer transparent conductive films," *Materials Science and Engineering: B*, vol. 130, pp. 295-299, 2006.

[113] A. El Hajj, B. Lucas, M. Chakaroun, R. Antony, B. Ratier, and M. Aldissi, "Optimization of ZnO/Ag/ZnO multilayer electrodes obtained by Ion Beam Sputtering for optoelectronic devices," *Thin Solid Films*, vol. 520, pp. 4666-4668, 2012.

[114] M. Shrestha, A. Asundi, and G.-K. Lau, "Smart Window Based on Electric Unfolding of Microwrinkled TiO2 Nanometric Films," *ACS Photonics*, 2018.

[115] P. Van Konynenburg, S. Marsland, and J. McCoy, "Solar radiation control using NCAP liquid crystal technology," *Solar Energy Materials*, vol. 19, pp. 27-41, 1989.

[116] C. G. Granqvist, S. Green, G. A. Niklasson, N. R. Mlyuka, S. von Kræmer, and P. Georén, "Advances in chromogenic materials and devices," *Thin Solid Films*, vol. 518, pp. 3046-3053, 2010.

[117] J. Murray, D. Ma, and J. N. Munday, "Electrically controllable light trapping for self-powered switchable solar windows," *ACS Photonics*, vol. 4, pp. 1-7, 2016.

[118] M. Wood, S. Duan, and S. T. China. (2012). *Non-Gaussian diffusers*.

[119] DuPont. (2017). Available: http://www.titanium.dupont.com

[120] M. P. Diebold, *Application of Light Scattering to Coatings: A User's Guide*: Springer, 2014.

[121] J. C. Fan, F. J. Bachner, G. H. Foley, and P. M. Zavracky, "Transparent heat-mirror films of TiO2/Ag/TiO2 for solar energy collection and radiation insulation," *Applied Physics Letters,* vol. 25, pp. 693-695, 1974.

[122] R. E. Dunham, *Stage Lighting: Fundamentals and Applications*: CRC Press, 2015.

[123] P. Brochu and Q. Pei, "Advances in dielectric elastomers for actuators and artificial muscles," *Macromolecular rapid communications,* vol. 31, pp. 10-36, 2010.

[124] S. Rosset and H. R. Shea, "Flexible and stretchable electrodes for dielectric elastomer actuators," *Applied Physics A,* vol. 110, pp. 281-307, 2012.

[125] C. Granqvist, "Transparent conductive electrodes for electrochromic devices: a review," *Applied Physics A,* vol. 57, pp. 19-24, 1993.

[126] M. P. Bendsoe and O. Sigmund, *Topology optimization: theory, methods, and applications*: Springer Science & Business Media, 2013.

[127] A. P. Raman, M. A. Anoma, L. Zhu, E. Rephaeli, and S. Fan, "Passive radiative cooling below ambient air temperature under direct sunlight," *Nature,* vol. 515, p. 540, 2014.

[128] K. Bertoldi, V. Vitelli, J. Christensen, and M. van Hecke, "Flexible mechanical metamaterials," *Nature Reviews Materials,* vol. 2, p. 17066, 2017.

[129] D. J. Lipomi, J. A. Lee, M. Vosgueritchian, B. C. K. Tee, J. A. Bolander, and Z. Bao, "Electronic Properties of Transparent Conductive Films of PEDOT:PSS on Stretchable Substrates," *Chemistry of Materials,* vol. 24, pp. 373-382, 2012.

[130] M. Zeman, R. A. C. M. M. van Swaaij, J. W. Metselaar, and R. E. I. Schropp, "Optical modeling of a-Si:H solar cells with rough interfaces: Effect of back contact and interface roughness," *Journal of Applied Physics,* vol. 88, pp. 6436-6443, 2000.

[131] R. Pelrine, R. Kornbluh, Q. Pei, and J. Joseph, "High-speed electrically actuated elastomers with strain greater than 100%," *Science,* vol. 287, pp. 836-839, 2000.

[132] T. Mirfakhrai, J. D. Madden, and R. H. Baughman, "Polymer artificial muscles," *Materials today,* vol. 10, pp. 30-38, 2007.

[133] I. A. Anderson, T. A. Gisby, T. G. McKay, B. M. O'Brien, and E. P. Calius, "Multi-functional dielectric elastomer artificial muscles for soft and smart machines," *Journal of Applied Physics,* vol. 112, p. 041101, 2012.

[134] S. Rosset and H. R. Shea, "Small, fast, and tough: Shrinking down integrated elastomer transducers," *Applied Physics Reviews,* vol. 3, p. 031105, 2016.

[135] M. Bozlar, C. Punckt, S. Korkut, J. Zhu, C. Chiang Foo, Z. Suo, *et al.*, "Dielectric elastomer actuators with elastomeric electrodes," *Applied physics letters,* vol. 101, p. 091907, 2012.

[136] N. Hasan, H. Kim, and C. H. Mastrangelo, "Large aperture tunable-focus liquid lens using shape memory alloy spring," *Optics Express,* vol. 24, pp. 13334-13342, 2016.

[137] W. M. Choi, J. Song, D.-Y. Khang, H. Jiang, Y. Y. Huang, and J. A. Rogers, "Biaxially stretchable "wavy" silicon nanomembranes," *Nano Letters,* vol. 7, pp. 1655-1663, 2007.

[138] C. J. Tavares, S. M. Marques, S. Lanceros-Méndez, V. Sencadas, V. Teixeira, J. O. Carneiro, *et al.*, "Strain analysis of photocatalytic TiO2 thin films on polymer substrates," *Thin Solid Films,* vol. 516, pp. 1434-1438, 2008.

[139] U. Lang, N. Naujoks, and J. Dual, "Mechanical characterization of PEDOT:PSS thin films," *Synthetic Metals,* vol. 159, pp. 473-479, 2009.

[140] 3M. (2015, Converting 3M Technology into Successful Applications.

[141] Federico Carpi , Gabriele Frediani, Simona Turco , and Danilo De Rossi, "Bioinspired Tunable Lens with Muscle-Like Electroactive Elastomers," *Adv. Funct. Mater.* , vol. 21, pp. 4152–4158, 2011.

[142] C. Keplinger, J.-Y. Sun, C. C. Foo, P. Rothemund, G. M. Whitesides, and Z. Suo, "Stretchable, transparent, ionic conductors," *Science,* vol. 341, pp. 984-987, 2013.

[143] Z. Lu, M. Shrestha, and G.-K. Lau, "Electrically tunable and broader-band sound absorption by using micro-perforated dielectric elastomer actuator," *Applied Physics Letters*, vol. 110, p. 182901, 2017.

[144] Strex USA. (2019). *Microscope-Mountable Biaxial Stretching System STB-190-XY*. Available: https://strexcell.com/cell-stretching-system/models/biaxial-stretching-system/

[145] Coco Engineering Inc. (2015). *Biaxial Film Stretcher*. Available: WWW.cocoengineering.com

[146] Bühler AG. (2018). *Large-area coating*. Available: https://www.buhlergroup.com/global/en/process-technologies/high-vacuum-thin-film-coating/large-area-coating.htm

[147] M. Thota and K. Wang, "Reconfigurable origami sonic barriers with tunable bandgaps for traffic noise mitigation," *Journal of Applied Physics*, vol. 122, p. 154901, 2017.

[148] L.-F. Zheng, T. Wang, and G.-X. Li, "Vibration and noise analysis of heavy-duty trucks based on powertrain lightweighting," *Journal of Vibroengineering*, vol. 19, 2017.

[149] Patchbay.wordpress.com. (2016). *Room Acoustics: Basic Principles of Sound Absorption*. Available: https://patchbay.wordpress.com/2011/01/19/room-acoustics-basic-principles/

[150] L. Cremer and H. A. Müller, *Principles and applications of room acoustics* vol. 1: Chapman & Hall, 1982.

[151] K. U. Ingard, "Notes on sound absorption technology(Book)," *Poughkeepsie, NY: Noise Control Foundation, 1994.*, 1994.

[152] L. L. Beranek and I. L. Ver, "Noise and vibration control engineering-principles and applications," *Noise and vibration control engineering-Principles and applications John Wiley & Sons, Inc., 814 p.*, 1992.

[153] J. Kang and M. W. Brocklesby, "Feasibility of applying micro-perforated absorbers in acoustic window systems," *Applied Acoustics,* vol. 66, pp. 669-689, 2005.

[154] X. Wang, H. Zhao, X. Luo, and Z. Huang, "Membrane-constrained acoustic metamaterials for low frequency sound insulation," *Applied Physics Letters,* vol. 108, p. 041905, 2016.

[155] Y. Li and B. M. Assouar, "Acoustic metasurface-based perfect absorber with deep subwavelength thickness," *Applied Physics Letters,* vol. 108, p. 063502, 2016.

[156] W. Frommhold, H. Fuchs, and S. Sheng, "Acoustic performance of membrane absorbers," *Journal of Sound and Vibration,* vol. 170, pp. 621-636, 1994.

[157] L. E. Kinsler, A. R. Frey, A. B. Coppens, and J. V. Sanders, "Fundamentals of acoustics," *Fundamentals of Acoustics, 4th Edition, by Lawrence E. Kinsler, Austin R. Frey, Alan B. Coppens, James V. Sanders, pp. 560. ISBN 0-471-84789-5. Wiley-VCH, December 1999.,* p. 560, 1999.

[158] K. Ginn, *Architectural acoustics*: Brüel & Kjaer, 1978.

[159] D. Herrin and J. Liu, "Properties and applications of microperforated panels," *Sound and Vibrations,* 2011.

[160] U. R. Kristiansen and T. E. Vigran, "On the design of resonant absorbers using a slotted plate," *Applied Acoustics,* vol. 43, pp. 39-48, 1994.

[161] A. Guess, "Calculation of perforated plate liner parameters from specified acoustic resistance and reactance," *Journal of Sound and Vibration,* vol. 40, pp. 119-137, 1975.

[162] D. A. Bies, C. Hansen, and C. Howard, *Engineering noise control*: CRC press, 2017.

[163] D.-Y. Maa, "Potential of microperforated panel absorber," *Journal of the Acoustical Society of America,* vol. 104, 1998.

[164] S. Min, K. Nagamura, N. Nakagawa, and M. Okamura, "Design of compact micro-perforated membrane absorbers for polycarbonate pane in automobile," *Applied Acoustics*, vol. 74, pp. 622-627, 2013.

[165] M. Toyoda, R. L. Mu, and D. Takahashi, "Relationship between Helmholtz-resonance absorption and panel-type absorption in finite flexible microperforated-panel absorbers," *Applied Acoustics*, vol. 71, pp. 315-320, 2010.

[166] T. Bravo, C. Maury, and C. Pinhede, "Vibroacoustic properties of thin micro-perforated panel absorbers," *J Acoust Soc Am*, vol. 132, pp. 789-98, Aug 2012.

[167] C. Li, B. Cazzolato, and A. Zander, "Acoustic impedance of micro perforated membranes: Velocity continuity condition at the perforation boundary," *J Acoust Soc Am*, vol. 139, pp. 93-103, Jan 2016.

[168] J. Zou, Y. Shen, J. Yang, and X. Qiu, "A note on the prediction method of reverberation absorption coefficient of double layer micro-perforated membrane," *Applied Acoustics*, vol. 67, pp. 106-111, 2006.

[169] H. Ruiz, P. Cobo, and F. Jacobsen, "Optimization of multiple-layer microperforated panels by simulated annealing," *Applied Acoustics*, vol. 72, pp. 772-776, 2011.

[170] J. Liu and D. W. Herrin, "Enhancing micro-perforated panel attenuation by partitioning the adjoining cavity," *Applied Acoustics*, vol. 71, pp. 120-127, 2010.

[171] C. Wang, L. Cheng, J. Pan, and G. Yu, "Sound absorption of a micro-perforated panel backed by an irregular-shaped cavity," *J Acoust Soc Am*, vol. 127, pp. 238-46, Jan 2010.

[172] H. Ruiz, P. Cobo, T. Dupont, B. Martin, and P. Leclaire, "Acoustic properties of plates with unevenly distributed macroperforations backed by woven meshes," *J Acoust Soc Am*, vol. 132, pp. 3138-47, Nov 2012.

[173] C. Wang and L. Huang, "On the acoustic properties of parallel arrangement of multiple micro-perforated panel absorbers with different cavity depths," *J Acoust Soc Am,* vol. 130, pp. 208-18, Jul 2011.

[174] S. Konishi, M. Yoda, N. Hosaka, S. Sugiyama, and S. Akishita, "Tunable acoustic absorbing system using a deep hole array," in *Micro Electro Mechanical Systems, 1998. MEMS 98. Proceedings., The Eleventh Annual International Workshop on*, 1998, pp. 655-660.

[175] S. Konishi, M. Yoda, S. Sugiyama, and S. Akishita, "Tunable acoustic absorber using a micro acoustic hole array," *Electronics and Communications in Japan (Part II: Electronics),* vol. 83, pp. 1-6, 2000.

[176] M. Yoda and S. Konishi, "Estimation of an open-loop compact adaptive passive noise control system with microstructures," *The Journal of the Acoustical Society of America,* vol. 110, pp. 638-641, 2001.

[177] O. Cherrier, V. Pommier-Budinger, and F. Simon, "Panel of resonators with variable resonance frequency for noise control," *Applied Acoustics,* vol. 73, pp. 781-790, 2012.

[178] Z. Chen, C. Xue, L. Fan, S. Y. Zhang, X. J. Li, H. Zhang, *et al.*, "A tunable acoustic metamaterial with double-negativity driven by electromagnets," *Sci Rep,* vol. 6, p. 30254, Jul 22 2016.

[179] X. Chen, X. Xu, S. Ai, H. Chen, Y. Pei, and X. Zhou, "Active acoustic metamaterials with tunable effective mass density by gradient magnetic fields," *Applied Physics Letters,* vol. 105, p. 071913, 2014.

[180] S. Xiao, G. Ma, Y. Li, Z. Yang, and P. Sheng, "Active control of membrane-type acoustic metamaterial by electric field," *Applied Physics Letters,* vol. 106, p. 091904, 2015.

[181] Z. Lu, Y. Cui, M. Debiasi, and Z. Zhao, "A Tunable Dielectric Elastomer Acoustic Absorber," *Acta Acustica united with Acustica,* vol. 101, pp. 863-866, 2015.

[182] Philippe Dubois, Samuel Rosset, Muhamed Niklaus, Massoud Dadras, and H. Shea, "Voltage control of the resonance frequency of dielectric electroactive polymer (DEAP) membranes," *Journal of Microelectromechanical systems,* vol. 17, 2008.

[183] J. Zhu, S. Cai, and Z. Suo, "Resonant behavior of a membrane of a dielectric elastomer," *International Journal of Solids and Structures,* vol. 47, pp. 3254-3262, 2010.

[184] Z. Lu, Y. Cui, J. Zhu, Z. Zhao, and M. Debiasi, "Acoustic characteristics of a dielectric elastomer absorber," *The Journal of the Acoustical Society of America,* vol. 134, pp. 4218-4218, 2013.

[185] S. Timoshenko, D. H. Young, and J. W. Weaver, *Vibrations problems in engineering*, 4th ed. Hobokenn, NJ: Wiley, 1974.

[186] X. Yu, Z. Lu, F. Cui, L. Cheng, and Y. Cui, "Tunable acoustic metamaterial with an array of resonators actuated by dielectric elastomer," *Extreme Mechanics Letters,* 2016.

[187] H. F. Olson and E. G. May, "Electronic sound absorber," *The Journal of the Acoustical Society of America,* vol. 25, pp. 1130-1136, 1953.

[188] D. Guicking and E. Lorenz, "An active sound absorber with porous plate," *Journal of vibration, acoustics, stress, and reliability in design,* vol. 106, pp. 389-392, 1984.

[189] P. Rothemund, X. P. Morelle, K. Jia, G. M. Whitesides, and Z. Suo, "A Transparent Membrane for Active Noise Cancelation," *Advanced Functional Materials,* p. 1800653, 2018.

[190] G. Mangiante, "Active sound absorption," *The Journal of the Acoustical Society of America,* vol. 61, pp. 1516-1523, 1977.

[191] S. J. York and H. K. Cho, "Active noise cancellation apparatus and method," ed: Google Patents, 2003.

[192] P. Cobo and M. Cuesta, "Hybrid passive-active absorption of a microperforated panel in free field conditions," *J Acoust Soc Am,* vol. 121, pp. EL251-5, Jun 2007.

[193] D. Guicking, K. Karcher, and M. Rollwage, "Coherent active methods for applications in room acoustics," *The Journal of the Acoustical Society of America,* vol. 78, pp. 1426-1434, 1985.

[194] W. Zheng, Q. Huang, S. Li, and Z. Guo, "Sound absorption of hybrid passive-active system using finite flexible micro-perforated panels," *Journal of Low Frequency Noise, Vibration and Active Control,* vol. 30, pp. 313-328, 2011.

[195] P. Cobo, A. Fernández, and O. Doutres, "Low-frequency absorption using a two-layer system with active control of input impedance," *The Journal of the Acoustical Society of America,* vol. 114, pp. 3211-3216, 2003.

[196] J. P. Smith, B. D. Johnson, and R. A. Burdisso, "A broadband passive–active sound absorption system," *The Journal of the Acoustical Society of America,* vol. 106, pp. 2646-2652, 1999.

[197] M. Furstoss, D. Thenail, and M.-A. Galland, "Surface impedance control for sound absorption: direct and hybrid passive/active strategies," *Journal of sound and vibration,* vol. 203, pp. 219-236, 1997.

[198] P. Cobo, J. Pfretzschner, M. a. Cuesta, and D. K. Anthony, "Hybrid passive–active absorption using microperforated panels," *The Journal of the Acoustical Society of America,* vol. 116, pp. 2118-2125, 2004.

[199] M. Shrestha, T.-G. La, and G. K. Lau, "Inkjet Printed Stretchable Electrodes For Tunable Focus Lens," in *2nd International Conference on Progress in Additive Manufacturing (Pro-AM 2016)* Singapore, 2016.

[200] L. Maffli, S. Rosset, M. Ghilardi, F. Carpi, and H. Shea, "Ultrafast All-Polymer Electrically Tunable Silicone Lenses," *Advanced Functional Materials,* vol. 25, pp. 1656-1665, 2015.

[201] F. Carpi, P. Chiarelli, A. Mazzoldi, and D. De Rossi, "Electromechanical characterisation of dielectric elastomer planar actuators: comparative evaluation of different electrode materials and different counterloads," *Sensors and Actuators A: Physical,* vol. 107, pp. 85-95, 2003.

[202] A. D. Wilson, "Inplane displacement of a stressed membrane with a hole measured by holographic interferometry," *Applied optics,* vol. 10.4, pp. 908-912, 1971.

[203] S. Timoshenko and J. N. Goodie, "Theory of Elasticity," 3rd ed: McGraw-Hill Education, 1987, pp. 90-97.

[204] G. Ma and P. Sheng, "Acoustic metamaterials: From local resonances to broad horizons," *Science advances,* vol. 2, p. e1501595, 2016.

[205] J. V. Sanchez-Perez, C. Rubio, R. Martinez-Sala, R. Sanchez-Grandia, and V. Gomez, "Acoustic barriers based on periodic arrays of scatterers," *Applied Physics Letters,* vol. 81, pp. 5240-5242, 2002.

[206] V. Romero-García, A. Krynkin, L. Garcia-Raffi, O. Umnova, and J. Sánchez-Pérez, "Multi-resonant scatterers in sonic crystals: Locally multi-resonant acoustic metamaterial," *Journal of Sound and Vibration,* vol. 332, pp. 184-198, 2013.

[207] N. Fang, D. Xi, J. Xu, M. Ambati, W. Srituravanich, C. Sun, *et al.*, "Ultrasonic metamaterials with negative modulus," *Nature materials,* vol. 5, p. 452, 2006.

[208] Z. Liu, X. Zhang, Y. Mao, Y. Zhu, Z. Yang, C. T. Chan, *et al.*, "Locally resonant sonic materials," *Science,* vol. 289, pp. 1734-1736, 2000.

[209] X. Hu, C. T. Chan, and J. Zi, "Two-dimensional sonic crystals with Helmholtz resonators," *Physical Review E,* vol. 71, p. 055601, 2005.

[210] M.-H. Lu, L. Feng, and Y.-F. Chen, "Phononic crystals and acoustic metamaterials," *Materials today,* vol. 12, pp. 34-42, 2009.

[211] U. Ackermann, H. Fuchs, and N. Rambausek, "Sound absorbers of a novel membrane construction," *Applied Acoustics,* vol. 25, pp. 197-215, 1988.

[212] Z. Yang, J. Mei, M. Yang, N. Chan, and P. Sheng, "Membrane-type acoustic metamaterial with negative dynamic mass," *Physical review letters*, vol. 101, p. 204301, 2008.

[213] Z. Yang, H. Dai, N. Chan, G. Ma, and P. Sheng, "Acoustic metamaterial panels for sound attenuation in the 50–1000 Hz regime," *Applied Physics Letters*, vol. 96, p. 041906, 2010.

[214] C. J. Naify, C.-M. Chang, G. McKnight, F. Scheulen, and S. Nutt, "Membrane-type metamaterials: Transmission loss of multi-celled arrays," *Journal of applied physics*, vol. 109, p. 104902, 2011.

[215] C. J. Naify, C.-M. Chang, G. McKnight, and S. R. Nutt, "Scaling of membrane-type locally resonant acoustic metamaterial arrays," *The Journal of the Acoustical Society of America*, vol. 132, pp. 2784-2792, 2012.

[216] Y. Chen, G. Huang, X. Zhou, G. Hu, and C.-T. Sun, "Analytical coupled vibroacoustic modeling of membrane-type acoustic metamaterials: Plate model," *The Journal of the Acoustical Society of America*, vol. 136, pp. 2926-2934, 2014.

[217] G. Ma, M. Yang, S. Xiao, Z. Yang, and P. Sheng, "Acoustic metasurface with hybrid resonances," *Nature materials*, vol. 13, p. 873, 2014.

[218] Z. Lu, H. Godaba, Y. Cui, C. C. Foo, M. Debiasi, and J. Zhu, "An electronically tunable duct silencer using dielectric elastomer actuators," *J Acoust Soc Am*, vol. 138, pp. EL236-41, Sep 2015.

[219] Z. Lu, Y. Cui, and M. Debiasi, "Active membrane-based silencer and its acoustic characteristics," *Applied Acoustics*, vol. 111, pp. 39-48, 2016.

[220] R. Pelrine, R. Kornbluh, J. Joseph, R. Heydt, Q. Pei, and S. Chiba, "High-field deformation of elastomeric dielectrics for actuators," *Materials Science and Engineering: C*, vol. 11, pp. 89-100, 2000.

[221] M. Yoda, S. Sugiyama, S. Akishita, and S. Konishi, "Tunable acoustic absorber with micro deep hole array," in *Micromechatronics and Human Science, 1998.*

MHS'98. Proceedings of the 1998 International Symposium on, 1998, pp. 177-182.

[222] M. Benslimane, P. Gravesen, and P. Sommer-Larsen, "Mechanical properties of dielectric elastomer actuators with smart metallic compliant electrodes," in *Proc. SPIE*, 2002, pp. 150-157.

[223] S. Hsien Low, L. Lynn Shiau, and G.-K. Lau, "Large actuation and high dielectric strength in metallized dielectric elastomer actuators," *Applied Physics Letters*, vol. 100, p. 182901, 2012.

[224] R. Sahu, K. Patra, and J. Szpunar, "Experimental Study and Numerical Modelling of Creep and Stress Relaxation of Dielectric Elastomers," *Strain*, vol. 51, pp. 43-54, 2015.

[225] S. Michel, X. Q. Zhang, M. Wissler, C. Löwe, and G. Kovacs, "A comparison between silicone and acrylic elastomers as dielectric materials in electroactive polymer actuators," *Polymer International*, vol. 59, pp. 391-399, 2009.

[226] J. Mei, G. Ma, M. Yang, Z. Yang, W. Wen, and P. Sheng, "Dark acoustic metamaterials as super absorbers for low-frequency sound," *Nat Commun*, vol. 3, p. 756, Mar 27 2012.

[227] S. Rosset, B. M. O'Brien, T. Gisby, D. Xu, H. R. Shea, and I. A. Anderson, "Self-sensing dielectric elastomer actuators in closed-loop operation," *Smart Materials and Structures*, vol. 22, p. 104018, 2013.

[228] J. D. Madden, N. A. Vandesteeg, P. A. Anquetil, P. G. Madden, A. Takshi, R. Z. Pytel, *et al.*, "Artificial muscle technology: physical principles and naval prospects," *IEEE Journal of oceanic engineering*, vol. 29, pp. 706-728, 2004.

[229] A. Maziz, A. Concas, A. Khaldi, J. Stålhand, N.-K. Persson, and E. W. Jager, "Knitting and weaving artificial muscles," *Science advances*, vol. 3, p. e1600327, 2017.

[230] J. Shintake, V. Cacucciolo, D. Floreano, and H. Shea, "Soft Robotic Grippers," *Advanced Materials*, p. 1707035, 2018.

[231] S. Shian, R. M. Diebold, A. McNamara, and D. R. Clarke, "Highly compliant transparent electrodes," *Applied Physics Letters*, vol. 101, p. 061101, 2012.

[232] J. K. Lett. (2013, Hydrogel electrodes: What you should know about hydrogel electrodes.

[233] T. A. Kosierkiewicz, "Dry and flexible elastomer electrodes outperform similar hydrogel and Ag/AgCl electrodes," in *Medical Measurements and Applications Proceedings (MeMeA), 2013 IEEE International Symposium on*, 2013, pp. 306-308.

[234] C. Christianson, N. N. Goldberg, D. D. Deheyn, S. Cai, and M. T. Tolley, "Translucent soft robots driven by frameless fluid electrode dielectric elastomer actuators," *Science Robotics*, vol. 3, p. eaat1893, 2018.

[235] G.-K. Lau, D. Di-Teng Tan, and T.-G. La, "Large axial actuation of pre-stretched tubular dielectric elastomer and use of oil encapsulation to enhance dielectric breakdown strength," *Smart Materials and Structures*, vol. 24, p. 045025, 2015.

[236] A. Nardes, M. Kemerink, and R. Janssen, "Anisotropic hopping conduction in spin-coated PEDOT: PSS thin films," *Physical Review B*, vol. 76, p. 085208, 2007.

[237] Y. Liu, T. Cui, and K. Varahramyan, "All-polymer capacitor fabricated with inkjet printing technique," *Solid-State Electronics*, vol. 47, pp. 1543-1548, 2003.

[238] H. Sirringhaus, T. Kawase, R. Friend, T. Shimoda, M. Inbasekaran, W. Wu, *et al.*, "High-resolution inkjet printing of all-polymer transistor circuits," *Science*, vol. 290, pp. 2123-2126, 2000.

[239] S. E. Burns, P. Cain, J. Mills, J. Wang, and H. Sirringhaus, "Inkjet printing of polymer thin-film transistor circuits," *MRS bulletin*, vol. 28, pp. 829-834, 2003.

[240] S. H. Eom, S. Senthilarasu, P. Uthirakumar, S. C. Yoon, J. Lim, C. Lee, *et al.*, "Polymer solar cells based on inkjet-printed PEDOT: PSS layer," *Organic Electronics*, vol. 10, pp. 536-542, 2009.

[241] S.-S. Yoon and D.-Y. Khang, "Roles of Nonionic Surfactant Additives in PEDOT:PSS Thin Films," *The Journal of Physical Chemistry C*, vol. 120, pp. 29525-29532, 2016.

[242] G.-K. Lau, K.-R. Heng, A. S. Ahmed, and M. Shrestha, "Dielectric elastomer fingers for versatile grasping and nimble pinching," *Applied Physics Letters*, vol. 110, p. 182906, 2017.

[243] I. FUJIFILM Dimatix. (2015, Dimatix Materials Printer DMP-2800 Series User Manual.

[244] G.-K. Lau and M. Shrestha, "Ink-Jet Printing of Micro-Electro-Mechanical Systems (MEMS)," *Micromachines*, vol. 8, p. 194, 2017.

[245] D. Soltman and V. Subramanian, "Inkjet-printed line morphologies and temperature control of the coffee ring effect," *Langmuir*, vol. 24, pp. 2224-2231, 2008.

[246] T.-G. La and G.-K. Lau, "Inhibiting electro-thermal breakdown of acrylic dielectric elastomer actuators by dielectric gel coating," *Applied Physics Letters*, vol. 108, p. 012903, 2016.

[247] K. F. I. C. C.). (2013). *Interior and exterior doors: life expectancy, cost and more*. Available: http://www.improvementcenter.com/doors/doors-life-expectancy-cost.html

[248] L. Sun, K. Y. Au-Yeung, M. Yang, S. T. Tang, Z. Yang, and P. Sheng, "Membrane-type resonator as an effective miniaturized tuned vibration mass damper," *AIP Advances*, vol. 6, p. 085212, 2016.

[249] F. Langfeldt, H. Kemsies, W. Gleine, and O. von Estorff, "Perforated membrane-type acoustic metamaterials," *Physics Letters A*, vol. 381, pp. 1457-1462, 2017.

[250] Pack-n-Tape. (2018). *3M 4905 VHB Tape Clear, 23 in x 72 yd 20.0 mil, 1 per case*. Available: https://pack-n-tape.com/3M-4905-VHB-Tape-Clear-23-in-x-72-yd-20.0-mil-1-per-case.html

[251] KJLC®. (2018). *Titanium Dioxide (TiO2) Black Pieces & Tablets Evaporation Materials*. Available: http://www.lesker.com/newweb/deposition_materials/depositionmaterials_evaporationmaterials_1.cfm?pgid=ti4b

[252] Sigma-Aldrich. (2018). *Poly(3,4-ethylenedioxythiophene)-poly(styrenesulfonate)*. Available: https://www.sigmaaldrich.com/singapore.html

[253] J. Elson and J. Bennett, "Relation between the angular dependence of scattering and the statistical properties of optical surfaces," *JOSA*, vol. 69, pp. 31-47, 1979.

[254] J. E. Harvey, "Fourier treatment of near-field scalar diffraction theory," *American Journal of Physics*, vol. 47, pp. 974-980, 1979.

[255] J. E. Harvey, "Light-scattering characteristics of optical surfaces," in *Stray Light Problems in Optical Systems*, 1977, pp. 41-48.

[256] D. H. Raguin and G. M. Morris, "Antireflection structured surfaces for the infrared spectral region," *Applied Optics*, vol. 32, pp. 1154-1167, 1993/03/01 1993.

[257] J. Chung and D. Blaser, "Transfer function method of measuring in-duct acoustic properties. II. Experiment," *The Journal of the Acoustical Society of America*, vol. 68, pp. 914-921, 1980.

[258] D. A. Russell, "Absorption coefficients and impedance," *Science and Mathematics Department, Kettering University, Flint, MI*, vol. 48504, 2004.

List of Publications

Refereed Journal Articles

1. M. Shrestha, Z. Lu, and G.-K. Lau, "Transparent tunable acoustic absorber membrane using inkjet printed PEDOT: PSS thin-film compliant electrodes," ACS applied materials & interfaces, 2018.
2. M. Shrestha, A. Asundi, and G.-K. Lau, "Smart Window Based on Electric Unfolding of Microwrinkled TiO2 Nanometric Films," ACS Photonics, 2018.
3. M. Shrestha and G.-K. Lau, "Tunable window device based on micro-wrinkling of nanometric zinc-oxide thin film on elastomer," Optics Letters, vol. 41, p. 4433, 2016.
4. Z. Lu, M. Shrestha, and G.-K. Lau, "Electrically tunable and broader-band sound absorption by using micro-perforated dielectric elastomer actuator," Applied Physics Letters, vol. 110, p. 182901, 2017.
5. H.-Y. Ong, M. Shrestha, and G.-K. Lau, "Microscopically crumpled indium-tin-oxide thin films as compliant electrodes with tunable transmittance," Applied Physics Letters, vol. 107, p. 132902, 2015.
6. G.-K. Lau and M. Shrestha, "Ink-Jet Printing of Micro-Electro-Mechanical Systems (MEMS)," Micromachines, vol. 8, p. 194, 2017.

Manuscripts Under Review or in Preparation

1. G.-K. Lau and M. Shrestha, "Review on new technologies for smart windows," to be submitted, 2018.
2. G.-K. Lau , M. Shrestha and Wei Deyuan, " Piezoresistive behavior of bi-axially microwrinkled thin film," to be submitted, 2018.

Refereed Conference Proceedings

1. M. Shrestha, Z. Lu, and G. K. Lau, "Ink-jet printing of transparent and stretchable electrodes for dielectric elastomer actuators," in *3nd*

International Conference on Progress in Additive Manufacturing (Pro-AM 2018) Singapore, 2018.

2. M. Shrestha, A. K. Asundi, and G. K. Lau, "Electrically tunable window based on wrinkled ZnO/Ag thin film," presented at the SPIE Smart Structures/NDE Portland, USA, 2017.
3. M. Shrestha, T.-G. La, and G. K. Lau, "Inkjet Printed Stretchable Electrodes For Tunable Focus Lens," in *2nd International Conference on Progress in Additive Manufacturing (Pro-AM 2016)* Singapore, 2016.
4. M. Shrestha and G.-K. Lau, " Full range transparency tuning by wrinkling of ZnO thin film," presented at the Conference: ThinFilms 2016, Singapore, 2016.
5. H.-Y. Ong, M. Shrestha, and G. K. Lau, "Crumpled indium-tin-oxide electrodes for transparency tuning," in Electroactive Polymer Actuators and Devices (EAPAD) 2016, 2016, p. 97981Z.
6. D. Wei, M. Shrestha, A. Asundi, and G.-K. Lau, "Controlled micro-wrinkling of ultrathin indium-tin-oxide films for transparency tuning," vol. 10449, p. 104492Q, 2017.